Resolving Many Mode Processes in Josephson Travelling Wave Parametric Amplifiers

T. Dixon

Department of Physics
Royal Holloway University of London

May 15, 2022

A thesis submitted in partial fulfilment for the degree of Doctor of Philosophy

Declaration

I confirm that the work presented in this thesis is my own. Where information has been derived from other sources, I confirm this has been indicated in the thesis.

T. Dixon

Abstract

In this thesis we quantify the generation of higher order tones in Josephson Travelling Wave Parametric Amplifiers (JTWPAs). We discuss the background theory of parametric amplification through optical non-linear wave mixing. Following this we show a set of experiments in which we observe unexpected tones. The first experiment describes a resonant device and gives an overview of standard measurement procedures and an insight into Josephson device behaviour. In the resonant device we demonstrate a single higher order tone being generated at a frequency which can be mapped back to the three wave mixing condition. The second experiment involves a more complex travelling wave device. Here we show that with a single tone one can generate a cascade of higher order harmonics. We then show that in the case of two input tones one can detect responses at various combinations of sums and differences of the two tones. This section motivates the rest of the work done in this thesis.

In order to gain insight into our experimental observations we use a circuit simulation software which includes the Josephson junction circuit element. We confirm the ability to model linear transmission lines with the software. We then explore the Josephson junction model and produce the standard results. We then model the travelling wave design which consists of a standard transmission line embedded with rf SQUIDs. Finally we discuss the observation of higher order tones in the simulation which are not present in the theory and relate the frequencies of these tones back to the tones observed in our experiment.

With a focus on these higher order tones we extend the standard coupled mode theory to allow for these higher order tones to be considered. We also consider the approximations made in the theory and subsequently alter the simulation to ensure their validity. We then finally resolve any discrepancies between the simulation and theory. This work forms the principles of my first manuscript which in turn has led to the further development of ideas to combat such higher order tones

Acknowledgements

I would like to thank Dr. Connor Shelly, who has been a truly formidable supervisor. As his first student (and potentially last as industry has snapped him up) I enjoyed many hours of his time. His relentless effort and ability has enabled huge growth and development for me, which I will never forget - for that I am very grateful. I would also like to thank Prof. Phil Meeson and Prof. Jonathan Williams whose experience and knowledge shone through in all of our discussions. I will always be impressed by their ability to see right to the heart of any problem and have appreciated any and all of their time. I wholeheartedly thank my colleagues and lab mates Dr. George Long and Dr. Jacob Dunstan, they have endured an unparalleled badgering and this work would not have been possible without their support - garden beers were essential. By being part of a large collaboration, I have enjoyed many illuminating conversations with collaborators these include; Prof. Yuri Pashkin, Prof. Alexander Zorin, Dr. Ralf Dolata, Dr. Marat Khabipov, Christoph Kißling, Angelo Greco, Searbhán Patton, Erik Jellyman. I have been surrounded by many thoughtful and supportive individuals at both institutions; Royal Holloway and the National Physical Laboratory. From Royal Holloway, I am grateful to Dr. Rais Shaikhadarov, Prof. Vladamir Antonov, Jan Knapp, Dr. Lev Levitin, Ian Murray, Andy Alway and the administration team at Royal Holloway, all of whom have provided expert guidance. From the National Physical laboratory I am grateful to; Dr. Jonathan Burnett, Dr. Sebastian De Graaf, Dr. Patrick See, Dr. Tobias Lindström, Prof. Alexander Tzalenchuk and Jon Virgo all of whom have provided some combination of guidance, ideas, equipment and support. To have the opportunity to work in both institutions has been hugely beneficial and I hope the strong collaboration remains into the future.

On a personal level I am eternally appreciative of Elise, who has been a pillar of support and patience during this time. To grow with her and watch us both flourish has made me so proud of

everything we have overcome together. Her blog[1] shows where she was at, at the start of this PhD, shortly after our undergraduate. To see where we both are now fills me with joy and excitement for the next chapter of our lives. I would also like to thank my large, and ever-growing, family for all that they have done for me. When the pandemic gives us a chance I look forward to seeing the new additions in person and sitting down with you all. I owe much to my friends who have encouraged me to keep going while they kept the beers flowing. And finally, I want to end where this all began, with my son - Archie. I went back to school when he was born, he is now 11 years old. He is the reason I have endured this endeavour. I hope that this serves as an example. I dedicate this thesis to him.

[1] https://glamourduck.tumblr.com/

For Archie.

Contents

1 Introduction **16**

1.1 Motivation 16

1.2 Prerequisite Understanding 17

1.2.1 Non-linear Wave Mixing 17

1.2.2 Transmission Line Theories 21

1.2.3 The Josephson Junction 24

1.2.4 The rf SQUID 25

1.3 Review 27

1.3.1 Josephson Parametric Amplifiers 27

1.3.2 Josephson Travelling Wave Parametric Amplifiers 29

1.4 This Thesis 32

1.4.1 Thesis Statement 34

2 Background Theory **35**

2.1 Parametric Amplification in Superconducting Circuits 35

2.1.1 Superconducting Transmission Line with Embedded Junction 35

2.1.2 rf SQUID embedded Travelling Wave Parametric Amplifier 38

2.2 Three wave mixing in rf SQUID Travelling Wave Parametric Amplifier 40

2.2.1 Control of the Centrosymmetry 40

2.2.2 Three Wave Mixing Model up to Three Tones 41

2.2.3 Practical Considerations of the Three Tone Model 42

3 Experimental Observations **48**

3.1 Higher Order Tones in a Resonant Device 49

3.1.1 Resonant Device 49

3.1.2 Resonator Characterisation Measurements 51

3.1.3 Resonator Wave Mixing 58

3.2 Higher Order Tones in Travelling Wave Device 64

3.2.1 Cascaded Harmonic Generation 64

3.2.2 Sum Frequency Generation 69

3.3 Summary 74

4 Simulations **75**

4.1 SPICE Network Analysis 75

4.2 Linear Transmission Line Modelling 76

4.2.1 LC Transmission Line Simualtion 76

4.2.2 Capacitvely Shunted M-line Model 78

4.3 Josephson Simulations 80

4.3.1 RCSJ Theory 80

4.3.2 DC Josephson Simulations 81

4.3.3 AC Josephson Simulations 83

4.4 rf SQUID JTWPA Simulation 85

4.5 Summary 91

5 Resolving WRspice Simulation and Theory **93**

5.1 Controlling the WRspice Simulation 94

5.2 Input Power Handling 97

5.2.1 Pump Input Power 97

5.2.2 Signal Input power 99

5.3 Extension to Coupled Mode Theory 103

5.3.1 Extension to Resolve WRspice and Coupled Mode Equations 110

5.4 Quasi Phase Matching Approach 119

5.5 Summary 126

6 Conclusion **128**

6.1 Conclusion 128

6.2 Further Work 130

Appendices **132**

A Theory **134**

A.1 Optical Wave Mixing 134

A.1.1 Non-linear Polarization 134

A.1.2 Difference Frequency Generation 135

A.1.3 Optical Parametric Amplification 136

A.2 Josephson Wave Mixing 139

A.2.1 Yaakobi Wave Equation 139

A.2.2 Flux Node 140

A.2.3 Yaakobi Total Current 141

A.2.4 Zorin Wave Equation 142

A.2.5 rf SQUID Embedded TWPA Reduced Wave Equation 145

A.2.6 Generating CMEs from the Wave Equation 146

B Simulations **151**

B.1 RCSJ Matlab Script 151

B.2 WRspice Netlist 153

C Extended Theory CME-5 **155**

C.1 Extension to CME-5 155

C.2 Quasi Phase Matching Matlab 158

List of Figures

1.1 Schematic of nonlinear tone generation in an optical crystal. 20

1.2 Qualitative plot of signal and idler gain through parametric amplification. 21

1.3 Circuit diagram of an infinitely long transmission line. 22

1.4 Circuit diagram of the lumped element LC transmission line. 23

1.5 Circuit diagram of capacitively shunted M-Line lumped element model. 24

2.1 Circuit diagram of Josephson Junction embedded transmission line. 36

2.2 Circuit diagram of an rf SQUID embedded transmission line. 39

2.3 β and γ curve for rf SQUID 41

2.4 3 tone model for parametric conversion and signal/idler gain. 43

2.5 Bandwidth sweep of three tone model 43

2.6 Example of bandwidth profiles taken at different output nodes. 44

2.7 Signal input power sweep of the three mode model. 45

2.8 Signal input power sweep of the three mode model in terms of amplifier gain. 46

2.9 Plot highlighting the $3\ \mathrm{dB}$ compression point for three physical amplifiers of length $N = 300,\ 400,\ 500$. 46

2.10 Sliced volume plot showing gain as function of frequency and power for amplifiers of total length $N = 300,\ 400,\ 500$. 47

3.1 Photo of resonant device and travelling wave device. 48

3.2 Cartoon of resonant modes in $\lambda/2$ resonator. 50

3.3 Experimental setup for Resonator calibration. 51

3.4 Example of Fano fit to resonant mode data. 52

3.5 Power bifurcation data of resonant device. 53
3.6 Fundamental response of resonant device over flux bias. 54
3.7 Second mode response of resonant device over flux bias. 54
3.8 Third mode response of resonant device over flux bias. 55
3.9 Fano fit for peak detection and conversion to frequnecy modulation plot over few added flux quanta. 55
3.10 Frequency modulation plot over many flux quanta to gauge optimum bias position. . 56
3.11 Resonator wave mixing experimental set up 57
3.12 Peak detection and recreation algorithm example. 59
3.13 Large sweep of fundamental response over flux bias and pump power. 60
3.14 Comparison of the peak positions of quasi fit function Ξ with the high and low power regimes in fig. 3.13 61
3.15 Correspondence of peak in fundamental mode and third mode. 61
3.16 Determination of the frequency relation between fundamental and third mode peaks. 62
3.17 Qualitative fit, motivating both three and four wave mixing regimes to produce peak in third mode of the resonator. 63
3.18 Experimental setup for travelling wave device single tone spectroscopy. 65
3.19 Large voltage sweep to deduce voltage to added flux ratio for travelling wave device. 67
3.20 Zoom in over the assigned range of one added flux quanta $\approx 3.3V$. 67
3.21 3d plot of cascaded harmonic generation over flux and power through single tone spectroscopy. 68
3.22 Experimental set up for two tone spectroscopy to demonstrate harmonic generation as well as up conversion tones in a travelling wave device. 70
3.23 3d plot of pump and signal behaviour through two tone spectroscopy in high power regime. Second harmonic also plotted to show flux dependence. 71
3.24 3d plot showing flux dependence of up-conversion terms in relation to second harmonic generation in high power regime. 72
3.25 3d plot showing second harmonic generation reaching an amplitude above the signal in the low signal power regime. 72

3.26 Plot showing power dependence of six tones incl. harmonic generation, idler and up conversion tones as well as pump and signal. 73

4.1 Circuit diagram of lumped element model transmission line 76

4.2 Plot comparing simulation of LC lumped line to theory including front end transmission through mismatched port (insertion loss). 77

4.3 Plot comparing the measured simulation phase shift per unit cell with the theoretical phase shift from lumped element network analysis. 78

4.4 Circuit diagram of lumped element model for a capacitively shunted M-line 78

4.5 Plot showing the reduce cut-off frequency simulated and compared to theory for a capacitively shunted M-line 79

4.6 Plot comparing the super-linear phase relation derived from the continuum approximation with the lumped element network theory and simulation extracted phase shift per cell. 80

4.7 RCSJ model of the current branches used in the simulation tool WRspice. 81

4.8 Basic simulation to construct DC I-V characteristics of a single Josephson junction . 82

4.9 Voltage-time trace of the over the Josephson junction for varies bias DC currents. . . 82

4.10 Theoretical I-V curve comparison with the simulated I-V curve showing the standard DC behaviour of a Josephson junction. 83

4.11 RCSJ model of Josephson junction with AC current source. 84

4.12 AC I-V characteristics of Josephson junction showing Shapiro steps. 84

4.13 Circuit diagram of flux biased rf SQUID embedded JTWPA. 85

4.14 Extracted source current and input current from WRspice simulation. 87

4.15 Extracted output currents from WRspice simulation showing signal, pump and idler indicative of wave mixing but at amplitude inconsistent with three mode theory. . . . 88

4.16 Example of current vs time raw data and Hann window. 89

4.17 Plot comparing the current amplitude of pump, signal and idler over entire 500 node JTWPA for both simulation and 3-mode CME. 90

4.18 3d surface showing all frequencies up to 60 GHz over the entire simulated JTWPA. . 90

4.19 Plot of the pump and the second harmonic of the pump in the simulated JTWPA. . . 91

4.20 Heatmap perspective of the spectrum up to 60 GHz over all 500 nodes of simulated JTWPA. 92

5.1 Heatmap showing the large phase swing in the simulation of the TWPA, an indicator that some theoretical assumptions may need to be reviewed. 95

5.2 The junction phase evolution through the ramp time showing the lag for middle junctions as well as the small ripple before settling down. 95

5.3 Qualitative plot showing the time taken for the wave to reach the end of the device. . 96

5.4 Snapshot phase vs. node plot compared to a 12 GHz wave using the dispersion relation for an M-line. 97

5.5 Plots showing the reduction in phase caused by lowering the input pump power. . . . 98

5.6 Heatmap of the reduced phase swing over entire TWPA. 98

5.7 Plot of low signal gain in the case of reduced pump power. 99

5.8 Comparison of the CME result with WRspice result after the pump is lowered and then for decreasing signal input currents. 100

5.9 Surface plot of the low pump and signal regime showing a much less complex behaviour of the tones over the entire device. 100

5.10 Heatmap which shows clearly the oscillation between pump and second harmonic as well as the frequencies of up-conversion tones extending up to 60 GHz. 101

5.11 Plot showing a qualitative description of third harmonic generation through a 3WM SFG process between pump and second harmonic. 102

5.12 Comparison of the extended CME example to WRspice and the qualitative approximation to third harmonic generation. 109

5.13 Plots showing successive imporvements between CME fit and WRspice as we include more tones in the CME's. 111

5.14 Surface plots showing the ability to fit all tones in the extended CME's to WRspice result. 112

5.15 Summary plot showing the improved fit of signal profile and how the final extension gain value approaches the simulated gain value at the output node. 114

5.16 Vector representation of the considered tones in CME extension. 115

5.17 Mixing matrix representation for all 3WM mechanisms up to third harmonic of pump. 116

5.18 Mixing matrix after any non-pump-mediated mixing is removed from the original mixing matrix. 118
5.19 Poling scheme for the tapered QPM design. 121
5.20 Plot of the phase shift per unit cell with far reduced cut off frequnecy in the QPM design. 121
5.21 Theoretical QPM profile for showing the characteristic oscillations with saddle points at the same position as the zeroes of the η function. 123
5.22 Pump and SHG profiles for the QPM design which shows the reduction in SHG, particularly in the region of maximum signal gain. 124
5.23 Signal and idler growth in comparison to a non QPM device showing large 20dB gain and flat profile around maximum gain indicative of flat bandwidth. 125
5.24 Snapshot in time of the measured Josephson junction phase showing the poling periodicity being replicated in the WRspice simulation. 125
5.25 Fit between the WRspice model showing exponential current gain, akin to linear power gain, and CME model where a reasonable fit is achieved. 126

B.1 WRspice circuit file for the JTWPA 154

Chapter 1

Introduction

1.1 Motivation

Quantum computing was first envisaged by Richard Feynman in 1982. The proposal was simple, if a system can be reduced such that quantum states can be differentiated between and manipulated, then quantum mechanical behaviour can be efficiently simulated. This began the race for a quantum computer, whose processor would be made of quantum bits (qubits). These are typically two level systems (TLS), where the considered states of the system are the two lowest energy level states. These qubits can then be in either of the energy states or any linear superposition of the states. Combining this with entanglement between qubits would allow for a quantum processor to rapidly outperform a classical processor comprising of classical bits for certain problems.

Over the last 40 years, a lot of focus was devoted to the development of the qubit. Qubits came in various forms such as; Superconducting microwave qubits, optical ion trap qubits, semiconductor quantum dots, and diamond nitrogen vacancy (NV) centres. Each of these have attached pros and cons. However, at the time of writing this thesis, the first work claiming to demonstrate quantum supremacy was achieved using superconducting microwave qubits [1].

This "flavour" of superconducting microwave qubits has risen to prominence and is now widely regarded as the front running technology for a realisable practical quantum computer. From the first demonstration of superconducting qubits [2] the community has rapidly evolved to overcome many of the engineering challenges of making, manipulating and measuring these qubits. For the purpose of this thesis we will solely discuss this superconducting microwave technology and further mention of

devices will be based around this type of architecture.

Fundamentally, any useful qubit will always suffer from a near-paradoxical point. *In order to maintain quantum mechanical behaviour, the qubit must be isolated from the highly classical environment. However to be useful, we as classical entities, must interact with it.* This has led to further development in the wider community. In the same way that a classical computer is more than just a processor, a practical quantum computer is more than just a qubit. So following this, focus shifted to further hardware considerations for use in quantum information processing. Of these, low-noise amplifiers have been quintessential in the reliable measurement of qubits.

Typically superconducting qubits emit photons at the transition energy corresponding to the difference between the ground and first excited state. For the superconducting qubits these photons are in the microwave regime $f \sim 5$ GHz and thus have energies of order $E_f \approx 3.3 \times 10^{-24}$ J. To aid in the detection of these the "Josephson Parametric Amplifier" (JPA) has been developed whose noise is limited by the standard quantum limit [3]. The underlying physics of parametric amplification via the non-linear response of the Josephson junction is the key phenomena which is studied in this thesis. The Josephson Travelling Wave Parametric Amplifier (JTWPA) is a broadband extension of the JPA which at the time of writing this thesis is the state of the art technology in broadband, low noise amplification and is the main focus of this thesis.

1.2 Prerequisite Understanding

1.2.1 Non-linear Wave Mixing

Optical Wave Mixing Example

The core principle of parametric amplification derives from the more general phenomenon of Wave Mixing (WM). This WM phenomenon is typically described by wave equations which contain non-linear dependencies. The theoretical study of such equations predates the 19th Century [4, 5, 6]. To gain an intuition for the origin of parametric amplification deriving from non-linear WM we consider the phenomenon in terms of an optical WM example [7] and discuss the underlying theory following the method described in [8].

Optical WM was experimentally recorded in maser technology [7], whereby pulsing an optical

beam through a material with a non-linear dielectric coefficient produced a harmonic pulse. The experiment used a monochromatic source (Trion technologies pulsed ruby optical maser) and filtered out other (Xenon flashes in this case) background radiation using a red filter. This was then focused onto a quartz crystal, which in the presence of an electric field has a non-linear polarization state. To understand this we progress from the linear polarization approximation that

$$\tilde{P} = \epsilon_0 \chi \tilde{E}. \tag{1.1}$$

This is simply a first order approximation to avoid any non-linear dependence of the polarization on the applied field. In general we write,

$$\vec{P} = \epsilon_0 \chi \vec{E}, \tag{1.2}$$

which is expanded into a power series

$$\vec{P}^{(1)} + \vec{P}^{(2)} + \vec{P}^{(3)} + ... = \epsilon_0 \Big(\chi^{(1)} E^1 + \chi^{(2)} E^2 + \chi^{(3)} E^3 + ... \Big). \tag{1.3}$$

We then derive the wave equation (see Appendix A.1.1) in the usual manner from Maxwell's equations under the assumption that there are no free charges $\vec{J} = 0$ and the material has no magnetization $\vec{B} = \mu_0 \vec{H}$,

$$\nabla^2 \vec{E} - \frac{1}{c^2} \frac{\partial^2}{\partial t^2} \vec{E} = \frac{1}{\epsilon_0 c^2} \frac{\partial^2 \vec{P}}{\partial t^2}. \tag{1.4}$$

A "simple" model of three wave mixing (3WM) can be found in [8], for example. Propose that $\vec{E}$ is comprised of two electric fields of at two different frequencies (ω_1, ω_2),

$$\vec{E} = E_1 e^{-i\omega_1 t} + E_2 e^{-i\omega_2 t} + c.c. \, , \tag{1.5}$$

where $c.c.$ stands for the complex conjugate. Then the second order non-linear polarization states ($P^{(2)}$) given by the expansion in equation 1.3,

$$\begin{aligned}\vec{P}^{(2)} =&\epsilon_0\chi^{(2)}\Big[E_1^2e^{-2i\omega_1 t}+E_2^2e^{-2i\omega_2 t}+2\Big[E_1E_2e^{-i(\omega_1+\omega_2)t}+E_1E_2^*e^{-i(\omega_1-\omega_2)t}\Big]+c.c.\Big]\\ &+2\epsilon_0\chi^{(2)}\Big[E_1E_1^*+E_2E_2^*\Big],\end{aligned} \tag{1.6}$$

which gives rise to electric field oscillating at sums and differences of the input fields. The names for these in the community are:

- $E_i^2e^{-2i\omega_i t}$ - Second Harmonic Generation (SHG)
- $2E_iE_je^{-i(\omega_i\pm\omega_j)t}$ - Sum/Difference Frequency Generation (SFG)/(DFG)
- $E_1E_1^*+E_2E_2^*$ - Optical Rectification (OR)

Parametric Amplification

Consider the example of difference frequency generation. There is a response at the difference of the input frequencies ($\omega_3=\omega_1-\omega_2$). This means that if we input two signals; one at ω_1 the other at ω_2. We write down our wave equation in terms of the output signal generated at ω_3 (the third wave in 3WM),

$$\nabla^2E_3-\frac{1}{c^2}\frac{\partial^2E_3}{\partial t^2}=\frac{1}{\epsilon_0c^2}\frac{\partial^2\vec{P}_3(\omega_1-\omega_2)}{\partial t^2}. \tag{1.7}$$

By assuming a plane wave with spatially dependent amplitude and non-linear coefficient $\chi^{(2)}=4k_3^2d_{eff}$, one can show (see Appendix A.1.2) that in one dimension,

$$\frac{\partial^2A_3}{\partial z^2}+2ik_3\frac{\partial A_3}{\partial z}=-4k_3^2d_{eff}A_1A_2^*e^{i(k_1-k_2-k_3)z}. \tag{1.8}$$

If the amplitude of the field only varies slowly along the propagation axis $A(z)$ such that

$$\frac{\partial^2A_i}{\partial z^2}\ll k\frac{\partial A_i}{\partial z}\ll k^2A_i(z), \tag{1.9}$$

then,

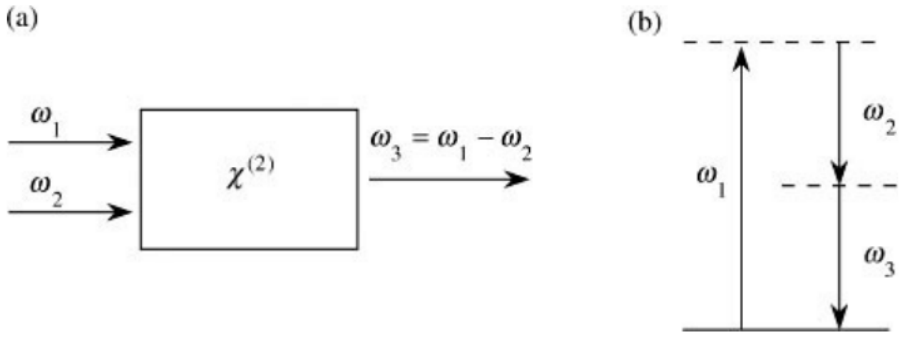

Figure 1.1: Image reproduced from [8]. (a) Schematic of a non linear crystal mixing two waves at frequency ω_1 and ω_2 to generate another wave at frequency $\omega_3 = \omega_1 - \omega_2$. In the case where one wave (assigned as the pump) frequency is larger than the other (assigned the signal) frequency one simply considers a photon energy conservation rule (b) $\hbar\omega_1 = \hbar\omega_2 + \hbar\omega_3$. The interpretation is that in the presence of the signal 1 pump photon is down converted into 1 signal photon and 1 idler photon inside the non-linear medium.

$$\frac{\partial A_3}{\partial z} = 2ik_3 d_{eff} A_1 A_2^* e^{i(k_1 - k_2 - k_3)z}. \tag{1.10}$$

We draw this schematically as two waves incident (ω_1 and ω_2) upon a non-linear medium, giving rise to a third wave at the difference of the two input frequencies ($\omega_3 = \omega_1 - \omega_2$):

We derive an equation analogous to eq. (1.10) for the signal,

$$\frac{\partial A_2}{\partial z} = i2d_{\text{eff}} k_2 A_1 A_3^* e^{i\Delta kz}, \tag{1.11}$$

where,

$$\Delta k = k_1 - k_2 - k_3. \tag{1.12}$$

Following the strong pump approximation and zero phase mismatch ($\Delta k = 0$) we arrive at the two non trivial solutions for signal and idler amplitudes as shown in appendix A.1.3,

$$A_s(z) = A_{s0} \cosh(\kappa z) \tag{1.13}$$

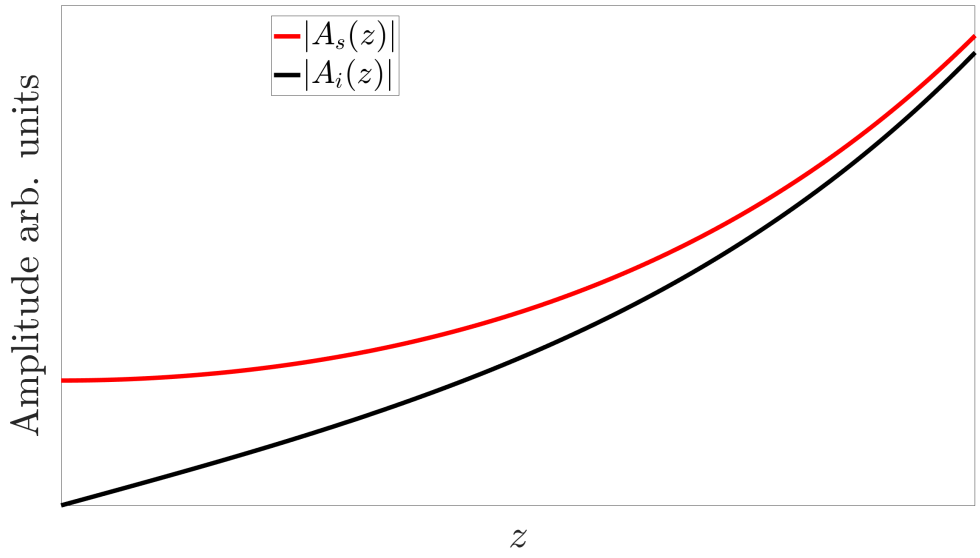

Figure 1.2: Qualitative plot showing the exponential rise in absolute signal and idler amplitudes along the z direction. Under the case of strong pump and zero phase mismatch the exponential rise continues up to $z \to \infty$.

$$A_i(z) = i\sqrt{\frac{k_s}{k_i}}\frac{A_p}{|A_p|}A_{s0}^{*}\sinh(\kappa z), \tag{1.14}$$

where

$$\kappa = 2\sqrt{k_s k_i}d_{eff}|A_p|. \tag{1.15}$$

1.2.2 Transmission Line Theories

In this thesis we focus on wave mixing and parametric amplification within superconducting devices. We briefly discuss a wave mixing observation in a resonant device in section 3.1.3 and then move on to analysing travelling wave devices throughout the rest of the thesis. The travelling wave device is an extension of the linear transmission line which we discuss in this section.

Continuous LC Transmission Line

An infinitely long, lossless, continuous transmission line consists of series inductance per unit length and parallel capacitance to ground as shown below.

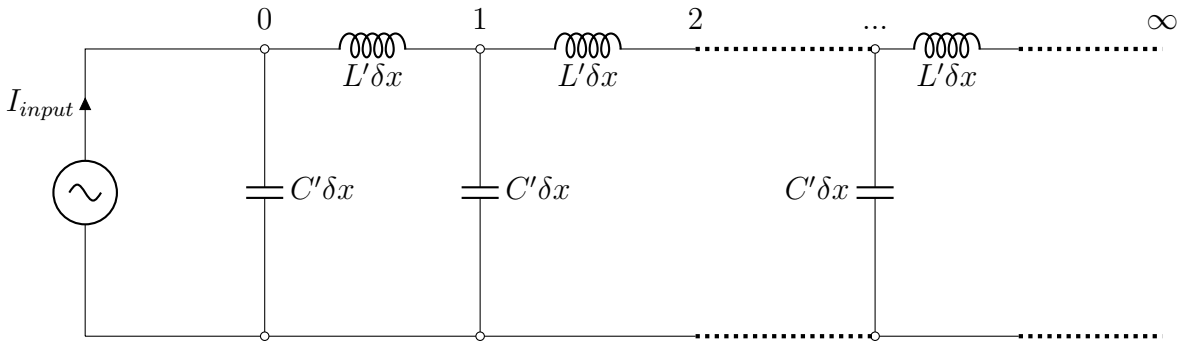

Figure 1.3: Circuit diagram of an infinitely long transmission line in the continuum limit. Here δx describes an infinitesimal length of line, with C' and L' representing the capacitance and inductance per unit length.

The difference in current through each successive inductor is given by the current through the ground capacitor,

$$\Delta I = \frac{I(x+dx) - I(x)}{dx}\delta x = -C'\delta x \frac{\partial V(x)}{\partial t}. \tag{1.16}$$

Similarly the difference between voltage over successive capacitors is given by the voltage over an inductor,

$$\Delta V = \frac{V(x+dx) - V(x)}{dx}\delta x = -L'\delta x \frac{\partial I(x)}{\partial t}. \tag{1.17}$$

The Telegraphers wave equation is then be derived to show,

$$\frac{\partial^2 I}{\partial x^2} = LC\frac{\partial^2 I}{\partial t^2}. \tag{1.18}$$

There exists an analogous equation for the voltage. With a plane wave solution $I = I_0 e^{i(kx-\omega t)}$, phase velocity $\theta' = w/k$ and line impedance $Z = V_0/I_0$, one can deduce the standard results,

$$\theta^{'} = \frac{1}{\sqrt{L'C'}}, \tag{1.19}$$

$$Z = \sqrt{\frac{L'}{C'}}. \tag{1.20}$$

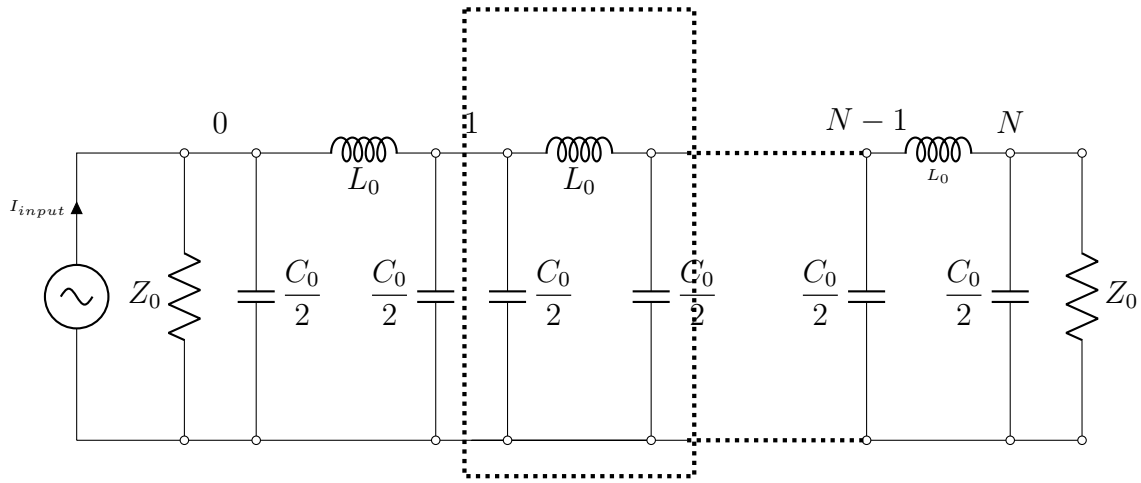

Figure 1.4: Circuit diagram of the lumped element model of a standard LC transmission line. Here the inductors and capacitors are single "lumped elements" in an array and the dashed line encompasses a repeating Π cell.

Lumped Element Model

We can also use a lumped element analysis as shown in fig. 1.4. This is detailed in [9] for transmission lines as well as more exotic variants. In such an analysis we define a repeated section of the line as the unit cell.

The ratio of currents flowing around each Π section (unit cell), $I_1/I_2 = I_\mathrm{n}/I_{\mathrm{n}+1} = F$, gives the propagation constant F. This constant is rewritten as $F = e^{-\zeta}$ where $\zeta = \alpha + i\theta$. The correct termination for this finite line is given in [9]. By inspection ζ consists of an attenuation constant α, and a phase shift θ. Here θ defines the phase shift per unit cell and for this standard LC line analysis it is given that [9],

$$\cos(\theta) = 1 - \frac{\omega^2 L_0 C_0}{2}. \tag{1.21}$$

This is satisfied for $0 < \omega < 2/\sqrt{L_\mathrm{g} C_0}$ where the upper limit describes a cut off frequency of the line $\omega_\mathrm{c} = 2/\sqrt{L_\mathrm{g} C_0}$. Frequencies above this will result in a non-zero attenuation constant α and a $\theta = \pm\pi$ phase shift in each unit cell. Through this analysis the characteristic impedance of the line also has a frequency dependence given by,

$$Z(\omega) = \sqrt{\frac{L_0}{C_0}} \frac{1}{\sqrt{1 - \omega^2/\omega_\mathrm{c}^2}}. \tag{1.22}$$

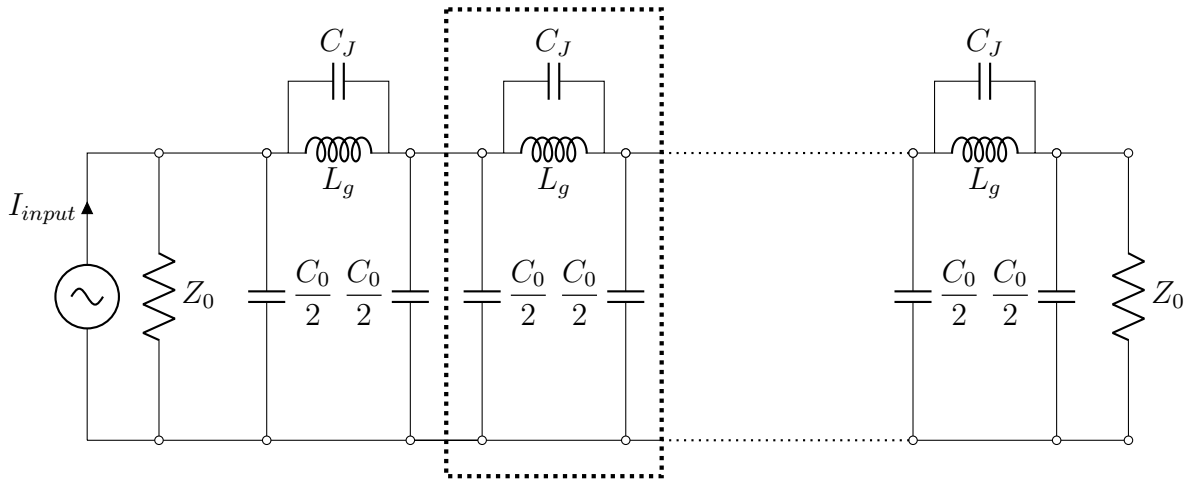

Figure 1.5: Circuit diagram of capacitively shunted M-Line lumped element model. The shunt capacitors C_{J} alter the line properties giving additional curvature to the dispersion relation.

For frequencies much lower than the cut off frequency eq. (1.22) approaches eq. (1.20).

Shunt Capacitance Model

In this thesis we make use of a slightly modified model when considering a linear transmission line by including a shunt capacitor C_{J} in parallel with the inductors L_{g} as shown in fig. 1.5.

Analysis of this capacitively shunted line (M-line) gives a new cut off frequency, [10] - see appendix C in [11] for a brief discussion,

$$\omega_{\mathrm{c}} = \frac{2}{\sqrt{L_{\mathrm{g}}(C_0 + 4C_{\mathrm{J}})}}. \tag{1.23}$$

This is due to a revised phase shift per unit cell,

$$\theta = \arccos\Big(1 - \frac{\omega^2 L_{\mathrm{g}} C_0}{2(1 - \omega^2 L_{\mathrm{g}} C_{\mathrm{J}})}\Big). \tag{1.24}$$

1.2.3 The Josephson Junction

Josephson Relations

In the early 60s Brian Josephson mathematically formulated the theory of tunneling Cooper pairs across tunnel junctions, now referred to as Josephson junctions, and gave the two Josephson relations [12]

$$I_{\mathrm{J}} = I_{\mathrm{c}} \sin\varphi \tag{1.25}$$

$$V_{\mathrm{J}} = \frac{\partial \Phi}{\partial t} = \frac{\hbar}{2e}\frac{\partial \varphi}{\partial t} \tag{1.26}$$

Here, I_{J} is the current through the Josephson junction, I_{c} is the critical current of the Josephson junction, and φ represents the phase difference in the superconducting wave functions at the interfaces of the Josephson junction. With some simple manipulation of the standard voltage-inductance relation,

$$V = L\frac{\partial I}{\partial t},$$

the Josephson inductance is found to be,

$$L_{\mathrm{J}} = V_{\mathrm{J}} \frac{1}{\left(\frac{\partial I}{\partial \varphi}\frac{\partial \varphi}{\partial t}\right)}$$

$$= \frac{\hbar}{2eI_{\mathrm{c}}\cos\varphi} = \frac{\Phi_0}{2\pi I_c \cos\varphi}, \tag{1.27}$$

where the flux quantum $\Phi_0 = h/2e$. This then gives a source of non-linear inductance modulated by a coefficient of order Φ_0/I_c. The argument $\varphi = 2\pi\phi/\Phi_0$ gives an oscillation periodicity in flux per unit flux quanta and thus, this is a highly sensitive non-linearity on the order of single quantum parameters ($e, \Phi_0, ...$). A year after the theory, Anderson and Rowell recorded the first measurement of these effects [13]. This brought the theory of a new highly sensitive non-linear medium to the forefront of modern physics, and facilitated realisations of the quantum theory predictions with experimental results for applicable electrical-engineering purposes.

1.2.4 The rf SQUID

By creating a ring or loop of superconducting material and embedding a JJ inside this ring, one creates a Superconducting Quantum Interference Device (SQUID). The wave function around the loop must

be continuous, meaning the superconducting phase must evolve by 2π integers, this further lead to flux quantisation. The phase drop over the junction φ and phase of the superconductor - related to the total field through the loop (Φ_{T}), are then given by,

$$\varphi + 2\pi\frac{\Phi_{\mathrm{T}}}{\Phi_0} = 2\pi n. \tag{1.28}$$

Where Φ_0 is the flux quantum. If an external field (Φ_{ext}) is applied to the loop then φ reacts to maintain eq. (1.28). This causes a screening current to flow as per eq. (1.25) which provides additional field inside the loop,

$$\Phi_{\mathrm{T}} = \Phi_{\mathrm{ext}} + L_{\mathrm{g}} I_{\mathrm{J}} = \Phi_{\mathrm{ext}} - L_{\mathrm{g}} I_{\mathrm{c}} \sin(2\pi\frac{\Phi_{\mathrm{T}}}{\Phi_0}). \tag{1.29}$$

Where we have set $n = 0$ for simplicity. Equation (1.29) is further simplified by introducing the screening parameter $\beta_{\mathrm{L}} = 2\pi L_{\mathrm{g}} I_{\mathrm{c}}/\Phi_0$ and rewriting in terms of the superconducting phase difference over the junction $\varphi = 2\pi\Phi/\Phi_0$,

$$\varphi_{\mathrm{ext}} = \varphi + \beta_{\mathrm{L}} \sin(\varphi). \tag{1.30}$$

Furthermore we can inject rf tones into one side of the SQUID, where the rf splits through either the junction or the inductive branch, and exits the other side of the SQUID. The total inverse inductance (L_{T}^{-1}) of the rf SQUID as seen from the rf is then [14],

$$\frac{1}{L_{\mathrm{T}}} = \frac{1}{L_{\mathrm{g}}} + \frac{1}{L_{\mathrm{J}}}. \tag{1.31}$$

If a constant DC flux bias $\Phi_{\mathrm{DC}} = (\Phi_0/2\pi)\varphi_{\mathrm{DC}}$ is applied to the rf SQUID then the current-phase relation associated to any additional AC current injected into the rf SQUID is given by [14],

$$I(\varphi_{\mathrm{AC}}) = \frac{I_{\mathrm{c}}}{\beta_{\mathrm{L}}}\varphi_{\mathrm{AC}} + I_{\mathrm{c}}\Big[\sin(\varphi_{\mathrm{DC}} + \varphi_{\mathrm{AC}}) - \sin(\varphi_{\mathrm{DC}})\Big]. \tag{1.32}$$

In this thesis we will be using this current phase relationship (CPR) of the rf SQUID to describe the AC tones as waves, in line with the previous wave mixing section.

1.3 Review

1.3.1 Josephson Parametric Amplifiers

The first mention of JPA measurements was made by H. Zimmer in 1967 [15]. By depositing a thin strip diagonally across a face on a cube rutile resonator, oxidising in atmosphere for 15 minutes and then depositing another thin strip at right angles they formed the Josephson junction. This was not a well controlled procedure and by Zimmer's own admission "... *the formation of a junction in an evaporated layer is more or less a question a lucky chance...*".

Critically, the junction was known to be a dissipation-less circuit element below its critical current. With this the attention turned to noise in Josephson circuits. It was known that, by the Heisenberg uncertainty principle, any bosonic signal must incorporate an uncertainty ($S(\omega)$) of at least $S(\omega) = \hbar\omega/2$. In 1982, Caves [3], showed that a "phase-insensitive" amplifier must add at least this noise due to quantum mechanics. However, Caves also showed that this is overcome if one is only interested in one quadrature phase of the signal. In this case noise can be "squeezed" in the measured quadrature at the expense of added noise in the unmeasured quadrature. Kuzmin, Likharev, Migulin and Zorin studied these noise properties directly in the case of JPAs [16]. They found that by operating a JPA in the degenerate mode, that is where the signal and idler frequency are the same $f_{\mathrm{s}} = f_{\mathrm{i}}$, then the added noise can indeed be lower than the standard quantum limit.

Three years later, in 1985, Smith *et. al.* [17] specifically measured a JPA in terms of its noise properties. While a low noise temperature $T_{\mathrm{N}} \approx 6$ K was deduced, they also highlighted many of the sub-optimal properties of the device, which are closely related to this thesis. Firstly, they measured the device in the three wave mixing (3WM) condition, ($f_{\mathrm{p}} = f_{\mathrm{s}} + f_{\mathrm{i}}$). Second, they noted the possibility of other idler frequencies, predominantly the pump harmonic $f_{2\mathrm{p}} = 2f_{\mathrm{p}}$ or near zero frequency terms, analysis of these further generated tones form a substantial discussion in this thesis.

Following this, engineering steps were made to optimise the device and in 1989 Yurke measured both the gain as well as the noise squeezing properties of the JPA [18]. While this demonstration of an amplifier operating at the fundamental limit of quantum mechanics was novel, practical requirements for such an amplifier were sparse.

A decade later in 1999 Nakamura, Pashkin and Tsai demonstrated the capability to control the quantum mechanical states of a two level system (TLS) solid-state device, named the cooper-pair

box [2]. This discovery was the first time macroscopic control over the quantum states was shown in solid-state superconducting devices.

Following this discovery, Wallraff *et. al.* [19] demonstrated that by embedding such a TLS in a resonator one can make a continuous transmission measurement by measuring the transmission properties of the resonator to infer the qubit state. This work led the way for coupling between the photonic behaviour of qubits to the electrical properties of microwave resonators. Due to the delicate nature of the measurement previous work in JPAs was revisited. Since JPAs already operate in the microwave regime, and had been shown to introduce low noise to the system, the community quickly took to re-purposing these devices in the context of quantum information processing readout tools.

At the same time other single-shot dispersive readout systems were being considered. For example, Siddiqi *et. al.* demonstrated a Josephson Bifurcation Amplifier (JBA) [20] which was then used for single shot qubit readout [21]. Biasing the JJ near a bifurcation point of the system means that an additional, small, rf-drive can tip the system into one of two distinct oscillation states. These meta-stable states then apply low back action. Also, by the nature of a bifurcation, these two states are distinct and stable meaning a latched readout scheme can be achieved. JBAs have been used in qubit readout as already mentioned as well as platforms for so-called quantum non-demolition measurement [22]. The latching bifurcation style readout has also been extended to more exotic HyQUID type devices [23] and Josephson Parametric Oscillators (JPOs) [24, 25]. The latter of these also reported single-shot qubit readout [26] with a fidelity (maximum state discrimination) of 81.5%.

While many of these system demonstrated promising results for single shot readout of a qubit the community was aware of the scalability of such schemes. The resonant nature of all of these devices constrained the bandwidth of operation to be within the line-width of the cavity modes. By utilising two junction Superconducting QUantum Interference Devices (DC SQUIDs) Castellanos-Beltran and Lehnart [27] were able to tune the resonant mode of a superconducting cavity between $4 - 7.8$ GHz by applying magnetic flux to adjust the DC SQUID inductance. In this experiment the JPA was measured over nearly an octave ($\#_{\mathrm{octave}} = \log_2(f_{max}/f_{min})$) of frequencies by adjusting the magnetic field. They also achieved up to 28 dB gain. The noise temperature T_{N} in the degenerate case $f_{\mathrm{p}} = f_{\mathrm{s}} = f_{\mathrm{i}} \approx 6.95$ GHz was found to be $T_{\mathrm{N}} \approx 300$ mK where the standard quantum limit noise temperature at this frequency would be $\hbar\omega/2k_B \approx 166$ mK, inferring that the input noise of the amplifier was less than twice the standard quantum limit.

As an example of other uses, Hatridge *et. al.* [28] performed very sensitive magnetometry with a similar JPA using an embedded DC SQUID to achieve an effective flux noise of $0.14\ \mu\Phi_0\mathrm{Hz}^{-1/2}$ over a bandwidth of $0.6\ \mathrm{MHz}$. Returning to qubit readout, Abdo *et. al.* [29] designed an exotic device consisting of two perpendicular resonators with four Josephson junctions arranged in a Wheatstone bridge configuration at the centres (antinodes) of the resonators. Here they achieved modest gain $G > 10\ \mathrm{db}$ across an instantaneous bandwidth $B \approx 60\ \mathrm{MHz}$, and an added photon noise number of $\eta = 1 \pm 0.5$ at the signal frequency. This is an example of the implementation of JJs into known circuitry, such as the Wheatstone bridge to add non-linear wave mixing properties to well understood circuitry. Still these devices suffered from the gain-bandwidth trade off inherent in resonant devices. As such, attention turned to travelling wave designs free from the resonator constraints.

1.3.2 Josephson Travelling Wave Parametric Amplifiers

Discussions around general travelling wave parametric amplifiers predate the Josephson junction [30]. These devices were called upon for broadband sensitive amplification and again relied upon a non-linear component to activate the parametric interaction and the wave mixing. These devices were then reviewed from the point of view of superconducting solid state devices.

Initially, the kinetic inductance of the superconducting film itself provided the non-linearity in so called Kinetic Inductance Travelling Wave Parametric Amplifiers (KITWPA) [31]. Here, the critical current of a thin superconducting wire (I_*) gives an upper bound and obvious current scale, much like the critical current of a JJ (I_c). Well below this critical current one can realise a simple, non-linear, current dependent result for the kinetic inductance, $L_\mathrm{k} \approx L_k(0)[1 + (I/I_*)^2]$ [31]. Typically $L_\mathrm{k} << L_\mathrm{T}$ where L_T is the total inductance of the line. This means that the non-linearity is very weak in the superconducting wire. However using Titanium nitride (TiN) or Niobium-Titanium nitride (NbTiN) one can increase the normal state resistivity by up to three orders of magnitude [32] which drastically increases the relative non-linearity of the system.

Such a device was developed and tested by Eom *et. al* [31]. It was known that harmonic generation of the pump tone will be the largest generated tone in a bare device. As such, band gap engineering was utilised by implementing periodic loading along the line. This blocks the generation of the third harmonic of the pump, and the subsequent cascade of tone generation via waves mixing with this tone. The coupled mode theory for kinetic inductance devices is very similar to that of Josephson based

devices, which are the focus of this thesis.

This coupled mode theory was then extended to include JJs embedded in a transmission line by Yaakobi *et. al.* [33]. Here the JJs replace the linear inductor in a standard ladder type transmission line to form a Josephson Travelling Wave Parametric Amplifier (JTWPA). With this one can consider the finite differences between voltage to ground at successive nodes and convert this to flux through Maxwells equations. In the limit that the unit cell size between nodes is sufficiently smaller than the wavelength of waves considered these finite differences are converted to a differential wave equation. These coupled mode equations are discussed in detail in appendix A.2.6.

The theory for JTWPA was then further extended to include resonant phase matching by O'Brien *et. al.* [34]. They describe a process whereby simultaneously diminishing the phase matching of up-converted tones (SFG, harmonic generation) and promoting the phase matching of down-converted tones (DFG, signal amplification) one can achieve larger and more broadband gain [34]. This is achieved by capacitively coupling resonators along the line. One can then tune the dispersion relation of the device such that an asymptotic pole is produced at the resonators frequency. If the pump is then situated near this frequency, the pump phase can be adjusted, in a tight frequency range, anywhere between $\pm\pi/2$. This allows for a linear relationship between pump, signal and idler wave vectors. This resonant phase matching can also cause a greater phase mismatch in higher frequency tones, reducing the up-conversion to higher modes.

This idea was developed and tested by T. C. White *et. al.* [35] in 2015. The device consisted of 1326 JJs in total, separated into 17 sections of 78 JJs each. Each section had a $\lambda/4$ resonator capacitively coupled at its centre. The spacing between resonators was also carefully chosen to be at a spacing sufficient to suppress third harmonic generation of the pump, as per the band gap engineering in the KITWPA mentioned previously. However this device only achieved $6-8\ \mathrm{dB}$ of gain. This was then increased by joining two devices together, however the target $20\ \mathrm{dB}$ was not shown.

Shortly after this C. Macklin. *et. al.* also demonstrated a resonant phase matched JTWPA [36]. This time it consisted of 2037 JJs and 700 resonators spaced every three JJs. This led to considerable improvements in the gain and bandwidth characteristics, $G > 20\ \mathrm{dB}$ over a $3\ \mathrm{GHz}$ bandwidth. This coupled with the large bandwidth, high gain and low pump power requirements defined the state-of-the-art in JTWPA experiments at the start of this project. The main problems with this device were gain ripples associated with improper impedance matching. Also a pump power dependent phase shift can

cause calibration uncertainties and makes in-situ tuning of the device difficult. Fabrication complexity was also undesirable. In fact Tan and Yassin suggested a uniplanar fabrication method with spiral $\lambda/4$ resonators to aid with fabrication complexity shortly after [37].

The natural progression from this was more complex non-linear elements. Bell and Samolov proposed a JTWPA consisting of a chain of asymmetric Superconducting QUantum Interference Devices (SQUIDs) [38]. This would allow for a flux tunable device. This device was again an extension of the ladder type transmission line. In this case, the pump power dependant phase modulation terms (self- and cross- phase modulation) are dependent on both the pump power and the flux bias point of the SQUID. They derive a total phase mismatch along the line:

$$\kappa = -\alpha_{\mathrm{p}} \frac{2\omega_{\mathrm{p}}^2}{k_{\mathrm{p}}^3} \Big(\frac{k_{\mathrm{s}}^3}{\omega_{\mathrm{s}}^2} + \frac{k_{\mathrm{i}}^3}{\omega_{\mathrm{i}^2}} - \frac{k_{\mathrm{p}}^3}{\omega_{\mathrm{p}^2}} \Big) - \Delta k. \tag{1.33}$$

Here the subscripts $\mathrm{p},\ \mathrm{s},\ \mathrm{i}$ represent the pump, signal and idler waves based on the mixing condition $2\omega_{\mathrm{p}} = \omega_{\mathrm{s}} + \omega_{\mathrm{i}}$. Δk is the usual linear phase mismatch due to the transmission line properties, $\Delta k = -2k_{\mathrm{p}} + k_{\mathrm{s}} + k_{\mathrm{i}}$. The point here is that k_{p} and the pump complex amplitude a_{p} can be tuned by the flux. If they have opposite sign (shown for a flux $0.31\Phi_0 < \Phi < 0.5\Phi_0$), then the total phase mismatch $\kappa \approx 0$ and exponential signal gain can theoretically be achieved in this tunable system.

Following this, Zorin [14] developed a novel concept of an rf SQUID embedded transmission line. Its model was simpler in principle to the SQUID model mentioned previously. In Zorin's model there is no JJ coupling between SQUIDS. Also, the rf SQUIDS are biased identically with no asymmetry. But the core principle of tunability remains.

However Zorin showed that one can do more than phase matching by tuning the flux. He showed that tuning the flux in a rf SQUID can alter the symmetry of the system. Biasing the rf SQUID with flux, thus producing a circulating current, initiates a phase difference over the junctions. Since the rf SQUIDs are all symmetric and oriented identically the phase drop across the junctions caused by the screening current is identical. When this phase drop φ is 0 or a multiple of π then no current is flowing through the junction. This can be seen from the Josephson relation eq. (1.25). In this case there is no directionality to the biased system. However at any other flux bias a net current flows through the junction and the system inherits a directionality based on the sign of this current. At flux bias positions $\Phi = (2n+1)\Phi_0/2 \implies \varphi = n\pi/2$ the current flowing through the JJ is biased at its critical current

and the non-linearity becomes even.

Zorin shows that by expanding the rf SQUID current phase relation about this even point one can operate in the "three wave mixing" (3WM) scheme. This has certain benefits over the 4WM scheme and is discussed in detail in this thesis.

The fabrication of such a device is simpler than the RPM JTWPAs as it doesn't require additional insulator layers. The footprint of the device is also reduced without the need for additional resonators. The main features of this proposal are that the gain and bandwidth can be achieved in a tunable device without the need for additional fabrication complexity. This also constitutes the most current theoretical proposals in terms of JTWPAs at the beginning of this project. The rf SQUID embedded transmission line is studied in detail in this thesis.

1.4 This Thesis

In this thesis we will ultimately look to quantify the generation of higher order tones in Josephson Travelling Wave Parametric Amplifiers. We provide a background overview to the main phenomena of nonlinear wave mixing in microwave circuitry. We then show two experiments which highlight the generation of unwanted higher order modes in such devices. We then move on to SPICE simulations which further demonstrate the generation of unwanted tones which cascade outside the bandwidth of our experimental set up. We conclude by developing a numerical model which can account for higher order tone generation in rf SQUID JTWPAs and demonstrate the accuracy of this model with the circuit simulation giving insight into the underlying wave mixing mechanisms.

Chapter 2

To highlight the underlying physics, we first discuss the general background theory of parametric amplification from the point of view of non-linear wave mixing first observed in the optics community. We discuss how these ideas migrated into the microwave community via the Josephson junction. For an in-depth understanding of the main topic of this thesis we will analyse two poignant theoretical papers [14, 33]. This will provide all of the background theory necessary to understand the key points of the rest of the thesis.

Chapter 3

Following this, we show a brief set of experiments. In these experiments we observe the generation of unwanted higher order tones. We will begin with a resonant based device which will give an overview of some standard measurement procedures as well as insight into Josephson device behaviour. In the resonant device we will finally demonstrate a single higher order tone being generated at a frequency which is mapped back to a three wave mixing condition. We then move on to the more complex travelling wave device. Here we first show that with just a single tone one can generate a cascade of higher order harmonic tones. We then show that in the case of two input tones one can detect responses at various combinations of sums and differences of the two tones. This section motivates the rest of the work done in this thesis.

Chapter 4

In order to gain insight into our experimental observations, we use a circuit simulation software package, WRspice, which includes the Josephson Junction circuit element. We first confirm the ability to model linear transmission lines with the software. We then explore the Josephson junction model and produce the standard results for single Josephson junctions. We model the theoretical proposal in [14], which consists of a standard transmission line embedded with rf SQUIDs. Finally, we discuss the observation of higher order tones in the SPICE simulation which are not present in the current three mode theory and relate the frequencies of these tones back to the tones observed in our experiment.

Chapter 5

Finally, we focus on these higher order tones, we extend the standard coupled mode theory to allow for these higher order tones to be considered. We also consider the approximations made in the theory and subsequently alter the simulation to ensure these approximations are respected. We then finally resolve the discrepancies between the simulation and theory. This work forms the principles of my first manuscript [11]. Which has led to the further development of ideas to combat such higher order tones [39, 40]. We complete this chapter with a brief overview of one such method, quasi-phase matching. We show through the extended coupled mode theory and circuit simulation that this method significantly reduces the amplitude of higher order tones, particularly at the output of the quasi-phase

matched rf SQUID embedded JTWPA.

1.4.1 Thesis Statement

To summarise, the aim of this thesis is to resolve many mode interactions in rf SQUID embedded JTWPAs. We observe these higher order tones both experimentally and through circuit simulation. We provide an extended numerical model, highlighting the mixing mechanisms and intuition on how these tones cascade through the device. We demonstrate excellent quantitative agreement between the circuit simulation and our numerical model. Thus we simultaneously highlight the problem of generation of unwanted tones, provide a model to explain them and use this understanding to promote engineering solutions to mitigate this problem.

Chapter 2

Background Theory

2.1 Parametric Amplification in Superconducting Circuits

This section will describe the background theory for implementing Josephson junctions into standard electrical circuitry. First, by looking at a standard transmission line with embedded Josephson junctions as described by Yaakobi *et al.* [33], we will see how the non-linear current phase relation enables wave mixing through a non-linear wave equation. Then we will show how this wave equation may be modified by replacing the Josephson junction with an rf SQUID as proposed by Zorin [14]. The introduction of the rf SQUID allows for flux tuning of the device and we will show in detail how this alters the operating principles of the device. Finally in this section, we will discuss general considerations one must make when describing practical specifications of such a device.

2.1.1 Superconducting Transmission Line with Embedded Junction

We follow the theory of Yaakobi *et. al.* to describe a transmission line with embedded Josephson junctions [33]. The circuit is set up as shown in fig. 2.1.

By stating that the current flowing into a node must be equal to the current flowing out of a node, we find,

$$I_{n-1} = I_{C,n} + I_n,$$

$$I_n = I_{C_\mathrm{J},n} + I_{L,n},$$

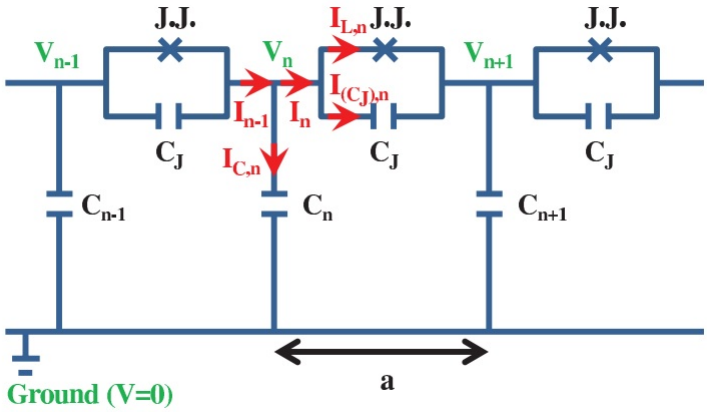

Figure 2.1: Circuit diagram of Josephson Junction embedded transmission line. Here the Josephson junction is a non-linear inductor. If the Josephson junction is swapped for a linear inductor then the circuit is equivalent to the capacitively shunted line discussed in section 1.2.2. Image taken from [33].

$$\implies 0 = I_{C,n} + (I_{C_{\mathrm{J}},n} - I_{C_{\mathrm{J}},n-1}) + (I_{L,n} - I_{L,n-1}). \tag{2.1}$$

The current across each of the capacitors C_J are given by the time derivative of the relative potential difference of the nodes spanning the capacitor, i.e,

$$I_{C_{\mathrm{J}},n} = -C_{\mathrm{J}} \frac{d}{dt}\Big[V_{n+1} - V_n\Big]. \tag{2.2}$$

Using the Josephson equations, the Maxwell relation $V_{\mathrm{n+1}} - V_{\mathrm{n}} = -d\Phi_{\mathrm{n}}/dt$ and some elementary manipulations (see Appendix A.2.1), we find the time derivative of flux at the nth node to be,

$$\frac{d\Phi_n}{dt} = \frac{\Phi_0}{2\pi I_c}\frac{dI_{L,n}}{dt} + \frac{\Phi_0}{12\pi I_c^3}\frac{d}{dt}[I_{L,n}]^3. \tag{2.3}$$

We then define [33] the absolute voltage in terms of the node fluxes Φ_{n},

$$V_n \equiv \frac{d\Phi_n}{dt}. \tag{2.4}$$

We derive an expression for the current through the nth junction (see Appendix A.2.2),

$$I_{L,n} \approx -\frac{1}{L}(\Phi_{n+1} - \Phi_n) + \frac{\Phi_0}{12\pi L^4 I_c^3}(\Phi_{n+1} - \Phi_n)^3. \tag{2.5}$$

The current through the capacitor at the nth node is defined using the grounded capacitor equation,

$$I_{n-1} - I_n = C_n \frac{dV_n}{dt} + \frac{V_n}{R_n} = I_{C,n}. \tag{2.6}$$

And finally combining the currents entering and exiting a node one finds (see Appendix A.2.3),

$$\begin{aligned} 0 = {} & C_n \frac{d^2\Phi_n}{dt^2} + \frac{1}{R_n}\frac{d\Phi_n}{dt} - C_J \frac{d^2}{dt^2}\Big[\Phi_{n+1} + \Phi_{n-1} - 2\Phi_n\Big] \\ & - \frac{1}{L}(\Phi_{n+1} + \Phi_{n-1} + 2\Phi_n) - \frac{\Phi_0}{12\pi L^4 I_c^3}\Big((\Phi_{n+1} - \Phi_n)^3 - (\Phi_n - \Phi_{n-1})^3\Big). \end{aligned} \tag{2.7}$$

We then move to forming a derivative by way of the continuum theory. We define the node flux difference between nodes as follows; first we define the second derivative,

$$\frac{\partial^2\Phi(x)}{\partial\tilde{x}^2} = \lim_{h\to 0}\frac{\Phi(x+h) - 2\Phi(x) + \Phi(x-h)}{h^2}.$$

The derivative is formed in the limit where our step size h, instead of going to zero, goes to the length of unit cell, a. We then replace $h \to a$. We also note that $\Phi(x) \equiv \Phi_n,\ \Phi(x+a) \equiv \Phi_{n+1},\ \Phi(x-a) \equiv \Phi_{n-1}$, to give,

$$\Phi_{n+1} + \Phi_{n-1} - 2\Phi_n = a^2\frac{\partial^2\Phi}{\partial\tilde{x}^2}. \tag{2.8}$$

An ansatz is given in [33], namely,

$$\Phi_{n+1} - \Phi_n \approx a\frac{\partial\Phi}{\partial\tilde{x}} + \frac{1}{2}a^2\frac{\partial^2\Phi}{\partial\tilde{x}^2}, \tag{2.9}$$

$$\Phi_n - \Phi_{n-1} \approx a\frac{\partial\Phi}{\partial\tilde{x}} - \frac{1}{2}a^2\frac{\partial^2\Phi}{\partial\tilde{x}^2}. \tag{2.10}$$

Subtracting eq. (2.10) from eq. (2.9) results in eq. (2.8). More importantly eqs. (2.9) and (2.10) gives a good approximation for the cubic terms in eq. (2.7). Note, we rewrite the two continuum approximation equations as,

$$\Phi_{n+1} - \Phi_n = A + B, \tag{2.11}$$

$$\Phi_n - \Phi_{n-1} = A - B, \tag{2.12}$$

where $A = a\frac{\partial \Phi}{\partial \tilde{x}}$ and $B = \frac{1}{2}a^2\frac{\partial^2 \Phi}{\partial \tilde{x}^2}$. It then follows that,

$$(A+B)^3 - (A-B)^3 = 2B^3 + 3A^2B \tag{2.13}$$

$$= \frac{1}{4}a^6\Big(\frac{\partial^2\Phi}{\partial\tilde{x}^2}\Big)^3 + 3a^4\frac{\partial^2\Phi}{\partial\tilde{x}^2}\Big(\frac{\partial\Phi}{\partial\tilde{x}}\Big)^2. \tag{2.14}$$

It is at this point we make the assumption that $\frac{\partial^2\Phi}{\partial\tilde{x}^2} \ll \frac{\partial\Phi}{\partial\tilde{x}} \ll \Phi$ and thus we neglect the first term in the bottom line of eq. (2.14) to give,

$$(\Phi_{n+1} - \Phi_n)^3 - (\Phi_n - \Phi_{n-1})^3 \approx 3a^4\frac{\partial^2\Phi}{\partial\tilde{x}^2}\Big(\frac{\partial\Phi}{\partial\tilde{x}}\Big)^2, \tag{2.15}$$

We then take eq. (2.8) and eq. (2.15) substitute into our quasi-differential equation eq. (2.7),

$$\begin{aligned} 0 = {} & C_n\frac{d^2\Phi_n}{dt^2} + \frac{1}{R_n}\frac{d\Phi_n}{dt} - C_J a^2\frac{d^2}{dt^2}\frac{\partial^2\Phi}{\partial\tilde{x}^2} \\ & - \frac{1}{L}a^2\frac{\partial^2\Phi}{\partial\tilde{x}^2} - \frac{\Phi_0 a^4}{4\pi L^4 I_c^3}\Big(\frac{\partial^2\Phi}{\partial\tilde{x}^2}\Big)\Big(\frac{\partial\Phi}{\partial\tilde{x}}\Big)^2. \end{aligned} \tag{2.16}$$

This describes the process for setting up the non-linear wave equation including Josephson junctions embedded into a transmission line.

2.1.2 rf SQUID embedded Travelling Wave Parametric Amplifier

Following the Josephson junction embedded transmission line, Zorin [14] has compiled a wave equation for a series of embedded SQUID arrays as shown in fig. 2.2.

Using the rf SQUID current phase relationship eq. (1.32) Zorin derives (see Appendix A.2.4) an analogous wave equation for the rf SQUID embedded JTWPA,

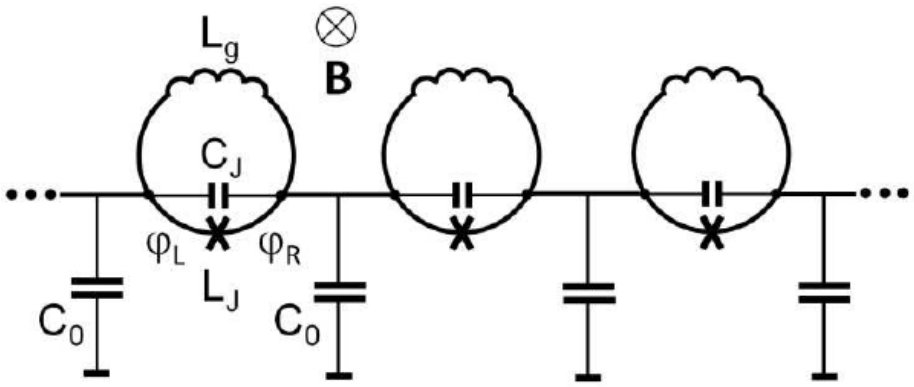

Figure 2.2: Circuit diagram of an rf SQUID embedded transmission line as proposed by Zorin. Here the current may flow through an additional branch given by the geometric inductance L_{g}. This allows flux tuning of the system as discussed in section 1.2.4. Image taken from [14].

$$\frac{\partial^2 \varphi_{AC}}{\partial x^2} - \beta \frac{\partial}{\partial x}\Big[\Big(\frac{\partial \varphi_{AC}}{\partial x}\Big)^2\Big] - \gamma \frac{\partial}{\partial x}\Big[\Big(\frac{\partial \varphi_{AC}}{\partial x}\Big)^3\Big] - \omega_j^{-2} \frac{\partial^4 \varphi_{AC}}{\partial x^2 \partial t^2} + \omega_0^{-2} \frac{\partial^2 \varphi_{AC}}{\partial t^2} = 0, \tag{2.17}$$

where,

$$\beta = \beta_{\mathrm{L}} \sin(\varphi_{\mathrm{DC}})/2,$$

$$\gamma = \beta_{\mathrm{L}} \cos(\varphi_{\mathrm{DC}})/6,$$

are coefficients controlled by the external field Φ_{ext} applied to the rf SQUIDs, this dependence is expanded upon in the next section. Also, we have transformed to a more natural position of $x = \tilde{x}/a$, i.e position in units of node number. We also now drop the AC notation as we are only interested in AC terms $\varphi_{\mathrm{AC}} \rightarrow \phi = 0.5 \sum_m \{[A_m(x) e^{i(k_m x - \omega_m t)} + c.c.]\}$ in a similar manner to Yaakobi, where m is assigned to the tones being considered. In the super-linear case where $\beta = \gamma = 0$ eq. (2.17) reduces to,

$$\frac{\partial^2 \phi}{\partial x^2} - \omega_0^{-2} \frac{\partial^2 \phi}{\partial t^2} + \omega_J^{-2} \frac{\partial^4 \phi}{\partial x^2 \partial t^2} = 0. \tag{2.18}$$

This is solved with a 1 dimensional plane wave solution, $\phi = e^{i(kx - \omega t)}$, which gives the characteristic, continuous dispersion relationship,

$$k(\omega) = \frac{\omega}{\omega_0} \frac{1}{\sqrt{1 - \frac{\omega^2}{\omega_J^2}}}. \tag{2.19}$$

Here $k = 2\pi a/\lambda$, $\omega_0 = 1/\sqrt{L_g C_0}$ and $\omega_J = 1/\sqrt{L_g C_J}$, N.B. k is unitless from our transform $x = \tilde{x}/a$. Comparing eq. (2.19) to the phase change per unit cell in eq. (1.24), with the approximation $\arccos(1-x) \approx \sqrt{2x}$, one can see that $k \approx \theta$ and the continuous dispersion is an approximation to the lumped element phase shift per cell.

Using the dispersion relation eq. (2.19) and the wave equation above one can derive a simplified wave equation for the system (see appendix A.2.5),

$$ik\frac{d\phi}{dx} = \beta\frac{d}{dx}\Big[\Big(\frac{\partial\phi}{\partial x}\Big)^2\Big] + \gamma\frac{d}{dx}\Big[\Big(\frac{\partial\phi}{\partial x}\Big)^3\Big]. \tag{2.20}$$

2.2 Three wave mixing in rf SQUID Travelling Wave Parametric Amplifier

2.2.1 Control of the Centrosymmetry

A key feature of the rf SQUID JTWPA is the ability to control the strength of β and γ with an external flux. We calculate these through the transcendental equation eq. (1.29) and plot as per Fig. 2 of [14], which we have reproduced in fig. 2.3, for a range of SQUID parameters (β_L).

Coupling magnetic flux into the rf SQUID loop produces a non-zero phase drop across the junction. When $\varphi_{DC} \neq 0$, $\sin(\varphi_{DC}) \neq 0$ and thus the even terms in the φ_{AC} expansion contribute. This means the current phase relationship is non-symmetric about its centre, mathematically $I(-\varphi_{AC}) \neq -I(\varphi_{AC})$, or non-centrosymmetric.

From fig. 2.3 and eq. (1.32), we see that maximising the even non-linearity coefficient β (red) inherently brings $\gamma = 0$ (blue) and thus by tuning the DC phase (via tuning the flux threading the SQUID loop) we tune the contribution of even and odd terms in the expansion.

Typically the language used to describe mixing mechanisms with $\beta = \text{maximum}, \gamma = 0$ is "three wave mixing (3WM)" (non-centrosymmetric) while the $\gamma = \text{maximum}, \beta = 0$ coefficient describes a "four wave mixing (4WM)" mechanism (centrosymmetric). In an unbiased scheme the parametric

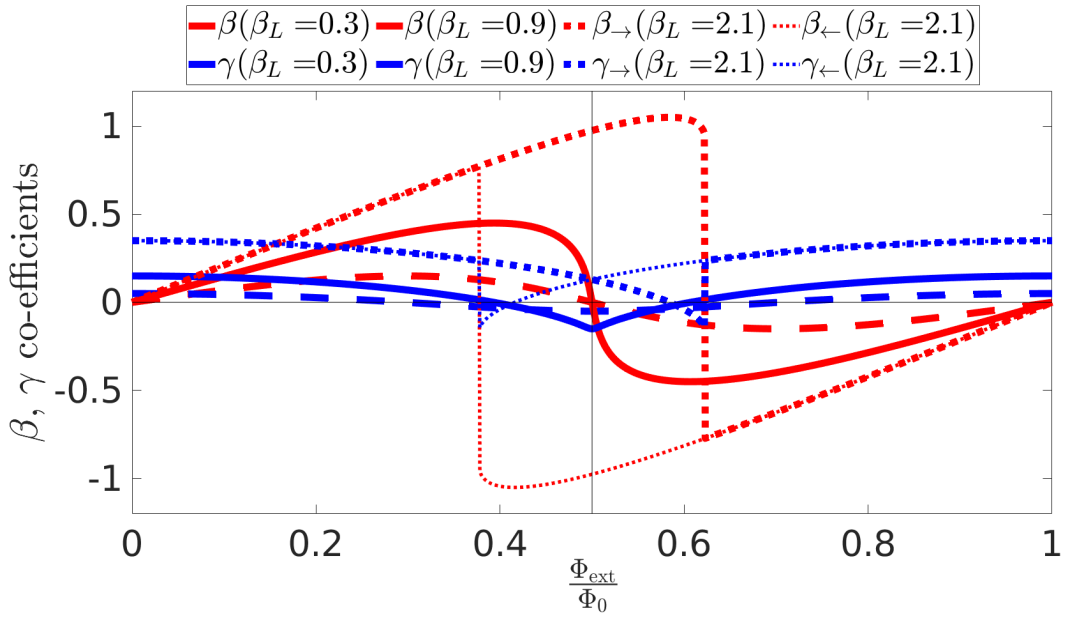

Figure 2.3: Tunability of the rf SQUID parameters β (red) and γ (blue) for various $\beta_{\mathrm{L}} = 0.3,\ 0.9,\ 2.1$ (solid, dashed, dotted and circles respectively). Note the hysteretic nature for $\beta_L > 1$ (dotted lines) mapped in both the up (thick) and down (thin) sweep of externally applied magnetic flux.

amplification of the signal depends on the γ coefficient however this also introduces modulation of the pump phase via its self-interaction. This puts a limit on the amount of signal gain to self-phase modulation in the "4WM regime" that can be achieved and is saturated by pump power. However, by applying an external flux bias (Φ_{ext}) β, ($\gamma \approx 0$, see fig. 2.3), "3WM regime" then the gain is now controlled by the β parameter.

2.2.2 Three Wave Mixing Model up to Three Tones

Under the assumption that we bias the rf SQUID loop such that $\gamma = 0$, the reduced wave equation eq. (2.20) becomes,

$$ik\frac{d\phi}{dx} = \beta\frac{d}{dx}\Big[\Big(\frac{\partial\phi}{\partial x}\Big)^2\Big]. \tag{2.21}$$

Here, the wave mixing is completely described by the nonlinear term on the right hand side. By prescribing the tones (m) we wish to consider into ϕ we construct the coupled mode equations. For example, if $m = \mathrm{p},\ \mathrm{s},\ \mathrm{i}$ corresponding to pump, signal and idler tones respectively we recreate a set of

CMEs (see appendix A.2.6) similar to that considered in [14].

$$\frac{dA_{\mathrm{p}}}{dx} = -\frac{\beta}{2} k_{\mathrm{s}} k_{\mathrm{i}} A_{\mathrm{s}} A_{\mathrm{i}} e^{i((k_{\mathrm{s}}+k_{\mathrm{i}})-k_{\mathrm{p}})x}, \tag{2.22}$$

$$\frac{dA_{\mathrm{s}}}{dx} = \frac{\beta}{2} k_{\mathrm{i}} k_{\mathrm{p}} A_{\mathrm{i}}^{*} A_{\mathrm{p}} e^{i((k_{\mathrm{p}}-k_{\mathrm{s}})-k_{\mathrm{i}})x}, \tag{2.23}$$

$$\frac{dA_{\mathrm{i}}}{dx} = \frac{\beta}{2} k_{\mathrm{s}} k_{\mathrm{p}} A_{\mathrm{s}}^{*} A_{\mathrm{p}} e^{i((k_{\mathrm{p}}-k_{\mathrm{s}})-k_{\mathrm{i}})x}. \tag{2.24}$$

The three wave mixing condition implies that the pump frequency $f_{\mathrm{p}} = f_{\mathrm{s}} + f_{\mathrm{i}}$. One common assumption is to propose an undepleted pump, that is to suggest that the pump is a large unchanging reservoir. This is done analytically in [14], however, here we set the derivative of the pump (eq. (2.22)) to zero. Alternatively, we could model the situation for a variable pump power, and in both cases the amplitude of the signal and idler will begin to rise as shown in fig. 2.4, which is a recreation of fig. 3 in [14].

The prediction of these CME's describes 20dB signal gain. This gain is at a fixed frequency and input power of the "pump" and "signal". In an ideal amplifier, we would like to achieve this over a range of signal parameters and have the ability to tune the pump. This means that we characterise our amplifier over a range of input signals (based at a static pump in frequency and power) and record the output signal power. So long as the output signal is higher than the input, then we have achieved amplification.

2.2.3 Practical Considerations of the Three Tone Model

In order to characterise gain in a way compatible with a real device, the output measurements must be all taken at the same node. This point may seem obvious but can cause confusion later, and thus a simple demonstration is made here. To study the bandwidth characteristics of this model we sweep the signal frequency holding the signal input constant ($I_{\mathrm{s}}^{\mathrm{rms}} \approx 0.12\ \mu\mathrm{A}$) as shown in fig. 2.5.

The node at which the signal is maximised changes as we sweep the signal frequency, particularly as we approach the pump frequency $f_{\mathrm{s}} \to f_{\mathrm{p}} = 12\ \mathrm{GHz}$. For signal frequencies between $4 - 8\ \mathrm{GHz}$

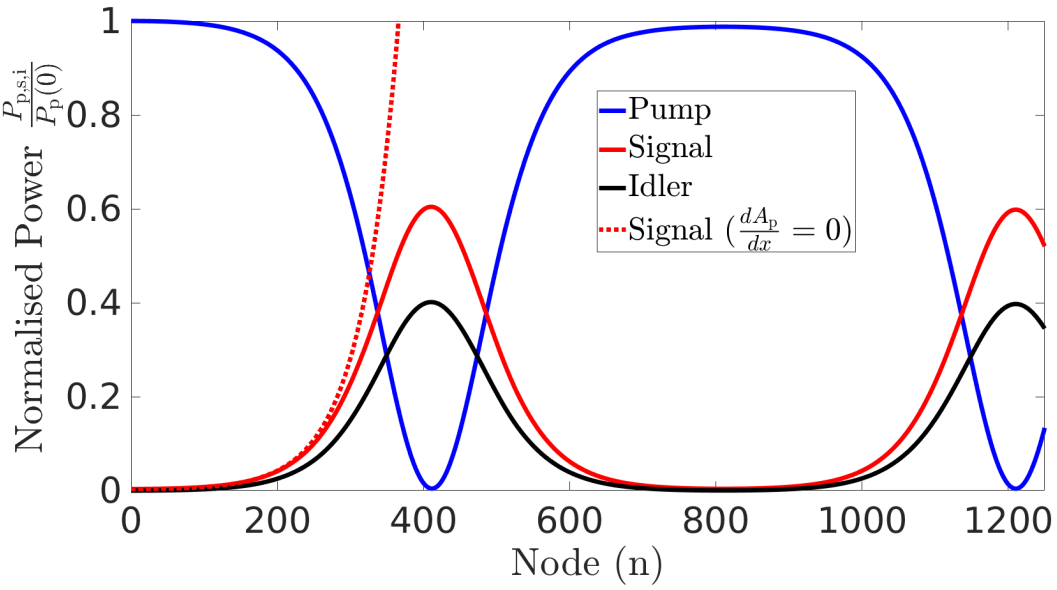

Figure 2.4: Recreation of fig. 3 in [14] where we have extended the "length" of the amplifier to demonstrate the repeating amplification and de-amplification process. The signal (red) approaches 60% pump input power at the coincidence of maximal pump depletion. The idler (black) reaches 40%, and the pump (blue) is fully depleted giving rise to a maxima in the signal and idler curves. The dashed red line shows the signal power in the case of an undepleted pump. The signal power becomes nonphysical ($P_{\mathrm{s}}(x) > P_{\mathrm{p}}(0)$) for $n \gtrapprox 400$ in the undepleted case.

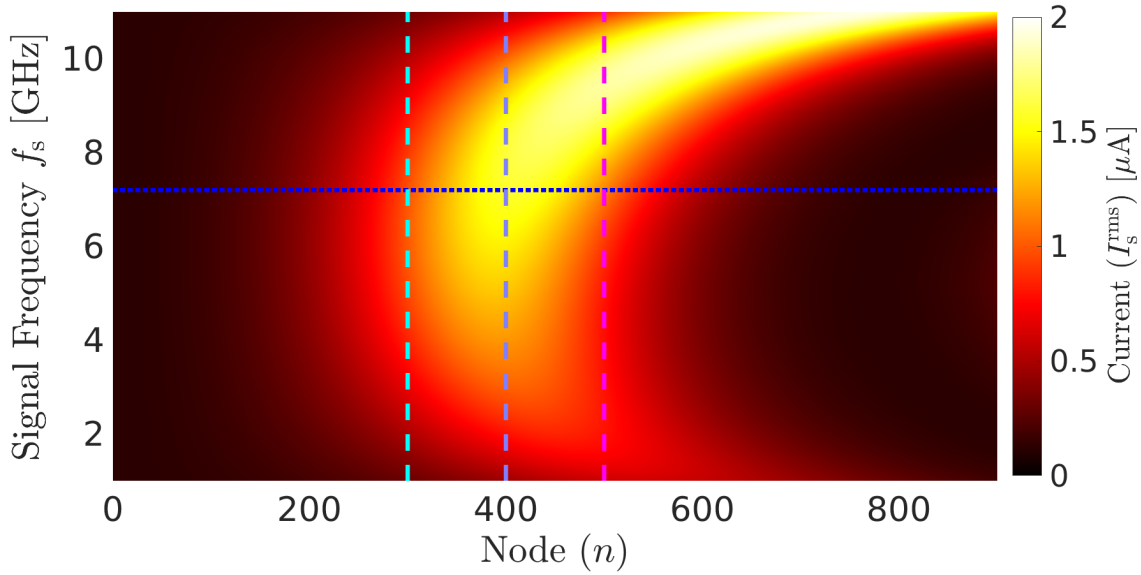

Figure 2.5: Heatmap of the signal current at each node (n) of the amplifier, for signal frequencies $1 < f_{\mathrm{s}} < 11$ GHz. A horizontal slice at $f_{\mathrm{s}} = 7.2$ GHz (blue dotted line) corresponds to the signal in fig. 2.4. The maxima of signal around node $n \approx 400$ (blue dashed line) is seen for $f_{\mathrm{s}} = 7.2$ GHz. Note that the maxima of signal occurs at different nodes as we vary signal frequency. The three vertical slices (dashed lines) at nodes $n = 300,\ 400,\ 500$ (cyan, blue, magenta) give the various bandwidth profiles for different length amplifiers.

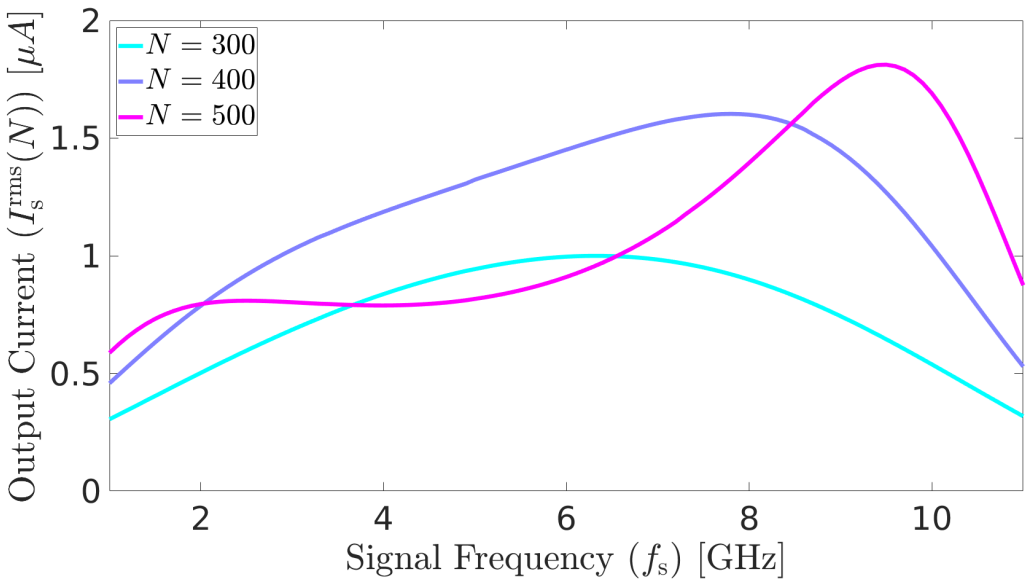

Figure 2.6: Plot showing the bandwidth profiles of three vertical slices taken from fig. 2.5 at nodes $n = 300,\ 400,\ 500$. The bandwidth profile is both qualitatively and quantitatively affected by choice of total length of amplifier.

we can take node $n = 400$ as an optimum output node. We have highlighted this length amplifier in the central vertical slice (blue) in fig. 2.5. The other two vertical slices at $n = 300$ (cyan) and $n = 500$ (magenta) give very different profiles over the bandwidth, as highlighted in fig. 2.6.

We have shown how the frequency response of the amplifier is affected by the choice of length. Next, we discuss how the power response may be affected by the choice of amplifier length. In figs. 2.5 and 2.6, the signal level is reported in rms current. However, a more useful scale is the decibel system which provides a relative unit of logarithmic power. For example, the dBm scale references the measured power relative to $1\ \mathrm{mW}$,

$$P_x = 10 \log_{10} \left(\frac{(I_x^{\mathrm{rms}})^2 \cdot Z}{1\ \mathrm{mW}} \right). \tag{2.25}$$

Note, that as we are following the device parameters given in [14], the impedance $Z \approx 23.87\Omega$. The input signal power in figs. 2.5 and 2.6 is $P_s(0) \approx -95\ \mathrm{dBm}$.

Figure 2.7 shows that as the signal input power is increased, for a constant signal frequency ($f_s = 7.2$ GHz), the maximum signal output power is reached at a lower node number. However, the

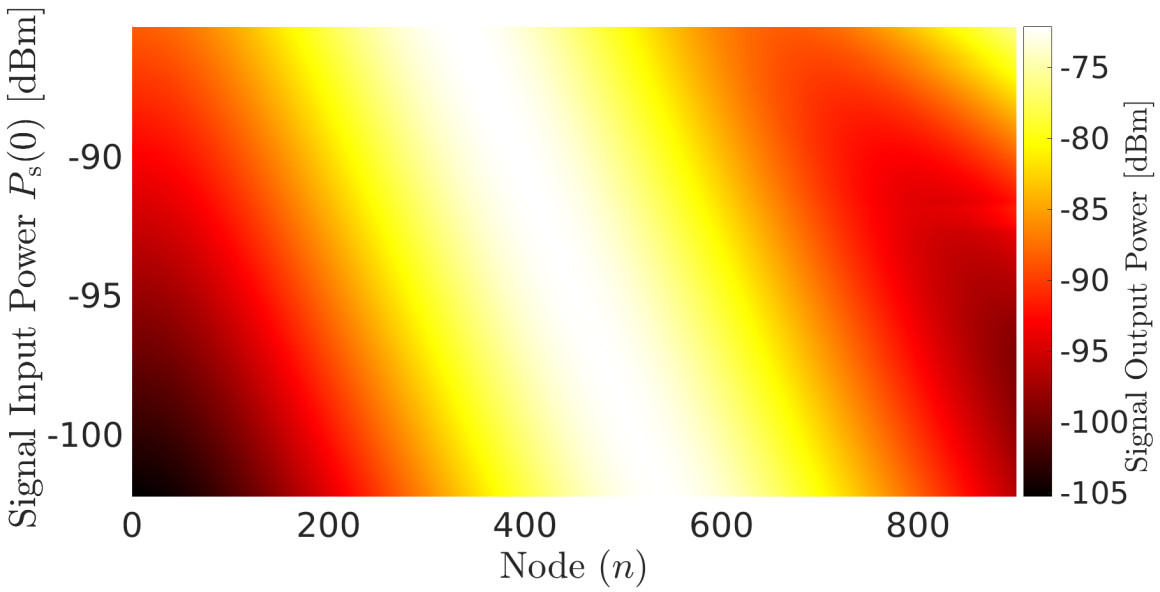

Figure 2.7: Heatmap of the signal power at each node (n) of the amplifier. Note that the maxima of signal occurs at different nodes as we the signal input power.

maximum amplitude that is achieved for any signal input power, $P_{\mathrm{s,\,max}} \sim -73\ \mathrm{dBm}$ is intuitively limited by the pump power $P_{\mathrm{p}} \approx -70\mathrm{dBm}$. In terms of amplification, it is useful to measure the relative change from signal input to signal output. This provides the gain figure of merit which is given in dB and defined as,

$$G_{\mathrm{s}} = P_{\mathrm{s}}(N) - P_{\mathrm{s}}(0) = 20\log_{10}\Big(\frac{I_{\mathrm{s}}^{\mathrm{rms}}(N)}{I_{\mathrm{s}}^{\mathrm{rms}}(0)}\Big). \tag{2.26}$$

Replotting fig. 2.7 in terms of the gain of the amplifier gives insight into the power handling capabilities of the amplifier, and is shown in fig. 2.8. Intuitively high gain is achieved for low signal input power.

However, designing an amplifier to have a total number of nodes $N = 500$ (magenta dashed line fig. 2.8) gives a greater gain variance as the signal input power is increased. A typical measure of this gain variance is the $3\ \mathrm{dB}$ compression point. This is taken at the maximum signal power where the maximum gain has reduced by $3\ \mathrm{dB}$. This is highlighted in fig. 2.9 where the three lines represent amplifiers of total length $N = 300,\ 400,\ 500$. This corresponds to the vertical slices in fig. 2.8.

The choice over output node number ($n = N$) influences both the total maximum gain achieved, as well as the $3-\mathrm{dB}$ compression point. If $G_{\mathrm{s}} > 20\ \mathrm{dB}$ is required, then the total length of the amplifier must be $300 < N < 800$, where the maximum gain is achieved around $N \approx 500$. However, for an

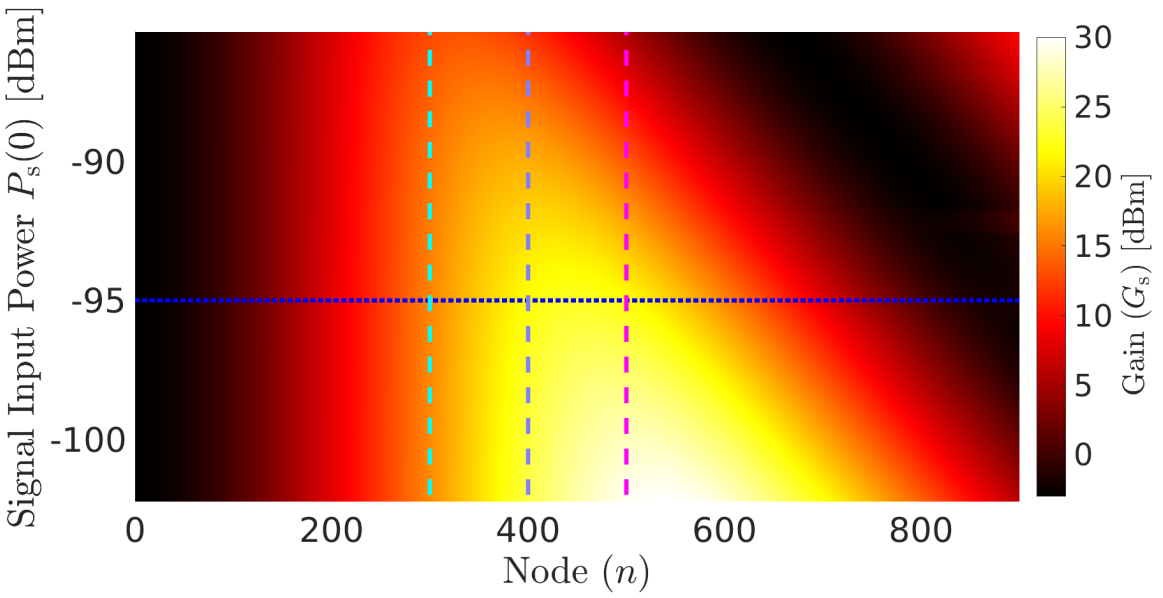

Figure 2.8: Heatmap of the gain as a function of signal input power and node number. Vertical slices represent a physical amplifier constructed of length n. We have highlighted three examples for $n = 300,\ 400,\ 500$ (cyan, blue, magenta respectively). The horizontal blue dotted line corresponds to the signal input power shown previously in figs. 2.4 to 2.6.

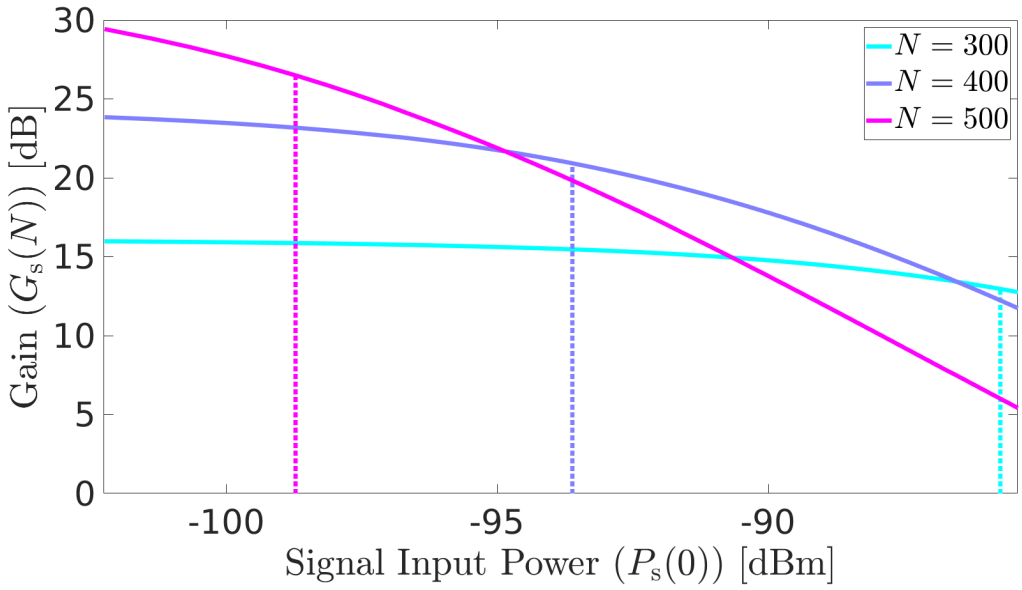

Figure 2.9: Plot showing the gain as a function of signal input power for three amplifiers of lengths $N = 300,\ 400,\ 500$. The dashed lines show the 3 dB compression point. Note that for lower maximum gain, the compression point is larger and the gain profile is flatter across a larger range of signal powers.

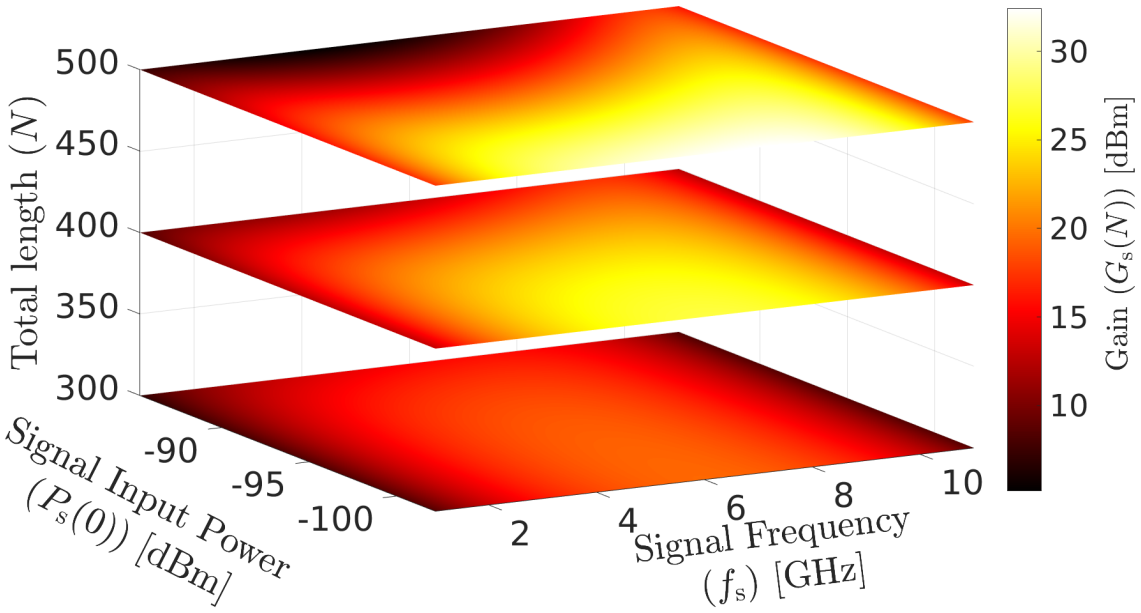

Figure 2.10: Sliced volume plot showing the gain characteristics for three different length amplifiers ($N = 300,\ 400,\ 500$). The longer amplifier ($N = 500$) shows high gain, low bandwidth, and low 3 dB compression point. The shorter amplifier ($N = 300$) inversely shows a flat frequency and power response at lower overall gain.

increased $3-$dB compression point one can design an amplifier with total length $N = 300$, at the cost of reduced overall gain.

The gain, bandwidth, and compression considerations for an amplifier must be optimised for the intended purpose. Here, we simply show the additional parameter of amplifier length and how this may affect these parameters. This is summarised for the travelling wave device in fig. 2.10, where we show three amplifiers of lengths $N = 300,\ 400,\ 500$.

In the frequency and power ranges discussed, a longer amplifier ($N = 500$) shows high gain. However, the gain profile varies in both signal frequency (low bandwidth) and signal input power (low 3 dB compression point).

For much shorter amplifiers ($N = 300$), the frequency and power response is flat (high bandwidth and 3 dB compression point). However, the gain never reaches the desired 20 dB.

For the case where $N = 400$, an optimal middle ground may be achieved. This highlights the additional consideration of total amplifier length when designing a practical travelling wave device.

Chapter 3

Experimental Observations

In this section, we discuss experiments conducted to demonstrate the mixing predicted in [11]. The experiments described here were performed on devices fabricated at Physikalisch-Technische Bundesanstalt (PTB), the national metrology institute in Germany, examples of which are shown in fig. 3.1. These are niobium based devices building upon PTB's robust niobium tri-layer Josephson junction technology. The measurements were performed using a dip probe, at liquid helium temperature $T_{\mathrm{Lq\ He.}} \approx 4.2$ K. During these measurements we observed higher order interactions beyond the three mode interaction model.

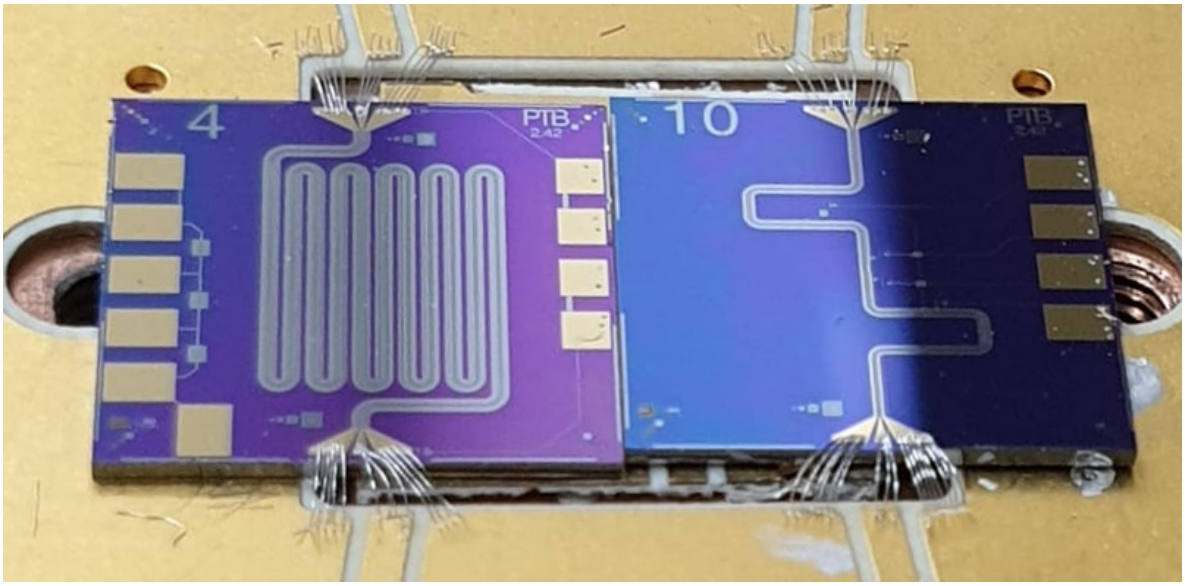

Figure 3.1: Photo of an example travelling wave device (left) and resonator (right) sent from PTB. The samples are mounted on a 50Ω matching PCB (gold surround) and connectorised to soldered SMA adapters (not shown).

First we discuss these in terms of a resonant based device. This simplifies the discussion to just one higher order interaction, where we show that the three wave mixing frequency condition is quantitatively met over a range of input power and mode frequencies.

We then move to travelling wave devices where multiple higher order tones are observed. Some of these tones can only be explained by additional mixing mechanisms beyond the three tone model described previously.

3.1 Higher Order Tones in a Resonant Device

Our first observation of potential up-conversion to higher tones was noted during an experiment on a device discussed in detail in a previous thesis in the group [41], where additional characterisation details can be found. This device was originally designed to exploit the period-doubling bifurcation predicted in [42]. While resonant devices are not the main subject of this thesis the qualitative results of this experiment are both interesting and insightful in the understanding of higher order tone generation.

3.1.1 Resonant Device

The resonant device is a coplanar waveguide transmission line coupled by two capacitors C_{in} and C_{out} separated by physical length l. Similar to a Fabry-Perot cavity, this physical length defines the modes (f_{n}) of the resonator,

$$f_{\mathrm{n}} = \frac{nc}{2\pi l\sqrt{\mu_{\mathrm{r}}\epsilon_{\mathrm{r}}}} = \frac{n}{2\pi\sqrt{L'C'}}, \tag{3.1}$$

where L' and C' are inductance and capacitance per unit length of the transmission line between input and output capacitors respectively.

There are rf SQUIDs located at the $l/3$ and $2l/3$ position and a narrow short to ground "resistor" at the $l/2$ position. The rf SQUIDs provide a tunable anharmonicity to the modes through the nonlinear inductance given by eq. (1.32) and widely discussed in qubit technology (see for example, [43]). The rf SQUIDs also enable wave mixing as described in previous chapters. The resistor broadens the second mode of the resonator. The current and voltage distributions help highlight how the positioning of the rf SQUIDs interact with specific modes of the resonator as shown in fig. 3.2.

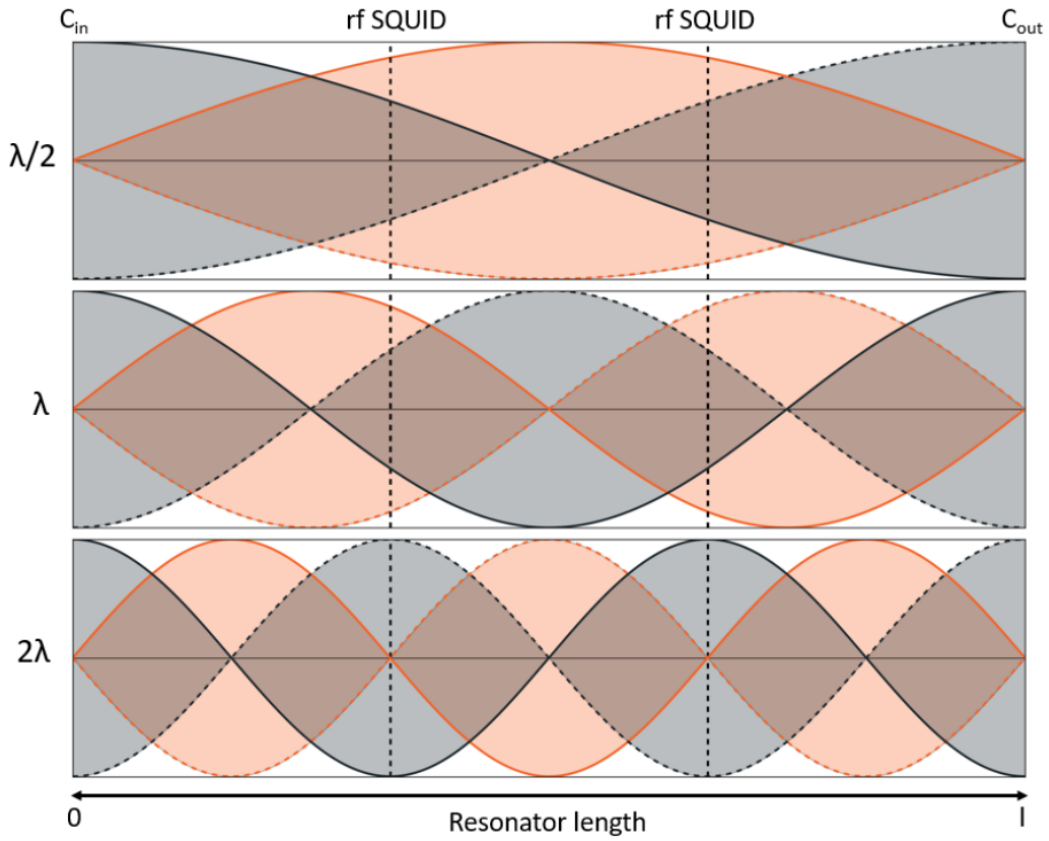

Figure 3.2: Image taken from [41]. Current (red) and Voltage (grey) distributions inside a resonator of length l.

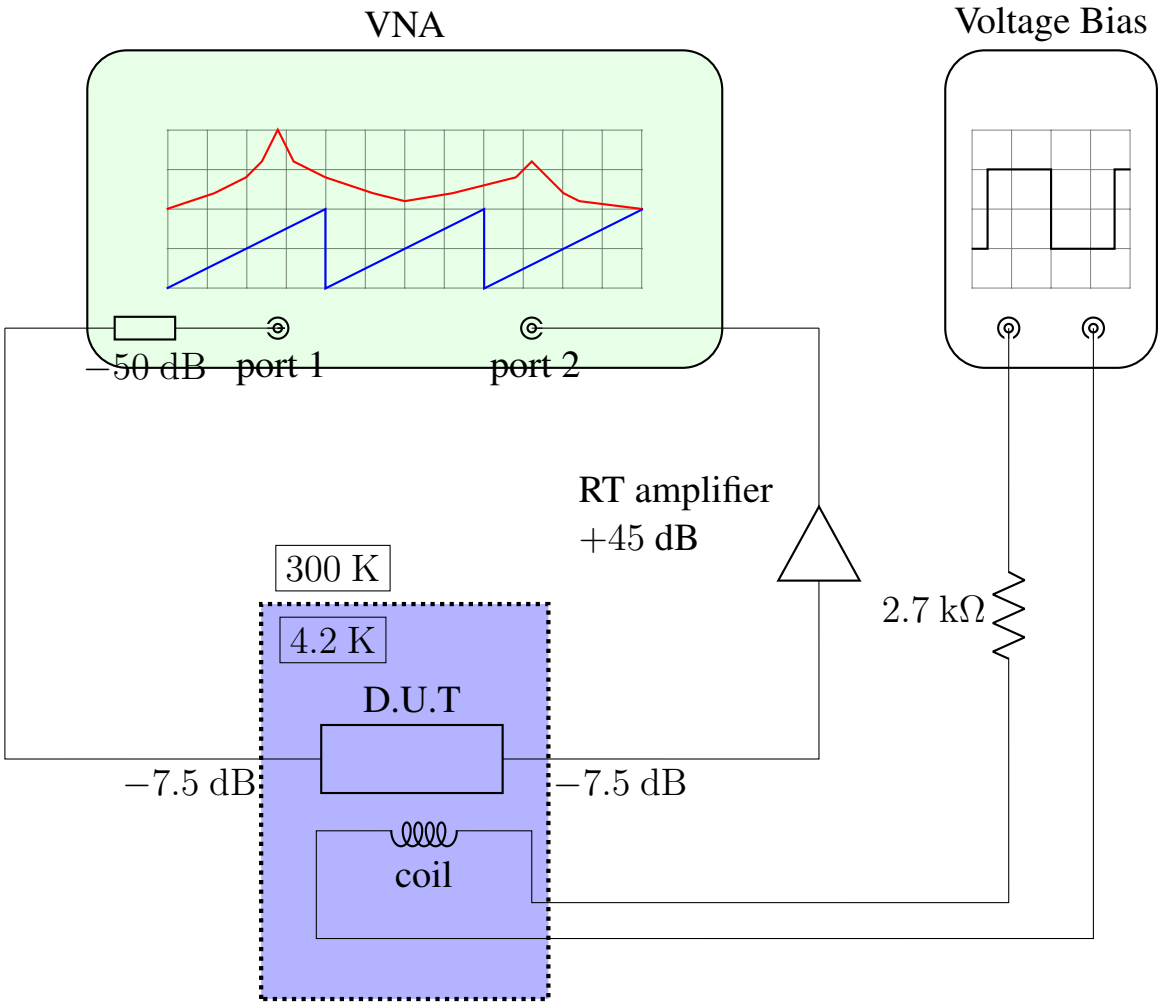

Figure 3.3: Experimental set up for the characterisation of the resonant device using a Vector Network Analyser (VNA). The leads provided 7.5 dB attenuation. The coil was biased from a Yokogowa 7651 DC voltage source

The current through the rf SQUIDS is nonzero for the first and second mode. The voltage at the resistor position is maximised for the second mode, providing the aforementioned dampening effect on the second mode.

3.1.2 Resonator Characterisation Measurements

In order to determine key features of the resonant device some simple characterisation measurements are carried out. For a deeper discussion of the theory behind these measurements see [41, 44, 45] where the modes had been previously identified.

We measure S_{21} transmission measurements through the device using the Vector Network Analyser

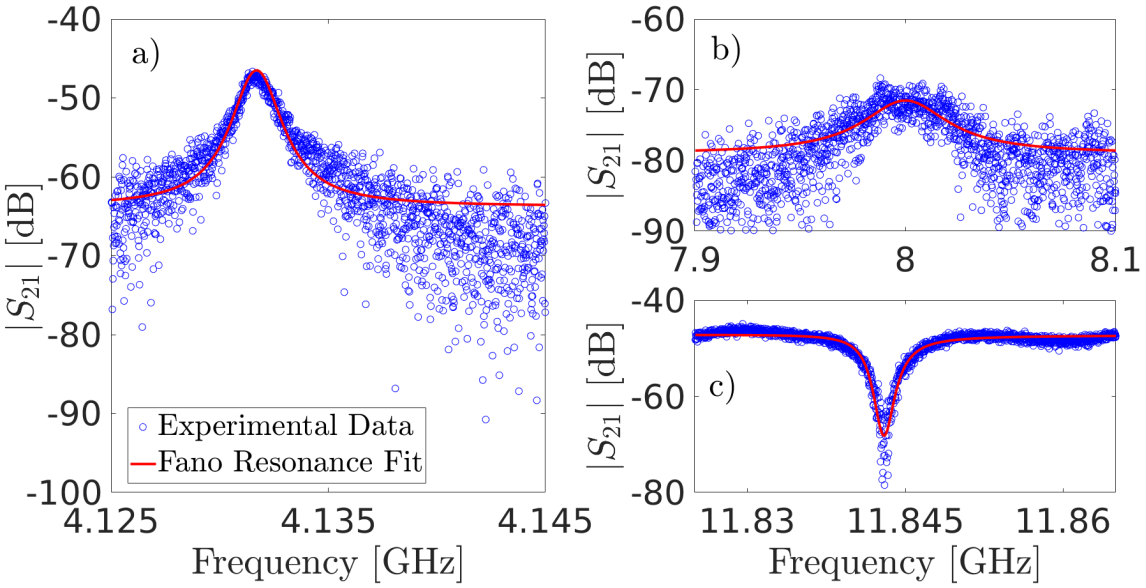

Figure 3.4: An example of a single VNA trace at the a) first, b) second and c) third mode of the resonator. The Fano resonance is fit to the data using eq. (3.2). From this we extract the resonant frequency and quality factor of the device. Note the anharmonicity between the modes and dampened second mode, with the characteristic broader line width. The fundamental mode has much lower skew and is a more typical Lorentzian shape, while the third mode in c) shows a more skewed Fano response with larger skew.

(VNA) to find the frequencies of the first three modes of the device. A schematic of this is shown in fig. 3.3. The VNA S_{21} response is typically a peak at the resonant mode of the cavity qualitatively shown in fig. 3.3 (top red on VNA "screen"). It is important to note that for an rf SQUID embedded resonator there are two oscillators interacting, the cavity and the rf SQUIDs. These coupled oscillators can produce a symmetric Lorentzian response, which is well documented in the literature. But also, they may produce an asymmetric Fano resonance, an interference phenomena which is nicely summarised in [46]. We fit the data to a standard Fano Resonance $F(f)$, eq. (3.2) [44, 47],

$$F(f) = F_0 \frac{[s + 2(f - f_n)/\delta f_n]^2}{1 + [2(f - f_n)/\delta f_n]^2}. \tag{3.2}$$

Here, f_n defines the resonant frequency of the nth mode of the resonator. The fit parameters $\delta f_n = f_n/Q$ is the Full Width at Half Maximum (FWHM) of the resonance peak, F_0 and s describe the amplitude and skew of the peak. An example of typical VNA data and fit is shown in fig. 3.4.

To confirm that we are interacting with the rf SQUIDs, we drive the system to an amplitude bifurcation [41, 42] by driving the resonator with increasing power. We then track the power dependent

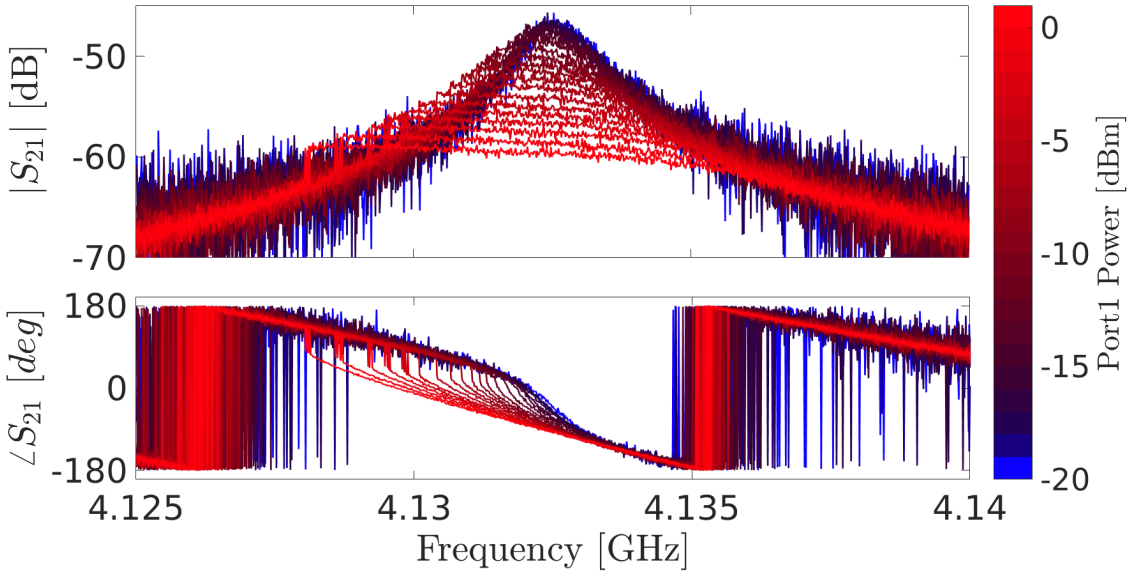

Figure 3.5: Increasing the drive tone power shifts the resonant frequency lower, until the rf SQUID becomes unstable and a bifurcation appears.

shift of the resonant frequency. This is discussed in detail in [41, 44, 45]. Increasing power eventually results in the system entering the bifurcation. This is measured and shown in fig. 3.5.

We interact with the rf SQUIDs by tuning the device with magnetic field. We apply a voltage bias V_b across a bias resistor and superconducting coil which generates a field perpendicular to the rf SQUID loop. This creates a change in the superconducting phase over the junction and as per eqs. (1.27) and (1.31) the inductance periodically modulates thus modulating the resonant frequency of the device eq. (3.1). The flux dependence of the resonant frequency is seen most clearly in the first mode of the resonator, shown in fig. 3.6.

From this, we relate the applied voltage to added flux in the loop, where we see that a voltage bias of $\Delta V_\mathrm{b}(\Phi_0) \approx 0.2$ V induces a flux in the loop equal to 1 flux quantum Φ_0. We then sweep the flux and measure the S_{21} response of the second and third mode of the device as shown in figs. 3.7 and 3.8.

Using the Fano resonance (eq. (3.2)), we extract the resonant frequency at each position in flux. From this we construct a frequency modulation plot as a function of added flux quanta into the rf SQUID loop.

The voltage related to added flux is useful to give a relative flux position, however the absolute flux threading the loop is still unknown. Because there are two rf SQUIDs in the cavity, any non-uniformity, such as but not limited to; applied flux, loop area, geometric inductance, positions of the SQUIDs, etc.

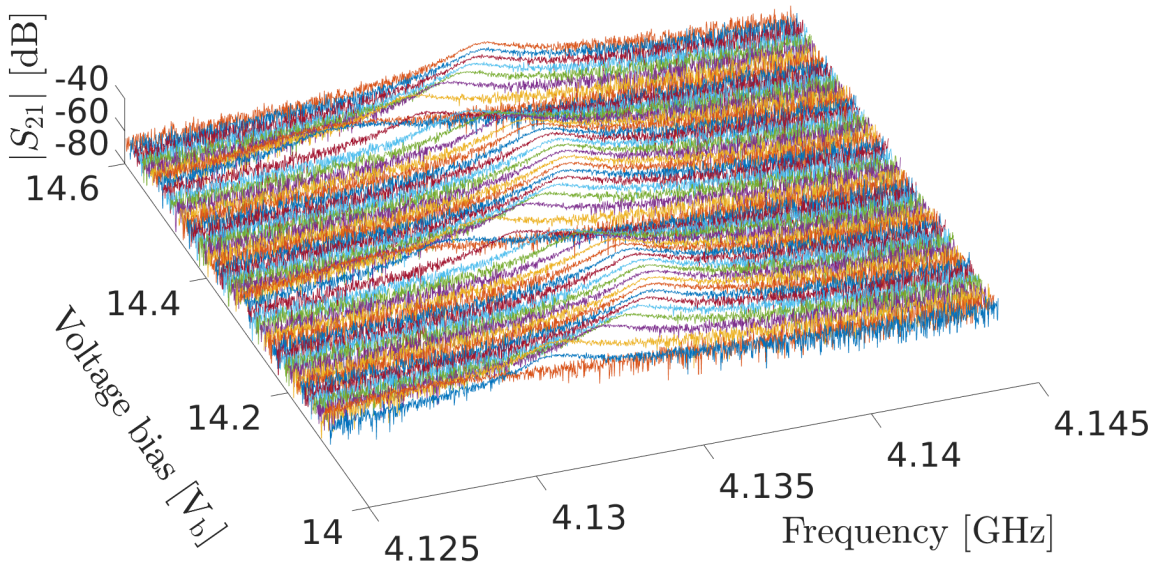

Figure 3.6: Multiple VNA traces (colours) over the fundamental mode of the resonator each taken at stepped bias voltages across the magnet. The resonant frequency, which is identified by the peak in each trace, varies periodically with flux. Each successive minimum resonant frequency is taken to correspond to a complete 2π rotation of the Josephson phase, i.e. a flux equal to the flux quantum threads the loop.

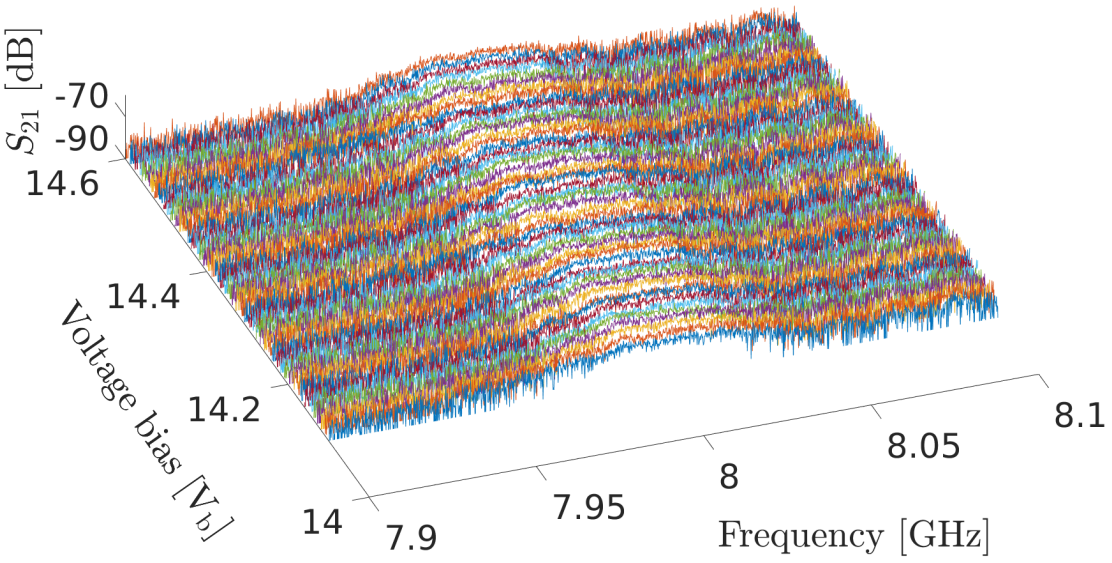

Figure 3.7: Multiple VNA traces (colours) over the second mode of the resonator taken at stepped bias voltages across the magnet. The mode is damped and so frequency modulation is obscured.

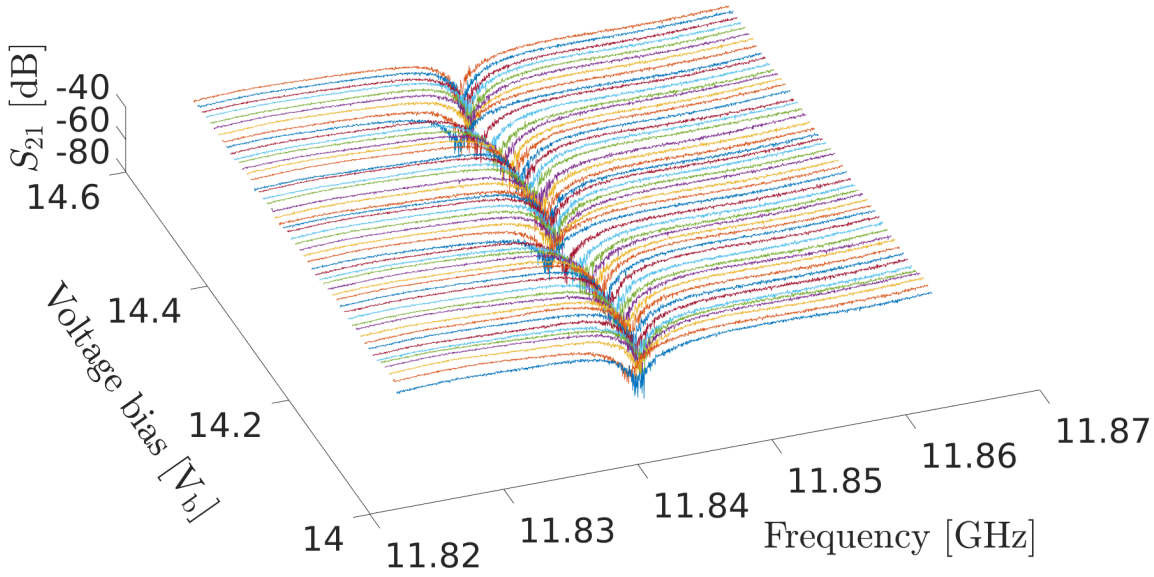

Figure 3.8: Multiple VNA traces (colours) over the third mode of the resonator taken at stepped bias voltages across the magnet. Here the periodicity in flux of the minimum frequency is identical to the first mode of the resonator.

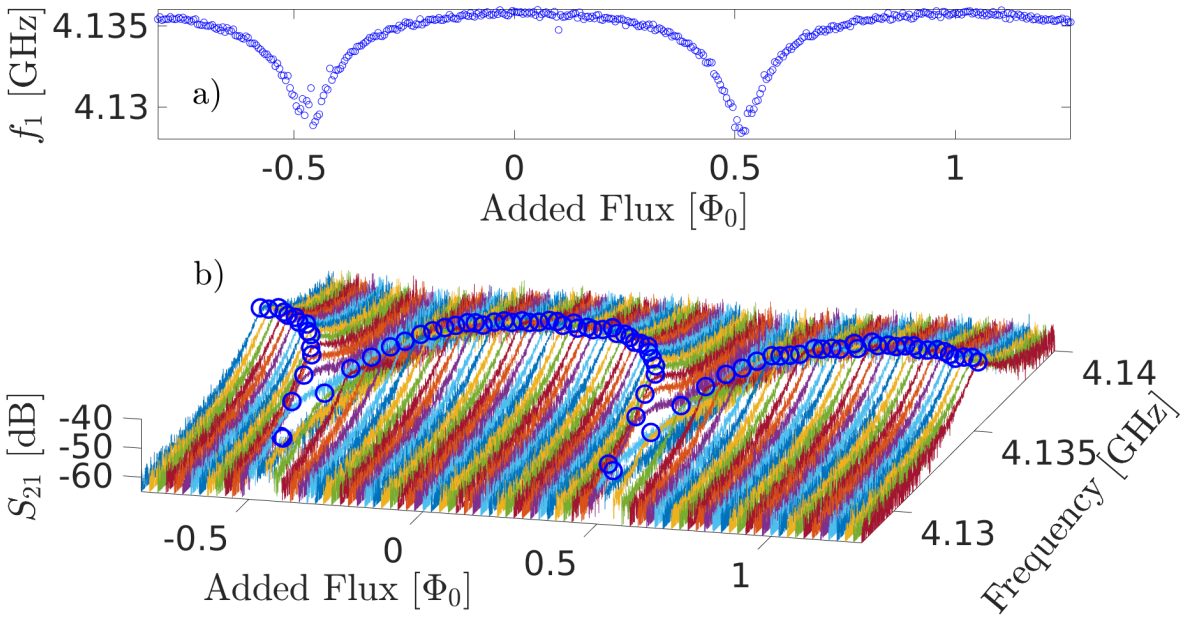

Figure 3.9: Fano resonance fitting to extract resonant frequency of the first mode f_1. Plot a) shows the frequency modulation curve extracted from b) a high density of VNA traces over 2 added flux quanta.

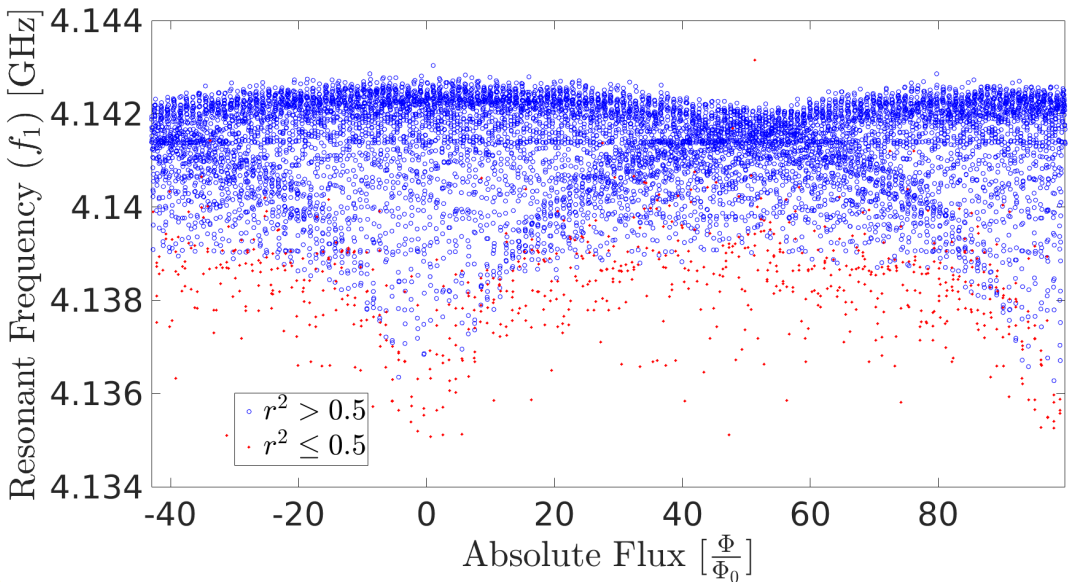

Figure 3.10: Frequency modulation curve of the fundamental mode f_1 as a function of flux quanta Φ_0 threading the loop over many flux quanta. The r^2 value in MATLAB is a representation of the goodness of the fano fit, where the red data may be regarded as a poor fit. Considering only the blue data we centre the largest modulation depth at $\Phi = 0$, assuming both rf SQUIDs are in phase.

will result in a different bias point in each rf SQUID. This causes a beating effect which is discussed in detail in [44].

To define an optimum position in flux we sweep over many flux quanta to find where the two rf SQUIDS are most similarly biased, we designate this as the zero of flux in the loop. Since the beating effect of the two rf SQUIDs is minimised this optimal position coincides with the place where the resonant frequency change is most severe as shown in fig. 3.10.

From fig. 3.10 we have determined an appropriate flux bias for the largest SQUID response and found the optimum bias point for the two rf SQUIDS around $-\Phi_0 \leq \Phi \leq \Phi_0$. We have determined the voltage to flux ratio such that we sweep over this region in reasonable step size. We have characterised the frequency and flux space of the first three nodes in figs. 3.6 to 3.8. We have determined an upper bound to the fundamental power based on the bifurcation onset in fig. 3.5. With this, we have characterised the necessary features of the device to move on to a wave mixing set up.

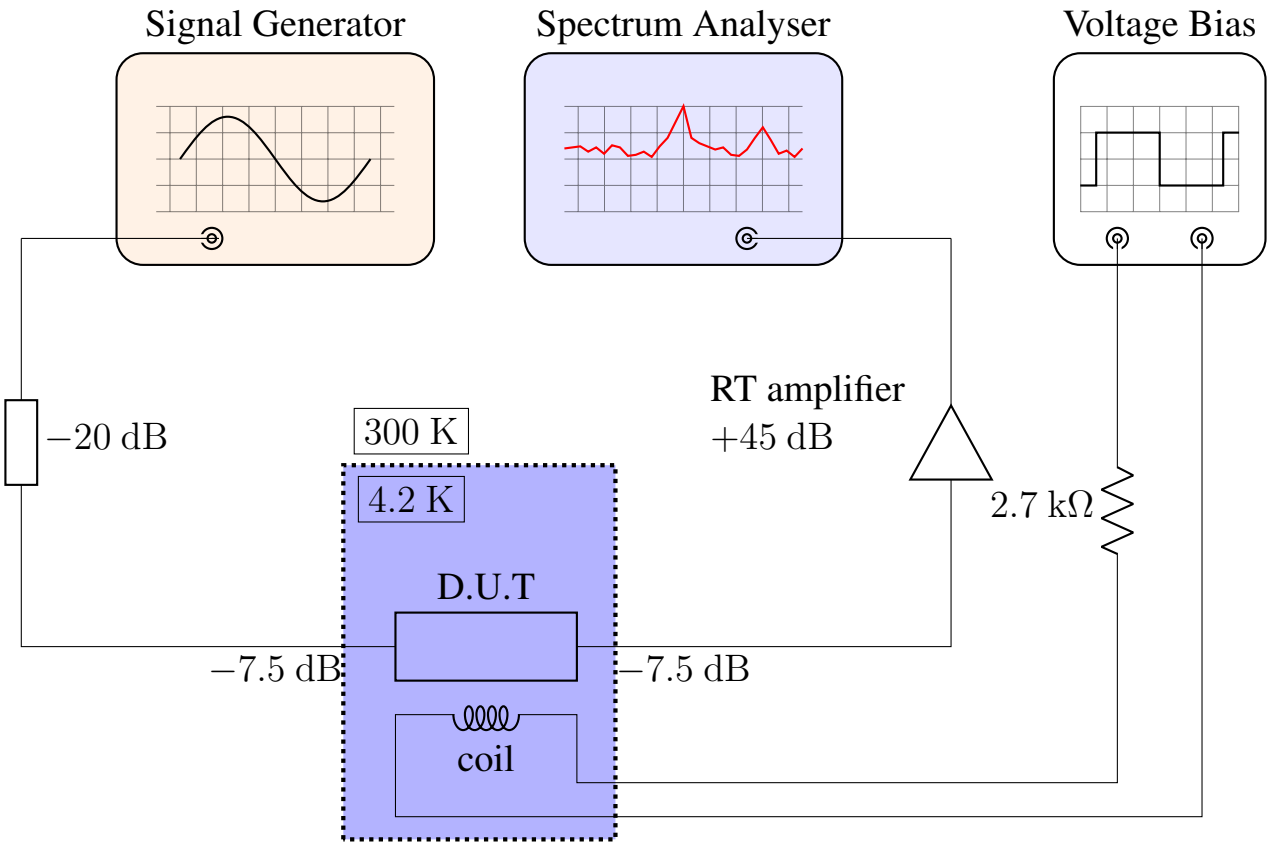

Figure 3.11: Experimental set up to implement wave mixing in the resonant device using a Signal Generator (SG) and Spectrum Analyser (SA).

3.1.3 Resonator Wave Mixing

We use a signal generator and spectrum analyser set up. The signal generator produces one tone, the pump f_{p}, which is the sole input tone to the device. The wave mixing mechanism is achieved by spontaneous emission at the fundamental mode $f_1 = f_{\mathrm{s}}$ which we refer to as the signal. This is detected by the spectrum analyser. The full set up is shown in fig. 3.11.

As an example, we pump the resonator with a tone at $f_{\mathrm{p}} = f_2 = 8$ GHz. We measure the amplitude P_1 of the response over the possible frequency modulation depth shown in fig. 3.9 of the the fundamental mode $f_{\mathrm{s}} = f_1 \approx 4.13$ GHz. Because we are pumping at a frequency f_{p} and measuring the response at f_{s} we use a signal generator and spectrum analyser (as opposed to the VNA used previously) and thus there is no reference probe tone. Because of this we will deduce a noise floor power ($[P_{\mathrm{N}}] = [\mathrm{dBm}]$) in each experiment, then measure a peak amplitude above that noise floor $[P_{j=\mathrm{p},\,\mathrm{s}\,...}] = [\mathrm{dB}]$. We must measure the fundamental response in the window $4.125 < f_s < 4.135$ GHz as shown in fig. 3.10 to account for any frequency modulation but detect a peak with a line-width of order ~ 100 kHz. This means that each sweep must be done over a large range but with sufficient detail to capture a peak. Also to ensure that we do not bifurcate the fundamental mode we must do this at low powers, as such averaging was used in our acquisition. Combined, this adds substantial time to the acquisition procedure.

The routine for the raw data analysis is shown in fig. 3.12. We fit the data with eq. (3.2) using a large s such that a Lorentzian is approximated [44]. We then extract the fit parameters and interpolate the function using these parameters. This helps to substantially reduce acquisition time.

Prior to the experiment we were mainly interested in the half flux positions which we determine from fig. 3.9. Thus to save acquisition time we create a dynamic sweep where we broadly sweep between the half flux positions then decrease the step size at the $\Phi \approx (n + 1/2)\Phi_0$ region. This is highlighted in the granularity/pixel size in fig. 3.13. We sweep this flux over a range of pump powers (P_{p}) and extract the amplitude of the of the response (P_{s}) above the noise of the experiment (P_{N}), i.e. ($P_{\mathrm{s}} - P_{\mathrm{N}}$). This enables us to deduce flux and power positions where two tones are present in the device. These positions are highlighted in fig. 3.13.

The features around $P_{\mathrm{p}} \approx -40$ dBm and $\Phi \approx 0 \pm 0.135\Phi_0$ were unexpected. To understand the wave mixing here we define a quasi-fit function ($\Xi(\alpha, \Phi/\Phi_0)$) based on the wave mixing CMEs

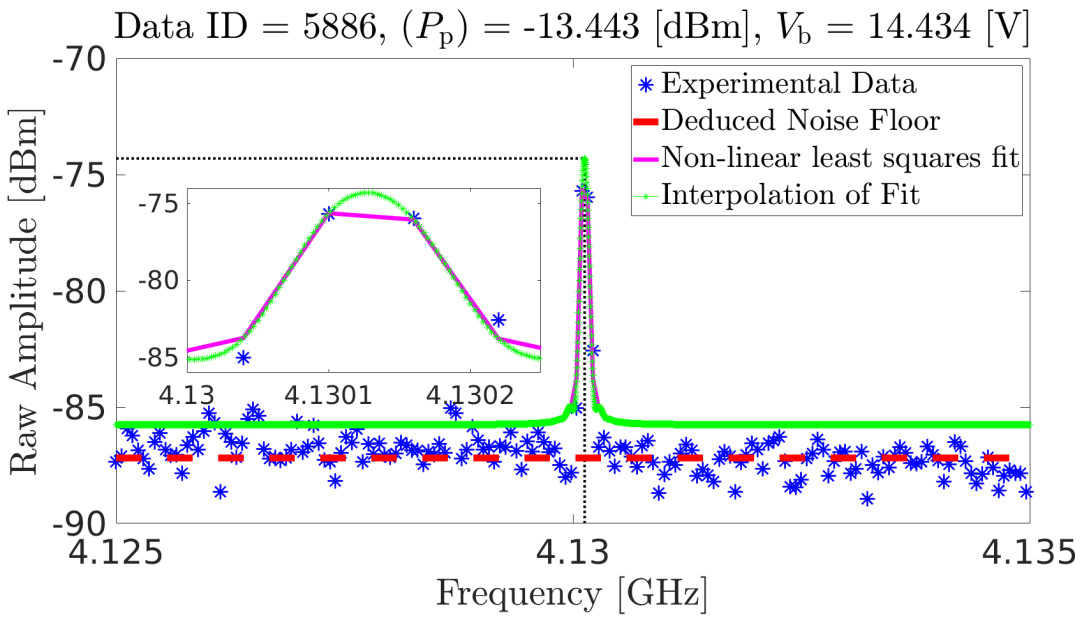

Figure 3.12: An example of the raw spectrum analyser output (blue). We deduce the experimental noise floor (red dash) from the mean of the data (assuming $> 99\%$ of the total data is noise). We then fit eq. (3.2) to the data (pink solid), excluding anything below the noise floor. Then we use the fit parameters to interpolate the eq. (3.2). This means that if 2 data points sit on the shoulders of a peak, (see inset), we reconstruct the peak through the interpolation. This increases the accuracy of frequency and amplitude (black dotted lines) over taking just a maximum value from the raw data.

including three and four wave mixing coefficients eqs. (A.46) to (A.48),

$$\Xi = c_1|\beta(\Phi/\Phi_0)|\alpha + c_2|\gamma(\Phi/\Phi_0)|\alpha^2. \tag{3.3}$$

Here, c_1 (c_2) is a fit parameter to account for coefficients of three (four) wave mixing. The term $\alpha \propto A_p$ gives the linear (quadratic) dependence of pump amplitude in the three (four) wave mixing process. From eq. (3.3), we see the flux dependence of the mixing is explained by the β and γ terms while the pump power dependence is accounted for by α. A comparison of Ξ for two different values of α is shown in fig. 3.14.

The largest amplitude observed at the fundamental mode was in the high power regime $-41 < P_p < -40$ dBm and in the mixed mixing state $-0.18 < \Phi/\Phi_0 < -0.95$, where both three wave and four wave mixing occur. We explored this further by measuring both the response within the fundamental mode and looking for a response in the vicinity of the third mode of the resonator around $f_3 \approx 11.87$ GHz.

Figure 3.15 shows the response detected above the assigned noise floor ($P_N = -100$ dBm)

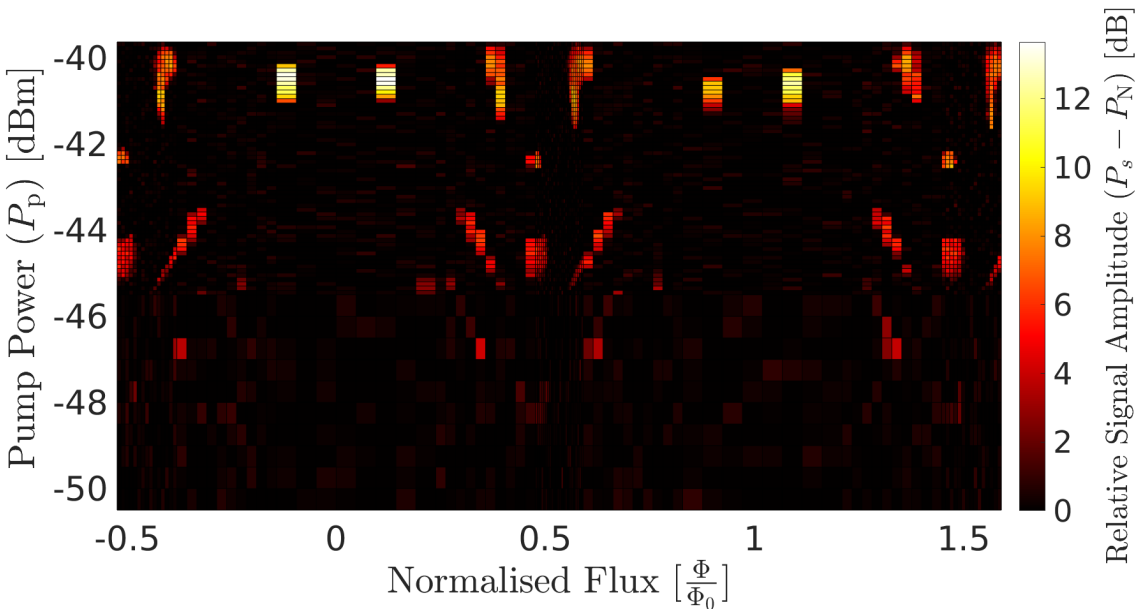

Figure 3.13: Measured fundamental response as a function of flux and power. The irregular granularity in the plot shows the non-uniform data acquisition technique. This was based on knowledge of flux behaviour from fig. 3.9 and the power behaviour from fig. 3.5. The purpose was to optimise acquisition time and find areas of interest. The pump is input at 8 GHz while the measured response is within the fundamental mode $4.134 - 4.144$ GHz as shown in fig. 3.10. The high power $P_\mathrm{p} \approx -40$ dBm and $\Phi \approx 0 \pm 0.125\Phi_0$ area produced an unexpected response, with higher amplitude than the response centred around $\Phi \approx \Phi_0/2$. The noise floor was deduced from the mean of the entire data set and found to be $P_\mathrm{N} = -85$ dBm.

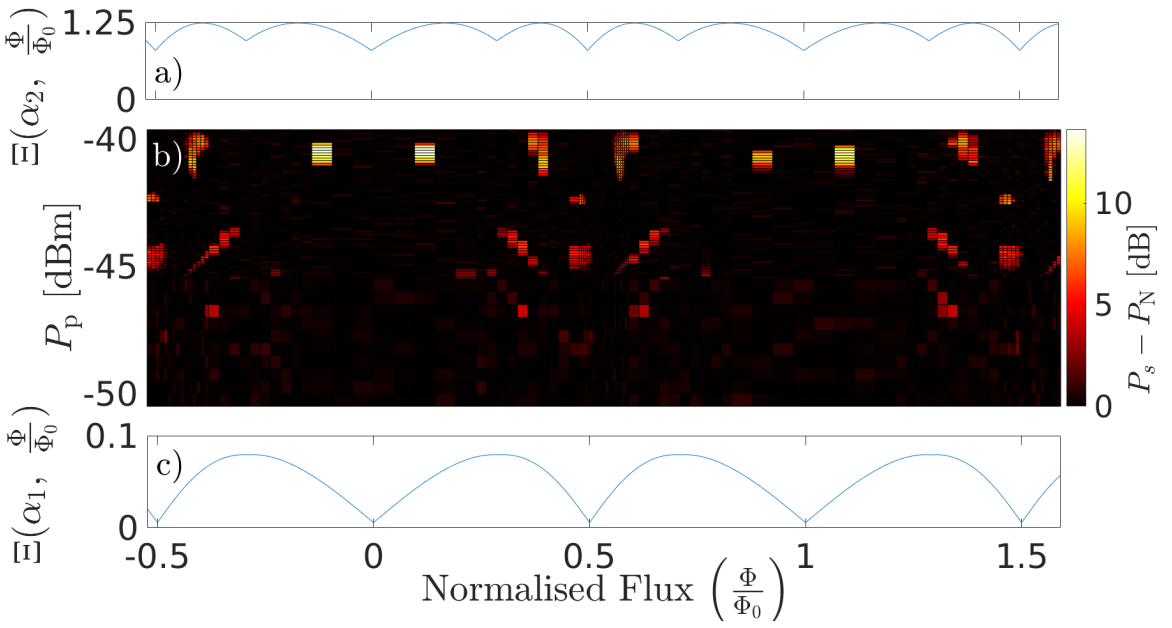

Figure 3.14: Comparison of the power and flux dependence of (a,c) the quasi-fit function Ξ with (b) the data shown in fig. 3.13. For both (a,c) $c_1 = 1$ and $c_2 = 0.3$. At high pump power $\alpha_1 = 7.6$ the maxima of $\Xi(\alpha_1)$ correspond to the flux positions for peak detection in the range $-42 < P_\mathrm{p} < -40$ dBm. At lower pump power $\alpha_1 = \alpha_2/12 = 0.6$ the maxima of $\Xi(\alpha_2)$ align with flux positions for peak detection in the range $-46 < P_\mathrm{p} < -44$ dBm. The factor 12 change of $\alpha_{1,2}$ is commensurate with the 4 dB relative change in the high and low power regime since $\alpha \propto I_\mathrm{p}$.

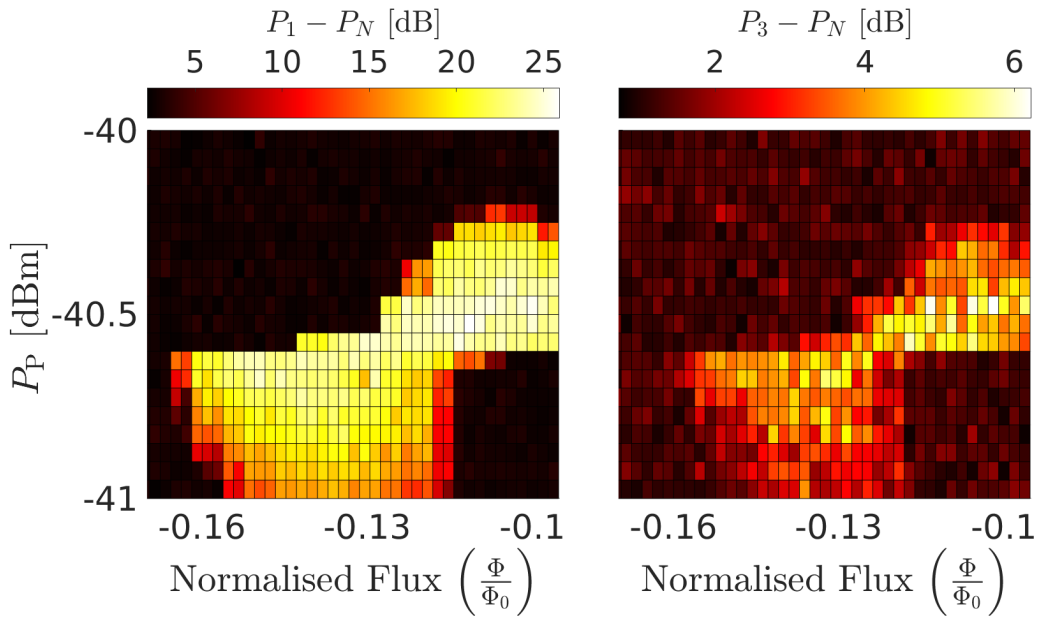

Figure 3.15: There is an obvious correspondence between the two peaks being detected in a) the fundamental mode of the resonator, and b) the third mode of the resonator. The noise floor $P_\mathrm{N} = -100$ dBm of this experiment was reduced 15 dB from fig. 3.13 by increasing the averaging, made possible due to a smaller span of flux and power. Importantly this meant the peak in b) is seen above the noise.

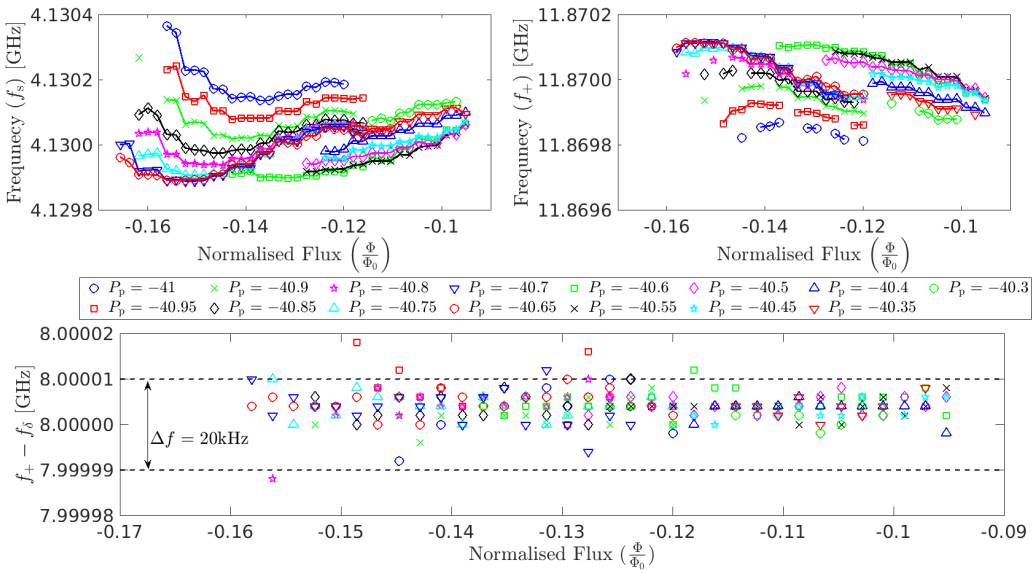

Figure 3.16: Frequency response of the fitted peak in a) the fundamental mode and b) the third mode over flux and powers of interest deduced from fig. 3.15. The fundamental mode a) spans ~ 600 kHz while the third mode b) spans ~ 400 kHz. Each colour line corresponds to a different power and any data point not present in both a) and b) is discarded in c). Note that there appears to be two subsets of data in a) and b); one from $-41 \leq P_\mathrm{p} \leq -40.65$ dB (blue circle - red circle), and another from $-40.6 \leq P_\mathrm{p} \leq -40.3$ dB (green square - green circle). These data sets are separated at the horizontal cut through $P_\mathrm{p} = -40.6$ in fig. 3.15. The majority of the considered points relate $f_+ - f_\delta$ back the pump frequency f_p at 8 GHz $\pm$ 10 kHz (black dashed boundaries). The ability to achieve higher resolution than the resolution bandwidth Δf of the spectrum analyser comes from the fitting routine described previously in fig. 3.12.

between the signal at f_s and a peak detected around the third mode $f_3 \approx 11.87$ GHz. In order to verify wave mixing, we extract the frequency of the peak inside the third mode using the procedure shown in fig. 3.12. We refer to this frequency as f_+. Since we now sweep over a smaller flux range, we decrease the frequency step size to $\Delta f = 20$ kHz and operate in a smaller window, due to less frequency modulation. We assign the difference of pump and signal frequency at each point in flux and power with $f_\delta = (f_\mathrm{p} - f_\mathrm{s})$, which we wish to relate back to the frequency of the peak inside the third mode $f_+ = f_\mathrm{p} + f_\delta$, as shown in fig. 3.16.

One might consider the response at f_+ to be the idler for the degenerate four wave mixing case where $f_\mathrm{i}^{4\mathrm{WM}} = 2f_\mathrm{p} - f_\mathrm{s} = f_+$. The idler of a three wave mixer in the three mode case $f_\mathrm{i}^{3\mathrm{WM}} = f_\mathrm{p} - f_\mathrm{s} = f_\delta$ sits outside any of the resonant modes at $f_\mathrm{i}^{3\mathrm{WM}} \approx 3.88$ GHz and would be difficult to detect directly. If one was to consider the up-conversion of the three wave mixing idler with the pump this would also coincide with a frequency $f_\mathrm{i}^{3\mathrm{WM}} + f_\mathrm{p} = 11.87$ GHz $= f_+$. Thus it is possible to describe the

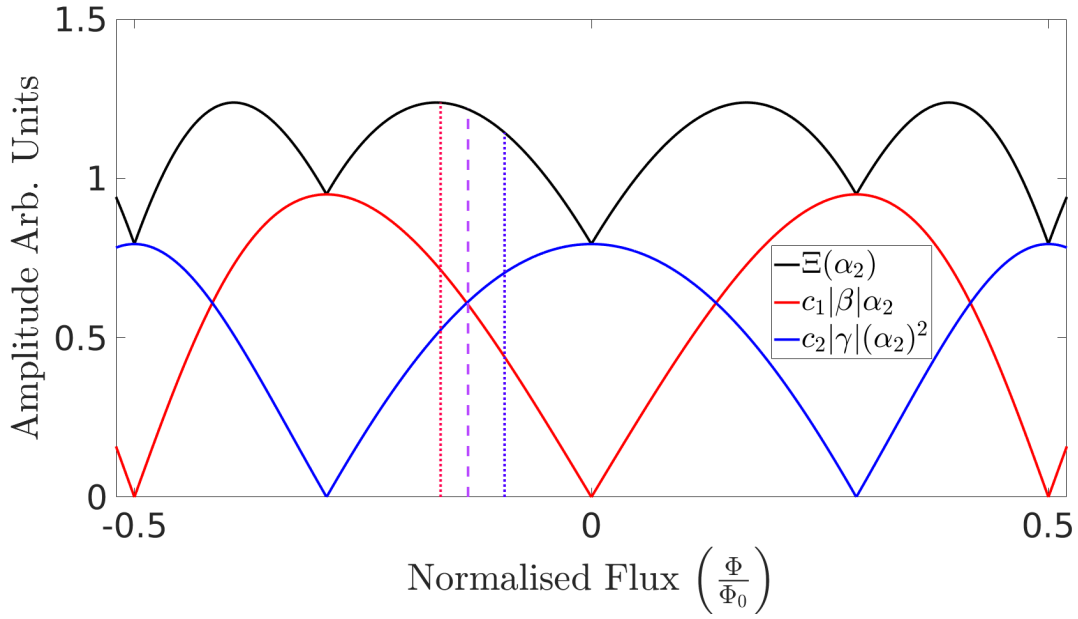

Figure 3.17: Comparison of the components of the quasi-fit function Ξ for the high power case where $\alpha = 7.6$, $c_1 = 1$, $c_2 = 0.3$. The purple dashed line (vertical centre line) represents the case where $c_1|\beta|\alpha = c_2|\gamma|\alpha^2$ and three and four wave mixing coefficients are equal. The left (salmon) and right (lilac) dotted lines show the lower and upper bounds of the response shown in fig. 3.15. For flux $-0.165 < \Phi/\Phi_0 < -0.135$ then $c_1|\beta|\alpha > c_2|\gamma|\alpha^2$, whereas for flux $-0.135 < \Phi/\Phi_0 < -0.1$ then $c_1|\beta|\alpha < c_2|\gamma|\alpha^2$. This provides a qualitative description of the two regimes seen in fig. 3.16 a) and b).

observation of this higher frequency peak as a Sum Frequency Generation (SFG) process in the three wave mixing case.

Decomposing the quasi-fit equation eq. (3.3) into the three and four wave mixing components shows that both elements are non-zero and of similar amplitude around the flux bias point measured in fig. 3.15 as shown in fig. 3.17. This shows that both three and four wave mixing is present and thus we conclude that up-conversion in the three wave mixing case must not be disregarded, even in this resonant device where the bandwidth is constrained to the resonant modes.

In fact, for the coefficients $c_1 = 1$, $c_2 = 0.3$ and $\alpha = 7.6$, we see that there is a crossover of the dominant coefficient β, γ. If we could describe a more quantitatively accurate fitting routine then we may be able to deduce the power on-chip inside the resonator based on the two regimes shown in fig. 3.16 a,b) and their power and flux dependence. Here we are interested in travelling wave designs and so investigating this much further is beyond the scope of this thesis.

Summary

Here, we have discussed in detail the measurement of a resonant device. The simplicity of measuring within the line width of resonant modes removed much of the frequency dependence from the measurement. Yet there are still complications in describing the mixing processes observed within the device. These observations led to a consideration of the effects in potential up-conversion to higher tones in a three wave mixing scheme. We note that off resonance pumping has been demonstrated in similar devices [48] using three wave mixing however higher order tone generation was not studied. This higher order tone generation has the potential to hamper device performance in a travelling wave device, which is free from resonant constraints and allows propagation of tones over a continuous bandwidth. As such, we now move to experiments with two travelling wave devices where we explore and demonstrate the generation of these higher order tones.

3.2 Higher Order Tones in Travelling Wave Device

Following from the observation of potential up conversion in resonant devices, we also measure two travelling wave devices sent from partners at Physikalisch-Technische Bundesanstalt (PTB) named JTWPA1 and JTWPA2. These devices consist of $N \approx 1000$ rf SQUIDs embedded in a co-planar wave-guide transmission line. The devices are first and second generation travelling wave parametric amplifiers respectively. For this thesis, we focus on the observation of higher order tone generation and how this can hamper parametric amplification. The most dominant tone generation is suspected to be pump harmonics. As such, we first discuss the case of a single input tone, the pump tone, and how that generates harmonics. We then look at two input tones, pump and signal, and how a myriad of tones are generated from these.

3.2.1 Cascaded Harmonic Generation

This device, JTWPA1 ($N = 1078$), was the first iteration of rf SQUID Josephson Travelling Wave Parametric Amplifiers (JTWPAs) from PTB. Previous experimentation showed that the amplifier characteristics were non-optimal and so I was tasked with understanding what may be affecting amplifier performance. One of the main concerns was harmonic generation of the pump tone. To measure just the cascaded pump harmonic generation we insert one tone, assigned as the pump tone.

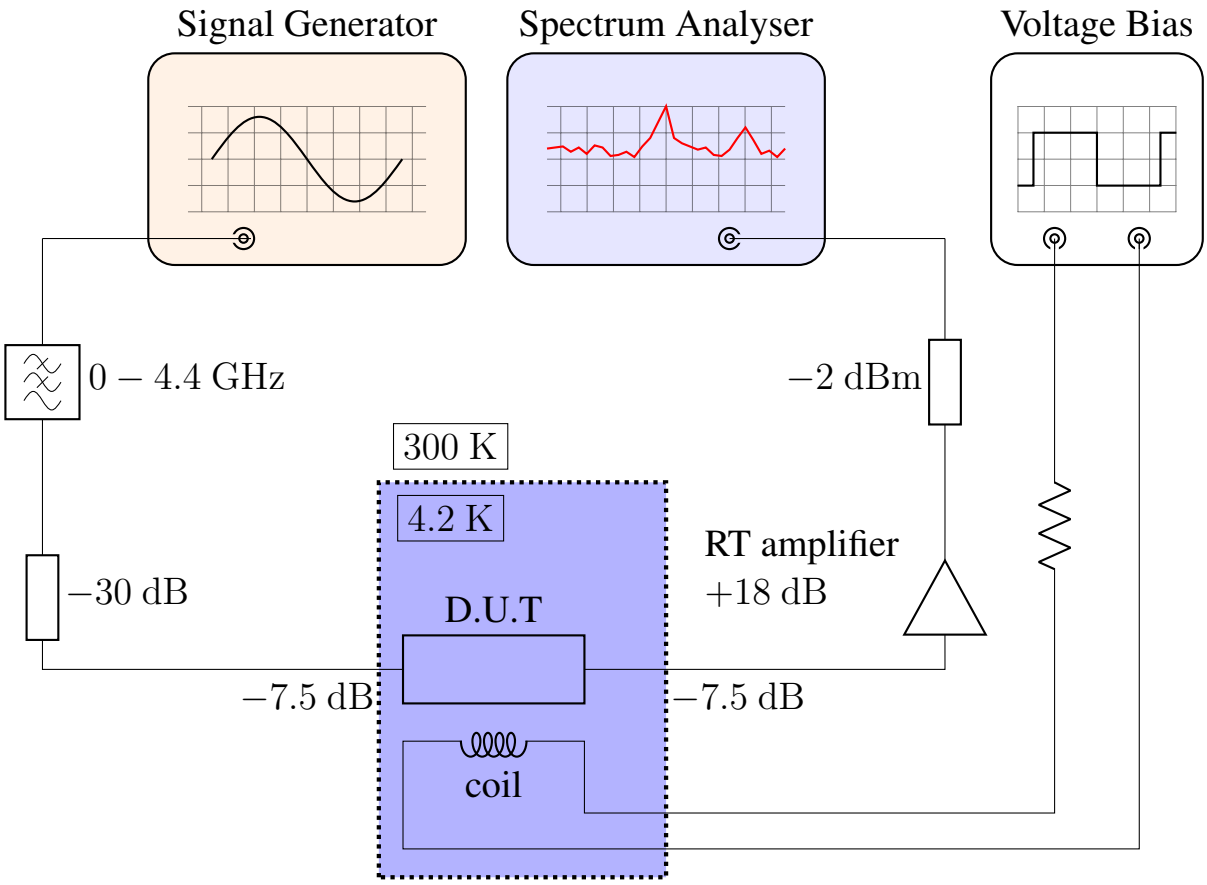

Figure 3.18: Experimental set up for single tone spectroscopy to demonstrate harmonic generation of a single input tone in a travelling wave device.

This is generated from the signal generator and passed through a low pass filter to attenuate any harmonics potentially generated in the instrument. The output from the device was amplified and then measured using a spectrum analyser. The experimental setup is shown in fig. 3.18. This measurement will now be referred to as single tone spectroscopy (STS) as only one tone is input.

Originally this device was designed to operate within a signal bandwidth of 1 octave, $4 - 8$ GHz. This means that measuring cascaded harmonics will be done outside of this bandwidth. Similarly, the experimental set up constrains the bandwidth of the measurement. As such, a pump tone $f_{\mathrm{p}} \approx 3.1\mathrm{GHz}$ was chosen such that the second harmonic generation at $f_{2\mathrm{p}} \approx 6.2$ GHz and third harmonic generation at $f_{3\mathrm{p}} \approx 9.3$ GHz all fit within the bandwidth of the measurement set up.

In this experiment the Spectrum Analyzer (Signal Hound USB-SA124B) limited the high frequency bandwidth to $f_{\max} \sim 12.4$ GHz. Importantly, a low pass filter was added to the input line such that any reflection or backward travelling tone could not enter the signal generator as well as filter any higher harmonics potentially generated in the signal generator.

In this experiment the frequency dependence of the tones being generated $f_{2\mathrm{p}}$ and $f_{3\mathrm{p}}$ is independent of the flux applied to the device. However, the amplitude of each tone being generated is expected to follow the same wave mixing argument from figs. 3.14 and 3.17 a), c). In order to ascertain the voltage to flux coefficient of the coil, we sweep a bias voltage V_{b} again over the coil and look for a response in the harmonics of the pump tone as shown in fig. 3.19.

From eq. (A.34) and fig. 2.3 we assume two peaks in the second harmonic response associated with maximum β, per flux quanta. With such a large array of rf SQUIDs and as we are only interested in the cascaded pump harmonic behaviour, we do not attempt to find the global flux position. Instead, we note the voltage required to add a flux quanta into the loop. Zooming in over the assumed single added flux quanta we find that $\Delta V_{\mathrm{b}} \approx 3.3$ V is the voltage required to add a single flux quanta to the loop, as shown in fig. 3.20.

The relationship between the second harmonic amplitude shown in fig. 3.20 and the curve of β in fig. 2.3 gives a strong indication that this second harmonic is generated due to three wave mixing. Following this we initially assumed that the third harmonic generation would be the result of four wave mixing and then follow the magnitude of γ (see fig. 2.3) in much the same way. However, we see that the third harmonic does not follow this trend. We will discuss this in detail in section 5.2. For now we state qualitatively that this is due to a cascade of the pump harmonics. Consider that in the device

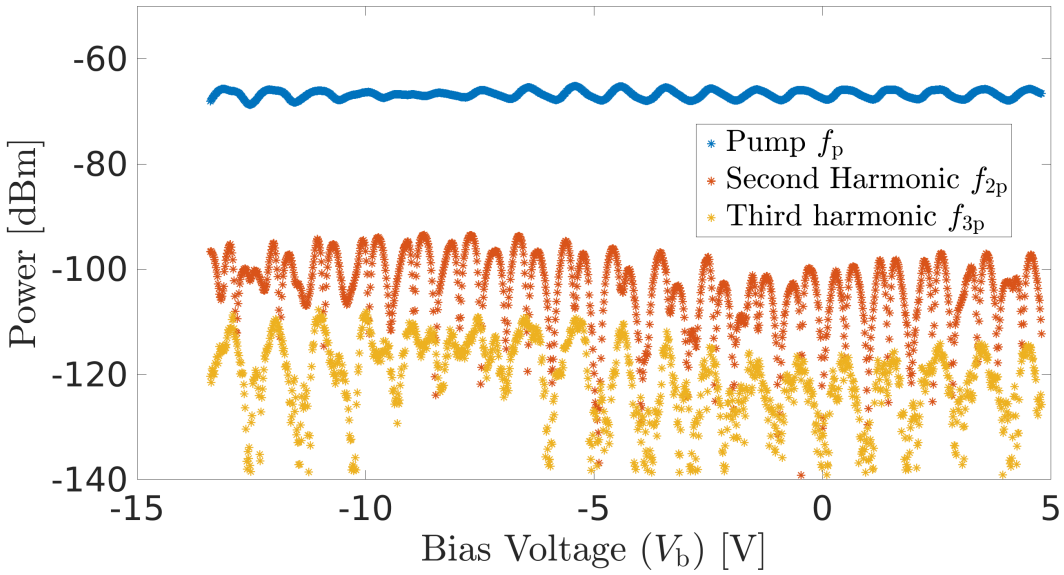

Figure 3.19: Power of the pump, second and third harmonic generation tones as a function of the flux applied from a voltage biased superconducting coil. We expect two peaks in the second harmonic tone per flux quanta as per the magnitude of $|\beta|$ from eq. (A.34) and fig. 2.3.

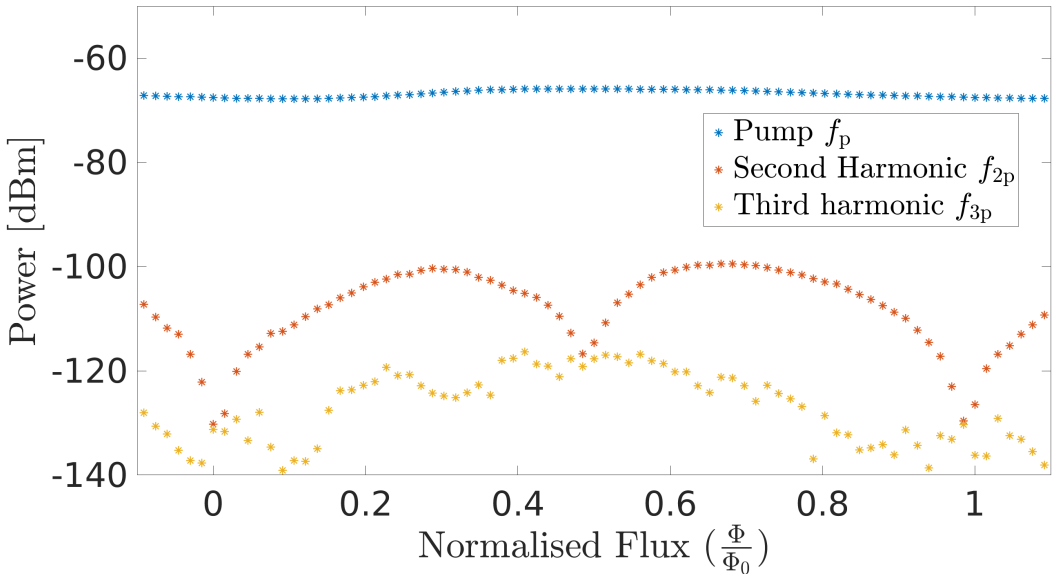

Figure 3.20: Pump and cascaded harmonics versus the bias voltage over a smaller range. From this plot we assume a voltage-flux quanta ratio of 3.3 V/Φ_0.

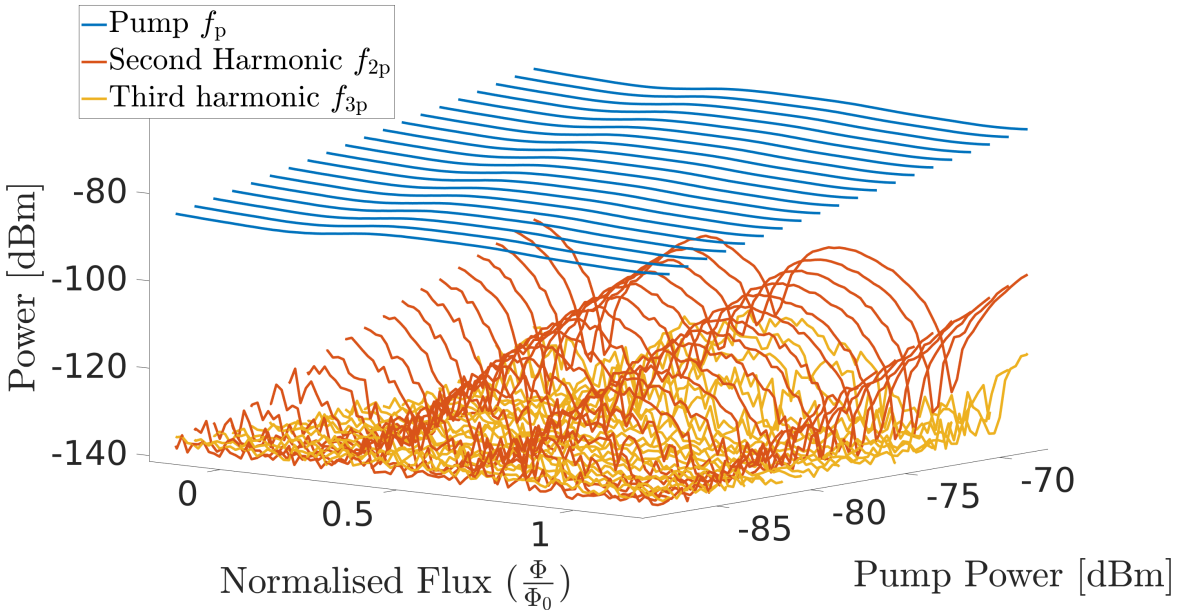

Figure 3.21: Cascaded pump harmonic powers as a function of flux and pump power. Here we have normalised the external flux bias $m + \Phi_e/\Phi_0$, where m is an unknown integer of flux quanta in the loop. The range is the same as shown in fig. 3.20 but over a number of pump powers showing the increasing amplitude of the cascaded harmonics with increasing pump power.

there exists a pump tone, as well as the second harmonic generation of the pump. Then, through sum frequency generation in the three wave mixing scheme, these two tones can sum to make a third tone, $f_{\mathrm{SFG(p,\,2p)}} = f_p + f_{2p} = 3f_p = f_{3p}$. This, then cascades through the device, and in the case of a strong pump tone, this cascade could be the dominant mixing mechanism in the device. This, could cause a more dominant pump depletion mechanism, and thus be detrimental to signal amplification.

In fig. 3.19 we aim for a pump power of $P_P = -68$ dBm which in current relative to the critical current of the junction is $I_p/I_c \approx 0.5$, where the junction critical current is $I_c \sim 5\ \mu A$. One consideration was that this pump power may be too large and that by reducing this, second harmonic generation may be decreased. We capture the power dependence of the cascaded harmonic generation in fig. 3.21 which shows that second harmonic generation persists over a 20 dB range of pump powers.

The cascade of the third harmonic reduces into the noise floor around $P_p \approx -80$ dBm in fig. 3.21. The pump behaviour linearly follows the pump power as expected. The growth of the second harmonic is ~ 40 dB over the 20 dB pump increase. This follows the standard result from inter-modulation distortion, in particular the theory of second order intercept point, (see [49] for example) which is discussed in more detail in section 3.2.2.

3.2.2 Sum Frequency Generation

In this section we describe an experiment on a second generation JTWPA sent from PTB, JTWPA2. This JTWPA comprises of $N = 1056$ rf SQUIDs. The purpose of this experiment was to look for other up-conversion terms when two input tones are injected into the device. As such this type of measurement is referred to as Two Tone Spectroscopy (TTS). The principle of this device was again to be used as a parametric amplifier however signal gain was again non optimal. As previously discussed the higher frequency tone is also larger in amplitude and is referred to as the pump. The lower frequency tone is lower in amplitude and is the signal. The standard operating procedure is to hold the pump at a fixed frequency, while sweeping the signal frequency over some bandwidth we wish to measure in. Since we wish to observe potential Sum Frequency Generation (SFG) between the two input tones and their mixing products we again must consider the bandwidth of our experimental set up, shown in fig. 3.22. As such, for all subsequent measurements the pump frequency $f_{\mathrm{p}} = 6.0132$ GHz, while the signal frequency is swept from $2 < f_{\mathrm{s}} < 4$ GHz. The same fitting routine described in section 3.1.3 is used.

To gauge an initial response of the device we measure the pump, signal and second harmonic generation (SHG) tones. The pump and signal are injected from signal generators and fed through filters to reduce any crosstalk in the signal generators. The second harmonic of the pump is outside of the band pass filter on the pump line and thus any detected SHG of the pump tone is deemed to originate inside JTWPA2. We now include the signal tone which is swept from $2 < f_{\mathrm{s}} < 4$ GHz adding an additional dependency to the measurement. Again, to gauge the flux dependence of this device we look for a pattern in the SHG of the pump tone shown in fig. 3.23.

The signal and pump remain flat over the entire added flux range in fig. 3.23. The SHG tone shows the same flux dependence as described previously in section 3.2 and thus we again infer the optimal flux position. As we see from fig. 3.23 there is no frequency and flux dependence in the amplitude of the signal. Another method is to check for first order interactions as described in section 1.2.1, which involve pump and signal interactions. The primary interaction for parametric amplification derives from the Difference Frequency Generation (DFG) of pump and signal and produces a tone typically referred to as the "idler" at a frequency $f_{\mathrm{i}} = f_{\mathrm{p}} - f_{\mathrm{s}}$. However as shown in section 1.2.1 there is also the possibility of Sum Frequency Generation (SFG) between the pump and signal. This SFG tone is

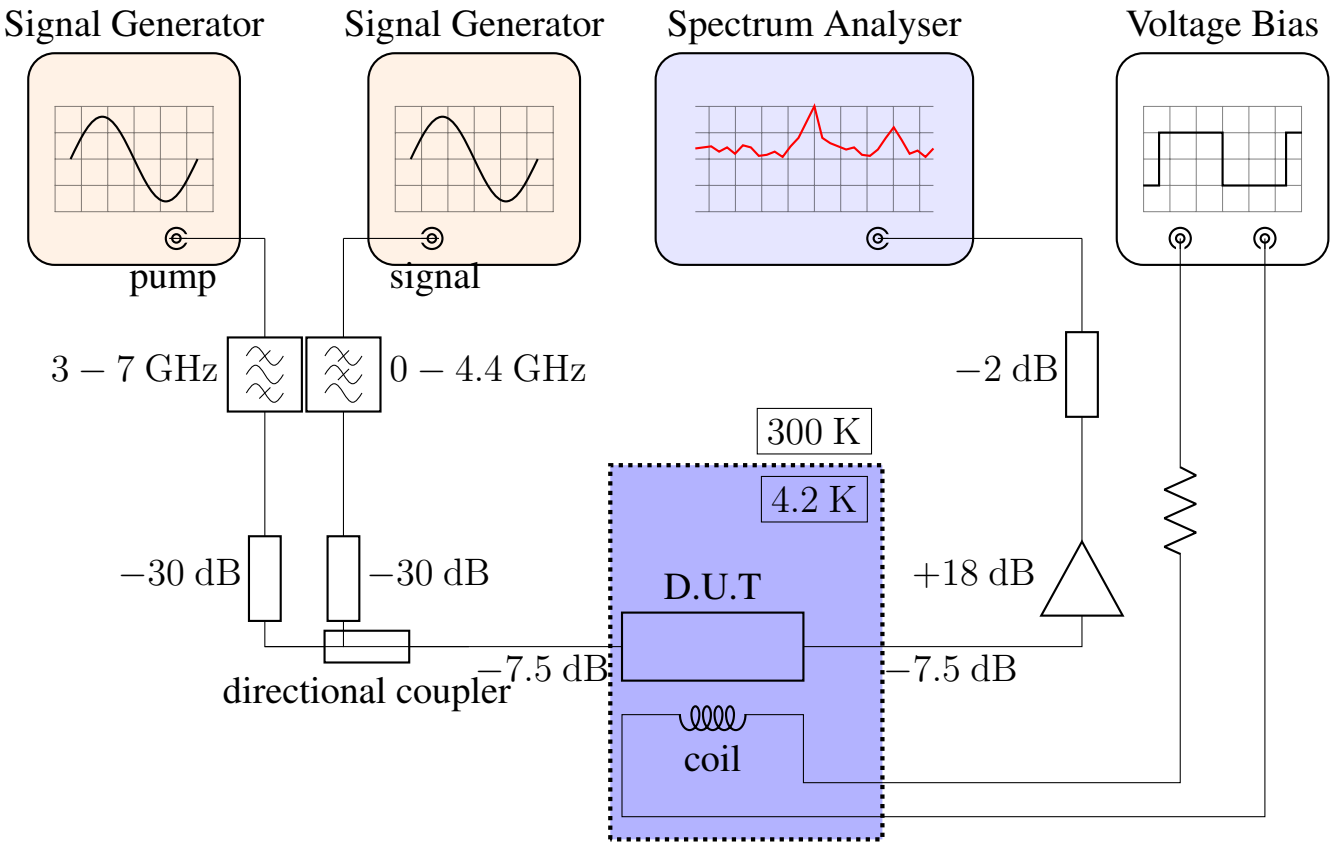

Figure 3.22: Experimental set up for two tone spectroscopy to demonstrate harmonic generation as well as up conversion tones in a travelling wave device.

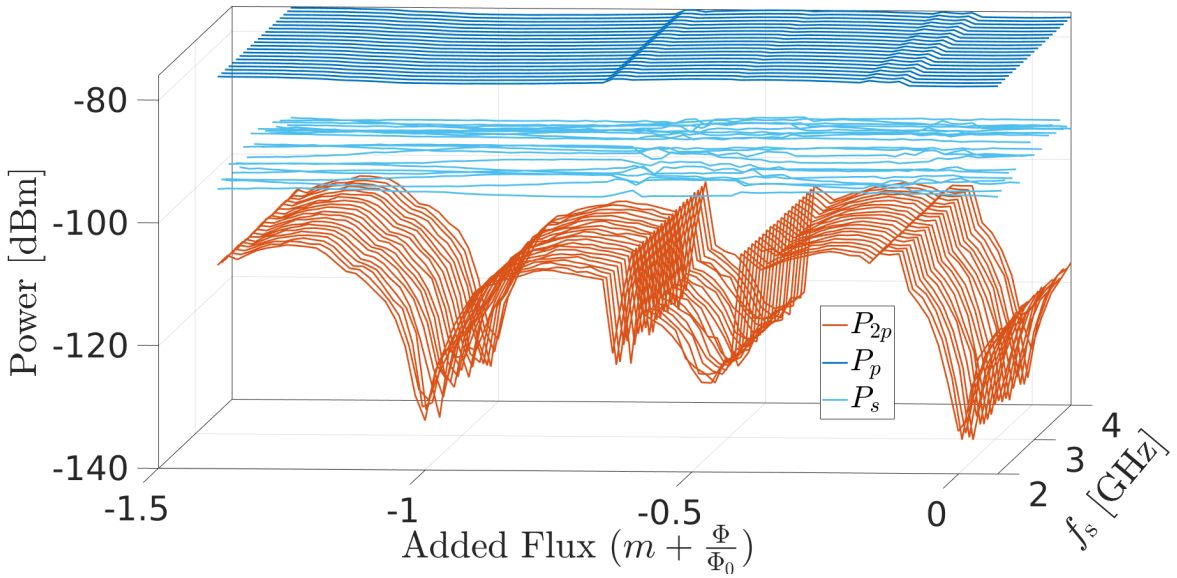

Figure 3.23: Plot of pump (dark blue) and signal (cyan) amplitudes over a range of flux and signal frequencies. Here the amplitude of the second harmonic of the pump tone (red) follows the flux dependence of the amplitude of β shown in fig. 2.3. The signal and pump are both considerably large, however the second harmonic approaches the signal level at the assumed maximal three wave mixing flux bias points. However the signal tone is still flat over a large signal frequency (f_s) range.

also a generated tone and in this sense is another "idler" tone, however to formulate a simple naming convention this idler is referred to as the "pump + signal" tone and is at a frequency $f_{\mathrm{p+s}} = f_\mathrm{p} + f_\mathrm{s}$. In fig. 3.24 we measured both of these up(down) conversion S(D)FG tones over the same signal frequency and flux bias range.

The idler and SFG (pump + signal) tone are maximal at the same flux positions as the SHG tone. This indicates that the three wave mixing process is optimal for all three tones and that the pump and signal tone are mixing. However, it may be that the signal tone is being driven with too much power. In fig. 3.23 the pump power is measured to be around $P_\mathrm{p} \approx -78$ dBm, while the signal power is $P_\mathrm{s} \approx -93$ dBm. Since the pump and signal are only ~ 15 dB apart the signal may be saturated. To check this, we simultaneously raise the pump power to $P_\mathrm{p} \approx -61$ dBm and lower the signal power to P_s 110 dBm and look over a smaller flux range $0.17 < m + \Phi/\Phi_0 < 0.44\Phi_0$ as shown in fig. 3.25.

In fig. 3.23, the reduced signal still does not show flux or frequency dependence. In the region $0.15 < m + \Phi/\Phi_0 < 0.4$ the SHG tone is larger than the signal. This is a concern since the pump is interacting to generate harmonics in favour of modifying the signal amplitude.

We then investigate the power dependence of a number of tones. Since we have already observed

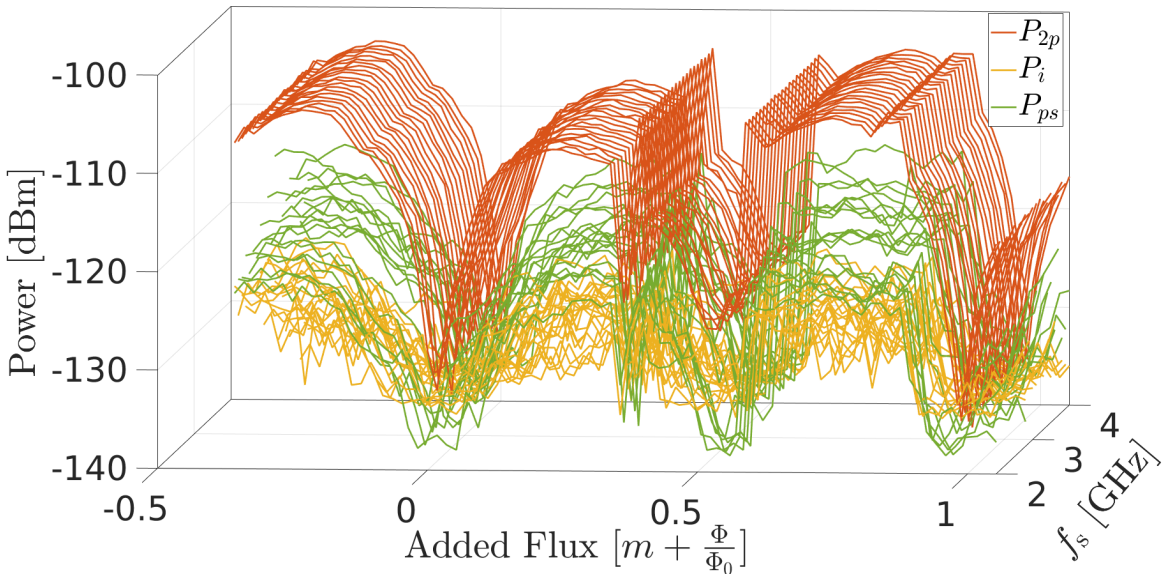

Figure 3.24: Plot of second harmonic generation (red), idler (yellow) and sum frequency generation of pump and signal (green). Here we see that the idler and SFG tone at $f_{\mathrm{p+s}}$ follow the expected curve as a function of inferred flux, rising at the half integer positions. The SFG tone is considerably larger than the idler tone, this is exacerbated for higher signal frequencies.

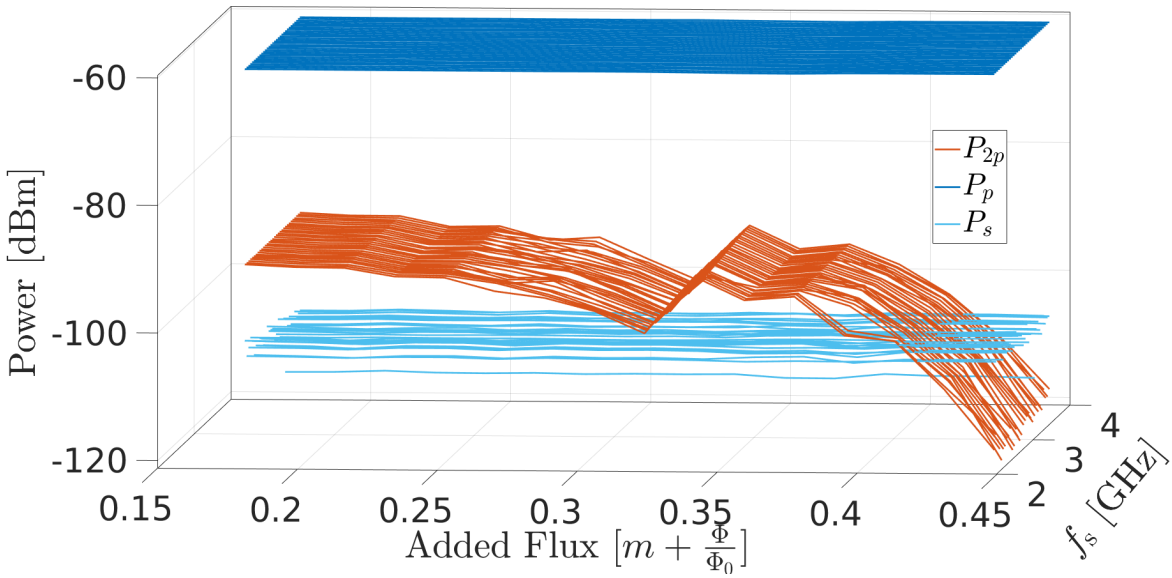

Figure 3.25: Plot of pump (dark blue) and signal (cyan) amplitudes over a range of flux and signal frequencies. Here the amplitude of the second harmonic of the pump tone (red) is now seen well above the signal level over a range of signal frequencies (f_{s}). The signal input power is reduced to $P_{\mathrm{s}} \approx 110$ dBmbut the signal tone is still flat over a large frequency range.

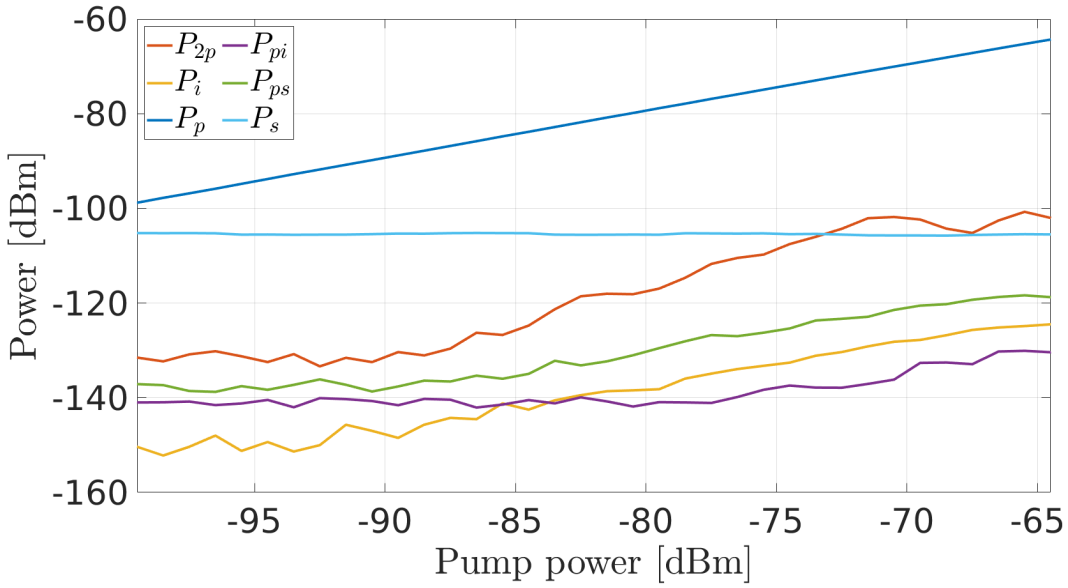

Figure 3.26: Plot of six tones considered; pump (dark blue), signal (cyan), SHG (red), $f_{\mathrm{p+s}}$ (green), $f_{\mathrm{p+i}}$ (purple), and the idler (yellow). As mentioned in [14] we see considerable second harmonic generation. In fact in the linear regime this rises by 2 $\mathrm{dB/dB_p}$ of pump power as expected in standard intermodulation theory of the second order intercept point. (see for example [49], where transitioning from third order intercept to second order is trivial)

the generation of tones at frequencies $f_{\mathrm{2p}},\ f_{\mathrm{i}},\ f_{\mathrm{p+s}}$ it may be possible that second order mixing occurs due to the presence of these tones plus the input pump and signal.

The major tone of this second order mixing process would be a tone at $f_{\mathrm{p+i}} = f_{\mathrm{p}} + f_{\mathrm{i}}$. Interestingly, this now opens up degeneracy in the mixing mechanisms from all other tones based on the three wave mixing condition. As an example, the newly considered tone $f_{\mathrm{p+i}} = f_{\mathrm{p}} + f_{\mathrm{i}} = f_{\mathrm{2p}} - f_{\mathrm{s}}$ begins to highlight the complexity that occurs when considering the higher order mixing mechanisms. In fig. 3.26 we show the power dependence of six tones. Again the signal is swept and each line corresponds to a different signal frequency however we find there is no signal frequency dependence and so for clarity we simply plot the power of each measured tone for a fixed signal frequency $f_{\mathrm{s}} = 3.1$ GHz against the input pump power.

From fig. 3.26 we see that the mixing begins for pump powers $P_{\mathrm{p}} > -87$ dBm. The signal has very little change over the range of pump powers, while the SHG has the largest change. In fact the gradient of $1(2)\mathrm{dB/dB_p}$ measured pump(SHG) follows the standard intermodulation, second order intercept point theory [49]. In the SHG saturation limit, (where SHG no longer grows by 2 $\mathrm{dB/dB_p}$), the SHG tone grows larger than the signal. Figure 3.26 also shows that the up-conversion term is

larger in amplitude at every pump power than the idler generation. This consolidates the need for an expansion to our previous theory and to look to other modelling methods, to gain insight into the behaviour of the device beyond the three tone model.

3.3 Summary

We have made a number of experimental observations that show the existence of tones which are not considered in the standard treatment of parametric amplifiers. First, we showed in a resonant based device that we could explain the existence of a tone situated at the third mode of the resonator through an up conversion three wave mixing process. We then showed in a more complex device and experimental set up that these tones may be generated in travelling wave parametric amplifiers. It is these observations that motivate the rest of the thesis, where we analyse the generation of higher order tones in more detail.

Chapter 4

Simulations

4.1 SPICE Network Analysis

To aid in understanding what may be happening inside the device we have used a SPICE-like circuit simulator, WRspice, to model the device. "Simulation Program with Integrated Circuit Emphasis" (SPICE) software originated from Berkeley and is widely used for detailed modelling of electrical systems. The model is a lumped element circuit model made by defining a "netlist" circuit file and passing it to the simulator.

Recently WRspice [50], a SPICE package which includes the Josephson junction (JJ) circuit element, became recently available as open-source. The JJ model is extensive and details of which can be found online or printed from the full manual. One key realisation of the following work was the ability to create netlists (circuit files) in MATLAB and be able to pipe (pass) them via the terminal (cmd line in Windows) to WRspice allowing for simulations to be scaled up with the aid of high-performance cluster based parallel processes. To do this the MINERVA High Performance Cluster (HPC) at Cambridge University was used.

In this section, we will show first that we can accurately model linear transmission lines as discussed in section 1.2.2. We will then show the ability to accurately describe the Josephson junction (JJ) as discussed in section 1.2.3. Finally, we will combine all of this to build up to a model of the rf SQUID embedded Josephson Travelling Wave Parametric Amplifier (JTWPA). We will centre this entire section around circuit parameters given in appendix A.2.4 for ease of discussion.

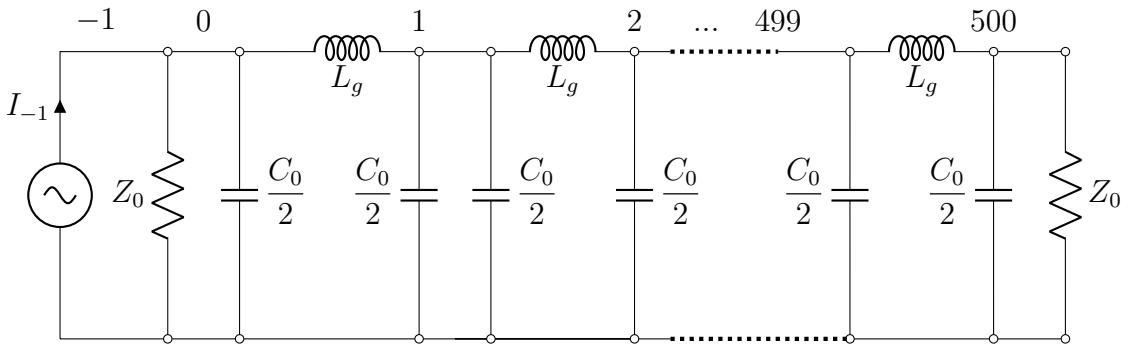

Figure 4.1: Circuit diagram of a lumped element model transmission line.

4.2 Linear Transmission Line Modelling

4.2.1 LC Transmission Line Simualtion

The circuit fig. 4.1 shows a non-infinite transmission line. The current source injects a sinusoidal AC current I_{-1} into the circuit at frequencies $1 - 140$ GHz. There is a "front end" resistor of value $Z_0 = \sqrt{L_\mathrm{g}/C_0}$ which matches the impedance of the simulated LC line. For completeness we use inductance and capacitance values taken from appendix A.2.4, where $L_\mathrm{g} = 57$ pH, $C_0 = 100$ fF meaning $Z_0 \approx 23.87\ \Omega$. In a physical system this is typically done within the signal generator or source and one would match the transmission line (load) to that impedance. In an ideal case the source current would split $50 : 50$ through the front end resistor and into the transmission line (through the 0 branch). We have shown in eq. (1.22) that the transmission line has a frequency dependent impedance $Z(\omega)$, thus perfect matching is not possible for all frequencies. This results in an impedance mismatch and a reflection given by the standard reflection coefficient Γ formula [51],

$$\Gamma(\omega) = \frac{Z(\omega) - Z_0}{Z(\omega) + Z_0}. \tag{4.1}$$

Considering current conservation and just this impedance mismatch the current which goes into the transmission line will then be the current injected minus any current reflected given by the formula,

$$\bar{I}(\omega) = I_0(1 - \Gamma(\omega)), \tag{4.2}$$

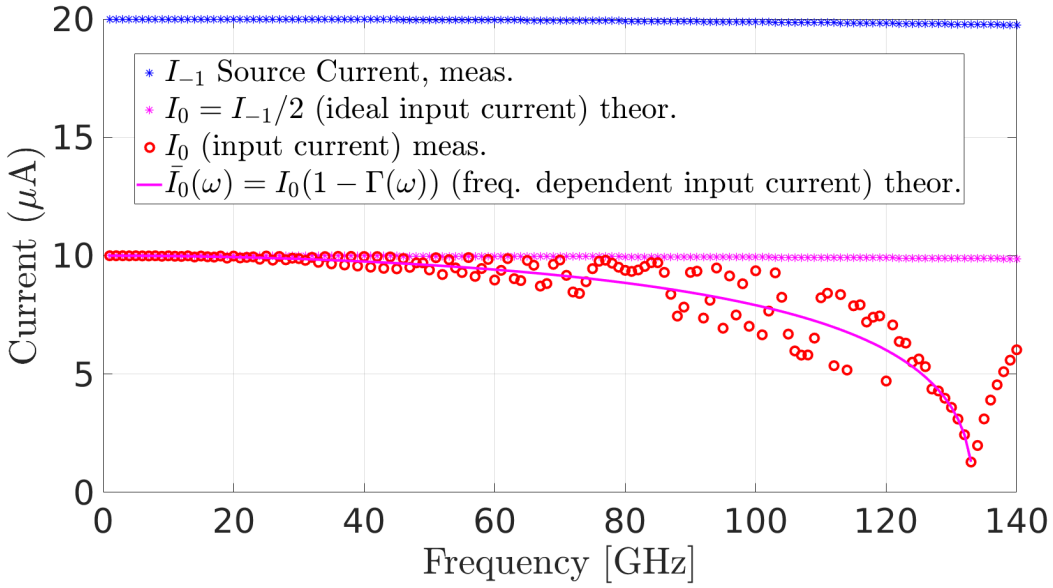

Figure 4.2: Plot showing the theoretical and measured current entering a standard linear transmission line. Here $L_g = 57$ pH and $C_0 = 100$ fF resulting in $f_c = \omega_c/2\pi \approx 133$ GHz. The source current I_{-1} is measured (blue stars) to check that 20 μA is being inserted at each frequency. The measured source current is then halved (pink stars) to give a theoretical idealised input current $I_0 = I_{-1}/2$. We then measure the input current through the 0 branch (red circles), and then compare this to the lumped element theory, eq. (4.2) (pink line).

where $I_0 = I_{-1}/2$ is the idealised current injected into the transmission line with no impedance mismatch. Figure 4.2 shows the simulation results of impedance mismatch up to and slightly above the cut off frequency $\omega_c/2\pi \approx 133$ GHz.

We also measure the phase shift per unit cell. By performing a Fast Fourier Transform at individual nodes along the line we extract the amplitude of each frequency, as well as the phase. Then, by taking the difference in phase between successive nodes we extract the phase shift per unit cell. We discussed the approximation θ' the exact lumped element result θ in section 1.2.2. Here, the approximate unitless phase shift $k' = \omega/\theta'$ and lumped element $k = \theta$ are compared with the phase evolution result from WRspice as shown in fig. 4.3.

As expected, the WRspice result tracks the lumped element model solution for the phase change per unit cell. As stated in appendix A.2.4, the approximate phase shift k' is a good approximation at frequencies f lower than the cut off frequency f_c. For $f > 0.4f_c$ the approximation for the phase shift diverges from the lumped element solution. This is will become relevant later when we discuss modelling higher order modes.

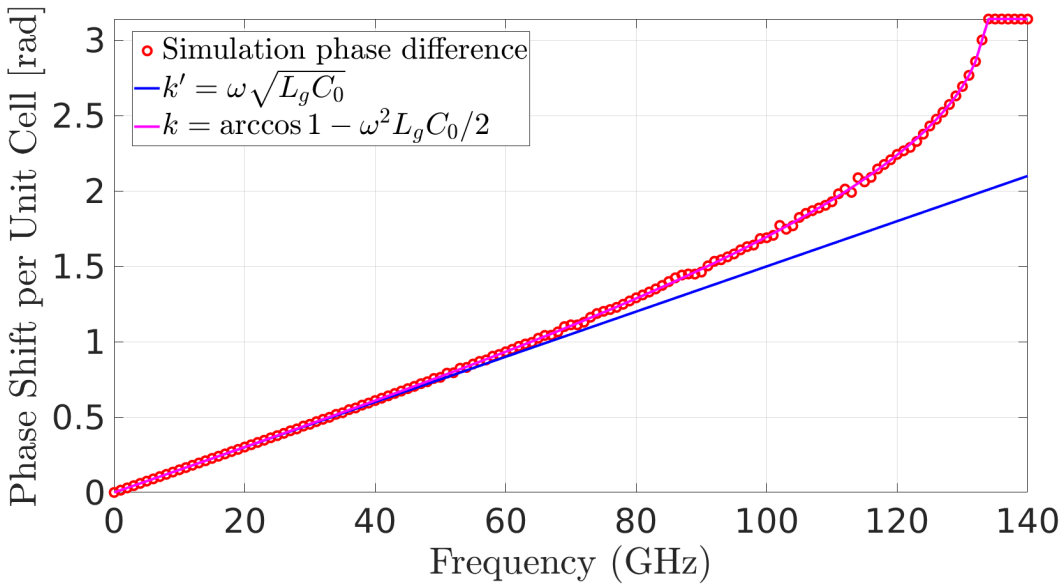

Figure 4.3: Plot comparing phase shift per unit cell for the infinite transmission line approximation (blue line) k' and the lumped element model (pink curve) k to the WRspice result (red circles) which is sampled from $0 - 140$ GHz with a 1 GHz spacing.

4.2.2 Capacitvely Shunted M-line Model

To more accurately describe the rf SQUID embedded JTWPA, we include a shunt capacitance in parallel with the inductive branch of the transmission line as shown in fig. 4.4. This capacitance derives from the formation of the Josephson junction, which in essence is two conducting (superconducting) plates separated by an insulating layer, i.e. a capacitor. We use the value $C_{\mathrm{J}} = 60$ fF taken from [14] to represent the parallel shunt capacitance. As per eq. (1.23), the cut off frequency, $f_{\mathrm{c}} \approx 73$ GHz, has

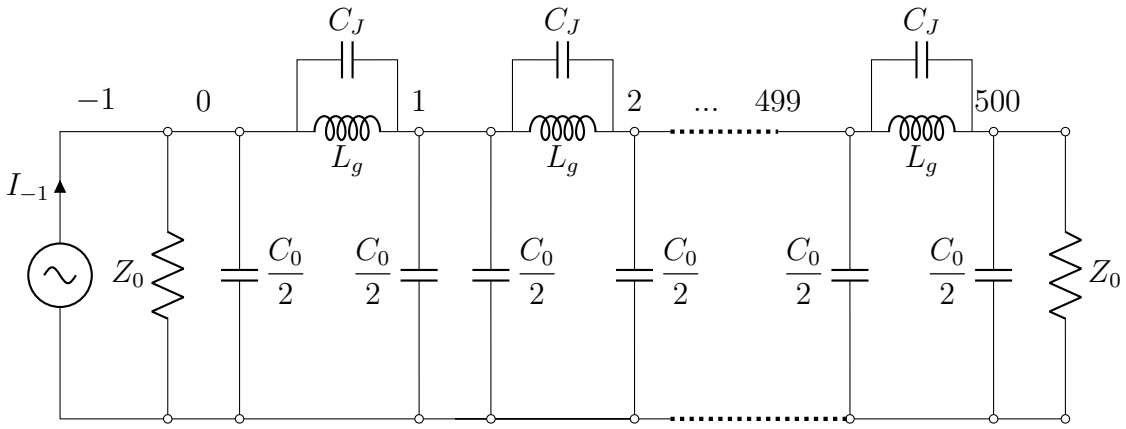

Figure 4.4: Circuit diagram of a lumped element model transmission line.

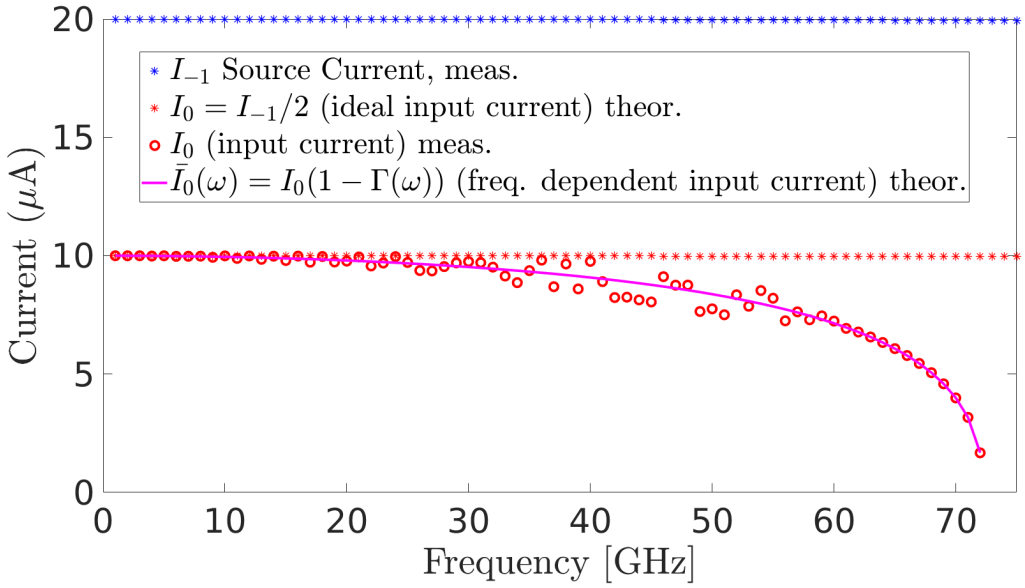

Figure 4.5: Plot showing the front end, frequency dependence of the impedance mismatch of the capacitively shunted M-line. The WRspice result (red circles) follows the standard lumped element theory (pink line). The cut-off frequency f_c of this line is reduced from the standard LC line shown in fig. 4.2.

been significantly reduced due to the shunt capacitance. The zero frequency impedance Z_0 is the same as the standard LC-line $Z_0 = \sqrt{L_g/C_0}$, however, the frequency dependent impedance is modified due to the modified cut-off frequency. This then alters the impedance mismatch for certain frequencies and a more exaggerated curve in the insertion loss, shown in fig. 4.5.

Also, in [14] the approximate phase shift per unit cell k' is derived from the plane wave solution to the super-linear wave equation (eq. (2.18)) and given by eq. (2.19), which now has a non-linear frequency dependence. The lumped element phase shift is also modified as discussed in section 1.2.2. From the Taylor expansion of the cosine function we note that the super-linear solution k is the first order approximation to the lumped element model. Again we compare both results with the simulated result in WRspice, shown in fig. 4.6.

Firstly again WRspice follows the lumped element analysis as expected. We also note that the inclusion of the shunt capacitance reduces the cut-off frequency of the line f_c. Frequencies above this propagate with a non-zero attenuation co-efficient, and since the elements are purely reactive, undergo an exponential evanescent decay [52]. Also note that the linear section of the dispersion relation is reduced and the pink line shows a larger portion of non-linear dispersion. As we have seen cascaded

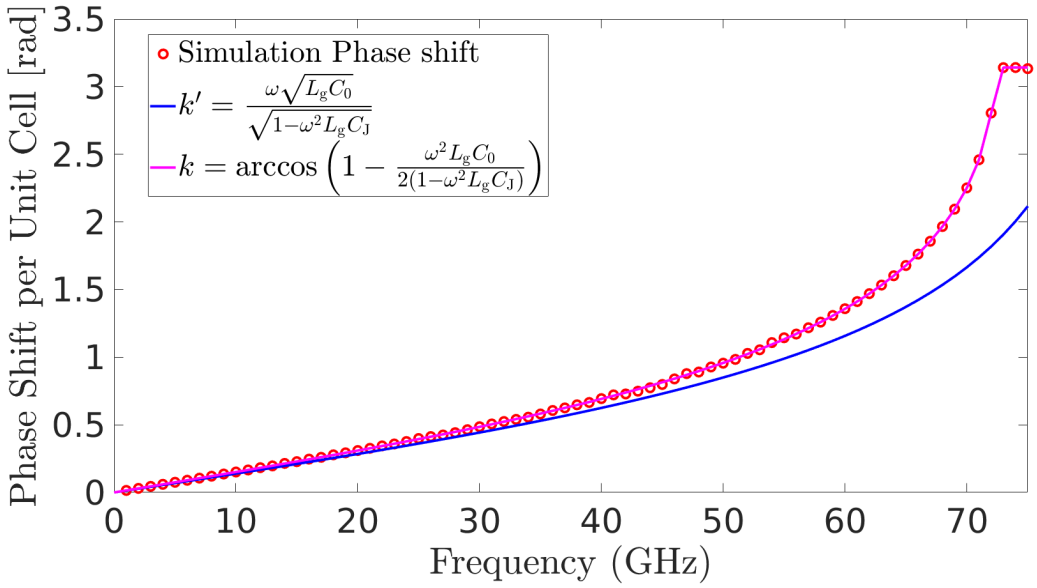

Figure 4.6: Plot showing the phase shift per unit cell (dispersion) of the capacitively shunted M-line. The WRspice result (red circles) follows the standard lumped element theory (pink line). The cut-off frequency f_c of this line is shown at the lowest frequency to achieve a π phase shift. The shape of the curve is much steeper and shows a higher non-linearity than in fig. 4.3.

harmonic generation from the large amplitude pump tone (which in [14] is $f_p = 12$ GHz) we see that tones at frequencies $f > 30$ GHz will be on the non-linear section of the dispersion curve. The analysis of this will be discussed in detail later.

4.3 Josephson Simulations

4.3.1 RCSJ Theory

A standard model for the Josephson junction is the Resistive and Capacitively Shunted Junction (RCSJ) Model. In this, one defines the current branches of the Josephson junction as a parallel combination of a capacitor C_J, resistor R_J and the junction itself as shown in fig. 4.7.

The capacitive and resistive current branches are given by the the standard electrical relations,

$$I(C_J) = C_J \frac{\partial V}{\partial t}, \tag{4.3}$$

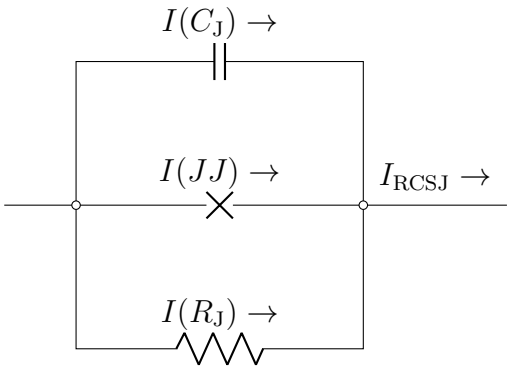

Figure 4.7: RCSJ model of a single Josephson junction which describes the basic set up used in the WRspice simulations.

$$I(R_\mathrm{J}) = \frac{V}{R_\mathrm{J}}.$$

The total current is then given by,

$$I_\mathrm{RCSJ} = I(C_\mathrm{J}) + I(R_\mathrm{J}) + I(JJ). \tag{4.4}$$

Then, using eq. (1.25) for the junction current $I(JJ)$ and eq. (1.26) for the voltage, one obtains the second order differential equation describing the RCSJ model,

$$I_\mathrm{RCSJ} = \frac{\hbar C_\mathrm{J}}{2e}\frac{\partial^2\varphi}{\partial t^2} + \frac{\hbar}{2eR_\mathrm{J}}\frac{\partial\varphi}{\partial v} + I_\mathrm{c}\sin(\varphi). \tag{4.5}$$

The RCSJ model is then solved numerically, an example MATLAB script is given in appendix B.1. In this section, we will compare the DC and AC josephson effects with the numerical result to show WRspice's ability to model the Josephson element.

4.3.2 DC Josephson Simulations

A current source injects a DC current through the Josephson junction. Then we measure the voltage over the junction for a certain length of time. The circuit set up is shown in fig. 4.8. The voltage time trace is shown in fig. 4.9 and shows the various ramp times and oscillations for different injected DC bias currents.

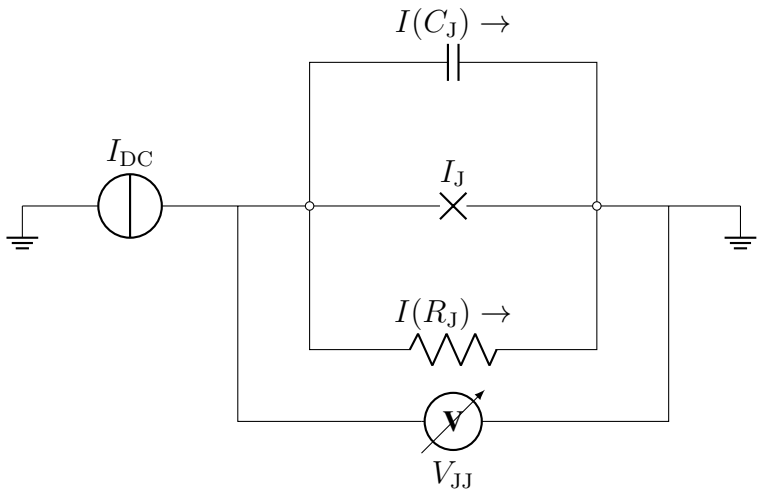

Figure 4.8: Josephson junction model with a DC current source attached and voltmeter measuring voltage over the junction.

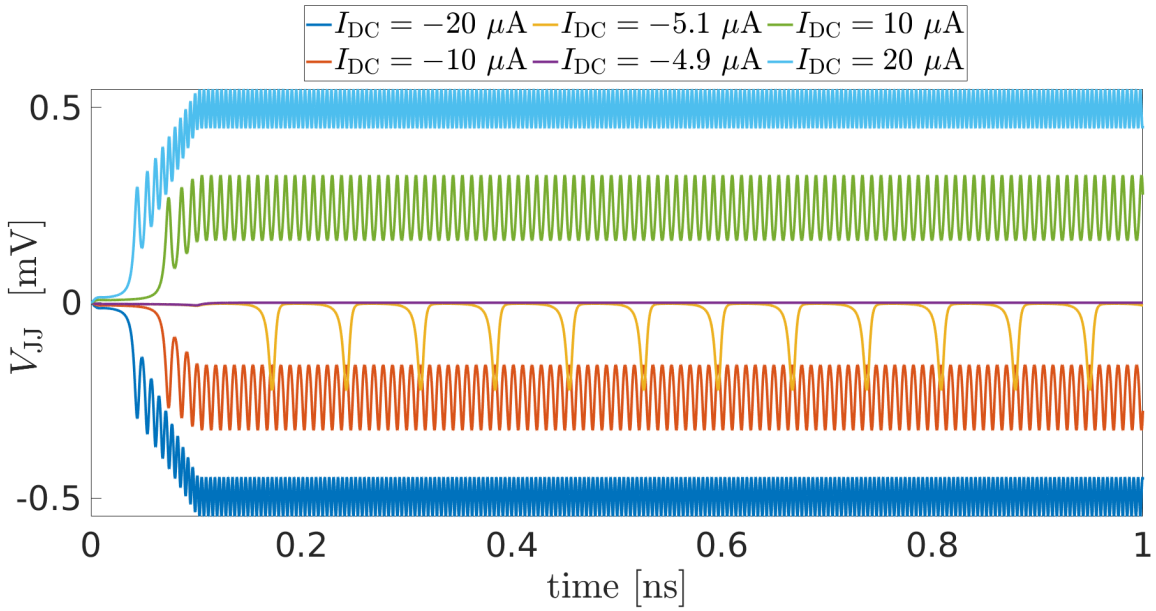

Figure 4.9: Plots of the voltage-time traces for various DC bias currents. The oscillation frequency is DC bias related as well as the ramp times. We integrate the entire trace ensuring that the total time is sufficiently long to capture at least 10 voltage oscillations when $|I_{DC}| > I_c$.

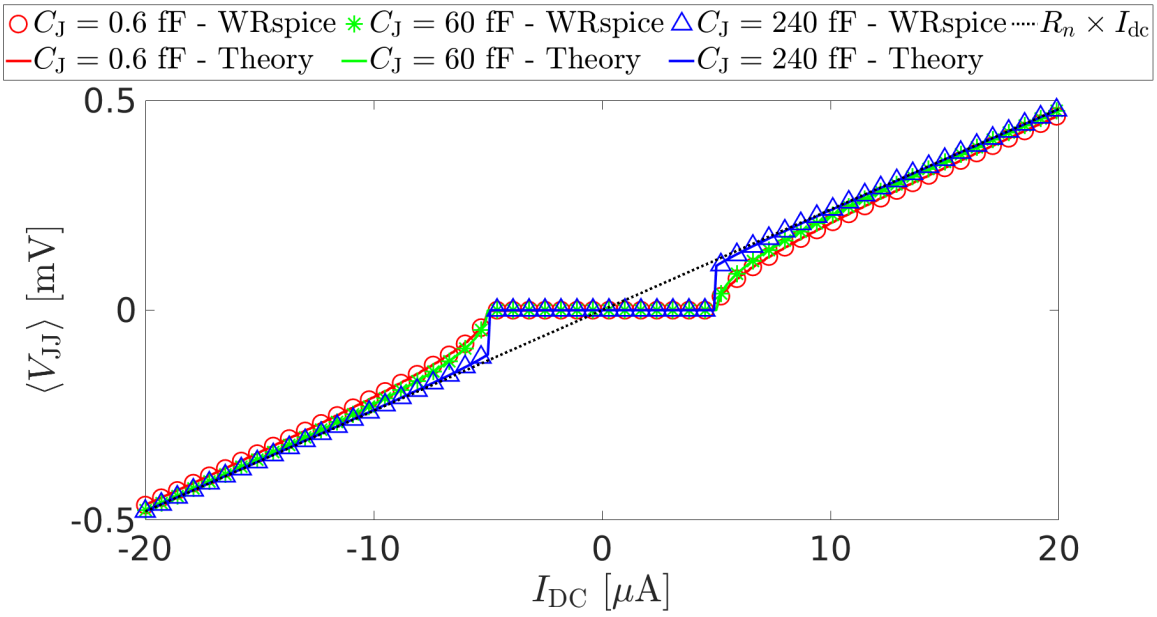

Figure 4.10: Theoretical (solid) and simulated (shapes) I-V curve of a single Josephson junction. The zero voltage regime of the junction for DC current below the critical current, $I_c = 5\ \mu A$, shows the non-dissipative nature of the Josephson junction. Low capacitance values, 0.6 fF (red) and 60 fF (green) introduce a "shoulder" to the sharp change around I_c and $\beta_C = 2\pi I_c(R_J^2)C_J/\Phi_0 < 1$. For higher capacitance values, $C_J = 240$ fF (blue), there is a sharp transition to the voltage state.

The junction values are, $R_J = 23.87\ \Omega$, $I_c = 5\ \mu$A. We show the result for three junction capacitance values in fig. 4.10.

We see that WRspice faithfully reproduces the RCSJ model in the DC biased case. WRspice captures the non-dissipative regime for $-I_c < I_{DC} < I_c$, as well as the bending of the I-V curve due to the parallel capacitance when $|I_{DC}| > I_c$.

4.3.3 AC Josephson Simulations

A key feature of the single Josephson junction is the observation of Shapiro steps [53] when microwave frequency (rf) radiation is applied to the junction. By introducing a DC and AC component to the RCSJ current eq. (4.5) becomes $I_{RCSJ} = I_{DC} + I_{AC}$. This is simply implemented in WRspice with the circuit shown in fig. 4.11.

The AC source has a fixed frequency $\omega_{rf}/2\pi = 0.5\left(2\pi\sqrt{L_j(0)C_J}\right)^{-1} = f_{rf} \approx 40$ GHz, and amplitude $I_{rf} = I_c/2 = 2.5\ \mu$A. As shown in fig. 4.12 the first two Shapiro steps are visible at voltages $V_{JJ} = n\hbar\omega_{rf}/2e$, where $n = 1, 2$.

With this we have confidence in our understanding of the junction model in WRspice. From this

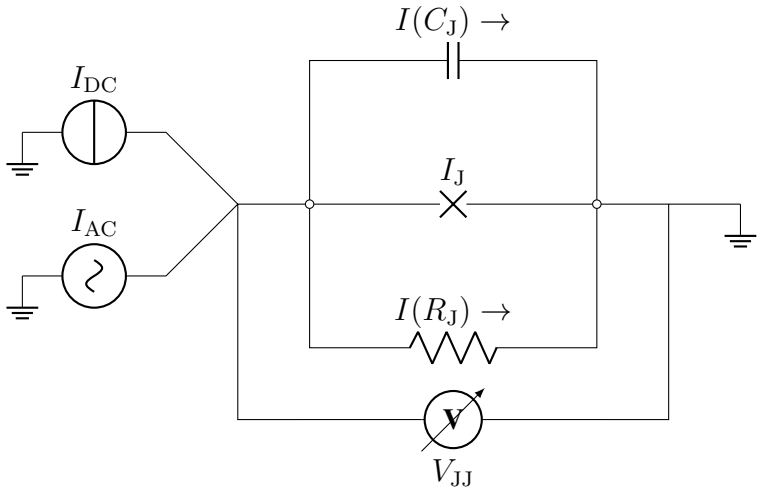

Figure 4.11: RCSJ circuit representation with an applied DC and AC source to show Shapiro steps formed through the AC Josephson effect.

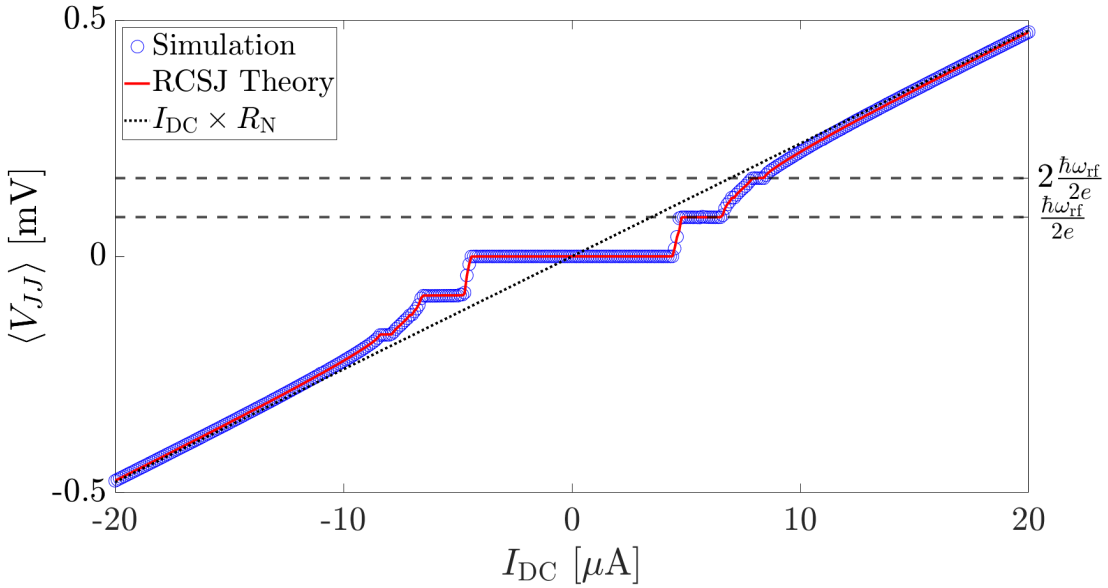

Figure 4.12: AC analysis of the Josephson junction model. The RCSJ model (red solid) and WRspice simulation (blue circles) show good agreement. The Shapiro steps, visible in the I-V curve, are at multiple integers of $V_\mathrm{Shapiro} = \hbar\omega_\mathrm{rf}/2e \approx 83\ \mu V$.

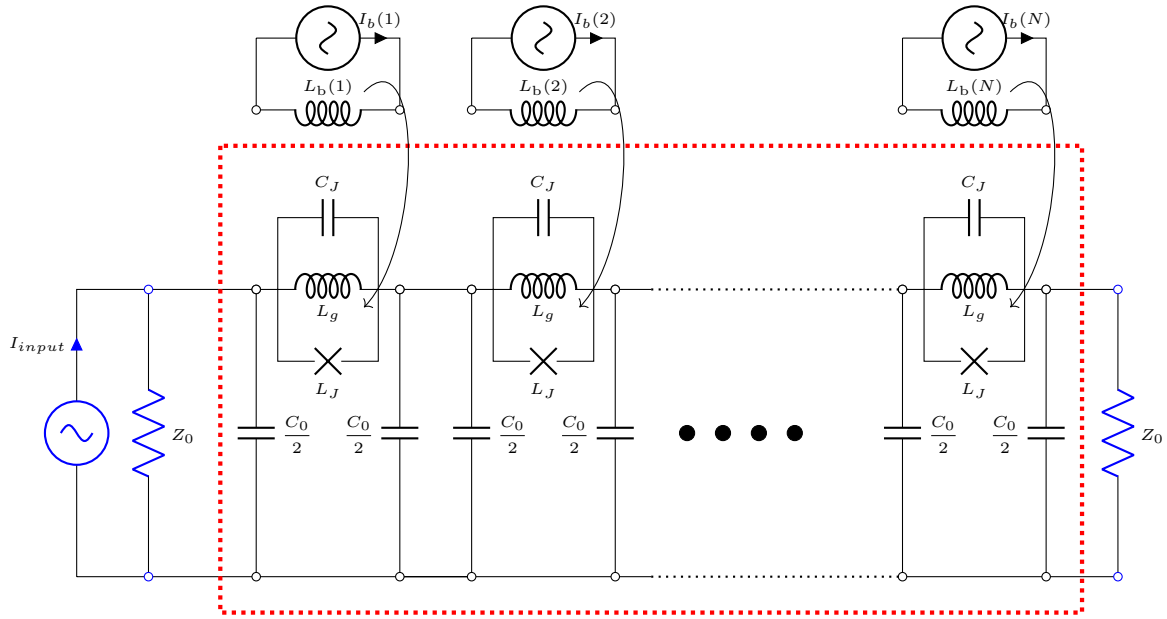

Figure 4.13: Circuit diagram showing the rf SQUID embedded JTWPA (red box) between input and output termination resistors (blue resistors) and input current (blue current source). The flux biasing is achieved through mutual inductors with separate bias currents coupled to the parallel inductor forming the individual rf SQUIDs.

point we remove the resistive shunt in the WRspice model. This removes quasiparticle generation and is done by simple setting the `rtype=0` in the junction model. We then move on to implementing a WRspice model of the full rf SQUID embedded JTWPA as proposed in [14].

4.4 rf SQUID JTWPA Simulation

We have discussed a number of considerations for simulating linear transmission lines in section 1.2.2, where we consider effects such as insertion loss through reflections and impedance mismatch. However, when including Josephson junctions, we note that the parallel inductance may have a non-linear contribution meaning the initialisation procedure may be more complex.

The circuit used is shown in fig. 4.13. The theoretical model simply considers the chain of rf SQUIDs (red), however in the SPICE model we need to include two parallel termination resistors, and an input current source (blue), as discussed previously.

The impedance mismatch comes from the mismatch between the impedance of the non-linear section, and the parallel termination resistors defining the “front end” source impedance and “back end” termination impedance. These resistors are set to a fixed impedance,

$$Z_0 = \sqrt{\frac{L_{\mathrm{g}}}{\mathrm{C}_0}}. \tag{4.6}$$

This is justified since we bias each junction to $\varphi = \pi/2$ and thus $L_J \to \infty$, implying no current goes through the junction and the inductance is dominated by L_{g}. In reality, and the simulation, when the AC tone is injected this phase will shift and the Josephson inductance will contribute.

The junction is intended to be DC flux biased. This is achieved by mutually coupling isolated and driven inductors L_{b} to the inductor representing the geometric inductance of the rf SQUID loop, L_{g}. With a mutual coupling coefficient $K = M/\sqrt{L_{\mathrm{b}} L_{\mathrm{g}}} = 1$, and both inductors being of identical inductance, the current driven through the bias inductor $I_{\mathrm{L_b}}(n) = I_{\mathrm{L_g}}(n)$ and thus a circulating current is set up in the rf SQUID loop.

The ideal circulating current for the given parameters is, $I_{\mathrm{b}} \approx 14\mu\mathrm{A}$, where, $L_{\mathrm{g}} I_{\mathrm{b}} \approx 0.39\Phi_0$, the value predicted for optimal three wave mixing (3WM) ($\varphi = \pi/2$). This sets the junction inductance $L_{\mathrm{J}} \propto \cos(\varphi)^{-1} = \infty$, and then the total inductance $L_{\mathrm{total}}^{-1} = L_{\mathrm{g}}^{-1} + L_{\mathrm{J}}^{-1} \implies L_{\mathrm{total}} = L_{\mathrm{g}}$ and eases the problem.

The introduction of the AC pump and signal shifts the junction phase, causing time dependence in the junction contribution. This is what allows the non-linear behaviour and the wave mixing, but may also modify the impedance and dispersion of the line by modulating the Josephson inductance, and causing possible reflections. It is worth noting that the most severe reflections will happen at either end of the device where the termination resistors are mismatched to the end rf SQUID impedance. “Front end” reflections are typically referred to as a source of insertion loss, this affects the input current to the device. While “back end” reflections are referred to as back action and the reflected backward travelling waves may interfere with forward travelling waves within the device and set up standing wave interference.

It is also worth noting that the impedance of the line is frequency dependent and thus can never be perfectly matched for all rf tones, and so even in a device with no phase oscillations, perfect impedance matching is impossible for any more than 1 input tone.

With the design values given in [14] namely, $L_{\mathrm{g}} = 57$ pH, $C_{\mathrm{J}} = 60$ fF and $C_0 = 100$ fF the calculated $Z_0 \approx 23.8747\Omega$. As a concrete example of the most complex simulation we show the netlist

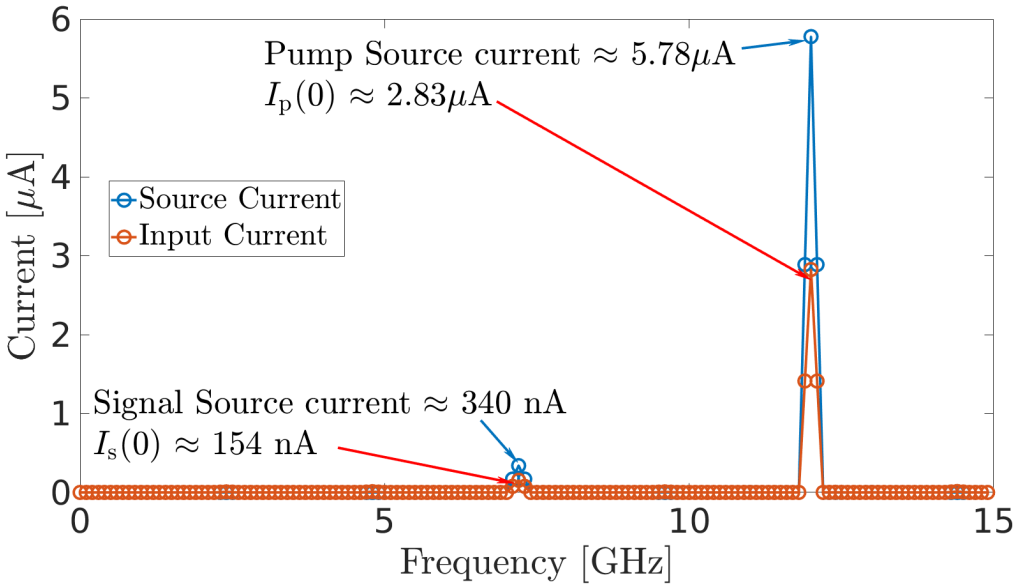

Figure 4.14: Measured source current (blue) and input current ($I(n = 0)$) (red) from the WRspice simulations. We see that the the measured pump input is $I_p(0) \approx 2.83\mu$A, slightly lower than anticipated. The signal input is $I_s(0) \approx 0.154\mu$A which is $\sim 10\%$ lower than expected due to impedance mismatch.

for the JTWPA in appendix B.2.

The two current sources, I_p and I_s, are set to 5.78 μA and 0.34 μA respectively. This should give an input to the JTWPA of $5.78/2 = 2.89$ μA and $0.34/2 = 0.17$ μA respectively, as we expect a $50:50$ splitting of the current into the JTWPA and through the resistor to ground for ideal impedance matching. The `Vmeas0` and `Vmeas1` components act like ammeters either side of the front end termination resistor allowing us to measure the output current from the source and the input current ($I_s(0)$) to the amplifier respectively. Figure 4.14 shows that the input current is not exactly half of the corresponding source current. Because of this, it is more accurate to measure the input current to the device for each simulation and then convert this to the initial boundary conditions of the CME theory for pump and signal amplitude.

We then directly compare the current on the output node ($n = 500$) `Vmeas501#branch` with the input current, as well as the expected output current from the CME calculations in fig. 4.15. While we note the generation of an idler in fig. 4.15 indicative of non-linear wave mixing, the final amplitudes for pump and signal are not in-line with the theoretical predictions from the CMEs. The frequencies of the much smaller peaks are at 9.6 GHz and 14.4 GHz, these are twice the idler and signal frequencies,

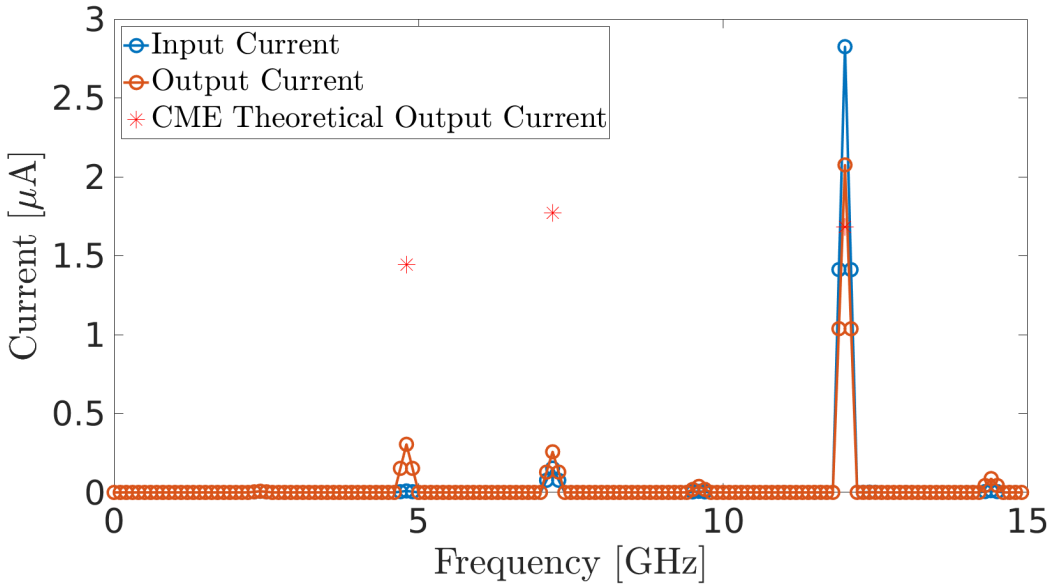

Figure 4.15: Measured input and output currents from simulation of the amplifier, along with the CME predictions. Here the input amplitudes to the CMEs are taken directly from the measured inputs in the simulator (thus taking insertion loss into account). Note generation of a response at the idler frequency ($f_\mathrm{i} = f_\mathrm{p} - f_\mathrm{s}$) consistent with three wave mixing.

$2f_\mathrm{i}$ and $2f_\mathrm{s}$ respectively. This second harmonic generation of tones is common in $\chi^{(2)}$ crystals in the optics community [54] and is known to scale with input power. Since the signal is much weaker than the pump input, and the idler is generated and zero amplitude at the input, we would expect these tones to be low in amplitude. However, we should also look for second harmonic generation (SHG) of the pump tone since this is a much larger amplitude tone.

It is worth mentioning that in order to obtain these current amplitudes we measure the current on the ammeter over a period of time t_meas. This measurement time must be taken after; piece wise linear ramp of the flux bias $0 < t_\mathrm{ramp} < 5$ ns, and after transients from the introduction of rf at $t = 9$ ns, this is shown in fig. 4.16. Since we are looking for a series of pure sine waves, a Hann window has been used. The Hanning window also helps to mitigate spectral leakage, which is problematic for low amplitude peaks [55]. An example of the full time trace and Hanning windowing is given in fig. 4.16 for node $n = 500$.

To investigate further we place ammeters between every rf SQUID cell and measure the current at each node n in the array. Then again applying a Hanning windowed Fourier transform, but this time at every node between rf SQUIDs, we investigate the spectral properties at every node along the device.

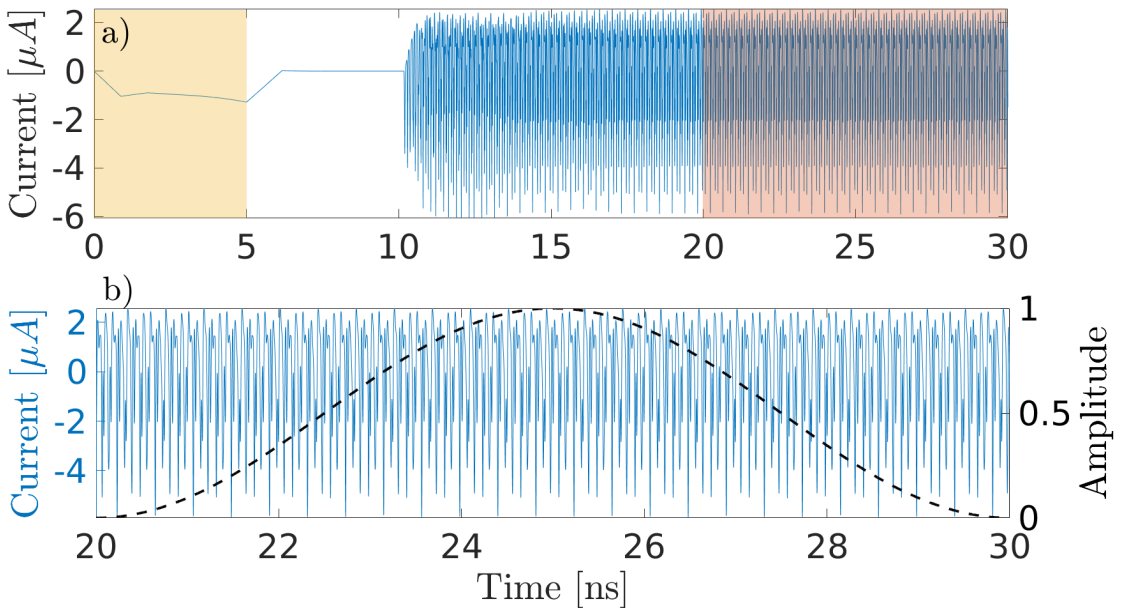

Figure 4.16: Plot showing a) the raw current data taken at node $n = 500$. We have highlighted the ramp time (yellow patch) and measurement time (red patch) in a) to emphasise the transient properties of the simulation. In b) we have taken just the measurement time data, $t_{\text{meas}} = 20 < t < 30$ ns, from a) (blue solid line) and overlayed the Hann window (black dashed line) used to reduce spectral leakage in the FFT.

We select the tones at frequencies of interest; pump, signal, and idler, to compare to the CMEs. This enables a direct comparison of the behaviour along the line for the circuit simulation and the theory.

Due to sampling rate $f_{\text{s}} = 1$ ps in the simulation we are able to detect frequencies up to multiple harmonics of the pump. In fact, fig. 4.18 shows the amplitude for the entire spectrum up to $5f_{\text{p}} = 60$ GHz, and for every node in the device, revealing a multitude of mixing processes taking place. This is shown in fig. 4.18, where we see the large pump and small signal, amongst many other tones up to 60 GHz. This implies that energy from the pump is not directly converted into the signal and idler bands. Instead all forms of non-linear wave mixing are present within the device. The broadband nature of the device supports, up to a limit, the generation of all tones via harmonic (HG), sum frequency generation (SFG) and difference frequency generation (DFG). The mixing is therefore much more complex than previously expected.

We plot the largest amplitude tones (pump (f_{p}) and SHG of pump ($f_{2\text{p}}$)) in fig. 4.19 which shows the maxima and minima of pump and SHG of the pump oscillate against each other. This suggests that the SHG of the pump is a more favourable mixing mechanism in the device and limits the amount of signal gain, a problem which is mentioned in [14]. By causing such a rapid pump decay, less energy is

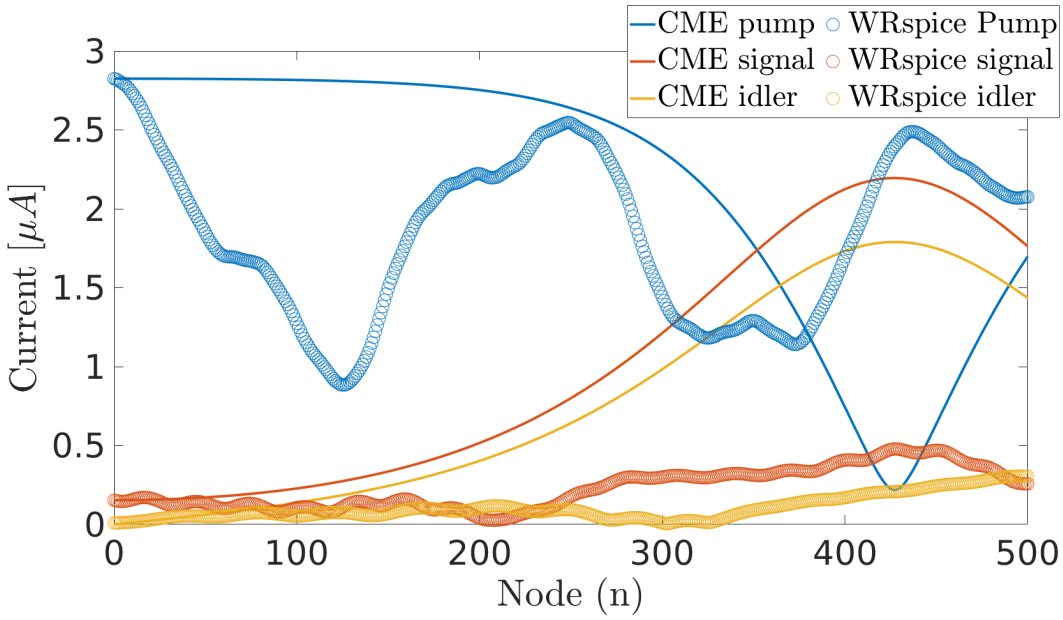

Figure 4.17: Comparison of WRspice (circles) and CMEs (solid) for pump (blue), signal (red) and idler (yellow) along all nodes in the device. The pump initially depletes much faster in the simulation than predicted by the CMEs. The signal also initially de-amplifies in the WRspice simulation, a phenomena we come to understand later in this thesis.

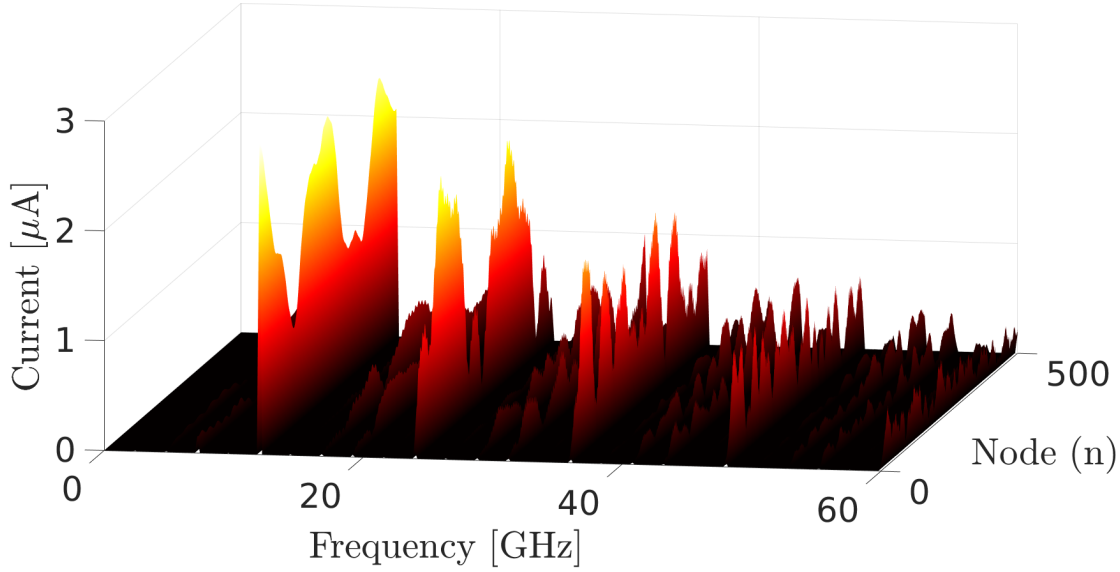

Figure 4.18: Surface plot showing the entire spectral output on every node in the device up to 60 GHz. The pump ($f_{\mathrm{p}} = 12$ GHz) tone is clearly the largest. The next largest tones are at harmonics (integer multiples) of the pump tone $f_{\mathrm{n,\,p}} = nf_{\mathrm{p}}$. There are also tones in the gaps between harmonics which are of significant amplitude, particularly between $f_{\mathrm{p}} < f < f_{2\mathrm{p}}$.

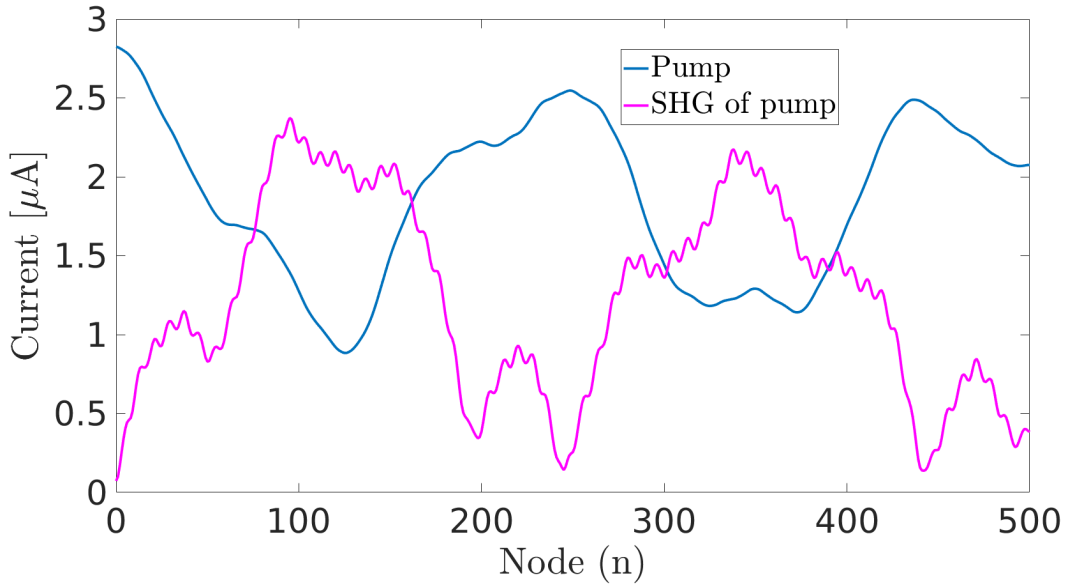

Figure 4.19: Comparison of the large tones; pump (blue) at f_{p}, and SHGp (magenta) at $f_{2\mathrm{p}}$ from the WRspice simulation. Here we note the sharp rise in the $f_{2\mathrm{p}}$ tone causes a much faster pump decay. The two tones also oscillate against each other, showing the process of SHG and subsequent period doubling down conversion as a major mixing mechanism in the device.

available for signal amplification. Similarly, any other mixing mechanism which draws energy from the pump tone will have a negative effect on signal growth.

Projecting fig. 4.18 to produce a heatmap highlights all of the major tones in the device as vetical strips as shown in fig. 4.20. The generation of higher order modes, which aren't accounted for in the current CME theory, has a severe affect on the theoretical device performance. As such, we would like to ensure that we account for this in a manner consistent with the current theory. We then check this quantitatively with simulation tools such as WRspice.

4.5 Summary

We have shown in this section that WRspice is able to accurately model simple transmission lines through a lumped element analysis. Furthermore, we have touched upon other practical considerations such as frequency dependent insertion loss and impedance mismatch which are not routinely discussed in the current literature. We have then shown how this is modified with the inclusion of a linear shunt capacitor to increase the dispersion curvature and reduce the cut-off frequency, again WRspice replicates the result of standard lumped element theory.

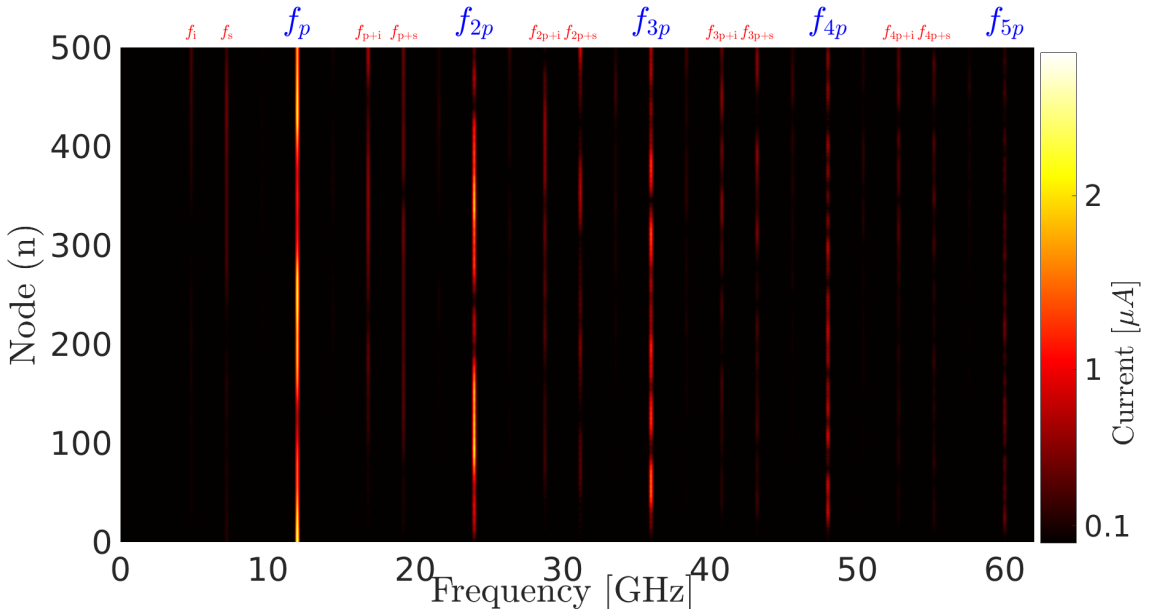

Figure 4.20: Heatmap of fig. 4.18 to highlight the frequencies of the significant tones. We see the large harmonics of the pump highlighted by the blue frequencies on the top x-axis. We also note the various SFG up conversion terms located at $f_{\mathrm{SFG}} = nf_{\mathrm{p}} + f_{\mathrm{s,\,i}}$.

We then show that the WRspice agrees with the RCSJ model for both DC and AC analysis of the Josephson junction. This gives us confidence to implement a full model of a flux biased rf SQUID embedded JTWPA. Primarily we are interested in the observation of higher order modes that may hamper device performance as we have seen this in the experiment section described in chapter 3.

Finally shown that a simulation of the full JTWPA as proposed in [14] shows that not only are higher order modes generated but that the cascaded harmonics grow larger in amplitude than the input signal tone. We show that this cascade is visible up to the 5th harmonic of the pump. Frequencies this high are well outside of the bandwidth of our measurement set up and there is concern for how the generation of these frequencies on chip may interact inside the experiment. Furthermore we show that the generation of up-conversion SFG terms also proliferate within the device.

We would like to develop a theory to understand the generation of these higher order tones and ultimately resolve what we see in the simulation.

Chapter 5

Resolving WRspice Simulation and Theory

Thus far we have shown, through simulation and experiment, that higher order tones exist in rf SQUID embedded Josephson Travelling Wave Parametric Amplifiers (JTWPAs). Previous theories describe an interaction of three tones, namely the pump, signal and idler. This model in the undepleted pump case relied solely on the Difference Frequency Generation (DFG) of pump and signal(idler) to generate(amplify) the idler(signal) tone. We have seen experimentally that higher order tones of Sum Frequency generation (SFG) and Harmonic Generation (HG) are observed in devices. We have then further showed that in a SPICE circuit simulator these tones cascade upwards through three wave mixing (3WM) mechanisms to frequencies which would be difficult to measure with off the shelf microwave circuitry.

What we would like to do is resolve the differences between the observations we have made in previous chapters with a theory which is extended from the standard treatment to many tones. To do this, we first want to see if we can reduce the complexity of the behaviour seen in the simulation. We then consider the implication of orders of interaction and how this cascades throughout the device. Then finally, we look to develop a theory which considers a logical set of frequencies defined by properties of the device which quantitatively compare to simulation results.

5.1 Controlling the WRspice Simulation

Firstly, it is understood that the simulation and the CME theory will not completely agree. The simulation includes things highlighted previously such as insertion loss, internal reflections and higher order corrections. Also within the simulation changes in parameters are dynamic such as the phase on the junction $\varphi \propto \arccos^{-1}(L_{\mathrm{J}})$ which modifies the junction contribution to the total inductance as per eq. (A.23). The simulations are akin to a black box theory, where we insert the inputs, crank the handle and plot the outputs.

WRspice benefits from an extensive manual outlining the simulation procedure. However we still confirm the results of the simulations with a theory derived from physical principles, such as the coupled mode theory. In order to do so it is worth examining the CMEs and understanding the assumptions made within the theory to see if we can bring the two models into a better agreement.

One assumption made was that the junction phase is set to $\pi/2$ and remains at this position such that the inductive path through the junction is infinite, and thus the total inductance is defined by the geometric inductance, eq. (A.23). Similarly the expansion of the rf SQUID current-phase relationship (CPR) in eq. (1.32) relies on a small AC variation in the junction phase. In fact, from eq. (1.32) we see that if the DC phase component φ_{DC} strays from $\pi/2$ then the odd terms in the expansion become non-zero, while for larger AC oscillations of φ then the approximation becomes less accurate. In WRspice, we are able to measure the phase drop across the junction with the use of a third node `Bx [node1] [node2] [`**`phase-node`**`] jj0` as is seen from appendix B.2. We then plot this phase difference for various times; through the DC ramp ($0 - 5$ ns), DC stabilising period ($5 - 9$ ns), rf-input period ($9 - 30$ ns), and the measurement time ($20 - 30$ ns).

The $\varphi_{\mathrm{min,\,max}}$ values in fig. 5.1 are taken during the measurement time $20 < t < 30$ ns and show that the maximal phase variance ($\Delta\varphi = \varphi_{\mathrm{max}} - \varphi_{\mathrm{min}}$) across all nodes and all measurement time is $\Delta\varphi > \pi/2$. Taking various slices of this plot highlights some of the phase dynamics within the system.

The DC ramp is piece-wise linear between $0 < t_{\mathrm{DC\ ramp}} < 5$ ns however we see that not all of the junctions set equally. Taking time slices of the junction phase at 50 ps intervals reveals the DC phase dynamics of the junctions. After 7 ns fig. 5.1 shows that the junctions then stabilise and are constant across the device at $1.57 = \pi/2$ rad. At $t = 9$ ns we insert the pump and signal tones. The AC tones then travel along the length of the amplifier as shown in fig. 5.3.

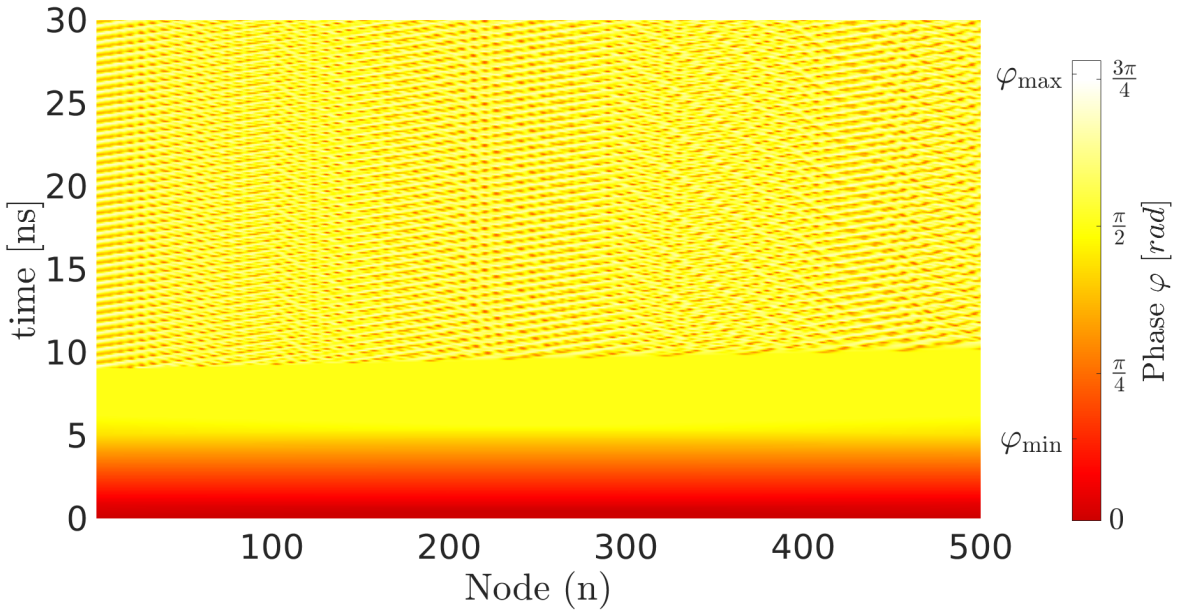

Figure 5.1: Complete plot of the phase on each junction in the n'th rf SQUID array throughout entirety of simulation. The DC ramp over the first 5 ns shows the phase building to $\pi/2$. The pump and signal are then input to the device at node 1 at $t = 9$ ns and reach node 500 at $t \approx 10.5$ ns. The insertion of these AC tones causes the phase to oscillate between $\pi/8 < \varphi < 3\pi/4$. The system is in a steady state between $20 < t_{\text{meas}} < 30$ ns where the measurement takes place.

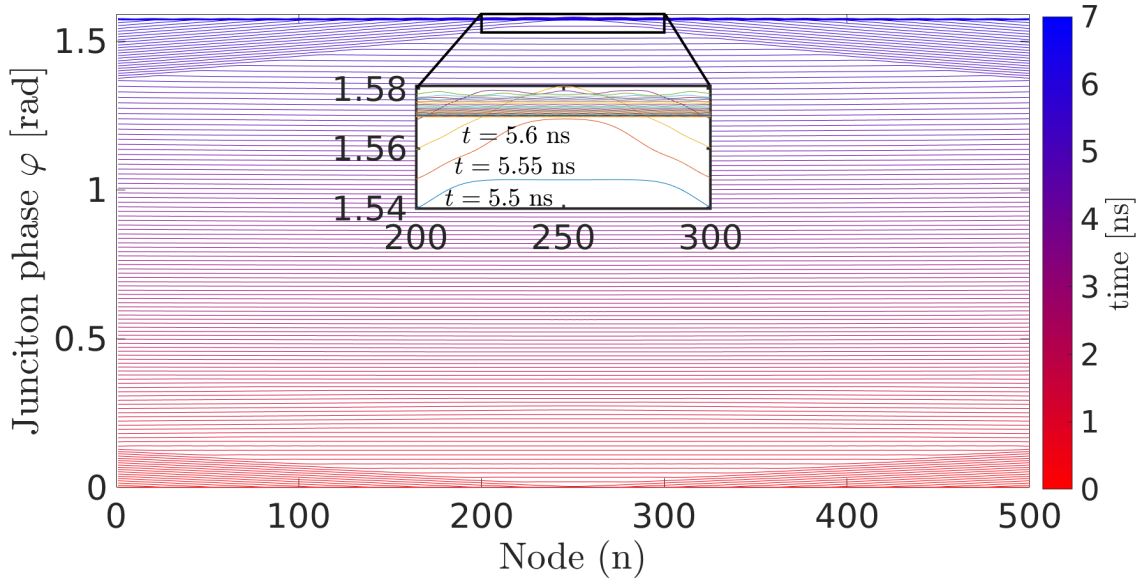

Figure 5.2: Junction phase evolution through the DC ramping time including a 2 ns settling time after the 5 ns DC ramp.

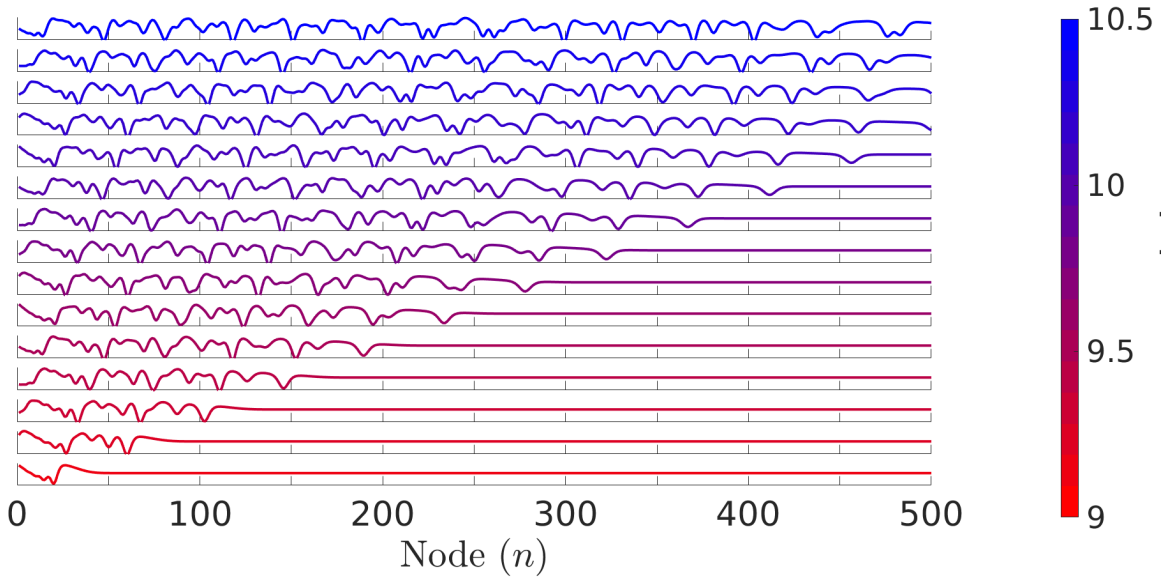

Figure 5.3: Qualitative plot, with y-ticks purposefully not shown but all to same scale, showing the DC offset of the junction phase $\varphi = \pi/2$ for all junctions before the AC shifts the phase. The travelling wave progresses along the line from node $n = 0$ at $t \approx 9$ ns to node $n = 500$ at $t \approx 10.2$ ns.

We then continue applying both the DC bias and rf tones to the device and allow for a steady state to form. The measurement time is then between $20 < t_{\text{meas}} < 30$ ns. It is during t_{meas} that the maximum and minimum of the junction phase is found and labelled in fig. 5.1. To qualitatively see this in more detail a slice at $t = 25$ ns is taken as a snapshot of the junction phases and we overlay a 12 GHz sine wave with arbitrary amplitude and offset to show the correlation with the phase offset and the pump tone in fig. 5.4.

We fit a 12 GHz wave (red line, fig. 5.4) with the dispersion relation eq. (1.24), which characterises the frequency dependent phase shift per unit cell from. Doing this over the first hundred nodes, where the pump is larger then the second harmonic of the pump, allows a qualitative agreement that the dispersion relation from the lumped element model is accurate.

However, after $n > 200$ higher order terms take over and fitting the phase of the waves becomes non-trivial with the inclusion of large amplitude harmonics. Figure 5.4 further highlights the dramatic phase excursion of the junctions from the optimum point of $\varphi = \pi/2$. This undermines the approximations used in deriving the CMEs for the purely 3WM regime. To reconcile this, we would first lower the power input to the device.

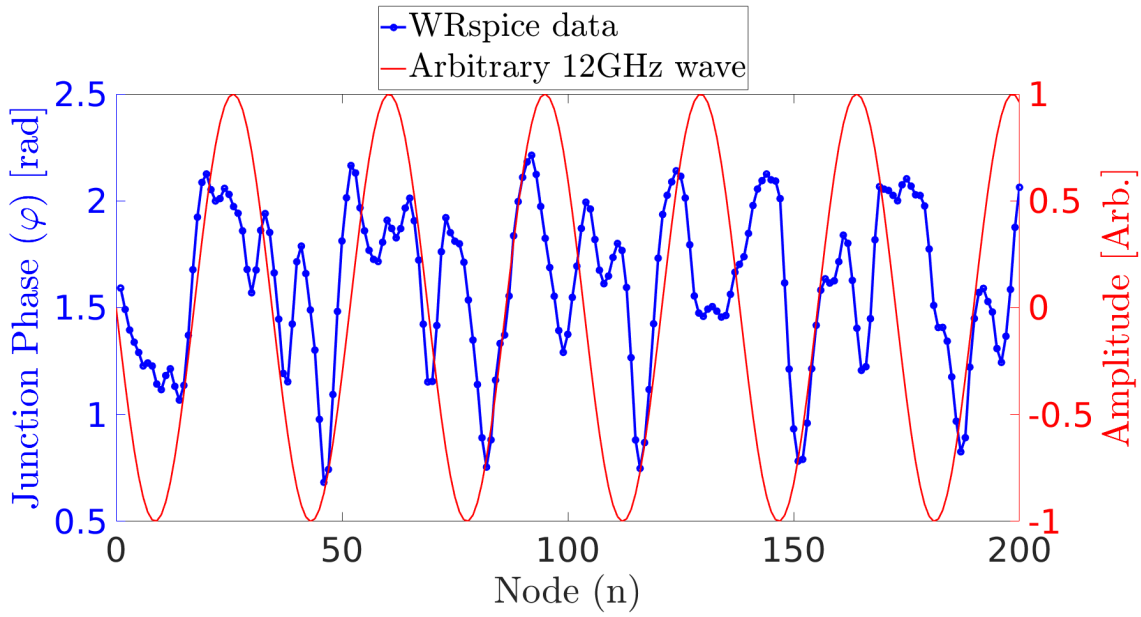

Figure 5.4: Snapshot at $t = 25ns$ showing the large oscillations in Junction phase for pump input of $I_{\mathrm{p}}(0) \approx 0.5I_{\mathrm{c}}$.

5.2 Input Power Handling

5.2.1 Pump Input Power

One way to minimise the oscillations in the phase is to lower the AC input power into the device. By reducing the large pump we reduce the phase oscillations as shown in fig. 5.5.

We get an overview of the entire phase in the low pump power regime where $I_{\mathrm{p}}(0) \approx 0.98\ \mu A = 0.2I_{\mathrm{c}}$ in fig. 5.6. Comparing this directly with fig. 5.1, we see that the variation from the optimal phase $2\pi/5 < \varphi < 3\pi/5$ is drastically reduced. Also, the asymmetry in the phase variation comes from the junction having larger excursions away from I_{c} instead of above it. This shows that the phase of the junction is now much more stable around the $\pi/2$, with a lowered pump amplitude and thus this regime will be more comparable to the theory presented in section 2.2.2.

Now the junction variation $\pi/5 < \Delta\varphi < \pi/2$, which justifies the truncation used in the Taylor expansion eq. (A.26). However, if we reduce just the pump current then the signal is no longer 'small' compared to the pump and secondly that the length for maximum signal amplification is extended. This is seen from the three tone CME calculation for this lowered pump regime and is shown in fig. 5.7.

Here, we see that the signal input amplitude $I_{\mathrm{s}}(0) = 0.2I_{\mathrm{p}}(0)$ is only $1/5^{\mathrm{th}}$ of the input current. From this model the signal reaches a peak current of $I_{\mathrm{s,\ max}} = 0.78\ \mu A$ corresponding to a factor four

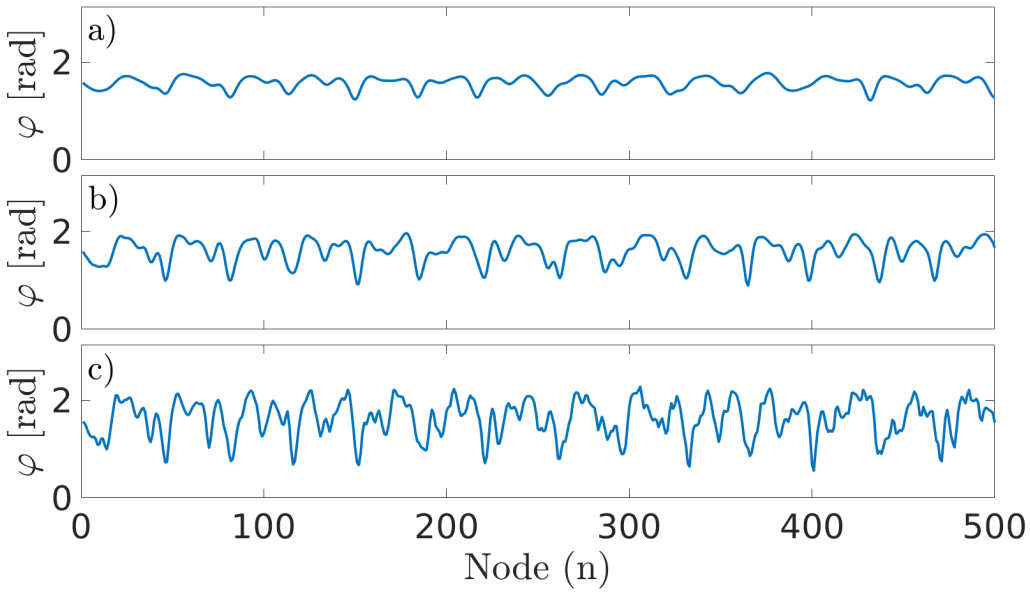

Figure 5.5: Plots of the junction phase across the device for pump current amplitude a) $I_{\mathrm{p}}(0) = 0.98\ \mu$A, b) $I_{\mathrm{p}}(0) = 1.90\ \mu$A, c) $I_{\mathrm{p}}(0) = 2.76\ \mu$A. By lowering the pump amplitude as shown in a) the phase fluctuation is greatly reduced compared to c). Note there is also a more regular oscillation in a) hinting at a less erratic regime.

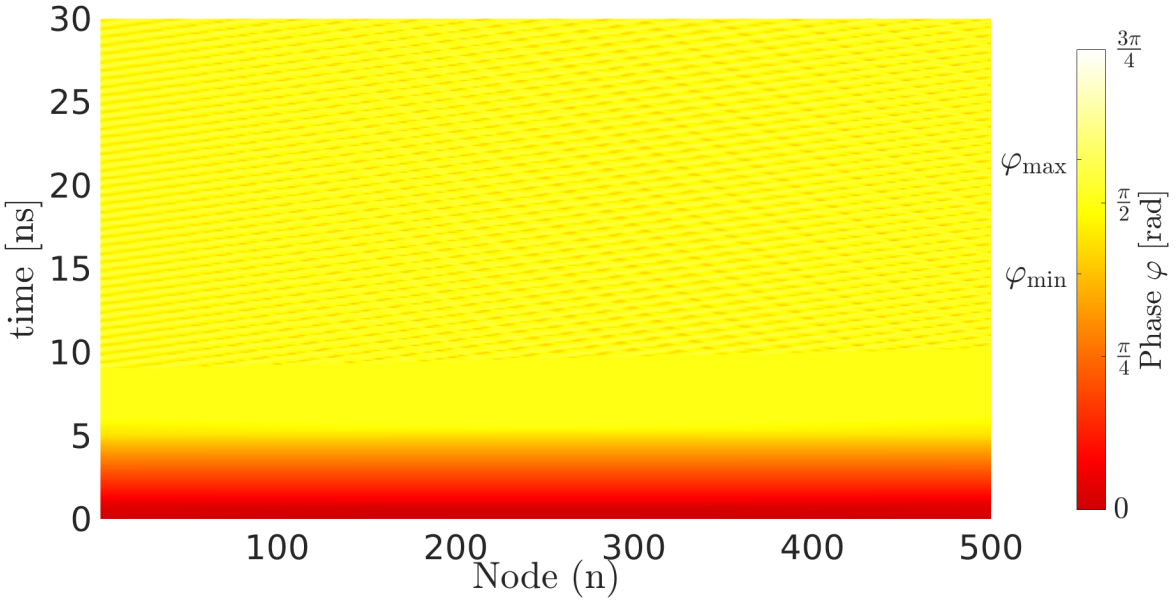

Figure 5.6: The reduction of input pump power reduces the phase oscillations in the junction to $\Delta\varphi \approx 0.6$ rad. Here the φ_{min} and φ_{max} are reduced compared to fig. 5.1.

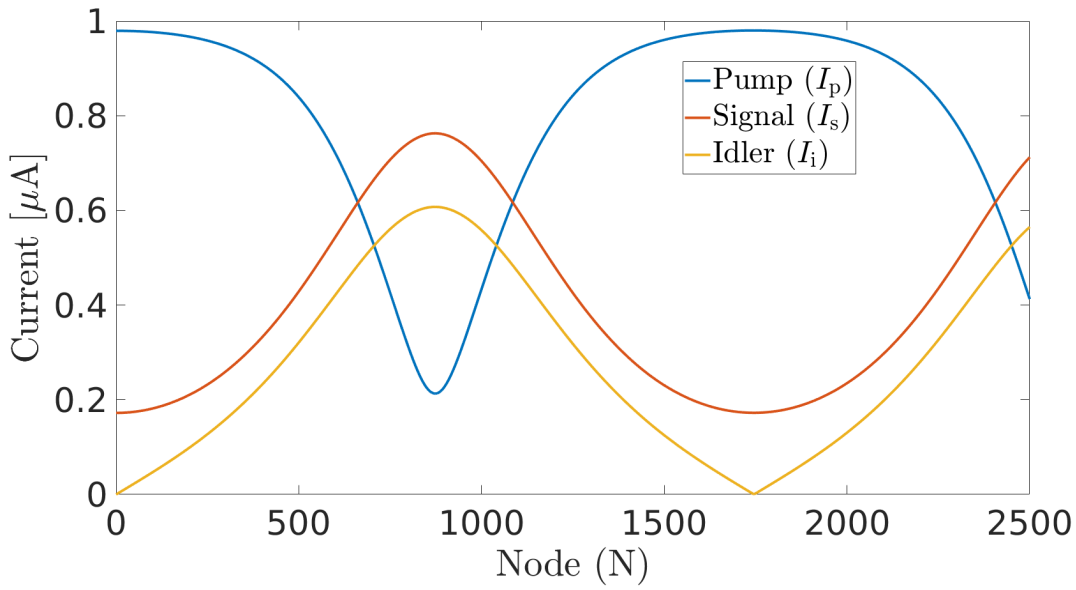

Figure 5.7: CME solution with the lowered pump, note signal gain $G_s(max) \approx 12$ dB.

increase in current, or $G_{\mathrm{s,\ max}} \approx 12$ dB. Furthermore, the signal requires nearly $n = 1000$ nodes to achieve this modest gain.

5.2.2 Signal Input power

In order to respect a small signal compared to the pump input, the signal input must also be reduced $I_s(0) \rightarrow 0.05\ \mu$A. This again results in the signal reaching a maximum further along the amplifier, as shown in fig. 5.8. We compare the results of this with the WRspice output in the same way as previously shown in fig. 4.17.

The pump behaviour in fig. 5.8 is less erratic than in fig. 4.17, however, the signal gain is still somewhat compromised. The maximum gain from CME-1 in fig. 5.8a) occurs at node $n \approx 1250$, thus the WRspice comparison must be made at the same node. In doing so, we find $G_{\mathrm{CME}}(1250) \approx 24$ dB while $G_{\mathrm{WRspice}}(1250) \approx 10$ dB. To investigate the differences, we again look at the entire spectral output from the WRspice simulation.

From fig. 5.9, it is now much clearer that the energy transfer between the pump at 12 GHz and the second harmonic of the pump at 24 GHz dominates as the main mixing mechanism. The amplitude of the pump and the second harmonic generation oscillate against each other and are over twice as large as the next highest tone. The next highest tone is then a tone at 36 GHz, the third harmonic of the pump.

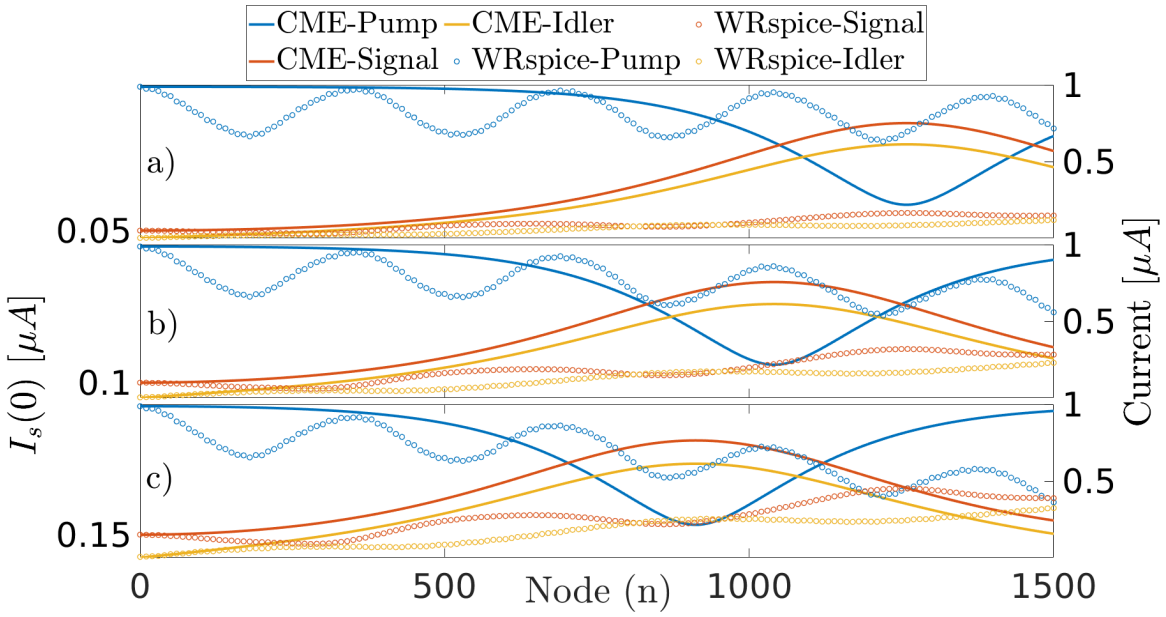

Figure 5.8: Comparison of CME three tone model (solid line) with WRspice (circles) pump (blue), signal (red) and idler (yellow) for input signal current amplitudes a) $I_s(0) = 0.05$ μA, b) $I_s(0) = 0.1$ μA, c) $I_s(0) = 0.15$ μA. Plot a) describes the low power regime which will be considered throughout the rest of this section.

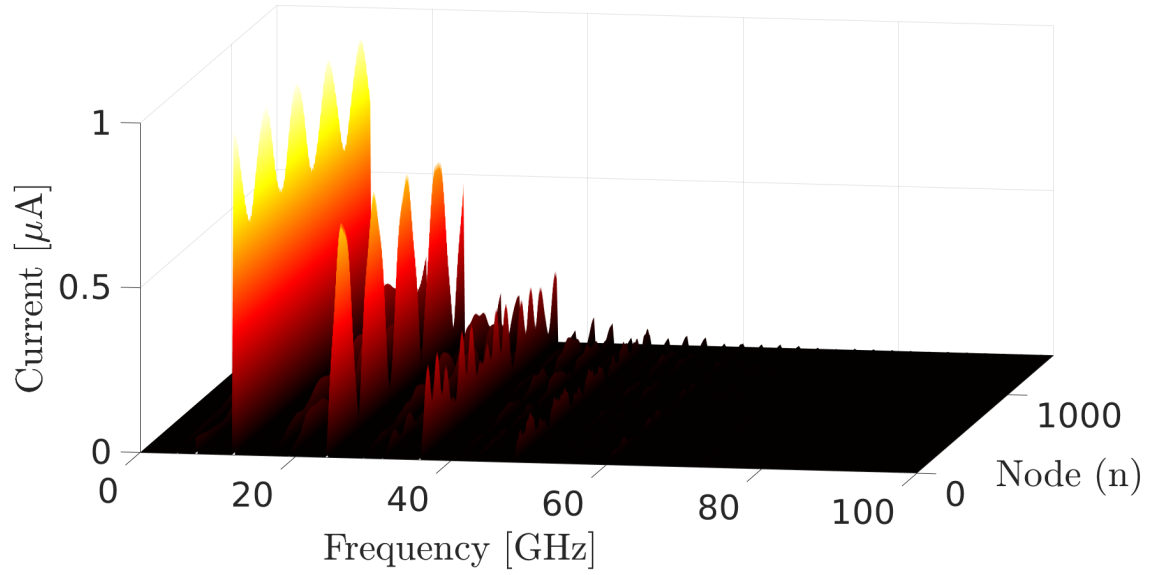

Figure 5.9: Full spectrum up to 100 GHz for the WRspice simulation in the low power regime. Note oscillations between the pump at $f_p = 12$ GHz and its second harmonic at $f_{2p} = 24$ GHz. The surface plots allows for the amplitude of pump and pump harmonics to be easily compared.

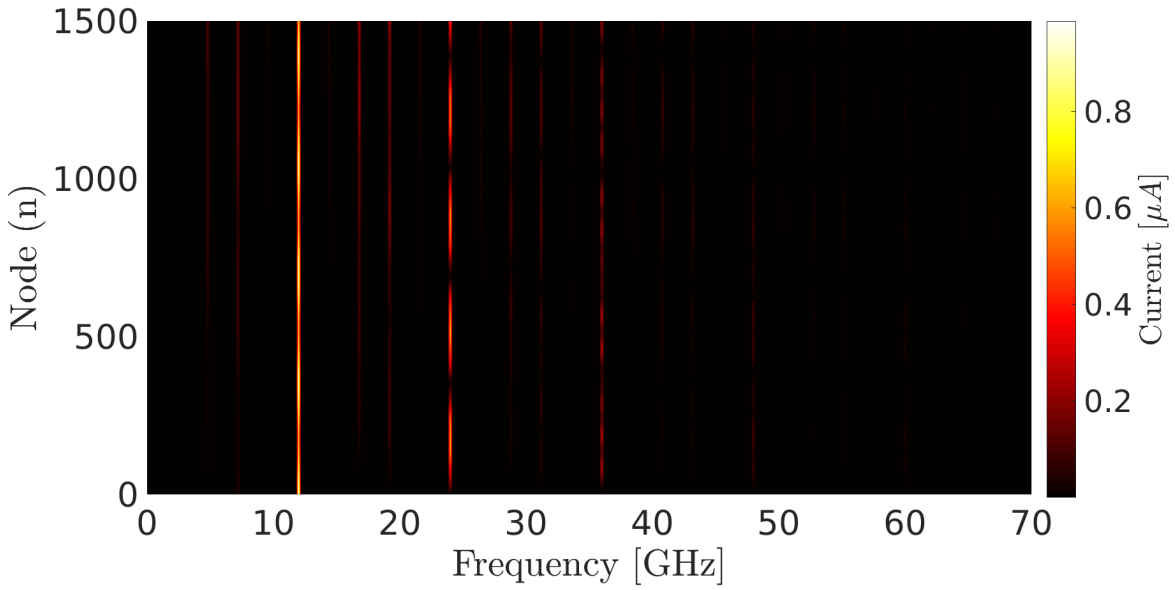

Figure 5.10: Heatmap of fig. 5.9 figure showing the tones up to 70 GHz in the low power regime. The heatmap allows for the frequencies of the tones generated in the device to be easily seen.

This is then accompanied by tones at 19.2 GHz and 16.8 GHz. These tones are generated from the sum frequency generation mentioned in eq. (1.6). From a top down view, we get a clearer picture of the frequencies of the tones being produced, (at the cost of amplitude clarity) shown in fig. 5.10.

There are three dominant tones in fig. 5.10 at 12, 24 and 36 GHz. These are the harmonics of the pump. The pump and second harmonic oscillate against each other with a beat period of ≈ 350 nodes. The third harmonic at $f_{3\mathrm{p}} = 36$ GHz shows a double peak feature. An interpretation of this is that the mixing mechanism is not third harmonic generation of the pump, (a 4WM process), but it is instead a 3WM SFG process, between pump and second harmonic. This is then dependent upon the amplitude of each tone at some node on the device.

Since we are now in a lower power regime it becomes easier to assign a crude estimate of the form of the main mixing mechanism producing the third harmonic. In fact if we make a very simple estimation that the generation of this tone is solely related to the averaged amplitude of the pump and SHG, i.e,

$$\bar{I}_{3\mathrm{p}}(n) \sim \frac{(I_{\mathrm{p}}(n) + I_{2\mathrm{p}}(n)) - (I_{\mathrm{p}}(0) + I_{2\mathrm{p}}(0))}{2} \tag{5.1}$$

then we get a broad description of the third tone generation. We show the WRspice result for the three large tones; pump, SHG, and Third Harmonic Generation (THG) in fig. 5.11.

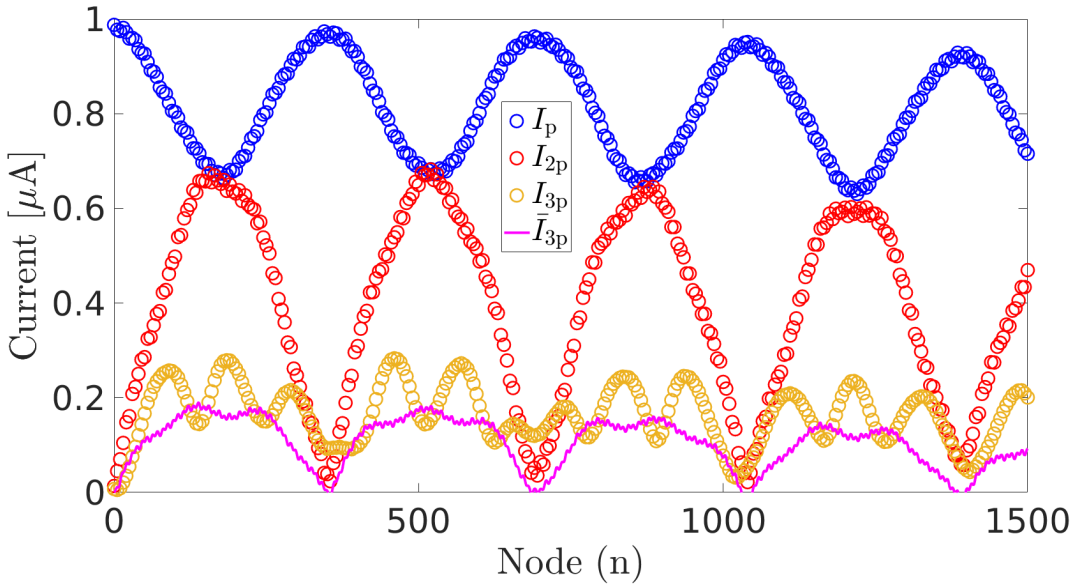

Figure 5.11: Qualitative description of the third harmonic generation envelop being produced by the average of the pump and second harmonic as described in eq. (5.1). The beat pattern between pump harmonics is more obvious in the low power regime.

Another qualitative feature is the generation of the SFG terms; pump+signal and pump+idler at frequencies $f_{\mathrm{p+s}}$ and $f_{\mathrm{p+i}}$ which is seen in fig. 5.10. In fact these terms grow in amplitude faster than the signal and idler. These tones are often referred to as further idlers. That is they are undesirable by-products of the wave mixing. To fully account for all mixing mechanisms, including these, we revisit the coupled mode equations and consider how one might extend them.

Summary

In the previous sections of this chapter we have shown that by lowering both the pump and signal input power then we can reduce the phase oscillations over the junction. The small angle approximation in the CME theory requires that the phase shift around the DC bias point is small and for the lower power regime we show that this assumption is now met. In reducing the power we have also seen more clearly the preferential mixing mechanism of pump second harmonic generation. This mixing mechanism draws energy from the pump and as a result reduces the signal amplification. We then further showed that the cascade of harmonic generation may still be via three wave mixing, i.e still apparent in the low power regime for small AC oscillations. This discovery forms the motivation for the key results in this thesis and that is being able to quantitatively describe the generation of these higher order modes.

5.3 Extension to Coupled Mode Theory

We first perform a brute force extension of the coupled mode equations as shown in [11] (specifically Appendices E-G). The thought process is that if an idler can exist with zero amplitude at the input, then we ask; what other tones might we expect to be generated and then assign those a zero amplitude at the input? We begin with an initial state vector ϕ_0 comprising of just the pump and signal, which are the only non-zero elements initially,

$$\phi_0 = \frac{1}{2}\begin{pmatrix} A_s e^{i(k_s x-\omega_s t)} + A_s^* e^{-i(k_s x-\omega_s t)} \\ A_p e^{i(k_p x-\omega_p t)} + A_p^* e^{-i(k_p x-\omega_p t)} \end{pmatrix}. \tag{5.2}$$

Following the method in appendix A.2.6 we find the frequencies generated in the first order interactions of the nonlinear part of eq. (2.21),

$$\begin{aligned}\left(\frac{\partial\phi_0}{\partial x}\right)^2\Bigg|_{\frac{\partial A}{\partial x}\to 0} = \frac{1}{4}\Bigg(& -\overbrace{k_{\mathrm{s}}^2 A_{\mathrm{s}}^2 e^{2i(k_{\mathrm{s}}x-\omega_{\mathrm{s}}t)}}^{\mathrm{HG}\to f_{2\mathrm{s}}} + \overbrace{2k_{\mathrm{s}}^2|A_{\mathrm{s}}|^2}^{\mathrm{OR}\to f_0=0} \\ & -\overbrace{2k_{\mathrm{s}}k_{\mathrm{p}}A_{\mathrm{s}}A_{\mathrm{p}}e^{i((k_{\mathrm{s}}+k_{\mathrm{p}})x-(\omega_{\mathrm{s}}+\omega_{\mathrm{p}})t)}}^{\mathrm{SFG}\to f_{\mathrm{p+s}}} + \overbrace{2k_{\mathrm{s}}k_{\mathrm{p}}A_{\mathrm{s}}A_{\mathrm{p}}^* e^{i((k_{\mathrm{s}}-k_{\mathrm{p}})x-(\omega_{\mathrm{s}}-\omega_{\mathrm{p}})t)}}^{\mathrm{C.C.\ DFG}\to -\mathrm{f_i}} \\ & -\overbrace{k_{\mathrm{s}}^2 A_{\mathrm{s}}^{*2} e^{-2i(k_{\mathrm{s}}x-\omega_{\mathrm{s}}t)}}^{\mathrm{C.C.\ HG}\to -f_{2\mathrm{s}}} + \overbrace{2k_{\mathrm{s}}k_{\mathrm{p}}A_{\mathrm{s}}^* A_{\mathrm{p}} e^{i((k_{\mathrm{p}}-k_{\mathrm{s}})x-(\omega_{\mathrm{p}}-\omega_{\mathrm{s}})t)}}^{\mathrm{DFG}\to f_{\mathrm{p-s}}=f_{\mathrm{i}}} \\ & -\overbrace{2k_{\mathrm{s}}k_{\mathrm{p}}A_{\mathrm{s}}^* A_{\mathrm{p}}^* e^{-i((k_{\mathrm{s}}+k_{\mathrm{p}})x-(\omega_{\mathrm{s}}+\omega_{\mathrm{p}})t)}}^{\mathrm{C.C.\ SFG}\to -f_{\mathrm{p+s}}} - \overbrace{k_{\mathrm{p}}^2 A_{\mathrm{p}}^2 e^{2i(k_{\mathrm{p}}x-\omega_{\mathrm{p}}t)}}^{\mathrm{HG}\to f_{2\mathrm{p}}} \\ & +\overbrace{2k_{\mathrm{p}}^2|A_{\mathrm{p}}|^2}^{\mathrm{OR}\to f_0} - \overbrace{k_{\mathrm{p}}^2 A_{\mathrm{p}}^{*2} e^{-2i(k_{\mathrm{p}}x-\omega_{\mathrm{p}}t)}}^{\mathrm{C.C.\ HG}\to -f_{2\mathrm{p}}}\Bigg).\end{aligned} \tag{5.3}$$

The angular frequency related to the idler is generated at $\omega_{\mathrm{i}} = (\omega_{\mathrm{p}} - \omega_{\mathrm{s}})$, the standard three wave mixing (3WM) frequency relation, which is seen on the right side of the third line in eq. (5.3). Note there is also harmonic generation (HG) of the two input tones on line 1 and 4, as well as the quasi-DC (Optical Rectification (OR)) terms in lines 1 and 5. There is also a Sum Frequency Generation (SFG) term in the first order interactions producing a first order up-conversion term at a frequency $f_{\mathrm{p+s}}$ in line

2 of eq. (5.3). Note that every complex term (i.e all but the the OR terms) has a Complex Conjugate (C.C.). These conjugate terms couple with conjugate terms of the original state vector to form a conjugate set of coupled mode equations which we do not solve. Thus the C.C. terms are discarded along with the conjugate left side of eq. (2.21) when we solve the CMEs. We also discard the OR terms in this analysis.

The approach used in this section is to then consider the frequencies of the HG, SFG, and DFG terms from eq. (5.3) to create a new state vector ϕ_1 and recompute more possible mixing terms. Under these conditions the initial state vector including first order interaction terms ϕ_1 then becomes[1],

$$\phi_1 = \frac{1}{2}\begin{pmatrix} A_{\mathrm{i}}e^{i(k_{\mathrm{i}}x-\omega_{\mathrm{i}}t)} + A_{\mathrm{i}}^{*}e^{-i(k_{\mathrm{i}}x-\omega_{\mathrm{i}}t)} \\ A_{\mathrm{s}}e^{i(k_{\mathrm{s}}x-\omega_{\mathrm{s}}t)} + A_{\mathrm{s}}^{*}e^{-i(k_{\mathrm{s}}x-\omega_{\mathrm{s}}t)} \\ A_{\mathrm{p}}e^{i(k_{\mathrm{p}}x-\omega_{\mathrm{p}}t)} + A_{\mathrm{p}}^{*}e^{-i(k_{\mathrm{p}}x-\omega_{\mathrm{p}}t)} \\ A_{\mathrm{p+s}}e^{i(k_{\mathrm{p+s}}x-\omega_{\mathrm{p+s}}t)} + A_{\mathrm{p+s}}^{*}e^{-i(k_{\mathrm{p+s}}x-\omega_{\mathrm{p+s}}t)} \\ A_{\mathrm{2p}}e^{i(k_{\mathrm{2p}}x-\omega_{\mathrm{2p}}t)} + A_{\mathrm{2p}}^{*}e^{-i(k_{\mathrm{2p}}x-\omega_{\mathrm{2p}}t)} \end{pmatrix}. \tag{5.4}$$

Then calculating the nonlinear part of eq. (2.21) and discarding the quasi-DC and conjugate components produces a larger vector of mixing mechanisms. We have labelled a number of these for further discussion,

$$\begin{aligned}\left(\frac{\partial\phi_1}{\partial x}\right)^2\Bigg|_{\frac{\partial A}{\partial x}\to 0} = \frac{1}{4}\Bigg(& - k_{\mathrm{i}}^2A_{\mathrm{i}}^2e^{2i(k_{\mathrm{i}}x-\omega_{\mathrm{i}}t)} - \overbrace{2k_{\mathrm{i}}k_{\mathrm{s}}A_{\mathrm{i}}A_{\mathrm{s}}e^{i((k_{\mathrm{i}}+k_{\mathrm{s}})x-(\omega_{\mathrm{i}}+\omega_{\mathrm{s}})t)}}^{\text{i) SFG}\to f_{\mathrm{p}}} \\ & - 2k_{\mathrm{i}}k_{\mathrm{p}}A_{\mathrm{i}}A_{\mathrm{i}}e^{i((k_{\mathrm{i}}+k_{\mathrm{p}})x-(\omega_{\mathrm{i}}+\omega_{\mathrm{p}})t)} - 2k_{\mathrm{i}}k_{\mathrm{p+s}}A_{\mathrm{i}}A_{\mathrm{p+s}}e^{i((k_{\mathrm{i}}+k_{\mathrm{p+s}})x-(\omega_{\mathrm{i}}+\omega_{\mathrm{p+s}})t)} \\ & - 2k_{\mathrm{i}}k_{\mathrm{2p}}A_{\mathrm{i}}A_{\mathrm{2p}}e^{i((k_{\mathrm{i}}+k_{\mathrm{2p}})x-(\omega_{\mathrm{i}}+\omega_{\mathrm{2p}})t)} + \overbrace{2k_{\mathrm{i}}k_{\mathrm{s}}A_{\mathrm{i}}^{*}A_{\mathrm{s}}e^{i((k_{\mathrm{s}}-k_{\mathrm{i}})x-(\omega_{\mathrm{s}}-\omega_{\mathrm{i}})t)}}^{\text{ii) DFG}\to f_\delta=f_{\mathrm{s}}-f_{\mathrm{i}}} \\ & + 2k_{\mathrm{i}}k_{\mathrm{p}}A_{\mathrm{i}}^{*}A_{\mathrm{p}}e^{i((k_{\mathrm{p}}-k_{\mathrm{i}})x-(\omega_{\mathrm{p}}-\omega_{\mathrm{i}})t)} + \overbrace{2k_{\mathrm{i}}k_{\mathrm{p+s}}A_{\mathrm{i}}^{*}A_{\mathrm{p+s}}e^{i((k_{\mathrm{p+s}}-k_{\mathrm{i}})x-(\omega_{\mathrm{p+s}}-\omega_{\mathrm{i}})t)}}^{\text{iii)(a) DFG}\to f_{\mathrm{p}+\delta}}\end{aligned}$$

[1]Notice here that the tones generated extend from the idler up to the second harmonic of the pump, however there is only the pump + signal up conversion tone. This is because the pump + idler tone is a second order interaction as the idler must first be generated by pump − signal DFG.

$$
\begin{aligned}
&+ 2k_{\mathrm{i}}k_{2\mathrm{p}}A_{\mathrm{i}}^{*}A_{2\mathrm{p}}e^{i((k_{2\mathrm{p}}-k_{\mathrm{i}})x-(\omega_{2\mathrm{p}}-\omega_{\mathrm{i}})t)} \overbrace{- k_{\mathrm{s}}^{2}A_{\mathrm{s}}^{2}e^{2i(k_{\mathrm{s}}x-\omega_{\mathrm{s}}t)}}^{\text{iii)(b) HG}\rightarrow f_{\mathrm{p}+\delta}} \\
&- 2k_{\mathrm{s}}k_{\mathrm{p}}A_{\mathrm{s}}A_{\mathrm{p}}e^{i((k_{\mathrm{s}}+k_{\mathrm{p}})x-(\omega_{\mathrm{s}}+\omega_{\mathrm{p}})t)} - 2k_{\mathrm{s}}k_{\mathrm{p}+\mathrm{s}}A_{\mathrm{s}}A_{\mathrm{p}+\mathrm{s}}e^{i((k_{\mathrm{s}}+k_{\mathrm{p}+\mathrm{s}})x-(\omega_{\mathrm{s}}+\omega_{\mathrm{p}+\mathrm{s}})t)} \\
&- 2k_{\mathrm{s}}k_{2\mathrm{p}}A_{\mathrm{s}}A_{2\mathrm{p}}e^{i((k_{\mathrm{s}}+k_{2\mathrm{p}})x-(\omega_{\mathrm{s}}+\omega_{2\mathrm{p}})t)} + 2k_{\mathrm{i}}k_{\mathrm{p}}A_{\mathrm{i}}^{*}A_{\mathrm{p}}e^{i((k_{\mathrm{p}}-k_{\mathrm{i}})x-(\omega_{\mathrm{p}}-\omega_{\mathrm{i}})t)} \\
&+ 2k_{\mathrm{s}}k_{\mathrm{p}}A_{\mathrm{s}}^{*}A_{\mathrm{p}}e^{i((k_{\mathrm{p}}-k_{\mathrm{s}})x-(\omega_{\mathrm{p}}-\omega_{\mathrm{s}})t)} + 2k_{\mathrm{s}}k_{\mathrm{p}+\mathrm{s}}A_{\mathrm{s}}^{*}A_{\mathrm{p}+\mathrm{s}}e^{i((k_{\mathrm{p}+\mathrm{s}}-k_{\mathrm{s}})x-(\omega_{\mathrm{p}+\mathrm{s}}-\omega_{\mathrm{s}})t)} \\
&+ 2k_{\mathrm{s}}k_{2\mathrm{p}}A_{\mathrm{s}}^{*}A_{2\mathrm{p}}e^{i((k_{2\mathrm{p}}-k_{\mathrm{s}})x-(\omega_{2\mathrm{p}}-\omega_{\mathrm{s}})t)} - k_{\mathrm{p}}^{2}A_{\mathrm{p}}^{2}e^{2i(k_{\mathrm{p}}x-\omega_{\mathrm{p}}t)} \\
&- 2k_{\mathrm{p}}k_{\mathrm{p}+\mathrm{s}}A_{\mathrm{p}}A_{\mathrm{p}+\mathrm{s}}e^{i((k_{\mathrm{p}}+k_{\mathrm{p}+\mathrm{s}})x-(\omega_{\mathrm{p}}+\omega_{\mathrm{p}+\mathrm{s}})t)} \overbrace{- 2k_{\mathrm{p}}k_{2\mathrm{p}}A_{\mathrm{p}}A_{2\mathrm{p}}e^{i((k_{\mathrm{p}}+k_{2\mathrm{p}})x-(\omega_{\mathrm{p}}+\omega_{2\mathrm{p}})t)}}^{\text{iv) SFG}\rightarrow f_{3\mathrm{p}}} \\
&+ 2k_{\mathrm{p}}k_{\mathrm{p}+\mathrm{s}}A_{\mathrm{p}}^{*}A_{\mathrm{p}+\mathrm{s}}e^{i((k_{\mathrm{p}+\mathrm{s}}-k_{\mathrm{p}})x-(\omega_{\mathrm{p}+\mathrm{s}}-\omega_{\mathrm{p}})t)} + 2k_{\mathrm{p}}k_{2\mathrm{p}}A_{\mathrm{p}}^{*}A_{2\mathrm{p}}e^{i((k_{2\mathrm{p}}-k_{\mathrm{p}})x-(\omega_{2\mathrm{p}}-\omega_{\mathrm{p}})t)} \\
&- k_{\mathrm{p}+\mathrm{s}}^{2}A_{\mathrm{p}+\mathrm{s}}^{2}e^{2i(k_{\mathrm{p}+\mathrm{s}}x-\omega_{\mathrm{p}+\mathrm{s}}t)} - 2k_{\mathrm{p}+\mathrm{s}}k_{2\mathrm{p}}A_{\mathrm{p}+\mathrm{s}}A_{2\mathrm{p}}e^{i((k_{\mathrm{p}+\mathrm{s}}+k_{2\mathrm{p}})x-(\omega_{\mathrm{p}+\mathrm{s}}+\omega_{2\mathrm{p}})t)} \\
&+ 2k_{\mathrm{p}+\mathrm{s}}k_{2\mathrm{p}}A_{\mathrm{p}+\mathrm{s}}^{*}A_{2\mathrm{p}}e^{i((k_{2\mathrm{p}}-k_{\mathrm{p}+\mathrm{s}})x-(\omega_{2\mathrm{p}}-\omega_{\mathrm{p}+\mathrm{s}})t)} \overbrace{- k_{2\mathrm{p}}^{2}A_{2\mathrm{p}}^{2}e^{2i(k_{2\mathrm{p}}x-\omega_{2\mathrm{p}}t)}}^{\text{v)HG}\rightarrow f_{4\mathrm{p}}} \Bigg). \quad (5.5)
\end{aligned}
$$

If we examine the labelled terms we get a deeper understanding of the mixing mechanisms present within the device:

(i) This term shows that the SFG mixing of the signal and idler then generates a tone at the pump frequency. This allows for a more general theory beyond the strong pump approximation. This has been shown in [14], as well as previously in our three tone model and is responsible for energy flow back and forth the pump and signal/idler tones.

(ii) This term shows that the DFG mixing of the signal and idler then generates a tone at the difference of the two frequencies f_{δ}. Conveniently, up until now, we have considered a signal with a frequency $f_{\mathrm{s}} = (3/5)f_{\mathrm{p}}$. This means that through the 3WM condition $f_{\mathrm{i}} = (2/5)f_{\mathrm{p}}$ and thus $f_{\delta} = (1/5)f_{\mathrm{p}}$ and that any combination of any tone considered through any further mixing will always be a multiple of f_{δ}. As such, there will not be a tone with a frequency lower than f_{δ}. To be complete; if the signal had been some irrational fraction of the pump, then an infinite number of smaller frequency tones may be generated through cascaded difference frequency generation.

(iii) These two terms show how a tone at $f_{\mathrm{p}+\delta} = (6/5)f_{\mathrm{p}}$ is generated through either (a) DFG between the (pump + signal) and (idler), $f_{\mathrm{p}+\mathrm{s}} - f_{\mathrm{i}} = f_{\delta}$ tone or, (b) SHG of the signal $f_{\mathrm{s}} + f_{\mathrm{s}}$.

Note that both of these mechanisms involve no pump or pump harmonic tone and thus are not pump mediated. By considering only pump mediated mixing (at least one tone being at the pump or pump harmonic) we avoid an infinite number of frequencies cascading downward in frequency, even for irrational ratios of $f_{\mathrm{s}}/f_{\mathrm{p}}$.

(iv) This term shows that the SFG of the pump and its own second harmonic generates a tone at the third harmonic of the pump frequency. This is an SFG term in the 3WM case (as opposed to THG in the 4WM regime). In the 3WM case, the coefficient of HG has a factor $1/2$ which is understood from the coefficients described by Pascal's triangle, which is true for every order of wave mixing.

(v) This term shows that the HG of the second harmonic of the pump generates a tone that is now at $f_{4\mathrm{p}}$. This highlights the fact that there must be some upper bound placed on the frequencies we consider to avoid an infinite number of frequencies cascading upward in frequency.

Here, we have highlighted the ideas behind a brute force extension to the CMEs used in section 2.2.2. Through this method we have found that it is possible to create an infinite number of tones at frequencies lower and higher than those previously considered.

Infinitely many, lower frequency tone generation, comes from the potential for cascaded DFG between signal and idler tones, for signal frequencies which are some irrational ratio of the pump tone. This is counteracted by considering only pump mediated tones, and as such, discarding any mixing between just signal and idler such that f_δ and its associated mixing products never proliferate through the maths.

Infinitely many higher frequency tones, may be generated from the cascaded SFG and HG of tones. This is counteracted by applying an upper limit on the maximum frequency considered, which may be taken from simulation or theoretical models specific for each device.

Example of Solving Extended Coupled Mode Equations

We show here explicitly and example of the extended CMEs up to the third harmonic of the pump with only pump mediated mixing. Starting from eq. (5.5) we relate all of the considered mixing mechanisms to an initial state vector ϕ_2,

$$\phi_2 = \frac{1}{2}\begin{pmatrix} A_{\mathrm{i}}e^{i(k_{\mathrm{i}}x-\omega_{\mathrm{i}}t)} \\ A_{\mathrm{s}}e^{i(k_{\mathrm{s}}x-\omega_{\mathrm{s}}t)} \\ A_{\mathrm{p}}e^{i(k_{\mathrm{p}}x-\omega_{\mathrm{p}}t)} \\ A_{\mathrm{p+i}}e^{i(k_{\mathrm{p+i}}x-\omega_{\mathrm{p+i}}t)} \\ A_{\mathrm{p+s}}e^{i(k_{\mathrm{p+s}}x-\omega_{\mathrm{p+s}}t)} \\ A_{\mathrm{2p}}e^{i(k_{\mathrm{2p}}x-\omega_{\mathrm{2p}}t)} \\ A_{\mathrm{2p+i}}e^{i(k_{\mathrm{2p+i}}x-\omega_{\mathrm{2p+i}}t)} \\ A_{\mathrm{2p+s}}e^{i(k_{\mathrm{2p+s}}x-\omega_{\mathrm{2p+s}}t)} \\ A_{\mathrm{3p}}e^{i(k_{\mathrm{3p}}x-\omega_{\mathrm{3p}}t)} \end{pmatrix} + c.c, \tag{5.6}$$

where c.c. is the complex conjugate part of the initial state vector. This initial state vector contains every tone we will be considering in our calculation, as such we repeat the mixing process again. By again finding $[\partial\phi_2/\partial x]^2|_{\partial A/\partial x\to 0}$ and then constructing a new state vector we iteratively find all of the considered tones. At each step we remove all of the non-pump-mediated mixing terms and any terms with frequencies higher than $f_{3\mathrm{p}}$, as explained in the previous section. We then collect the terms which oscillate at frequencies corresponding to the initial state vector ϕ_2 and write a set of coupled mode equations which we refer to as the CME-3 set,

$$\begin{aligned}\frac{dA_{\mathrm{i}}}{dx} = \frac{\beta}{2}\Big(&k_{\mathrm{s}}k_{\mathrm{p}}A_{\mathrm{s}}^*A_{\mathrm{p}}e^{i(k_{\mathrm{p}}-k_{\mathrm{s}})x} + k_{\mathrm{p}}k_{\mathrm{p+i}}A_{\mathrm{p}}^*A_{\mathrm{p+i}}e^{i(k_{\mathrm{p+i}}-k_{\mathrm{p}})x} + k_{\mathrm{2p}}k_{\mathrm{p+s}}A_{\mathrm{p+s}}^*A_{\mathrm{2p}}e^{i(k_{\mathrm{2p}}-k_{\mathrm{p+s}})x} \\ &+ k_{\mathrm{3p}}k_{\mathrm{2p+s}}A_{\mathrm{3p}}A_{\mathrm{2p+s}}^*e^{i(k_{\mathrm{3p}}-k_{\mathrm{2p+s}})x} + k_{\mathrm{2p+i}}k_{\mathrm{2p}}A_{\mathrm{2p+i}}A_{\mathrm{2p}}^*e^{i(k_{\mathrm{2p+i}}-k_{\mathrm{2p}})x}\Big)e^{-ik_{\mathrm{i}}x},\end{aligned} \tag{5.7}$$

$$\begin{aligned}\frac{dA_{\mathrm{s}}}{dx} = \frac{\beta}{2}\Big(&k_{\mathrm{i}}k_{\mathrm{p}}A_{\mathrm{i}}^*A_{\mathrm{p}}e^{i(k_{\mathrm{p}}-k_{\mathrm{i}})x} + k_{\mathrm{p}}k_{\mathrm{p+s}}A_{\mathrm{p}}^*A_{\mathrm{p+s}}e^{i(k_{\mathrm{p+s}}-k_{\mathrm{p}})x} + k_{\mathrm{2p}}k_{\mathrm{p+i}}A_{\mathrm{p+i}}^*A_{\mathrm{2p}}e^{i(k_{\mathrm{2p}}-k_{\mathrm{p+i}})x} \\ &+ k_{\mathrm{3p}}k_{\mathrm{2p+i}}A_{\mathrm{3p}}A_{\mathrm{2p+i}}^*e^{i(k_{\mathrm{3p}}-k_{\mathrm{2p+i}})x} + k_{\mathrm{2p+s}}k_{\mathrm{2p}}A_{\mathrm{2p+s}}A_{\mathrm{2p}}^*e^{i(k_{\mathrm{2p+s}}-k_{\mathrm{2p}})x}\Big)e^{-ik_{\mathrm{s}}x},\end{aligned} \tag{5.8}$$

$$\frac{dA_{\mathrm{p}}}{dx} = \frac{\beta}{2}\Big(- k_{\mathrm{s}}k_{\mathrm{i}}A_{\mathrm{s}}A_{\mathrm{i}}e^{i(k_{\mathrm{s}}+k_{\mathrm{i}})x} + k_{2\mathrm{p}}A_{2\mathrm{p}}k_{\mathrm{p}}A_{\mathrm{p}}^{*}e^{i(k_{2\mathrm{p}}-k_{\mathrm{p}})} + k_{\mathrm{p+s}}k_{\mathrm{s}}A_{\mathrm{p+s}}A_{\mathrm{s}}^{*}e^{i(k_{\mathrm{p+s}}-k_{\mathrm{s}})x} + k_{\mathrm{p+i}}k_{\mathrm{i}}A_{\mathrm{p+i}}A_{\mathrm{i}}^{*}e^{i(k_{\mathrm{p+i}}-k_{\mathrm{i}})x} + k_{3\mathrm{p}}k_{2\mathrm{p}}A_{3\mathrm{p}}A_{2\mathrm{p}}^{*}e^{i(k_{3\mathrm{p}}-k_{2\mathrm{p}})x} + k_{2\mathrm{p+s}}k_{\mathrm{p+s}}A_{2\mathrm{p+s}}A_{\mathrm{p+s}}^{*}e^{i(k_{2\mathrm{p+s}}-k_{\mathrm{p+s}})x} + k_{2\mathrm{p+i}}k_{\mathrm{p+i}}A_{2\mathrm{p+i}}A_{\mathrm{p+i}}^{*}e^{i(k_{2\mathrm{p+i}}-k_{\mathrm{p+i}})x}\Big)e^{-ik_{\mathrm{p}}x}, \tag{5.9}$$

$$\frac{dA_{\mathrm{p+i}}}{dx} = \frac{\beta}{2}\Big(- k_{\mathrm{p}}k_{\mathrm{i}}A_{\mathrm{p}}A_{\mathrm{i}}e^{i(k_{\mathrm{p}}+k_{\mathrm{i}})x} + k_{\mathrm{s}}k_{2\mathrm{p}}A_{\mathrm{s}}^{*}A_{2\mathrm{p}}e^{i(k_{2\mathrm{p}}-k_{\mathrm{s}})x} + k_{3\mathrm{p}}k_{\mathrm{p+s}}A_{3\mathrm{p}}A_{\mathrm{p+s}}^{*}e^{i(k_{3\mathrm{p}}-k_{\mathrm{p+s}})x} + k_{2\mathrm{p+i}}k_{\mathrm{p}}A_{2\mathrm{p+i}}A_{\mathrm{p}}^{*}e^{i(k_{2\mathrm{p+i}}-k_{\mathrm{p}})x}\Big)e^{-ik_{\mathrm{p+i}}x}, \tag{5.10}$$

$$\frac{dA_{\mathrm{p+s}}}{dx} = \frac{\beta}{2}\Big(- k_{\mathrm{p}}k_{\mathrm{s}}A_{\mathrm{p}}A_{\mathrm{s}}e^{i(k_{\mathrm{p}}+k_{\mathrm{s}})x} + k_{\mathrm{i}}k_{2\mathrm{p}}A_{\mathrm{i}}^{*}A_{2\mathrm{p}}e^{i(k_{2\mathrm{p}}-k_{\mathrm{i}})x} + k_{3\mathrm{p}}k_{\mathrm{p+i}}A_{3\mathrm{p}}A_{\mathrm{p+i}}^{*}e^{i(k_{3\mathrm{p}}-k_{\mathrm{p+i}})x} + k_{2\mathrm{p+s}}k_{\mathrm{p}}A_{2\mathrm{p+s}}A_{\mathrm{p}}^{*}e^{i(k_{2\mathrm{p+s}}-k_{\mathrm{p}})x}\Big)e^{-ik_{\mathrm{p+s}}x}, \tag{5.11}$$

$$\frac{dA_{2\mathrm{p}}}{dx} = \frac{\beta}{2}\Big(- \frac{1}{2}k_{\mathrm{p}}^{2}A_{\mathrm{p}}^{2}e^{i(2k_{\mathrm{p}})x} - k_{\mathrm{i}}k_{\mathrm{p+s}}A_{\mathrm{i}}A_{\mathrm{p+s}}e^{i(k_{\mathrm{i}}+k_{\mathrm{p+s}})x} - k_{\mathrm{p+i}}k_{\mathrm{s}}A_{\mathrm{p+i}}A_{\mathrm{s}}e^{i(k_{\mathrm{p+i}}+k_{\mathrm{s}})x} + k_{\mathrm{p}}k_{3\mathrm{p}}A_{\mathrm{p}}^{*}A_{3\mathrm{p}}e^{i(k_{3\mathrm{p}}-k_{\mathrm{p}})x} + k_{2\mathrm{p+s}}k_{\mathrm{s}}A_{2\mathrm{p+s}}A_{\mathrm{s}}^{*}e^{i(k_{2\mathrm{p+s}}-k_{\mathrm{s}})x} + k_{2\mathrm{p+i}}k_{\mathrm{i}}A_{2\mathrm{p+i}}A_{\mathrm{i}}^{*}e^{i(k_{2\mathrm{p+i}}-k_{\mathrm{i}})x}\Big)e^{-ik_{2\mathrm{p}}x}, \tag{5.12}$$

$$\frac{dA_{2\mathrm{p+i}}}{dx} = \frac{\beta}{2}\Big(- k_{\mathrm{p}}k_{\mathrm{p+i}}A_{\mathrm{p}}A_{\mathrm{p+i}}e^{i(k_{\mathrm{p}}+k_{\mathrm{p+i}})x} - k_{\mathrm{i}}k_{2\mathrm{p}}A_{\mathrm{i}}A_{2\mathrm{p}}e^{i(k_{\mathrm{i}}+k_{2\mathrm{p}})x} + k_{3\mathrm{p}}k_{\mathrm{s}}A_{3\mathrm{p}}A_{\mathrm{s}}^{*}e^{i(k_{3\mathrm{p}}-k_{\mathrm{s}})x}\Big)e^{-ik_{2\mathrm{p+i}}x}, \tag{5.13}$$

$$\frac{dA_{2\mathrm{p+s}}}{dx} = \frac{\beta}{2}\Big(- k_{\mathrm{p}}k_{\mathrm{p+s}}A_{\mathrm{p}}A_{\mathrm{p+s}}e^{i(k_{\mathrm{p}}+k_{\mathrm{p+s}})x} - k_{\mathrm{s}}k_{2\mathrm{p}}A_{\mathrm{s}}A_{2\mathrm{p}}e^{i(k_{\mathrm{s}}+k_{2\mathrm{p}})x} + k_{3\mathrm{p}}k_{\mathrm{i}}A_{3\mathrm{p}}A_{\mathrm{i}}^{*}e^{i(k_{3\mathrm{p}}-k_{\mathrm{i}})x}\Big)e^{-ik_{2\mathrm{p+s}}x}, \tag{5.14}$$

$$\frac{dA_{3\mathrm{p}}}{dx} = \frac{\beta}{2}\Big(- k_{\mathrm{p}}k_{2\mathrm{p}}A_{\mathrm{p}}A_{2\mathrm{p}}e^{i(k_{\mathrm{p}}+k_{2\mathrm{p}})x} - k_{\mathrm{p+s}}k_{\mathrm{p+i}}A_{\mathrm{p+s}}A_{\mathrm{p+i}}e^{i(k_{\mathrm{p+s}}+k_{\mathrm{p+i}})x} - k_{\mathrm{s}}k_{2\mathrm{p+i}}A_{\mathrm{s}}A_{2\mathrm{p+i}}e^{i(k_{\mathrm{s}}+k_{2\mathrm{p+i}})x} - k_{\mathrm{i}}k_{2\mathrm{p+s}}A_{\mathrm{i}}A_{2\mathrm{p+s}}e^{i(k_{\mathrm{i}}+k_{2\mathrm{p+s}})x}\Big)e^{-ik_{3\mathrm{p}}x}. \tag{5.15}$$

The dimensionless dispersion relation $k(\omega) = \theta$ (eq. (1.24)) is given for all frequencies and is real up to the cut off frequency of the line, see fig. 4.6. Note that if a frequency above the line cut off is considered and thus $k(\omega)$ has an imaginary component then the CMEs will diverge exponentially along the line, this may cause convergence issues in the ODE solver. The initial amplitudes of every tone other than pump and signal is set to 0, in conjunction with previous treatments of the idler tone. We then solve eqs. (5.7) to (5.15) using `ode45` in MATLAB and compare the results from our crude analysis (fig. 5.11) with the extended CME approach as shown in fig. 5.12.

In fig. 5.11, we showed a simple approximation to the third harmonic generation by way of a simple mixing mechanism between pump and the second harmonic of the pump. This only involved taking an

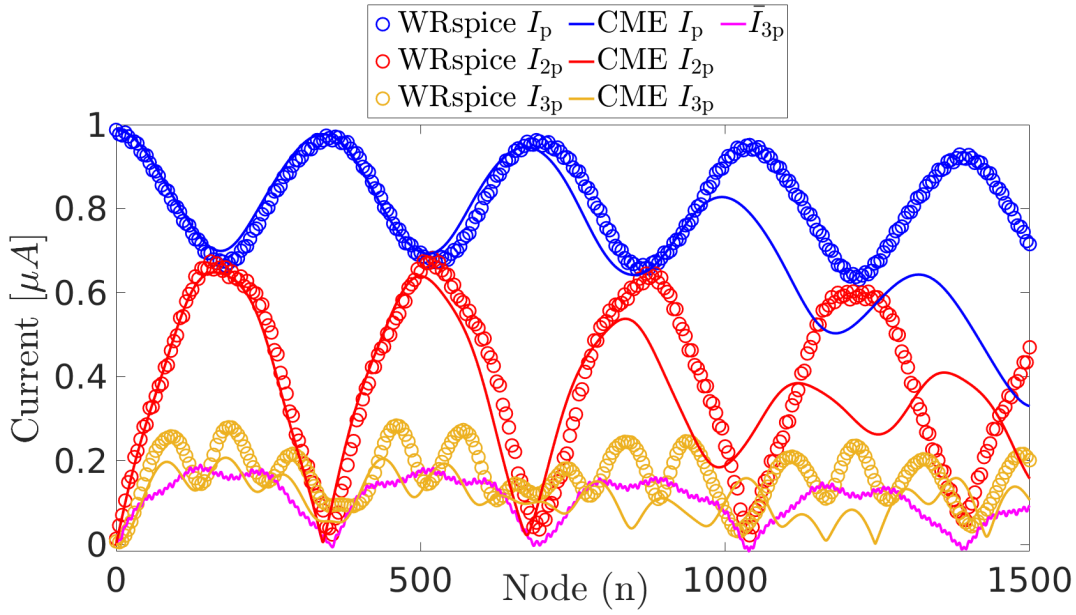

Figure 5.12: Comparison of the extended CME example up to third harmonic of the pump with WRspice result and previous crude extension shown in fig. 5.11. Note the pump and second harmonic fit is drastically improved. The third harmonic fit is better than the crude approximation however each fit deteriorates for increasing n.

average of the second harmonic pump amplitude and the pump amplitude at each position as given by eq. (5.1). The fit in fig. 5.12 is improved now that we dynamically solve the CMEs at each point with all possible mixing mechanisms that may generate the third harmonic of the pump, as given by eq. (5.15). At the start of the array, we capture the pump and second harmonic behaviour with a quantitatively accurate fit to the WRspice result over the first 500 nodes. The third harmonic (yellow) fit is not so quantitatively accurate since the amplitude of the first peak around node 100 for the CME (solid line) result never reaches the WRspice (circle) result. Toward the end of the array for nodes $n > 700$ the fit is lost for all of the nodes shown.

Since the amplitudes of every tone is interconnected in the CMEs, when any large tone deviates from the WRspice result it is expected that it will eventually lead to a deviation in all other tones. However, qualitatively, we see that we are capturing more of the complex behaviour with the use of this small extended set of CMEs, and in the next section we give the results of a much larger set of extended coupled mode equations, compared to the WRspice result.

Table 5.1: Example of pump mediated mixing mechanisms, capped at increasing pump harmonics. The naming convention (CME-k) contains all pump-mediated mixing tones up to, and including the kth-harmonic of the pump.

CME-1	CME-2	CME-3	CME-4	CME-5
f_{i}	f_{i}	f_{i}	f_{i}	f_{i}
f_{s}	f_{s}	f_{s}	f_{s}	f_{s}
f_{p}	f_{p}	f_{p}	f_{p}	f_{p}
	$f_{\text{p+i}}$	$f_{\text{p+i}}$	$f_{\text{p+i}}$	$f_{\text{p+i}}$
	$f_{\text{p+s}}$	$f_{\text{p+s}}$	$f_{\text{p+s}}$	$f_{\text{p+s}}$
	$f_{2\text{p}}$	$f_{2\text{p}}$	$f_{2\text{p}}$	$f_{2\text{p}}$
		$f_{2\text{p+i}}$	$f_{2\text{p+i}}$	$f_{2\text{p+i}}$
		$f_{2\text{p+s}}$	$f_{2\text{p+s}}$	$f_{2\text{p+s}}$
		$f_{3\text{p}}$	$f_{3\text{p}}$	$f_{3\text{p}}$
			$f_{3\text{p+i}}$	$f_{3\text{p+i}}$
			$f_{3\text{p+s}}$	$f_{3\text{p+s}}$
			$f_{4\text{p}}$	$f_{4\text{p}}$
				$f_{4\text{p+i}}$
				$f_{4\text{p+s}}$
				$f_{5\text{p}}$

5.3.1 Extension to Resolve WRspice and Coupled Mode Equations

In fig. 5.10, we show that the harmonics of the pump are noticeable up to the 5th harmonic, as such we systematically extend the CMEs to include all pump-meadited mixing mechanisms up to this point. We extend the CME's in order of the pump harmonics and label each extension accordingly as shown in table 5.1.

The largest set of CMEs (CME-5) is explicitly shown in appendix C.1. Any other lower order CME is made by removing any mechanism which involves a frequency higher than the desired highest considered frequency. For example, if we take CME-5 and remove all mixing mechanisms involving a tone with $f > f_{3\text{p}}$, then we would reduce to CME-3. We then directly compare the result of systematically extending the CME's from CME-1 $\rightarrow$ CME-5 looking first at the two largest amplitude tones, the pump and second harmonic of the pump, as shown in fig. 5.13.

In fig. 5.13 we see that the general fit is improved by each extension of the CME's to include higher order tones. We have shown the two largest amplitude tones, which are the pump and the second harmonic of the pump. These two tones oscillate against each other in the simulation which is captured in all extensions of the CME's above CME-1. Note that in fig. 5.13a) the pump tone in the CME

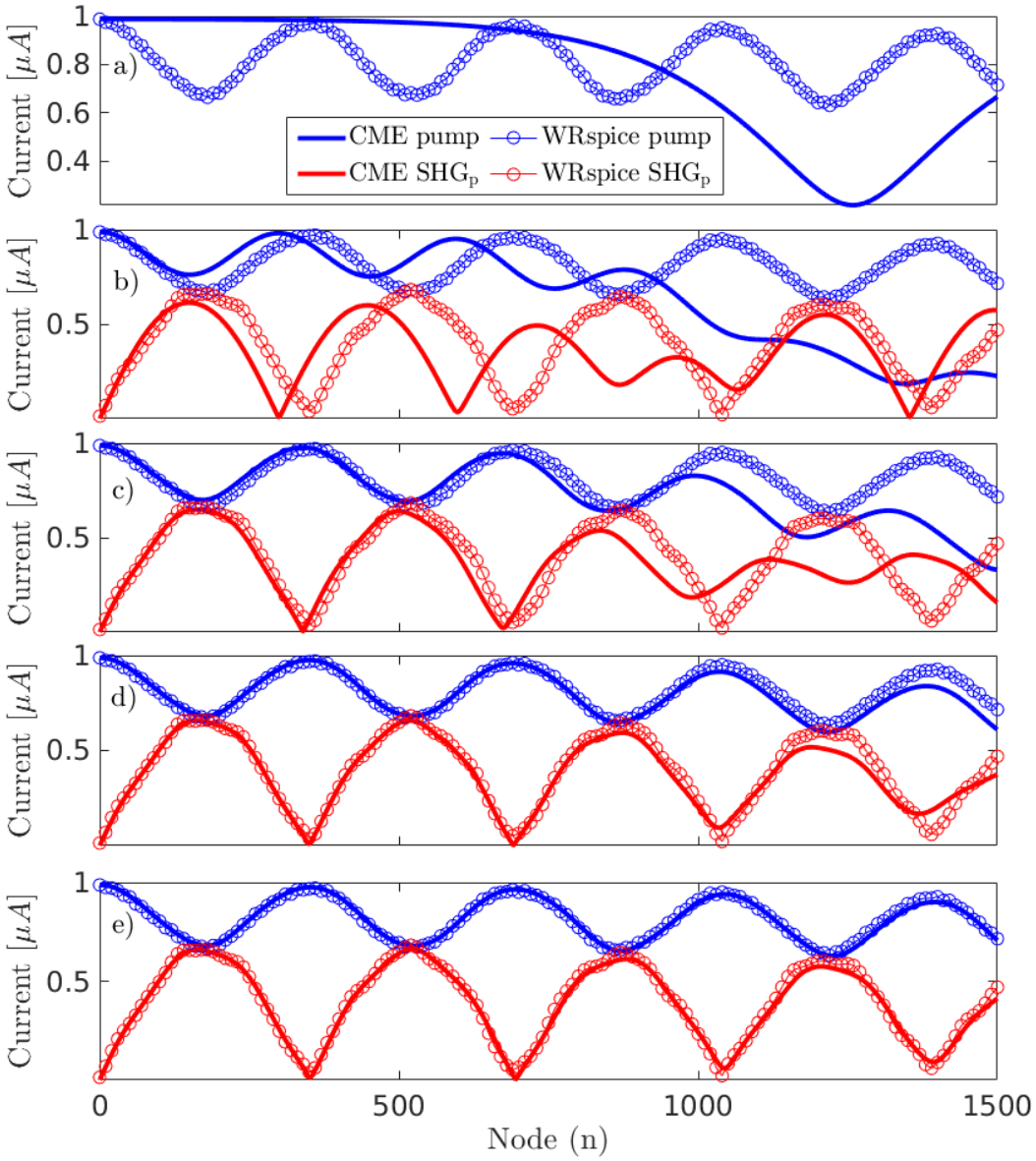

Figure 5.13: Plots a)-e) show the comparison of WRspice and CMEs for CME 1-5 respectively. Plot a) shows the comparison of just the pump tone, while plots b)-e) show the pump and the second harmonic generation of the pump tone (SHG_p), which are the largest tones seen in the WRspice simulation. The number of tones in each set of CMEs is seen in table 5.1 and in this figure we see the improvement of the fit as more tones are included.

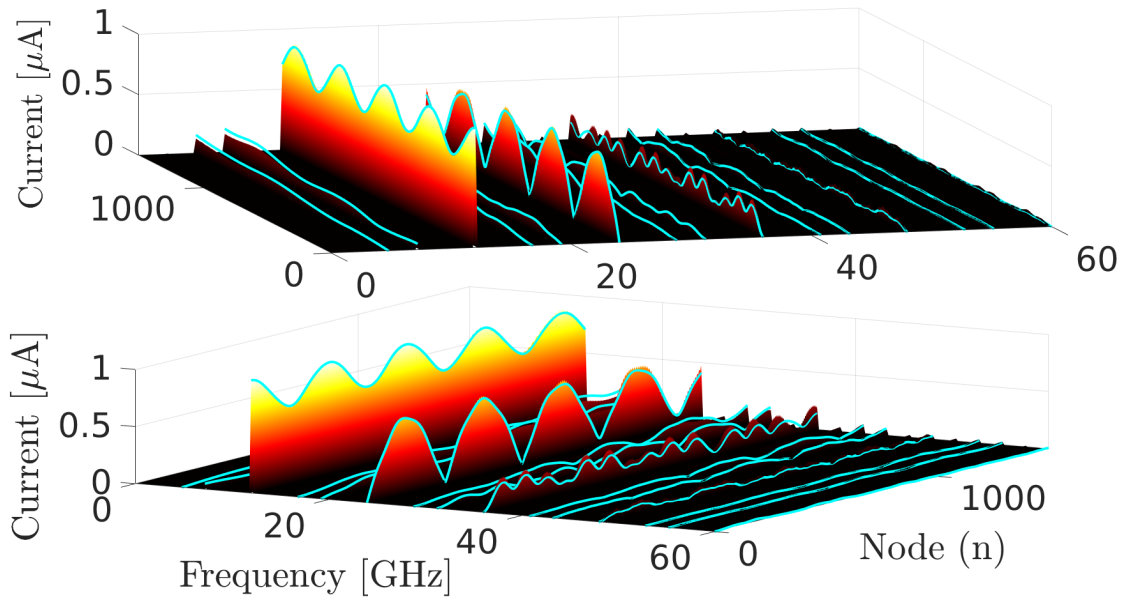

Figure 5.14: Both plots are the same data with a different view such that the full fit of each tone in CME-5 is appreciated. The WRspice result (3D surface) is compared to the CME-5 extension (cyan lines) result. We artificially space the CME-5 result in frequency such that each element overlaps with the correct frequency as per the FFT in WRspice.

calculation (solid blue line) reduces in the same manner as fig. 5.8. However, as we increase the number of tones considered in the calculation the pump amplitude is sustained over an increasing number of nodes.

It may be expected that considering more terms would increase the rate of pump depletion however we show through the CME calculation and WRspice simulation that in fact the opposite is true. For the greatest number of tones considered, CME-5 (fig. 5.13e)), the pump tone amplitude remains above 60% of its initial amplitude. The oscillation between the pump and the second harmonic of the pump is visible in CME-5. But even with the additional 13 tones considered in CME-5 the pump still reaches $> 98\%$ of the initial pump amplitude, even at the final maxima around $n \approx 1400$. As such, measuring a device whose length is equal to the nodes where a maxima of the pump occurs (n 350, 700, 1050, 1400) may lead to the conclusion of a stiff undepleted pump. However we see here that this is a happenstance of the length of the interaction between pump and second harmonic generation and the length of the device.

To demonstrate the "full fitting capability" of these extended CMEs, we fit all tones considered with the WRspice result shown in fig. 5.14.

Using an extension to the CMEs in comparison to the WRspice output we are able to explain and understand the complete behaviour of our simulated device. We have given an explicit example of an extension to the coupled mode equations. The brute force extension gives rise to additional tones oscillating at various sums and differences of both the initially input tones (pump and signal) as well as the cascade of generated tones (every other tone). This cascade of generated tones is produced in the 3WM condition, in contrast to a higher order power expansion of the Josephson relation, and thus is still feasible in the low power limit. However, this technique is extendable to arbitrary higher order wave mixing conditions (4WM, 5WM, ...), where only the frequency mixing conditions for each wave mixing scenario would need to be revised. While we have purposefully moved to a lower input power regime, which reduces the erratic behaviour of the device, we still see more complex behaviour than initially thought. The higher order tone generation cascades through the device and interacts with each other. In the CME-5 case there are 121 mixing mechanisms considered, compared to 3 in CME-1. Furthermore for brevity and pedagogical reasons we have not included the non-pump-mediated case, but we would expect that the fit may be improved further by including these tones. As a final message, we show in fig. 5.15 the possible issue of not including an extended CME theory when analysing the signal propagation and gain.

Figure 5.15 shows that if one was to model the circuit through CME-1 and neglect higher order terms then the JTWPA would be fabricated to be 1250 nodes long, fig. 5.15a) (blue solid line) such that the signal was maximised at the output. The gain from CME-1 at this node is $G_{\mathrm{CME}-1}(1250) \approx 24\ \mathrm{dB}$. However, the WRspice result in fig. 5.15b) shows that this gain would be closer to $G_{\mathrm{WRspice}}(1250)10.3\ \mathrm{dB}$, less than half that expected. In fact, through each sequential extension of the CMEs we see that the fit of the entire signal profile along the device is improved by each extension. By understanding the interactions of higher order tones within the extended theory, which has been verified by WRspice simulations, we may then look for potential solutions to suppress such interactions. Furthermore, we intend to develop this extended theory to include arbitrarily many tones by exploring symmetries in the brute force extension to the coupled mode equations.

Exploring the Extended Coupled Mode Equations

After extensively writing down and calculating the extension to the CMEs, it becomes clear that there are a number of patterns which emerge from the generation of tones. As an extension to this work,

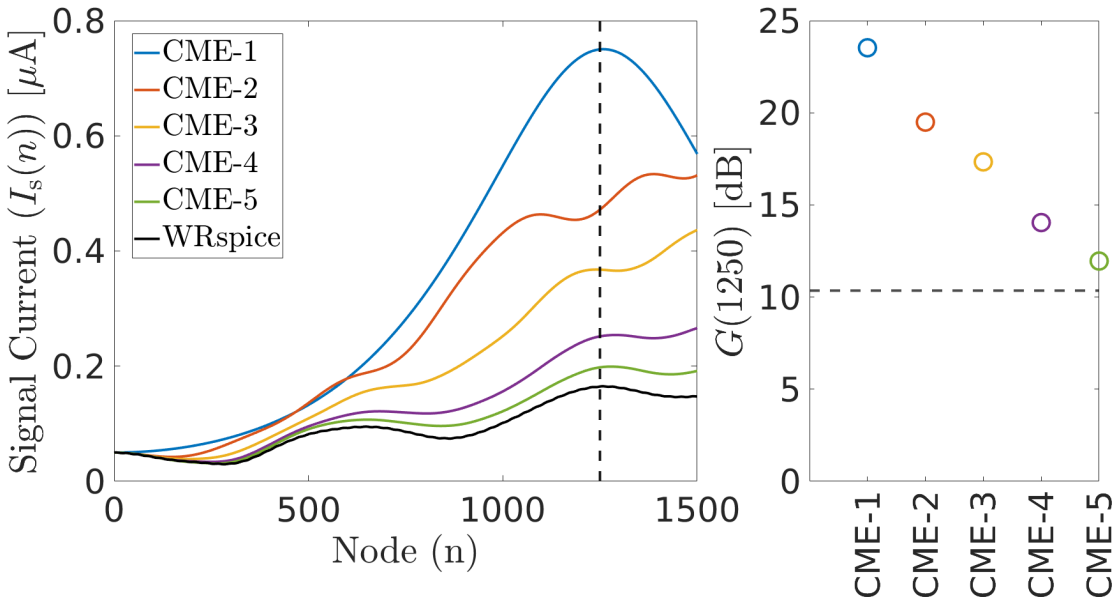

Figure 5.15: (a) Signal profiles for each CME (colours) and WRspice (black). (b) Signal gain measured at node $n = 1250$ ((a) black dashed line) for each extension of CME and WRspice. The signal profiles in a) approach the WRspice result where CME-5 in b) shows the most accurate gain calculation. The gain is calculated at the node of max gain in CME-1.

exploring these patterns may prove useful in future analysis of the non-linear differential equations which govern the mixing mechanisms in the CMEs. In this subsection, we introduce a way to represent the individual mixing mechanisms in a matrix form based on the initial state vector. We specifically focus on the 3WM matrix, which results in a 2-D matrix whose elements is mapped back to indicate which frequency the two input mixing tones were, which frequency is then generated, as well as the specific type of mixing involved (SFG, DFG, HG). Following this, we propose that this method is general in that it potentially accounts for all mixing mechanisms (with enough computing power) possible in the system. We also propose that this method is extendable to higher order mixing conditions, where the $x - D$ dimensional mixing matrix corresponds to $(x + 1)$WM, i.e the 4WM matrix is a 3-D matrix. To highlight this, we revisit the explicit example given in section 5.3. It helps to now give the initial input frequencies of $f_{\mathrm{p}} = 12$ GHz and $f_{\mathrm{s}} = 7.2$ GHz which is consistent with the previous work in this thesis. As we did before, we define an arbitrary cut off frequency of $f_{\mathrm{c}} = 3f_{\mathrm{p}} = 36$ GHz as our first constraint.

We make a simple frequency vector of just the pump and signal frequencies. We then find all the addition and subtraction permutations of each frequency, discarding any result that is below 0 or above

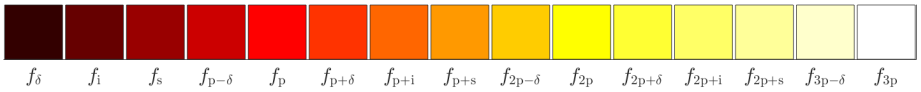

Figure 5.16: Representation of the frequency vector obtained for all possible permutations of considered frequency's with input tones $f_\mathrm{p} = 12$ GHz and $f_\mathrm{s} = 7.2$ GHz, up to $f_\mathrm{c} = 36$ GHz. Since $f_\delta = f_\mathrm{s} - f_\mathrm{i} = (1/5)f_\mathrm{p}$ all mixing mechanisms created are a multiple of f_δ and an infinite cascade of lower frequencies is avoided for this choice of pump and signal frequencies.

f_c, and storing the result left over in the frequency vector. We do this iteratively and if the length of the frequency vector has changed after this process then we repeat the permutation. If the length of the vector is constant after this process, then we have found all of the relevant frequencies and the number of elements in this vector indicates the number of mixing mechanisms possible for the next step. It is important at this step to remember that since $f_\mathrm{s} = (3/5)f_\mathrm{p}$, then there exists an $f_\delta = (1/5)f_\mathrm{p}$, which is a factor of every generated tone, and as such there are not infinitely many mixing mechanisms generated at lower frequencies. As a visual aid we assign each frequency a colour as shown in fig. 5.16.

If we now add and subtract every frequency in the frequency vector, represented in fig. 5.16, and remove any frequencies $f < 0$, or $f > f_{3\mathrm{p}}$, then we would find the same frequency vector. We then iterate over two identical frequency vectors with individual elements m, and a total number of elements M. Performing addition and subtraction on each $m_1 \pm m_2$ over all $m_{1,\,2} = 1 \rightarrow M$ elements. If $m_1 + m_2 > M$ then the mixing is discarded (higher than maximum frequency). The terms which are kept from the $m_1 + m_2$ correspond to the SFG terms if $m_1 \neq m_2$, and HG terms if $m_1 = m_2$. Similarly if $m_1 - m_2 \leq 0$ then the mixing is also discarded (0 frequencies corresponding to optical rectification, or negative frequencies corresponding to the conjugate equation). The terms which are kept from the $m_1 - m_2$ correspond to DFG terms where $m_1 > m_2$. For a frequency vector of M elements we create an $M\mathrm{x}M$ 3WM frequency matrix $\mathbf{\Omega}_{p,q}$ where single elements in the matrix are defined at positions $p,\ q$ which relate directly to the frequencies "mixing" $m_1,\ m_2$ mentioned previously. Such a matrix is shown in fig. 5.17.

This matrix is constructed such that the matrix index $p,\ q$ refers to the index of the initial mixing in the frequency vector between elements $m_1,\ m_2$ and shown in the row and column labels in fig. 5.17. Then the tone that is produced as a result of either the sum or difference of of frequencies $f_{p,\,q}$ is

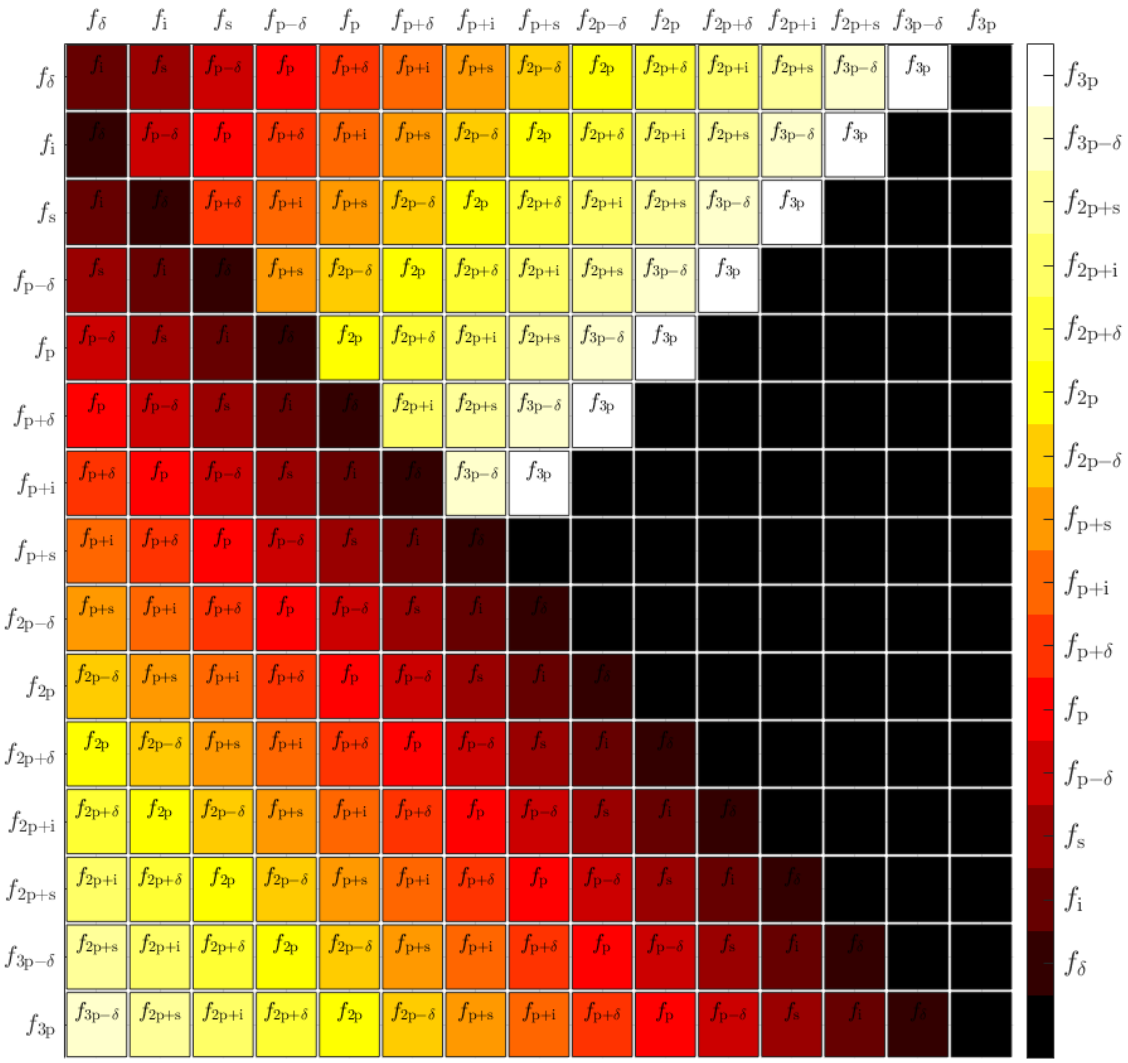

Figure 5.17: Representation of the frequency mixing matrix obtained for all possible permutations of considered frequency's with input tones $f_\mathrm{p} = 12$ GHz and $f_\mathrm{s} = 7.2$ GHz, up to $f_\mathrm{c} = 36$ GHz.

labelled (and coloured) at the site $\mathbf{\Omega}_{p,\,q}$. For an intuition into the inner workings we can inspect a number of the rows and columns. For example we see that row 1, relating to the lowest frequency tone, always describes an up conversion term and mixes with every tone up to the second highest frequency tone. This is understandable since the first element in the $(1,1)$ position describes HG and shows that $f(1) = f_{\mathrm{delta}} = 2.4$ GHz mixing with $f(1) = f_\delta = 2.4$ GHz results in a tone with frequency $f(1+1=2) = f_{\mathrm{i}} = 4.8$ GHz. Also, as expected, the lowest frequency tone can mix with all but the highest frequency tone to produce SFG tones, as shown in the rest of the first row. Similarly at the final row of the matrix the largest tone can produce DFG tones with every other frequency except itself. The DFG tone between the largest frequency $f(15) = f_{\mathrm{c}} = 3f_{\mathrm{p}} = 36$ GHz and lowest frequency tone $f(1) = f_\delta = 2.4$ GHz produces the largest frequency DFG tone $\mathbf{\Omega}_{(15,1)} = f(15) - f(1) = f(14) = f_{\mathrm{2p+s}} = 33.6$ GHz. Interestingly, the area of the matrix representing the DFG terms is larger than the SFG terms. This is because there are potentially two non-degenerate methods for a specific frequency to generate a specific tone through DFG. For example the $f(8) = f_{\mathrm{p+s}}$ tone generates the $f(5) = f_{\mathrm{p}}$ tone through DFG of $f(8) - f(3) = f_{\mathrm{p+s}} - f_{\mathrm{s}} = f_{\mathrm{p}} = f(5)$ as well as $f(13) - f(8) = f_{\mathrm{2p+s}} - f_{\mathrm{p+s}} = f_{\mathrm{p}} = f(5)$ which are two distinct mixing mechanisms. By studying the mixing matrix in this way we gain a deeper insight into the possible mixing mechanisms within the 3WM scheme.

We further reduce the number of considered tones and mixing mechanisms by excluding any mixing which does not involve a pump or pump harmonic tone. This we referred to previously as pump mediated mixing. By doing this both the number of tones considered and the number of mixing mechanisms producing each tone is reduced as shown in fig. 5.18.

This mixing matrix has 41 coloured squares. These relate directly to the 41 terms in eqs. (5.7) to (5.15) which is the explicit CME-3 set we derived previously. If we consider the elements generating the f_{2p} tone (yellow) we find that there are a total of 6 squares in the matrix. This is exactly the number of terms in eq. (5.12). The specific f_{2p} mixing mechanism located at $\mathbf{\Omega}_{3,3}$ corresponds to the HG of the pump tone ($f_{\mathrm{p}} + f_{\mathrm{p}}$), i.e the first term in eq. (5.12). The two f_{2p} squares in the upper right portion of fig. 5.18 at positions $\mathbf{\Omega}_{1,5}$ and $\mathbf{\Omega}_{2,4}$ represent the second and third SFG terms in eq. (5.12) respectively. The three f_{2p} squares in the lower left portion of the matrix at positions $\mathbf{\Omega}_{1,7}$ $\mathbf{\Omega}_{2,8}$, and $\mathbf{\Omega}_{3,9}$ represent the sixth, fifth and fourth DFG terms in eq. (5.12) respectively.

Following this for every tone reveals that by simply knowing the position p, q of each tone in the

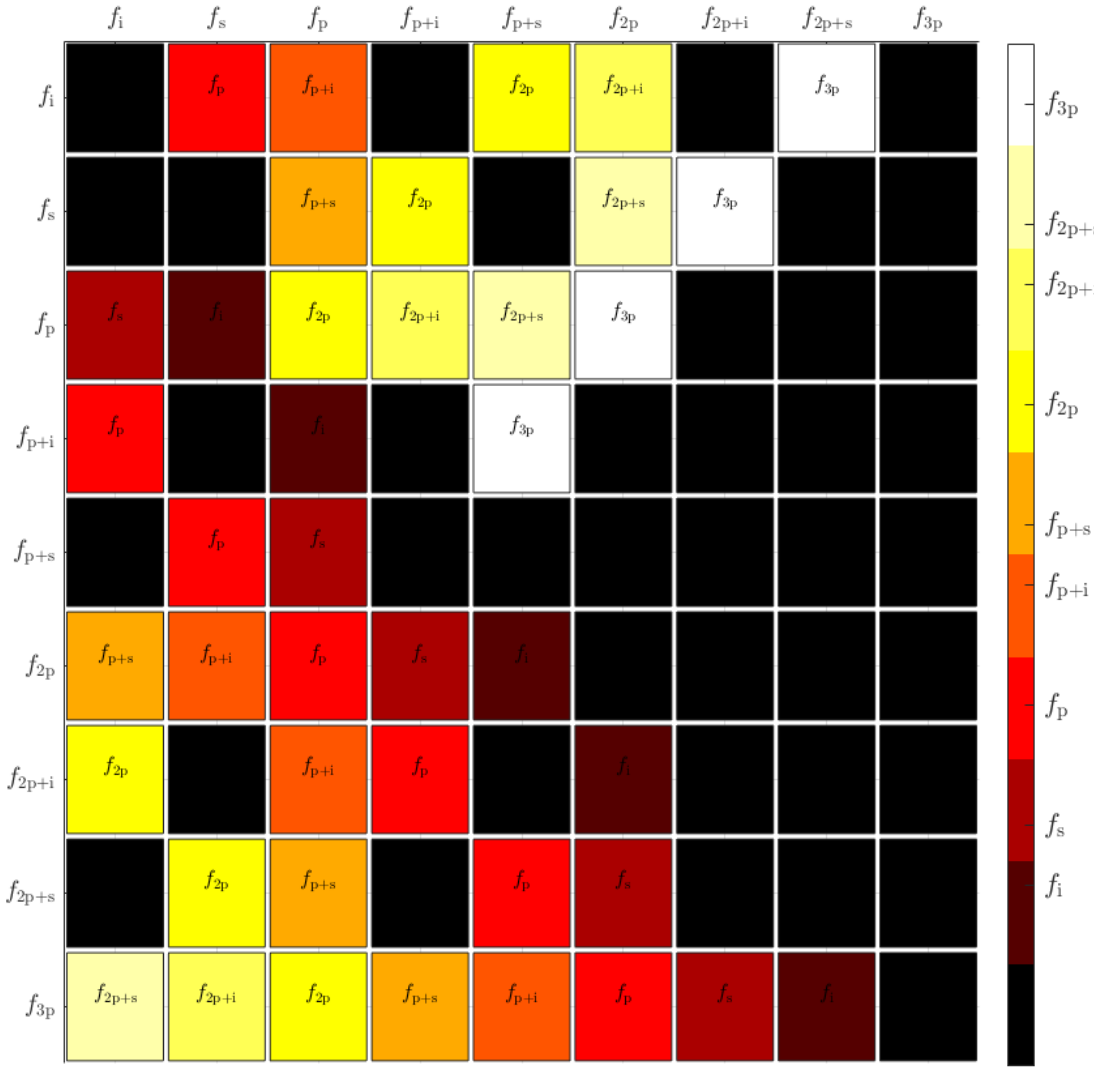

Figure 5.18: Three wave mixing matrix with a frequency cut off at the third harmonic of the pump $f_\mathrm{c} = f_\mathrm{3p}$ and only pump mediated mixing allowed.

mixing matrix $\boldsymbol{\Omega_{p,q}}$ we recreate a complete set of CMEs for arbitrary constraints. The $-$, $+$ or $-1/2$ coefficient in the CMEs is given by the general location, i.e. $p < q$ is SFG ($-$), $p > q$ is DFG ($+$), $p = q$ is HG ($-1/2$). The specific combination of $k_p k_q$ coefficients is given by the elements $p,\ q$. The amplitudes $A_p A_q$ are then also given by $p,\ q$ but in the case of DFG the amplitude of q is conjugate, i.e. DFG coefficients read $+k_p k_q A_p A_q^*$. The exponents similarly are such that for SFG terms the exponent reads $e^{i(k_p+k_q)}$, while the DFG exponents are $e^{i(k_p-k_q)}$. Finally we collect all of the mechanisms oscillating at each frequency and relate them back to the original frequency vector to create the CMEs.

Refining this work could open many possibilities to further understanding the complex behaviour in these devices. Firstly one is not necessarily limited to just a pump and signal input tone. If broadband amplification is required to detect multiple signals then it stands to reason that these signals may be input at the same time and different frequencies in the device. There is no immediately obvious reason why this could not be considered with this type of analysis by a) giving multiple input signals at the first step, b) then providing these input signals with a non-zero initial value in the ODE solver. Secondly one can extend this method to any other higher order mixing mechanism and thus potentially describe higher power 5WM, 7WM, ... mechanisms and try to understand the features at high powers in the device. Also there is no reason why at each iteration one could not describe a mixed mixing state of 3WM and 4WM simultaneously. One could input the pump and signal, perform the first 3WM iteration and collect the frequencies generated. Then with those frequencies perform the first 4WM iteration and collect those frequencies. repeating this step would lead to two mixing matrices representing each mixing condition. But then by simply collecting all of the same frequency mixing mechanisms from both matrices and applying the individual coefficients one produces a mixed 3WM and 4WM which may be useful for analysing devices which are at a mixed bias position, see fig. 2.3. Similarly any dispersion engineering is incorporated by adjusting the dispersion relationship used and subsequently the $k(\omega)$ entered into the CMEs. We believe there is a great deal of further application for this numerical approach to understand the complex behaviour of these devices.

5.4 Quasi Phase Matching Approach

Recently, Zorin proposed a method that could mitigate the generation of unwanted tones by using a technique referred to as Quasi Phase Matching (QPM) [39]. This technique has been used within

the optics community [56] with Lithium Niobate crystals. The QPM method is limited to non-centrosymmetric (quadratic in our case) non-linearities, which aligns with the operation of the rf SQUID embedded JTWPA. The simplest way to motivate this is by considering a nonlinear co-efficient $\beta \to \beta(x)$ with some x dependence. The proposal in [39] shows that this is done trivially with the rf SQUID in a two dimensional Co-Planar Waveguide (CPW) set up. By swapping the junction and geometric inductance arms while maintaining direction of flux threading the loop one reverses the direction of DC current through the junction. Since the coefficient $\beta \propto \sin(\varphi_{\mathrm{DC}})$ the reversal of the current changes the sign of $\beta \to \pm|\beta|$. By keeping the properties of the rf SQUID the same one introduces functions by the method of periodic poling [57]. As the wavelength of the tones are much larger than each individual rf SQUID element, the flipping of neighbouring rf SQUIDs smooths out to approximate a continuous function. For example the function,

$$\eta(x) = -a \ln\left(e^{-2x/abm} + e^{-1/a} + e^{(2x-m)/abm}\right), \tag{5.16}$$

is reconstructed by periodically poling $\beta(x)$ as shown in fig. 5.19. The constants a and b define the curvature of the taper and width of the peak respectively, m defines the half wavelength periodicity and its value will be calculated in the following discussion.

We take the circuit parameters from [39],

$$L_{\mathrm{g}} = 88 \text{ pH},\ I_{\mathrm{c}} = 1.8\ \mu\text{A},\ C_{\mathrm{J}} = 235 \text{ fF},\ \text{and } C_0 = 32 \text{ fF}.$$

Using these parameters, we obtain the zero frequency impedance $Z_0 = \sqrt{L_{\mathrm{g}}/C_0} \approx 52\Omega$, the SQUID parameter $\beta_{\mathrm{L}} = 2\pi L_{\mathrm{g}} I_{\mathrm{c}}/\Phi_0 \approx 0.48$ and importantly a cut-off frequency of $f_{\mathrm{c}} = 2/2\pi(\sqrt{L_{\mathrm{g}}(C_0 + 4C_{\mathrm{J}})}) \approx 34$ GHz. The reduction in cut-off frequency is largely due to the increase in Josephson capacitance C_{J}. In reality this could be any shunt capacitance in parallel with the Josephson junction. To achieve such large capacitance one may consider parallel plate capacitors shunting the rf SQUID. This does change the dispersion properties of the line considerably, the phase shift per unit cell k for the QPM device with these parameters is shown in fig. 5.20.

The purpose of the poling is to reverse the effect of phase mismatch, which causes the signal to deamplify after a certain length of the amplifier. If one considers the pump signal idler interaction as

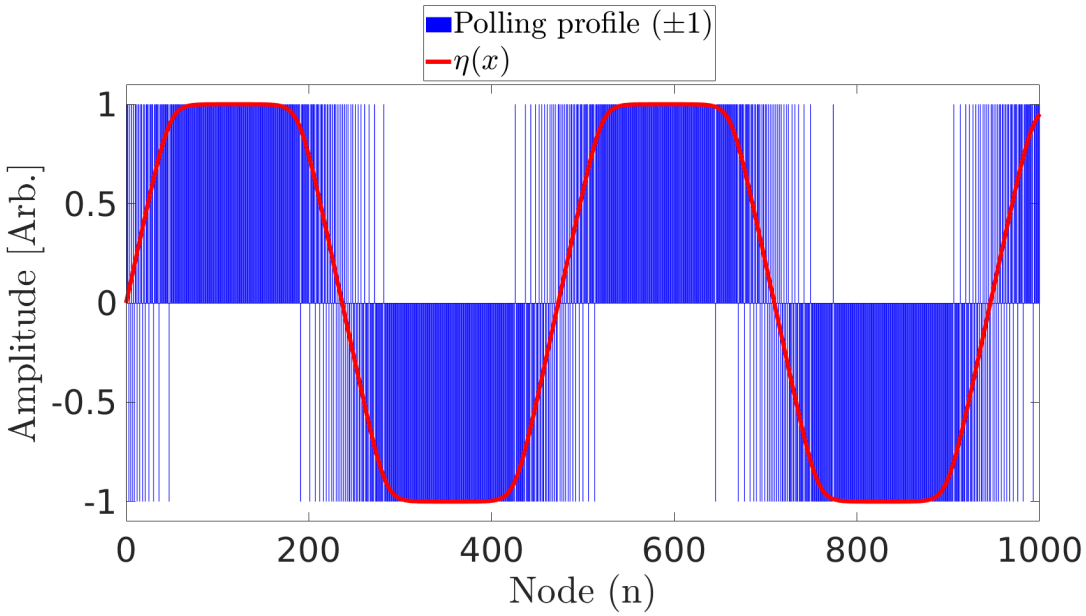

Figure 5.19: The poling of $\beta(x) = \pm|\beta|$ is represented by the poling profile (blue bars) and is modulated such that the tapered profile of $\eta(x)$ (red line) is reconstructed through the digitisation technique of pulse width modulation.

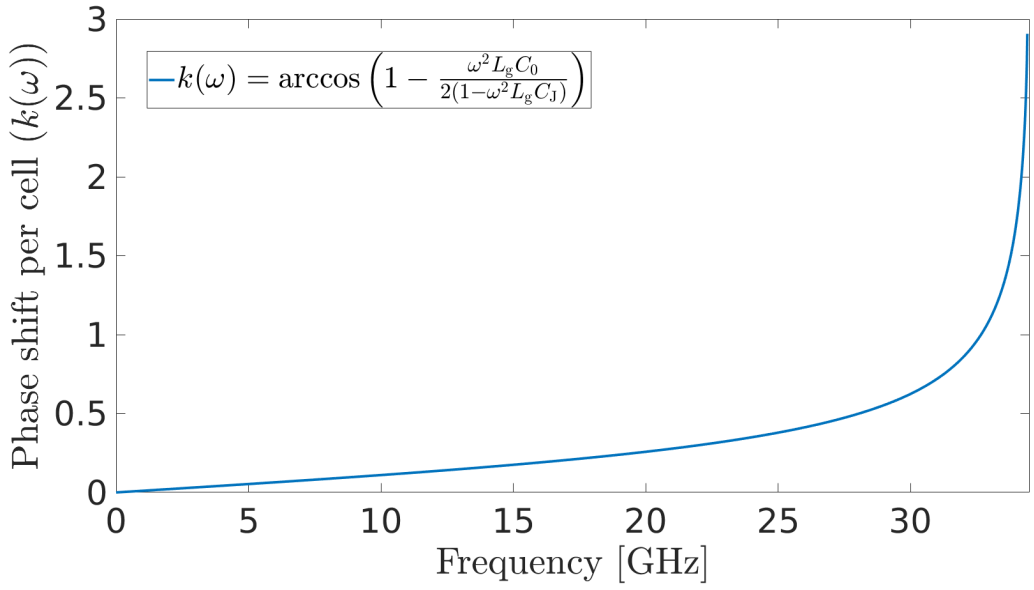

Figure 5.20: Phase shift per unit cell k for the QPM parameters given in [39]. The dispersion is now far more exaggerated due to the higher parallel shunt capacitance.

the dominant source of signal amplification then the phase mismatch of this particular interaction $\Delta k_{\uparrow}$ is defined as,

$$\Delta k_{\uparrow} = k_{\mathrm{p}} - k_{\mathrm{i}} - k_{\mathrm{s}} \approx 0.133. \tag{5.17}$$

Since we wish the function $\eta(x)$ to change sign when the phase of this interaction flips, we specifically choose $m/2 = \pi/\Delta k_{\uparrow} = 236$. This is in slight contrast to that given in [39] due to the approximation used for the dispersion relation. We also note that in [39] the pump power ($-70\ \mathrm{dBm}$) corresponds to a large pump input current $I_{\mathrm{p}}(0) \approx 1.9\ \mu\mathrm{A} > I_{\mathrm{c}}$. We have already shown that for pump currents at half the critical junction current the behaviour of the device is erratic. As such, we reduce the pump input current before simulating such a device $I_{\mathrm{p}}(0) \to 0.72\mu\mathrm{A}$ and for completeness $I_{\mathrm{s}}(0) \approx 50\ \mathrm{nA}$. The pump frequency now suggested is $f_{\mathrm{p}} = 15\ \mathrm{GHz}$ meaning that the cut-off frequency is situated just above the SHG tone. This should aid in avoiding transferring pump power into the cascaded harmonics. Furthermore, the sharp dispersion curve in fig. 5.20 coupled with the out of phase oscillations of $\eta(x)$ with all other mixing mechanisms should cause undesirable mixing mechanisms to rapidly deamplify at the point of maximal signal.

We test this by numerically solving the coupled mode equations but with the inclusion of the function $\eta(x)$. This is done simply using MATLAB's symbolic toolbox. By defining the $\eta(x)$ function symbolically we sample the function during the integration for any dynamic step size required and thus integration tolerances can always be met. An example script is given in appendix C.2. The CME's now take the form,

$$\frac{dA_{\mathrm{i}}}{dx} = \frac{\eta(x)\beta}{2}\Big(k_{\mathrm{p}}k_{\mathrm{s}}A_{\mathrm{p}}A_{\mathrm{s}}^{*}e^{i(k_{\mathrm{p}}-k_{\mathrm{s}})x} + k_{\mathrm{p}}k_{\mathrm{p+i}}A_{\mathrm{p+i}}A_{\mathrm{p}}^{*}e^{i(k_{\mathrm{p+i}}-k_{\mathrm{p}})x} + k_{2\mathrm{p}}k_{\mathrm{p+s}}A_{2\mathrm{p}}A_{\mathrm{p+s}}^{*}e^{i(k_{2\mathrm{p}}-k_{\mathrm{p+s}})x}\Big)e^{-ik_{\mathrm{i}}x}, \tag{5.18}$$

$$\frac{dA_{\mathrm{s}}}{dx} = \frac{\eta(x)\beta}{2}\Big(k_{\mathrm{p}}k_{\mathrm{i}}A_{\mathrm{p}}A_{\mathrm{i}}^{*}e^{i(k_{\mathrm{p}}-k_{\mathrm{i}})x} + k_{\mathrm{p}}k_{\mathrm{p+s}}A_{\mathrm{p+s}}A_{\mathrm{p}}^{*}e^{i(k_{\mathrm{p+s}}-k_{\mathrm{p}})x} + k_{2\mathrm{p}}k_{\mathrm{p+i}}A_{2\mathrm{p}}A_{\mathrm{p+i}}^{*}e^{i(k_{2\mathrm{p}}-k_{\mathrm{p+i}})x}\Big)e^{-ik_{\mathrm{s}}x}, \tag{5.19}$$

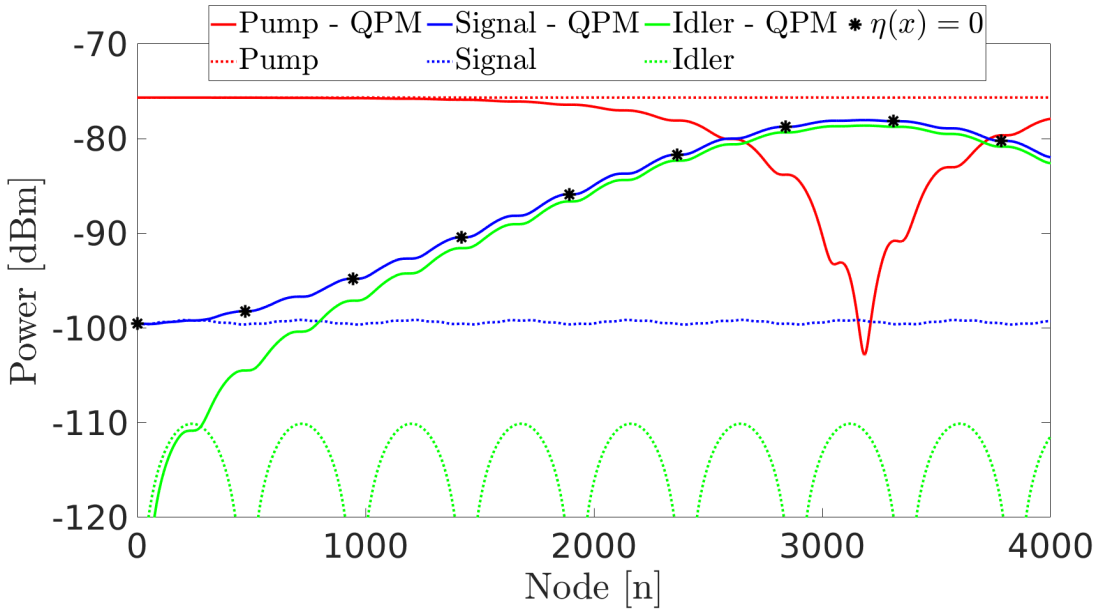

Figure 5.21: The QPM profiles (solid lines) for pump (red), signal (blue), and idler (green) compared to the non-QPM (dashed lines). The up-conversion tones are calculated here but not shown. The zeroes of $\eta(x)$ are also highlighted showing that they sit on the saddle points of the QPM signal, effectively reversing the deamplification process.

$$\frac{dA_{\mathrm{p}}}{dx} = \frac{\eta(x)\beta}{2}\Big(- k_{\mathrm{s}}k_{\mathrm{i}}A_{\mathrm{i}}A_{\mathrm{s}}e^{i(k_{\mathrm{s}}+k_{\mathrm{i}})x} + k_{\mathrm{p+s}}k_{\mathrm{s}}A_{\mathrm{p+s}}A_{\mathrm{s}}^{*}e^{i(k_{\mathrm{p+s}}-k_{\mathrm{s}})x} + k_{\mathrm{p+i}}k_{\mathrm{i}}A_{\mathrm{p+i}}A_{\mathrm{i}}^{*}e^{i(k_{\mathrm{p+i}}-k_{\mathrm{i}})x} + k_{2\mathrm{p}}k_{\mathrm{p}}A_{2\mathrm{p}}A_{\mathrm{p}}^{*}e^{i(k_{2\mathrm{p}}-k_{\mathrm{p}})x}\Big)e^{-ik_{\mathrm{p}}x}, \tag{5.20}$$

$$\frac{dA_{\mathrm{p+i}}}{dx} = \frac{\eta(x)\beta}{2}\Big(- k_{\mathrm{p}}k_{\mathrm{i}}A_{\mathrm{p}}A_{\mathrm{i}}e^{i(k_{\mathrm{p}}+k_{\mathrm{i}})x} + k_{2\mathrm{p}}k_{\mathrm{s}}A_{2\mathrm{p}}A_{\mathrm{s}}^{*}e^{i(k_{2\mathrm{p}}-k_{\mathrm{s}})x}\Big)e^{-ik_{\mathrm{p+i}}x}, \tag{5.21}$$

$$\frac{dA_{\mathrm{p+s}}}{dx} = \frac{\eta(x)\beta}{2}\Big(- k_{\mathrm{p}}k_{\mathrm{s}}A_{\mathrm{p}}A_{\mathrm{s}}e^{i(k_{\mathrm{p}}+k_{\mathrm{s}})x} + k_{2\mathrm{p}}k_{\mathrm{i}}A_{2\mathrm{p}}A_{\mathrm{i}}^{*}e^{i(k_{2\mathrm{p}}-k_{\mathrm{i}})x}\Big)e^{-ik_{\mathrm{p+s}}x}, \tag{5.22}$$

$$\frac{dA_{2\mathrm{p}}}{dx} = \frac{\eta(x)\beta}{2}\Big(- \frac{k_{\mathrm{p}}^{2}A_{\mathrm{p}}^{2}}{2}e^{i(k_{\mathrm{p}}+k_{\mathrm{p}})x} - k_{\mathrm{p+i}}k_{\mathrm{s}}A_{\mathrm{p+i}}A_{\mathrm{s}}e^{i(k_{\mathrm{p+i}}+k_{\mathrm{s}})x} - k_{\mathrm{p+s}}k_{\mathrm{i}}A_{\mathrm{p+s}}A_{\mathrm{i}}e^{i(k_{\mathrm{p+s}}+k_{\mathrm{i}})x}\Big)e^{-ik_{2\mathrm{p}}x}, \tag{5.23}$$

which we have solved numerically. Figure 5.21 shows the QPM solution versus the non-QPM solution for the above parameters.

The signal in fig. 5.21 shows over 20 dB gain at node $n = 3200$. Also, the signal shows a smooth rise and plateau. This generally indicates a smooth bandwidth when sweeping the signal frequency. The effect of SHG is shown in fig. 5.22.

Figure 5.22 shows that as expected the QPM coupled with the steeper dispersion curve, shown in fig. 5.20, reduces the amount of SHG. This allows for pump power to be effectively transferred into the

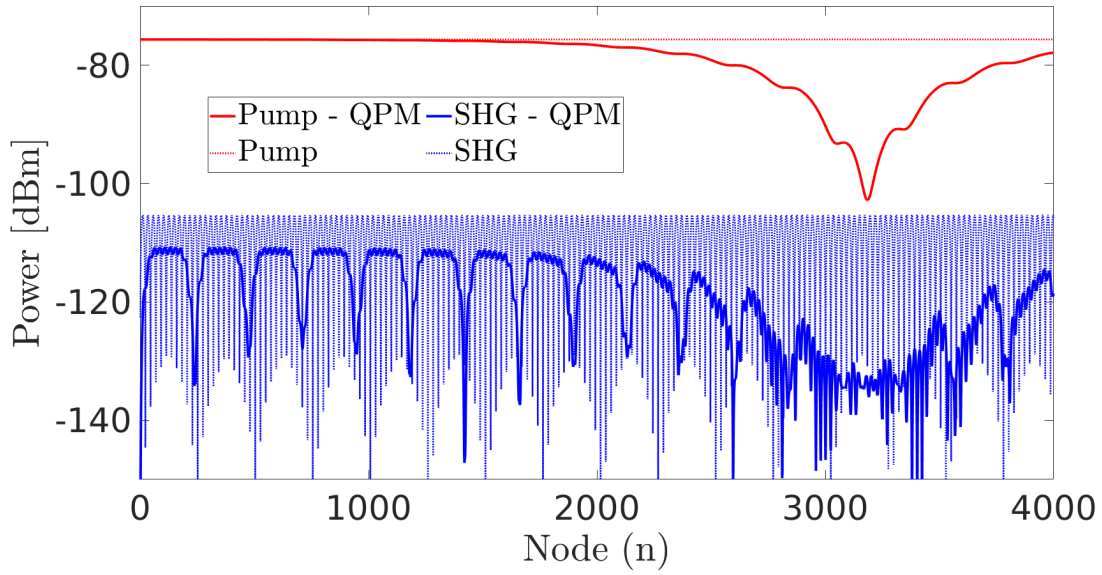

Figure 5.22: The QPM profiles (solid lines) for pump (red) and SHG (blue) compared to the non-QPM (dashed lines). The SHG is reduced generally for the QPM calculation. While in the area of maximum signal, around $n = 3200$ the SHG is considerably lower.

signal band. Similarly, the SFG of pump and signal is reduced, particularly at the node of maximum signal gain, shown in fig. 5.23

The shape of the SFG terms around $n \approx 3200$ is interesting. The power from the pump at this point has dropped by nearly 30 dB. The rapid decrease of the SFG terms at this point allows the signal and idler tone to slowly climb and remain flat between $300 < n < 3500$. This is an interesting result, since sweeping signal frequency shifts the curves horizontally. As such, a flat response in this region may signify a flat bandwidth response.

Finally, we have also begun testing this QPM idea in WRspice. By reversing the current source in the bias current one can simulate a current flowing in opposite directions around the poled rf SQUID loops. By plotting the phase on each junction, we see the outline of the tapered $\eta(x)$ function, shown in fig. 5.24.

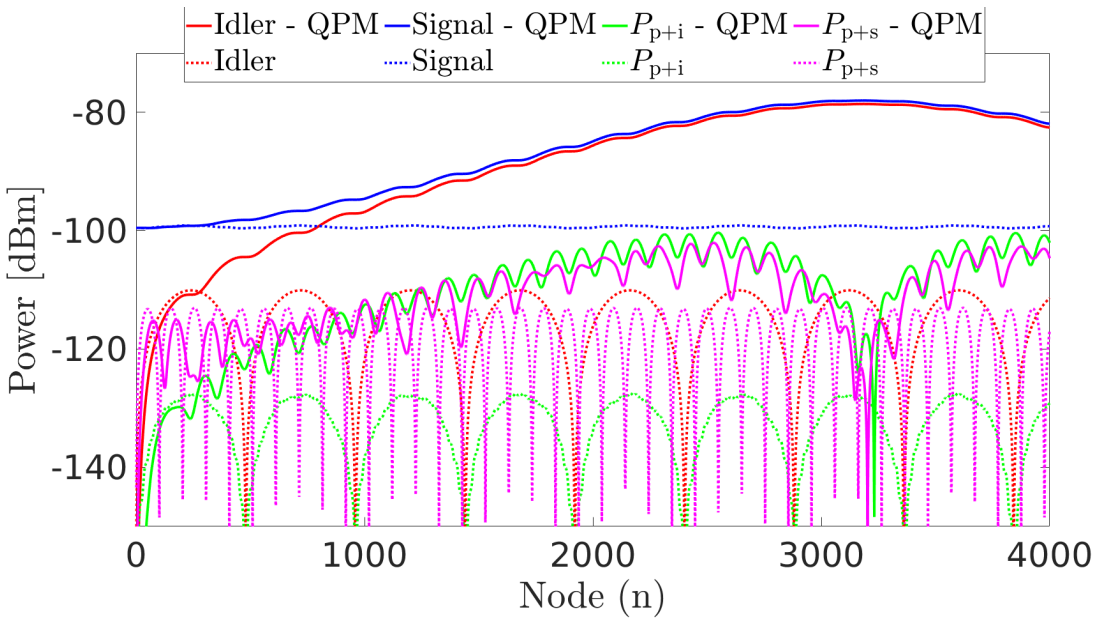

Figure 5.23: The QPM profiles (solid lines) for signal (red), idler (blue), pump + idler (green) and pump + signal (magenta) compared to the non-QPM (dashed lines). The SFG is generally increased for the QPM calculation. However around $n = 3200$ the SFG is rapidly de-amplified, showing how power is quickly transferred back to the signal band.

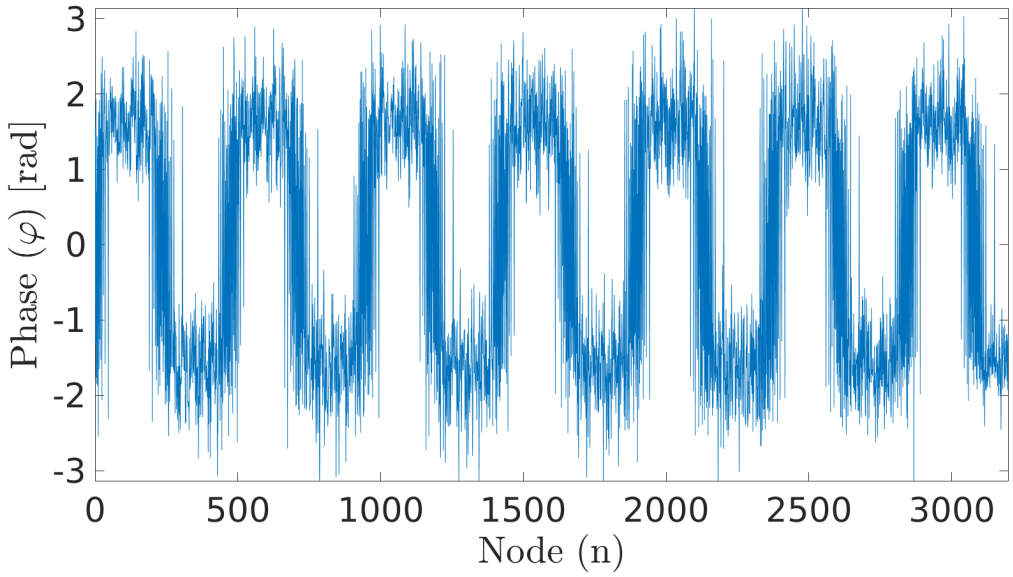

Figure 5.24: The phase on each Josephson junction in the device. The general shape shows the ability to use pulsewidth modulation in an effort to recreate the $\eta(x)$ function.

The final result is then a fit of the current amplitude in WRspice with our extended theory including the QPM $\eta(x)$ function given by eq. (5.16) shown in fig. 5.19

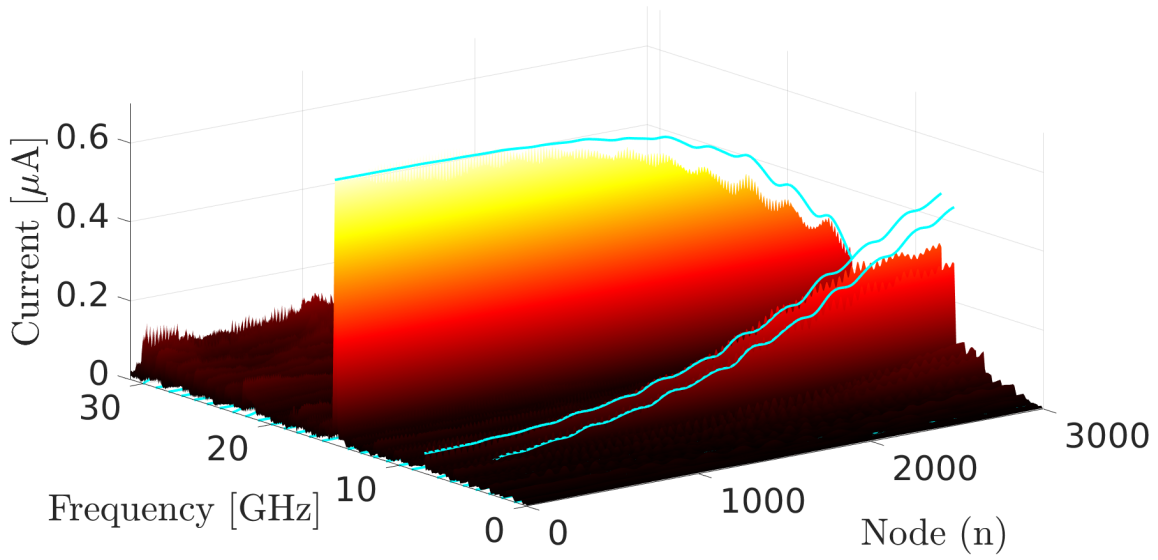

Figure 5.25: The spectral current amplitude of the device simulated in WRspice. The fit here is not as precise as was shown in fig. 5.14. There are small, rapid oscillations visible on the envelopes of the large tones. Also there is noticeable side bands spaced at 1 GHz intervals indicative of added four wave mixing.

While the CME solution from eqs. (5.18) to (5.23) does not fit the WRspice simulation in fig. 5.25 as well as the extended CME's in fig. 5.14 we are encouraged by the clear QPM behaviour. The signal does achieve 20 dB gain and the rise in signal current envelope is exponential over the first 2500 nodes. The phase of the junctions in fig. 5.24 shows that the pulse-width modulation achieves the desired effect, however we believe that this may be improved. Also we note that the spread in the phase of the junction may incur impedance mismatch, as well as unwanted four wave mixing which is not currently included in our CME analysis.

5.5 Summary

We have shown that by lowering the input power to the rf SQUID JTWPA, we move away from an erratic regime.

In this lower power regime the cascade of three wave mixing mechanisms became more clear and we were able to develop an extension to the CME theory. We did this by considering all of the possible generated frequencies based on an iteration of the three wave mixing condition. By doing this, we showed that even in the small signal limit the cascaded effect of the presence of higher order tones

allowed for many higher frequencies to be analysed.

We showed that by considering these tones, we produce a very good fit for a complex system over all tones as showed in fig. 5.14. Furthermore, we highlight to the community the dangers of not including such tones and showed in fig. 5.15 how this may manifest in a reduction in the expected gain at the output of a device.

Finally, we have briefly discussed on the idea of Quasi Phase Matching as suggested in [39]. This is a recent proposal, and the analysis we show in section 5.4 gives a hopeful outlook on the idea. The tools and understanding developed in this section have proven valuable resources to verify and optimise such proposals and in fig. 5.25 we show a device achieving $G < 20\mathrm{dB}$

Chapter 6

Conclusion

6.1 Conclusion

In this thesis, I have focused on the development of a robust, practical amplifier designed for the microwave regime, and in particular as the first stage in a chain of amplifiers targeted at quantum information processing.

Essential requirements of such a device were; gain, $G \approx 20$ dB over an instantaneous bandwidth $4 - 8$ GHz. Through measurement of partner devices and simulation of the design proposed by Zorin [14], I discovered that broadband devices are more complex then their resonant counterparts. As such, we refocused our efforts in to understanding this more complex behaviour outlined in chapter 4 and chapter 5 which resulted in publication [11]. These models have given us extensive insight into previously unexpected behaviour.

In our experiments, we first show up-conversion to higher modes in devices constrained to operate within resonant frequency conditions. The realisation of this led to the initial concern of up-conversion in devices which have a large bandwidth of operation.

We then show the effect of cascaded harmonic generation in such a travelling wave device. We show SHG at the three wave mixing (3WM) bias point, and THG at the four wave mixing (4WM) and 3WM bias point - THG in the 3WM demonstrates cascaded harmonic generation in JTWPAs. We also show the Sum Frequency Generation within a travelling wave device and show that these tones can grow larger than the idler, meaning they can no longer be neglected in the analysis of such a device.

I have extended the analytical model of three mode interactions for parametric amplification to

include higher order mixing processes. By solving this numerically, we can quantify the higher order effects and their implications for the total system, including detrimental effects on signal gain in broadband parametric amplifiers. To highlight this, we demonstrate their effects in a simulated JTWPA and compare numerical results with simulation. It is important to consider both of these methods. The analytic model gives functional dependencies which can help understand how the device responds to changes in parameters. While the numerical model allows for exploration of any assumptions made in deriving an analytic result.

In addition, we show that tools such as WRspice provide a more complete simulation than analytic or numerical solution of CME's can provide. We also note that WRspice has the capability to include device parameter spreads important for devices with extensive fabrication complexity such as the JTWPAs discussed, this is useful when evaluating experimental results. Ultimately, by understanding the mechanisms driving these higher order tones we can then look to develop devices which counteract the generation of unwanted tones.

One such recent development was proposed at the time of writing this thesis by Zorin [39], by using quasi-phase matching (QPM) one can simultaneously combat up-conversion tones and promote signal amplification. By using our extended theory we first corroborate that QPM reinforces signal gain along the line. Also, we can demonstrate by including higher order terms that QPM actively disrupts up-conversion to the sum frequency $f_{\mathrm{p+s,i}}$ and pump second harmonic $f_{2\mathrm{p}}$; thus inhibiting the cascade of higher order tone generation.

We then show, in WRspice, that while the signal growth does exponentially increases along the line there are a number of considerations that must be made when comparing with theory; such as phase stability, and pump power limitations.

Finally, we provide device parameters and optimal working points based on current technologies with which we believe a QPM-JTWPA can achieve high-gain. We conclude that this type of engineering which targets the core pump-signal interaction (high-gain), while broadly disrupting higher order loss mechanisms (broad-band), provides an exciting new development for practical small-signal amplification.

6.2 Further Work

The most pressing work is the fabrication and measurement of the rf SQUID embedded JTWPA. While in this thesis the simulation and extension of the CME's has shown the device may require further engineering it is feasible that a longer ($n > 2500$) JTWPA may still achieve modest gain ($G > 10$ dB) over a large ($4 - 8$ GHz) bandwidth. Further optimising this design through standard engineering techniques may yield greater gain figures and coupled with the tunability of the rf SQUID JTWPA this may still prove vital to the community.

We expect that work on fabricating and measuring a Quasi-phase matched JTWPA to demonstrate the proposal in [39] would yield an interesting and novel approach to increasing the performance of the rf SQUID JTWPA. Also this approach may be used to suppress specific frequencies and as such may be used for the specific elimination of unwanted tones. By comparing experimental results with circuit simulations we can further verify the accuracy of our simulation and this would allow us to further optimise designs.

We also note that the WRspice tool allows for simulation of variation of design parameters to be easily modelled. This work has been undertaken by collaborators and the results made available via a pre-print on the arXiv [58]. This will give more information to the community, particularly in the design and fabrication stages of JTWPA development.

In the experiment section we noted the observation of tones spontaneously generated inside modes of the pumped resonator. This observation is not fully understood however such instances of spontaneous tone generation have been noted previously [59]. More recently other collaborators have measured a similar sample and demonstrated a number of tones being generated through stimulated wave mixing (where both pump and signal are introduced) [60]. It would be interesting to explore these devices further to map out the regimes of both stimulated wave mixing and spontaneous emission of tones. These may be useful for on chip tone generation in future experiments.

We also note that the generation of tones in broadband devices may be useful for certain applications. The JTWPA has already been theoretically proposed as a squeezed state generator [61, 62]. However if a general quantum theory can be derived which maps to the extended coupled mode equations given here then we may expect the ability to generate multiple entangled states over a large frequency spectrum. Coupling this with the QPM engineering and tunabilty of the rf SQUID, one might propose a

broadband, tunable, squeezed state generator for use in quantum cryptography, information processing and quantum illumination.

Appendices

Appendix A

Theory

A.1 Optical Wave Mixing

A.1.1 Non-linear Polarization

Allowing for polarization of any order (to capture the non-linear nature) $\vec{D} = \epsilon_0 \vec{E} + \vec{P}$. By taking the curl of of Faraday's law, then using the ampere relation, then the non-liner relation for $\vec{D}$ and finally the curl of a curl, we get:

$$\nabla \times \nabla \times \vec{E} = -\frac{\partial(\nabla \times \mu_0 \vec{H})}{\partial t}$$

$$= -\mu_0 \frac{\partial^2 \vec{D}}{\partial t^2}$$

$$= -\mu_0 \frac{\partial^2(\epsilon_0 \vec{E} + \vec{P})}{\partial t^2} = \nabla(\nabla \cdot \vec{E}) - \nabla^2 \vec{E}$$

For the purpose of this report the $\nabla(\nabla \cdot \vec{E})$ term is considered negligible and we arrive at the non-linear wave equation:

$$\nabla^2 \vec{E} - \frac{1}{c^2} \frac{\partial^2}{\partial t^2} \vec{E} = \frac{1}{\epsilon_0 c^2} \frac{\partial^2 \vec{P}}{\partial t^2} \tag{A.1}$$

It is worth noting at this point the extension from the simple wave equation. Both $\vec{E}$ and $\vec{P}$ are potentially infinitely indexed levels of non-linearity while the time dependence of the electrical field can similarly be infinitely comprised of different frequency components.

A.1.2 Difference Frequency Generation

At this point I would like to mention that the polarization states (in this case we have the output wave of difference frequency generation state $\vec{P}_3(\omega_1 - \omega_2)$) all have individual susceptibility tensor coefficients. I have not included an analysis of this because: a) I don't understand it and b) the non-linear susceptibility matrix is important for non-linear optics (which this project is not). Importantly these are given to us for any point symmetry or permutation relation and thus we can if needed look them up. We simply note that in this case:

$$\vec{P}_3 = \tilde{P}_3 e^{-i\omega_3 t} + c.c. = 4\epsilon d_{eff} A_1 A_2^* e^{i((k_1-k_2)z-\omega_3 t)} + c.c. \tag{A.2}$$

Then, as usual we take some plane wave trial solution of the electric field and note that its amplitude does vary spatially along the axis of propagation:

$$\vec{E}_i = A(z)_i e^{i(k_i z-\omega_i t)} + c.c. = \tilde{E}_i(z) e^{-i\omega_i t} + c.c. \tag{A.3}$$

Please note subscripts ($x_{\rightarrow i \leftarrow}$) identify frequency, wave number and signal labels while an inline i is the imaginary number. The $\tilde{E}$ represents the entire spatial information of the field. We note that for the case where the amplitude change is defined only along the z-axis:

$$\begin{aligned}
\nabla^2 \vec{E}_3 &= \frac{\partial^2 E_3}{\partial z^2} \\
&= \frac{\partial}{\partial z}\Big[\Big(\frac{\partial A_3}{\partial z} + ik_3 A_3\Big) e^{i(k_3 z-\omega_3 t)}\Big] \\
&= \Big(\frac{\partial^2 A_3}{\partial z^2} + 2ik_3 \frac{\partial A_3}{\partial z} - k_3^2 A_3\Big) e^{i(k_3 z-\omega_3 t)}
\end{aligned} \tag{A.4}$$

Then, as usual:

$$\frac{1}{c^2}\frac{\partial \vec{E}_3}{\partial t^2} = \frac{\omega_3^2}{c^2}A_3 e^{i(k_3-\omega_3 t)} = -k_3^2 A_3 e^{i(k_3-\omega_3 t)} \tag{A.5}$$

When considering the left hand side of the wave equation we see:

$$\frac{1}{c^2}\frac{\partial^2 \vec{E}_3}{\partial t^2} - \frac{\partial^2 \vec{E}_3}{\partial z^2} = \Big(\frac{\partial^2 A_3}{\partial z^2} + 2ik_3\frac{\partial A_3}{\partial z}\Big)e^{i(k_3 z-\omega_3 t)}$$

We see that as expected we get cancellation of these terms in the usual way. Mathematically on the left hand side we are left with:

$$\frac{\partial^2 A_3}{\partial z^2} + 2ik_3\frac{\partial A_3}{\partial z}$$

In our general case $\vec{P}_3,\ \vec{E}_3 \neq 0$ and using the originally given identity for the polarization in equation A.2:

$$\Big(\frac{\partial^2 A_3}{\partial z^2} + 2ik_3\frac{\partial A_3}{\partial z}\Big)e^{i(k_3 z-\omega_3 t)} = \frac{4\epsilon_0 d_{eff}}{\epsilon_0 c^2}A_1 A_2^* \frac{\partial}{\partial t^2}\Big[e^{i((k_1-k_2)z-\omega_3 t)}\Big] \tag{A.6}$$

Performing the last simple differential and multiplying this entire thing by $e^{-i(k_3 z-\omega t)}$ yields:

$$\frac{\partial^2 A_3}{\partial z^2} + 2ik_3\frac{\partial A_3}{\partial z} = \frac{-4\omega_3^2 d_{eff}}{c^2}A_1 A_2^* e^{i(k_1-k_2-k_3)z} \tag{A.7}$$

This removes all temporal aspects and we use $c = {}^{\omega_i}/_{k_i}$ to get:

$$\frac{\partial^2 A_3}{\partial z^2} + 2ik_3\frac{\partial A_3}{\partial z} = -4k_3^2 d_{eff} A_1 A_2^* e^{i(k_1-k_2-k_3)z} \tag{A.8}$$

A.1.3 Optical Parametric Amplification

We make the approximations here in that $\Delta k = 0$ (perfect phase matching) and that $\partial A_1/\partial z = 0$ (strong pump approximation). We see from the schematic in Figure 1.1 and the equations that if the higher frequency wave is large in amplitude then the rate of change of the amplitude of the two lower frequencies $\omega_2,\ \omega_3$ is positive. This causes them to "amplify" and thus we can consider the case when a high frequency “pump" is treated like an infinite reservoir with which the two lower frequency waves

draw power $\propto |A|^2$. We can then define the $\omega_1 = \text{pump},\ \omega_2 = \text{signal}\ \&\ \omega_3 = \text{idler}$ and think about this as some infinite pump amplifying some small signal and generating an idler at the difference of the frequencies. We can simultaneously treat the coupled equations derived earlier by differentiating again to find:

$$\frac{\partial^2 A_s}{\partial z^2} = 2ik_s d_{eff}\Big[\frac{\partial A_p}{\partial z}A_i^* + \frac{\partial A_i^*}{\partial z}A_p + i\Delta k\Big]e^{i\Delta k z}$$

$$\xRightarrow[\text{strong pump}]{\text{phase match}} 2ik_s d_{eff}A_p\frac{\partial A_i^*}{\partial z} \tag{A.9}$$

Similarly for the idler at ω_3:

$$\frac{\partial^2 A_i}{\partial z^2} = 2ik_i d_{eff}A_p\frac{\partial A_s^*}{\partial z} \tag{A.10}$$

where we already have expressions for the first derivatives (which we must conjugate), which we substitute directly in to find:

$$\frac{\partial^2 A_s}{\partial z^2} = 4k_s k_i d_{eff}^2|A_p|^2 A_s \tag{A.11}$$

$$\frac{\partial^2 A_i}{\partial z^2} = 4k_i k_s d_{eff}^2|A_p|^2 A_i \tag{A.12}$$

The general solution to equation A.12 is:

$$A_s = A\sinh(\kappa z) + B\cosh(\kappa z) \tag{A.13}$$

$$A_i = C\sinh(\kappa z) + D\cosh(\kappa z) \tag{A.14}$$

where:

$$\kappa^2 = 4k_s k_i d_{eff}^2 |A_p|^2 \tag{A.15}$$

We already imposed that the idler is generated therefore at $z = 0$ we have $A_i(0) = 0$ and we choose an arbitrary $A_s(0) = A_{s0}$ and thus we find:

$$A_s(0) = B = A_{s0}$$

$$A_s(z) = A_{s0} \cosh(\kappa z)$$

The idler can then be determined:

$$A_i(0) = 0 = D$$

$$A_i(z) = C \sinh(\kappa z)$$

$$\left.\frac{\partial A_i}{\partial z}\right|_{z=0} = \kappa C \cosh(\kappa 0) = 2i d_{eff} k_s A_p A_{s0}^*$$

$$\implies C = i\sqrt{\frac{k_s}{k_i}} \frac{A_p}{|A_p|} A_{s0}^*$$

$$A_i(z) = i\sqrt{\frac{k_s}{k_i}} \frac{A_p}{|A_p|} A_{s0} \sinh(\kappa z)$$

It is then clear that both the signal and idler will grow in amplitude. This is why the process is also known as parametric amplification as the signal and idler are amplified by the strong pump at a frequency equal to the sum of the signal frequency and idler frequency.

A.2 Josephson Wave Mixing

A.2.1 Yaakobi Wave Equation

Starting with the given Josephson relation:

$$I_{L,n} = I_c \sin\Big(\frac{2\pi\Phi_n}{\Phi_0}\Big)$$

In order to correlate this to something useful, we perform some arbitrary maths and try to find some relationships.

$$\frac{dI_{L,n}}{dt} = \frac{2\pi I_c}{\Phi_0}\cos\Big(\frac{2\pi\Phi_n}{\Phi_0}\Big)\frac{d\Phi_n}{dt}$$

$$\implies V_n \equiv \frac{d\Phi_n}{dt} = \frac{\Phi_0}{2\pi I_c}\cos^{-1}\Big(\frac{2\pi\Phi_n}{\Phi_0}\Big)\frac{dI_{L,n}}{dt}$$

$$= \frac{\Phi_0}{2\pi I_c}\frac{1}{\sqrt{1-\sin^2\Big(\frac{2\pi\Phi_n}{\Phi_0}\Big)}}\frac{dI_{L,n}}{dt}$$

By rearranging the Josephson current phase relationship eq. (1.25), this can then be written:

$$\frac{d\Phi_n}{dt} = \frac{\Phi_0}{2\pi I_c}\frac{1}{\sqrt{1-\Big(\frac{I_{L,n}}{I_c}\Big)^2}}\frac{dI_{L,n}}{dt}$$

We then Taylor expand this to the third order (n=2) to give:

$$\begin{aligned}\frac{d\Phi_n}{dt} &= \frac{\Phi_0}{2\pi I_c}\Big(1+\frac{1}{2}\Big[\frac{I_{L,n}}{I_c}\Big]^2\Big)\frac{dI_{L,n}}{dt}\\ &= \frac{\Phi_0}{2\pi I_c}\frac{dI_{L,n}}{dt} + \frac{\Phi_0}{12\pi I_c^3}\frac{d}{dt}[I_{L,n}]^3\end{aligned} \tag{A.16}$$

A.2.2 Flux Node

From the definition of flux, voltage and he newly introduced "flux node":

$$\begin{aligned} -\frac{d\Phi_n}{dt} &= V_{n+1} - V_n \\ &= \frac{d\Phi_{n+1}}{dt} - \frac{d\Phi_n}{dt} \end{aligned}$$

$$\implies \Phi_n = \Phi_n - \Phi_{n+1}$$

This means that the phase difference $\varphi_n \propto \Phi_n, V_n$ can be related to the difference in what we call node fluxes. Using equations 2.3, 2.4 and 2.4 we get a an equation for the change of the node fluxes:

$$\frac{d\Phi_{n+1}}{dt} - \frac{d\Phi_n}{dt} = -\frac{\Phi_0}{2\pi I_c}\frac{dI_{L,n}}{dt} - \frac{\Phi_0}{12\pi I_c^3}\frac{d}{dt}(I_{L,n}^3) \tag{A.17}$$

By time integrating this equation and considering only oscillatory solutions, we find:

$$\Phi_{n+1} - \Phi_n = -\frac{\Phi_0}{2\pi I_c} I_{L,n} - \frac{\Phi_0}{12\pi I_c^3} I_{L,n}^3$$

$$\implies I_{L,n} = -\frac{2\pi I_c}{\Phi_0}(\Phi_{n+1} - \Phi_n) - \frac{1}{6I_c^2} I_{L,n}^3 \tag{A.18}$$

Yaakobi next introduces the linear inductance of the junction as $L(0) = \frac{\Phi_0}{2\pi I_c}$ which can be inserted into the expression as:

$$I_{L,n} = -\frac{1}{L}\Big((\Phi_{n+1} - \Phi_n) + (\frac{\Phi_0}{12\pi I_c^3} I_{L,n}^3)\Big)$$

$$= -\frac{1}{L}(\Phi_{n+1} - \Phi_n) - \frac{\Phi_0}{12\pi L}\frac{I_{L,n}^3}{I_c^3} \tag{A.19}$$

Then Yaakobi makes the assumption that the fraction $\frac{I_{L,n}}{I_c} \ll 1$, therefore we can make the approximation:

$$I_{L,n} \approx -\frac{1}{L}(\Phi_{n+1} - \Phi_n) \tag{A.20}$$

This is an approximation, but we input equation A.20 into the cubic term in equation A.19 to find:

$$I_{L,n} \approx -\frac{1}{L}(\Phi_{n+1} - \Phi_n) + \frac{\Phi_0}{12\pi L^4 I_c^3}(\Phi_{n+1} - \Phi_n)^3 \tag{A.21}$$

A.2.3 Yaakobi Total Current

We can rewrite equation 2.1 using equations; 2.2, 2.5 and 2.6 to find:

$$\begin{aligned}
0 = {} & C_n\frac{dV_n}{dt} + \frac{V_n}{R_n} \\
& - C_J\frac{d}{dt}\Big[V_{n+1} - V_n\Big] + C_J\frac{d}{dt}\Big[V_n - V_{n-1}\Big] \\
& - \Big(\frac{1}{L}(\Phi_{n+1} - \Phi_n) - \frac{\Phi_0}{12\pi L^4 I_c^3}(\Phi_{n+1} - \Phi_n)^3\Big) - \Big(\frac{1}{L}(\Phi_n - \Phi_{n-1}) - \frac{\Phi_0}{12\pi L^4 I_c^3}(\Phi_n - \Phi_{n-1})^3\Big)
\end{aligned}$$

We can collect like terms:

$$\begin{aligned}
0 = {} & C_n\frac{dV_n}{dt} + \frac{V_n}{R_n} - C_J\frac{d}{dt}\Big[V_{n+1} + V_{n-1} - 2V_n\Big] \\
& - \frac{1}{L}(\Phi_{n+1} + \Phi_{n-1} + 2\Phi_n) - \frac{\Phi_0}{12\pi L^4 I_c^3}\Big((\Phi_{n+1} - \Phi_n)^3 - (\Phi_n - \Phi_{n-1})^3\Big)
\end{aligned}$$

We then note the definition of the flux nodes in equation 2.4 to get:

$$\begin{aligned}
0 = {} & C_n\frac{d^2\Phi_n}{dt^2} + \frac{1}{R_n}\frac{d\Phi_n}{dt} - C_J\frac{d^2}{dt^2}\Big[\Phi_{n+1} + \Phi_{n-1} - 2\Phi_n\Big] \\
& - \frac{1}{L}(\Phi_{n+1} + \Phi_{n-1} + 2\Phi_n) - \frac{\Phi_0}{12\pi L^4 I_c^3}\Big((\Phi_{n+1} - \Phi_n)^3 - (\Phi_n - \Phi_{n-1})^3\Big)
\end{aligned} \tag{A.22}$$

A.2.4 Zorin Wave Equation

To find this inductance, first add the inductance's in parallel of the Josephson Junction and the geometric inductance. Thus, we find the total inductance (L_T):

$$\frac{1}{L_T} = \frac{1}{L_g} + \frac{1}{L_j} \tag{A.23}$$

where L_{J} is given by equation eq. (1.27), combining with the definition of the screening SQUID parameter $\beta_L = \frac{2\pi L_g I_c}{\Phi_0}$, and thus, the total inductance around the SQUID loop is:

$$\frac{1}{L_T} = \frac{1}{L_g}(1 + \beta_L \cos(\varphi_{DC})) \tag{A.24}$$

$$\implies \frac{L_g}{\beta_L L_T} = \frac{1}{\beta_L} + \cos(\varphi_{DC}) \tag{A.25}$$

One can expand Equation (1.32) about a small AC fluctuation to find,

$$I(\varphi_{\mathrm{AC}}) = \frac{I_{\mathrm{c}}}{\beta_{\mathrm{L}}}\varphi_{\mathrm{AC}} + I_{\mathrm{c}}\Big[\sin(\varphi_{\mathrm{DC}} + \varphi_{\mathrm{AC}}) - \sin(\varphi_{\mathrm{DC}})\Big]$$

$$= \frac{I_c\varphi_{AC}}{\beta_L} + I_c\Big[\cos(\varphi_{DC})\Big(\varphi_{AC} - \frac{\varphi_{AC}^3}{6} + ...\Big) + \sin(\varphi_{DC})\Big(1 - \frac{\varphi_{AC}^2}{2} + ...\Big) - \sin(\varphi_{DC})\Big]$$

$$\approx I_c\Big[\Big(\frac{1}{\beta_L} + \cos(\varphi_{DC})\Big)\varphi_{AC} - \frac{\cos(\varphi_{DC})}{6}\varphi_{AC}^3 - \frac{\sin(\varphi_{DC})}{2}\varphi_{AC}^2\Big]. \tag{A.26}$$

We introduce the constants; $\tilde{\beta} = \frac{1}{2}\sin(\varphi_{DC})$, $\tilde{\gamma} = \frac{1}{6}\cos(\varphi_{DC})$. Then we equate this inductive rf SQUID element to what Yaakobi calls $I_{L,n}$, i.e. $I(\varphi_{\mathrm{AC}}) \to I_{L,n}$ and $\varphi_{\mathrm{AC}} \to 2\pi\Phi/\Phi_0$using the above we get:

$$I_{L,n} = I_c\Big[\Big(\frac{1}{\beta_L} + \cos(\varphi_{DC})\Big)\frac{2\pi}{\Phi_0}(\Phi_{n+1} - \Phi_n) - \tilde{\beta}\frac{4\pi^2}{\Phi_0^2}(\Phi_{n+1} - \Phi_n)^2 - \tilde{\gamma}\frac{8\pi^3}{\Phi_0^3}(\Phi_{n+1} - \Phi_n)^3\Big] \tag{A.27}$$

Then, the total current through each unit cell (I_n) is,

$$\begin{aligned}
I_n &= I_{L,n} + I_{C_J,n}, \\
&= I_c\Big[\Big(\frac{1}{\beta_L} + \cos(\varphi_{DC})\Big)\frac{2\pi}{\Phi_0}(\Phi_{n+1} - \Phi_n) - \tilde{\beta}\frac{4\pi^2}{\Phi_0^2}(\Phi_{n+1} - \Phi_n)^2 \\
&- \tilde{\gamma}\frac{8\pi^3}{\Phi_0^3}(\Phi_{n+1} - \Phi_n)^3\Big] - C_j\frac{d}{dt}[V_{n+1} - V_n], \\
&= I_c\Big[\Big(\frac{1}{\beta_L} + \cos(\varphi_{DC})\Big)\frac{2\pi}{\Phi_0}(\Phi_{n+1} - \Phi_n) - \tilde{\beta}\frac{4\pi^2}{\Phi_0^2}(\Phi_{n+1} - \Phi_n)^2 \\
&- \tilde{\gamma}\frac{8\pi^3}{\Phi_0^3}(\Phi_{n+1} - \Phi_n)^3\Big] - C_j\frac{d}{dt}[\frac{d\Phi_{n+1}}{dt} - \frac{d\Phi_n}{dt}] \\
&= I_c\Big[\Big(\frac{1}{\beta_L} + \cos(\varphi_{DC})\Big)\frac{2\pi}{\Phi_0}(\Phi_{n+1} - \Phi_n) - \tilde{\beta}\frac{4\pi^2}{\Phi_0^2}(\Phi_{n+1} - \Phi_n)^2 \\
&- \tilde{\gamma}\frac{8\pi^3}{\Phi_0^3}(\Phi_{n+1} - \Phi_n)^3\Big] - C_{\mathrm{J}}\frac{d^2}{dt^2}[\Phi_{n+1} - \Phi_n]
\end{aligned} \tag{A.28}$$

We do the same as Yaakobi and simply use I_n to find I_{n-1},

$$\begin{aligned}
I_n - I_{n-1} &= I_c\Big[\Big(\frac{1}{\beta_L} + \cos(\varphi_{DC})\Big)\frac{2\pi}{\Phi_0}(\Phi_{n+1} - \Phi_n) - \tilde{\beta}\frac{4\pi^2}{\Phi_0^2}(\Phi_{n+1} - \Phi_n)^2 \\
&- \tilde{\gamma}\frac{8\pi^3}{\Phi_0^3}(\Phi_{n+1} - \Phi_n)^3\Big] - C_j\frac{d^2}{dt^2}[\Phi_{n+1} - \Phi_n] \\
&- I_c\Big[\Big(\frac{1}{\beta_L} + \cos(\varphi_{DC})\Big)\frac{2\pi}{\Phi_0}(\Phi_n - \Phi_{n-1}) - \tilde{\beta}\frac{4\pi^2}{\Phi_0^2}(\Phi_n - \Phi_{n-1})^2 \\
&- \tilde{\gamma}\frac{8\pi^3}{\Phi_0^3}(\Phi_n - \Phi_{n-1})^3\Big] + C_j\frac{d^2}{dt^2}[\Phi_n - \Phi_{n-1}] \\
&= I_c\Big[\Big(\frac{1}{\beta_L} + \cos(\varphi_{DC})\Big)\frac{2\pi}{\Phi_0}(\Phi_{n+1} + \Phi_{n-1} - 2\Phi_n) \\
&- \tilde{\beta}\frac{4\pi^2}{\Phi_0^2}((\Phi_{n+1} - \Phi_n)^2 - (\Phi_n - \Phi_{n-1})^2) \\
&- \tilde{\gamma}\frac{8\pi^3}{\Phi_0^3}((\Phi_{n+1} - \Phi_n)^3 - (\Phi_n - \Phi_{n-1})^3) \\
&- C_j\frac{d^2}{dt^2}(\Phi_{n+1} + \Phi_{n-1} - 2\Phi_n)\Big]
\end{aligned} \tag{A.29}$$

The result of the continuum method for the first third and fourth term are given in the main text, however, we now have a new quadratic term which we expand in the same way using equations 2.11

and 2.12

$$(A+B)^2-(A-B)^2=4AB=2a^3\frac{\partial\Phi}{\partial\tilde{x}}\frac{\partial^2\Phi}{\partial\tilde{x}^2} \tag{A.30}$$

Also, in the first term we have exactly equation A.25 which we substitute in to find:

$$\begin{aligned} I_n-I_{n-1}=I_c\Big[&\Big(\frac{L_g}{\beta_L L_T}\Big)\frac{2\pi}{\Phi_0}a^2\frac{\partial^2\Phi}{\partial\tilde{x}^2}\\ &-\tilde{\beta}\frac{4\pi^2}{\Phi_0^2}2a^3\frac{\partial\Phi}{\partial\tilde{x}}\frac{\partial^2\Phi}{\partial\tilde{x}^2}\\ &-\tilde{\gamma}\frac{8\pi^3}{\Phi_0^3}3a^4\Big(\frac{\partial\Phi}{\partial\tilde{x}}\Big)^2\frac{\partial^2\Phi}{\partial\tilde{x}^2}\\ &-C_{\mathrm{J}}\frac{\partial^2}{\partial t^2}\Big[\frac{\partial^2\Phi}{\partial\tilde{x}^2}\Big]\Big] \end{aligned} \tag{A.31}$$

Remembering that $\Phi=\Phi_0\varphi_{\mathrm{AC}}/2\pi$ and $x=\tilde{x}/a$ we obtain,

$$I_n-I_{n-1}=\frac{I_cL_g}{\beta_L L_T}\frac{\partial^2\varphi_{AC}}{\partial x^2}-I_c\tilde{\beta}\frac{\partial}{\partial x}\Big[\Big(\frac{\partial\varphi_{AC}}{\partial x}\Big)^2\Big]-I_c\tilde{\gamma}\frac{\partial}{\partial x}\Big[\Big(\frac{\partial\varphi_{AC}}{\partial x}\Big)^3\Big]-\frac{\Phi_0C_j}{2\pi}\frac{\partial^4\varphi_{AC}}{\partial x^2\partial t^2}$$

We then add back in the ground capacitor which sets the equation to zero as per current conservation,

$$\begin{aligned} 0&=I_n-I_{n-1}+I_{C_0}\\ &=\frac{I_cL_g}{\beta_L L_T}\frac{\partial^2\varphi_{AC}}{\partial x^2}-I_c\tilde{\beta}\frac{\partial}{\partial x}\Big[\Big(\frac{\partial\varphi_{AC}}{\partial x}\Big)^2\Big]-I_c\tilde{\gamma}\frac{\partial}{\partial x}\Big[\Big(\frac{\partial\varphi_{AC}}{\partial x}\Big)^3\Big]\\ &-\frac{\Phi_0C_{\mathrm{J}}}{2\pi}\frac{\partial^4\varphi_{AC}}{\partial x^2\partial t^2}+\frac{\Phi_0C_0}{2\pi}\frac{\partial^2\varphi_{AC}}{\partial t^2} \end{aligned}$$

We multiply by $\frac{2\pi L_T}{\Phi_0}$ and use the definition of β_L to get: (*N.B* $\tilde{\beta}\to\beta,\tilde{\gamma}\to\gamma$). We define the junction plasma frequency $\omega_{\mathrm{J}}=\frac{1}{\sqrt{L_TC_j}}$ and the grounded capacitor cut off frequency $\omega_0=\frac{1}{\sqrt{L_TC_0}}$. Also for rf SQUIDS with junctions of critical currents of order $I_{\mathrm{c}}\sim\mu\mathrm{A}$, and geometric inductance of order $L_{\mathrm{g}}\sim\mathrm{pH}$, $L_{\mathrm{T}}\approx L_{\mathrm{g}}$

$$\frac{\partial^2 \varphi_{AC}}{\partial x^2} - \beta \frac{\partial}{\partial x}\Big[\Big(\frac{\partial \varphi_{AC}}{\partial x}\Big)^2\Big] - \gamma \frac{\partial}{\partial x}\Big[\Big(\frac{\partial \varphi_{AC}}{\partial x}\Big)^3\Big] - \omega_{\mathrm{J}}^{-2} \frac{\partial^4 \varphi_{AC}}{\partial x^2 \partial t^2} + \omega_0^{-2} \frac{\partial^2 \varphi_{AC}}{\partial t^2} = 0 \tag{A.32}$$

A.2.5 rf SQUID Embedded TWPA Reduced Wave Equation

To simply derive the governing differential equation we can look at one mode,

$$\phi = \frac{1}{2}\Big[A(x)e^{i(kx-\omega t)} + A^*(x)e^{-i(kx-\omega t)}\Big]. \tag{A.33}$$

We assume a slow varying pump: $d^2A/dx^2 \ll k\ dA/dx \ll k^2\, A$ and thus neglect any second derivative terms. We also include the complex conjugate notation +c.c. to denote the complex conjugate:

$$\frac{\partial^2 \phi}{\partial x^2} = \frac{1}{2}\Big[2ik\frac{dA}{dx}e^{i(kx-\omega t)} - k^2 A e^{i(kx-\omega t)} + \text{c.c.}\Big]$$

$$= \Big[ik\frac{dA}{dx}e^{i(kx-\omega t)} + \text{c.c.}\Big] - k^2\phi$$

Then because the amplitude depends only on position,

$$\frac{\partial^2 \phi}{\partial t^2} = -\frac{\omega^2}{2}\Big[Ae^{i(kx-\omega t)} + \text{c.c.}\Big] = -\omega^2\phi,$$

combining these results allows us to simply state,

$$\frac{\partial^4 \phi}{\partial x^2 \partial t^2} = \frac{\omega^2}{2}\Big[k^2 A e^{i(kx-\omega t)} - 2ik\frac{dA}{dx}e^{i(kx-\omega t)} + \text{c.c.}\Big]$$

$$= \omega^2 k^2 \phi - \omega^2\Big[ik\frac{dA}{dx}e^{i(kx-\omega t)} + \text{c.c.}\Big].$$

Inserting these into the super-linear eq. (2.18) gives the linear section,

$$\Big[ik\frac{dA}{dx}e^{i(kx-\omega t)}+\text{c.c.}\Big]\underbrace{-k^2\phi+\frac{\omega^2}{\omega_0^2}\phi+\frac{\omega^2k^2}{\omega_j^2}\phi}_{=0}-\frac{\omega^2}{\omega_j^2}\Big[ik\frac{dA}{dx}e^{i(kx-\omega t)}+\text{c.c.}\Big]$$

$$=ik\Big(1-\frac{\omega^2}{\omega_j^2}\Big)\Big[\frac{dA}{dx}e^{i(kx-\omega t)}+\text{c.c.}\Big]$$

Where we have used the previously found dispersion relation in eq. (2.19) to eliminate the middle three terms. Here we can consider frequencies much below the plasma frequency such that $\omega^2/\omega_\text{J}^2 \approx 0$. Then the full wave equation eq. (2.17) is reduced to,

$$ik\frac{dA}{dx}+c.c.=\beta\frac{d}{dx}\Big[\Big(\frac{\partial\phi}{\partial x}\Big)^2\Big]+\gamma\frac{d}{dx}\Big[\Big(\frac{\partial\phi}{\partial x}\Big)^3\Big]. \tag{A.34}$$

A.2.6 Generating CMEs from the Wave Equation

By setting $\gamma = 0$ the reduced wave equation becomes,

$$ik\frac{dA}{dx}+c.c.=\beta\frac{d}{dx}\Big[\Big(\frac{\partial\phi}{\partial x}\Big)^2\Big]. \tag{A.35}$$

Then by considering the case where ϕ_m is constructed of tones $m = p,\ s,\ i$,

$$\phi=\frac{1}{2}\begin{pmatrix} A_ie^{i(k_ix-\omega_it)}+A_i^*e^{-i(k_ix-\omega_it)} \\ A_se^{i(k_sx-\omega_st)}+A_s^*e^{-i(k_sx-\omega_st)} \\ A_pe^{i(k_px-\omega_pt)}+A_p^*e^{-i(k_px-\omega_pt)} \end{pmatrix}. \tag{A.36}$$

Thus,

$$\frac{\partial \phi}{\partial x} = \begin{pmatrix} ik_i A_i e^{i(k_i x-\omega_i t)} - ik_i A_i^* e^{-i(k_i x-\omega_i t)} + \dfrac{\partial A_i}{\partial x} e^{i(k_i x-\omega_i t)} + \dfrac{\partial A_i^*}{\partial x} e^{-i(k_i x-\omega_i t)} \\ ik_s A_s e^{i(k_s x-\omega_s t)} - ik_s A_s^* e^{-i(k_s x-\omega_s t)} + \dfrac{\partial A_s}{\partial x} e^{i(k_s x-\omega_s t)} + \dfrac{\partial A_s^*}{\partial x} e^{-i(k_s x-\omega_s t)} \\ ik_p A_p e^{i(k_p x-\omega_p t)} - ik_p A_p^* e^{-i(k_p x-\omega_p t)} + \dfrac{\partial A_p}{\partial x} e^{i(k_p x-\omega_p t)} + \dfrac{\partial A_p^*}{\partial x} e^{-i(k_p x-\omega_p t)} \end{pmatrix},$$

Again under the assumption $\dfrac{\partial A_m}{\partial x} \ll k_m A_m$ the derivative terms can be neglected,

$$\begin{aligned} \left(\frac{\partial \phi}{\partial x}\right)^2 \Bigg|_{\frac{\partial A}{\partial x}\to 0} = \frac{1}{4}\Bigg(& - k_i^2 A_i^2 e^{2i(k_i x-\omega_i t)} + 2k_i^2 |A_i|^2 - 2k_i k_s A_i A_s e^{i((k_i+k_s)x-(\omega_i+\omega_s)t)} \\ & + 2k_i k_s A_i A_s^* e^{i((k_i-k_s)x-(\omega_i-\omega_s)t)} - 2k_i k_p A_i A_p e^{i(k_i+k_p)x-(\omega_i+\omega_p)t} \\ & + 2k_i k_p A_i A_p^* e^{i(k_i-k_p)x-(\omega_i-\omega_p)t} - k_i^2 A_i^{*2} e^{-2i(k_i x-\omega_i t)} \\ & + 2k_i k_s A_i^* A_s e^{-i((k_i-k_s)x-(\omega_i-\omega_s)t)} - 2k_i k_s A_i^* A_s^* e^{-i((k_i+k_s)x-(\omega_i+\omega_s)t)} \\ & + 2k_i k_p A_i^* A_p e^{-i((k_i-k_p)x-(\omega_i-\omega_p)t)} - 2k_i k_p A_i^* A_p^* e^{-i((k_i+k_p)x-(\omega_i+\omega_p)t)} \\ & - k_s^2 A_s^2 e^{2i(k_s x-\omega_s t)} + 2k_s^2 |A_s|^2 - 2k_s k_p A_s A_p e^{i(k_s+k_p)x-(\omega_s+\omega_p)t} \\ & + 2k_s k_p A_s A_p^* e^{i(k_s-k_p)x-(\omega_s-\omega_p)t} - k_s^2 A_s^{*2} e^{-2i(k_i x-\omega_i t)} \\ & + 2k_s k_p A_s^* A_p e^{-i((k_s-k_p)x-(\omega_s-\omega_p)t)} - 2k_s k_p A_s^* A_p^* e^{-i((k_s+k_p)x-(\omega_s+\omega_p)t)} \\ & - k_p^2 A_p^2 e^{2i(k_p x-\omega_p t)} + 2k_p^2 |A_p|^2 - k_p^2 A_p^2 e^{2i(k_p x-\omega_p t)} \Bigg). \end{aligned}$$

There are 6 DC offset terms, known as optical rectification $\propto k_n^2|A_n|^2e^0$. There is also a complex symmetry where each term has a corresponding conjugate term collecting these we find,

$$\left(\frac{\partial\phi}{\partial x}\right)^2\Bigg|_{\frac{\partial A}{\partial x}\to 0} = \frac{1}{4}\Bigg(- k_i^2A_i^2e^{2i(k_ix-\omega_it)} - 2k_ik_sA_iA_se^{i((k_i+k_s)x-(\omega_i+\omega_s)t)}$$

$$- 2k_ik_pA_iA_pe^{i(k_i+k_p)x-(\omega_i+\omega_p)t} + 2k_sk_iA_sA_i^*e^{i((k_s-k_i)x-(\omega_s-\omega_i)t)}$$

$$- k_s^2A_s^2e^{2i(k_sx-\omega_st)} - 2k_sk_pA_sA_pe^{i(k_s+k_p)x-(\omega_s+\omega_p)t}$$

$$+ 2k_pk_sA_pA_s^*e^{i((k_p-k_s)x-(\omega_p-\omega_s)t)} - k_p^2A_p^2e^{2i(k_px-\omega_pt)}$$

$$+ 2k_pk_iA_pA_i^*e^{i((k_p-k_i)x-(\omega_p-\omega_i)t)} + c.c. + DC_{offset}\Bigg).$$

By considering only the terms with frequencies which correspond back to the original ϕ_m tones and inserting into eq. (2.21) we get,

$$ik_i\frac{dA_i}{dx}e^{i(k_ix-\omega_it)} = -\frac{\beta}{2}\frac{d}{dx}\left[k_pk_sA_pA_s^*e^{i((k_p-k_s)x-(\omega_i)t)}\right] \tag{A.37}$$

$$ik_s\frac{dA_s}{dx}e^{i(k_sx-\omega_st)} = -\frac{\beta}{2}\frac{d}{dx}\left[k_pk_iA_pA_i^*e^{i((k_p-k_i)x-(\omega_s)t)}\right] \tag{A.38}$$

$$ik_p \frac{dA_p}{dx} e^{i(k_p x - \omega_p t)} = \frac{\beta}{2} \frac{d}{dx} \left[k_s k_i A_s A_i^* e^{i((k_s + k_i)x - (\omega_p)t)} \right]. \tag{A.39}$$

Again neglecting the amplitude derivatives on the right side,

$$ik_i \frac{dA_i}{dx} e^{i(k_i x - \omega_i t)} = -\frac{\beta}{2} i(k_p - k_s) \left[k_p k_s A_p A_s^* e^{i((k_p - k_s)x - (\omega_i)t)} \right] \tag{A.40}$$

$$ik_s \frac{dA_s}{dx} e^{i(k_s x - \omega_s t)} = -\frac{\beta}{2} i(k_p - k_i) \left[k_p k_i A_p A_i^* e^{i((k_p - k_i)x - (\omega_s)t)} \right] \tag{A.41}$$

$$ik_p \frac{dA_p}{dx} e^{i(k_p x - \omega_p t)} = \frac{\beta}{2} i(k_s + k_i) \left[k_s k_i A_s A_i^* e^{i((k_s + k_i)x - (\omega_p)t)} \right]. \tag{A.42}$$

Where we can assume a small phase mismatch $k_\mathrm{p} \approx k_\mathrm{s} + k_\mathrm{i}$,

$$\frac{dA_i}{dx} e^{i(k_i x - \omega_i t)} = -\frac{\beta}{2} \left[k_p k_s A_p A_s^* e^{i((k_p - k_s)x - (\omega_i)t)} \right] \tag{A.43}$$

$$\frac{dA_s}{dx} e^{i(k_s x - \omega_s t)} = -\frac{\beta}{2} \left[k_p k_i A_p A_i^* e^{i((k_p - k_i)x - (\omega_s)t)} \right] \tag{A.44}$$

$$\frac{dA_p}{dx} e^{i(k_p x - \omega_p t)} = \frac{\beta}{2} \left[k_s k_i A_s A_i e^{i((k_s + k_i)x - (\omega_p)t)} \right]. \tag{A.45}$$

As an aside, the following methodology can be used but in the case where $\gamma \neq 0$ and one arrives at the CMEs given in appendix A.2.4,

$$\frac{dA_p}{dx} = i\frac{3}{8}\gamma k_p^3 A_p |A_p|^2 - \frac{\beta}{2} k_s k_i A_s A_i e^{-i\Delta k x}, \tag{A.46}$$

$$\frac{dA_s}{dx} = i\frac{3}{4}\gamma k_s k_p^2 A_s |A_p|^2 + \frac{\beta}{2} k_i k_p A_i^* A_p e^{i\Delta k x}, \tag{A.47}$$

$$\frac{dA_i}{dx} = i\frac{3}{4}\gamma k_i k_p^2 A_i |A_p|^2 + \frac{\beta}{2} k_s k_p A_s^* A_p e^{i\Delta k x}, \tag{A.48}$$

where $\Delta k = k_\mathrm{s} + k_\mathrm{i} - k_\mathrm{p}$.

Appendix B

Simulations

B.1 RCSJ Matlab Script

```
clear

hbar = 1.0545718e-34;
e = 1.60217662e-19;
phi0 = 2.067e-15;

R = 1.42; %Rn (Normal state resistance)
R=70; %R must be such that the voltage ~ (hbar*wrf/2e) and Idc meet
R=23.8747;
%R=0;


Ic = 5e-6;
Irf = Ic/2;%Check what happens at large rf current (amplitude)
Irf=0;%Comment out for shapiro steps

Lj=phi0/(2*pi*Ic);
Cj=300e-15; % cant set this to zero currently
```

```
19 wj=1/sqrt(Lj*Cj);
20 fj=wj/(2*pi);
21
22 frf = 0.5*fj; %Link this to the voltage for shapiro steps later
23 wrf=2*pi*frf;
24
25 betaC=2*pi*Ic*(R^2)*Cj/phi0; %This should be less than 1
26
27 syms y(t)
28
29 Idcmax=4*Ic;
30 i=1;
31 for Idc=linspace(-Idcmax,Idcmax,101)
32
33     if R==0
34         eqn = (Cj*phi0/(2*pi))*diff(y,2) + Ic*sin(y)==Idc + Irf*sin
              (wrf*t);
35     else
36         eqn = (Cj*phi0/(2*pi))*diff(y,2) + (phi0/(2*pi*R))*diff(y
              ,1) + Ic*sin(y)==Idc + Irf*sin(wrf*t);
37     end
38     V = odeToVectorField(eqn);
39     M = matlabFunction(V,'vars',{'t','Y'});
40
41
42     tspan=linspace(0,20*(2*pi*sqrt(Lj*Cj)),5000);
43     [tplot,yplot]=ode45(M,tspan,[0 0]);
44     Vt=(hbar/(2*e)).*yplot(:,2);
45     Vplot(i)=(hbar/(2*e)).*trapz(yplot(:,2))./length(yplot(:,2));
```

```
46        I(i)=Idc;
47        figure(1)
48        plot(tspan,yplot(:,1))
49        drawnow
50        i=i+1;
51    end
52
53    figure(2)
54    plot(I.*1e6,Vplot.*1e3,'r-','LineWidth',3)
55    xlabel('$I_{\mathrm{dc}}$ [$\mu~\mathrm{A}$]','Interpreter','latex'
          )
56    ylabel('$V_{\mathrm{JJ}}$ [mV]','Interpreter','latex')
57    ax=gca;
58    ax.FontSize=22;
```

B.2 WRspice Netlist

The WRspice netlist is a list of circuit elements which is then parsed to the WRspice program via MATLAB. The .txt file is generated programatically to allow for iterative unit cells to be quickly written to the .txt file. The junction model is defined on line 3 to have zero shunt resistance, a critical current $I_c = 5\ \mu$A, and a junction capacitance $C_J = 60$ fF. The pump and signal current sources are then defined on lines $4,\ 5$ with the phase offset, amplitude, frequency, time delay respectively. Next we define the front end resistor with ammeters either side on lines $7,\ 6,\ 8$. This is then followed by a long list of the rf SQUID array. Following the rf SQUID netlist we include the termination resistor. This defines the circuit however the bottom 4 lines also describe some simulation parameters. The time step is controlled by the "`.tran`" line, where the time step $dt = 1$ ps, total time $t_{tot} = 30$ ns, wait time $t_{delay} = 0$ are defined. The time vector can also be returned from the simulation which aids in the Fourier analysis. The `uic` condition tells the simulator to use any initial conditions provided which in this example are not given. We also set the `maxdata` property to `8e8` as many timesteps on many nodes can produce a lot of data.

```
*** Zorin model 3WM JTWPA ***

.model jj0 jj(rtype=0, icrit=5.0000uA, cap=60.0000fF)
Ip 0 1 sin(0 5.7800uA 12.0000GHz 9ns 0 0)
Is 0 1 sin(0 0.3400uA 7.2000GHz 9ns 0 0)
Vmeas0 1 2 0V
Rtermfront 2 0 23.8747Ohm
Vmeas1 2 3 0V

***RF SQUID TRANS LINE ***
*Flux Biased Rf SQUID cell
Idc2 0 50002 pwl(0 0uA 5ns 14.0680uA)
Lflux2 50002 0 57.0000pH
K2 Lg2 Lflux2 1
Cg2 3 0 50.0000fF
Lg2 3 4 57.0000pH
B2 3 4 10001 jj0
Cgg2 4 0 50.0000fF
Vmeas2 4 5 0V
:::
:::
:::

*Flux Biased Rf SQUID cell
Idc501 0 50501 pwl(0 0uA 5ns 14.0680uA)
Lflux501 50501 0 57.0000pH
K501 Lg501 Lflux501 1
Cg501 1001 0 50.0000fF
Lg501 1001 1002 57.0000pH
B501 1001 1002 10500 jj0
Cgg501 1002 0 50.0000fF
Vmeas501 1002 1003 0V

Rtermend 1003 0 23.8747Ohm

.tran 1p 30n 0n uic
.control
set maxdata = 8e8
run
```

Figure B.1: WRspice circuit file for the JTWPA. The current is measured through all of the `Vmeas` branches, where `Vmeas0` is the source current, `Vmeas1` is the input current, `Vmeas501` is the output of the device and all other `Vmeas#` branches are inspected to see the propagation of tones inside the device.

Appendix C

Extended Theory CME-5

C.1 Extension to CME-5

The full list of tones included in CME-5 is shown in table 5.1. We show below in detail all of the terms included in the coupled mode equation forming CME-5.

$$\begin{aligned}\frac{dA_{\mathrm{i}}}{dx} = \frac{\beta}{2}\Big(&k_{\mathrm{s}}k_{\mathrm{p}}A_{\mathrm{p}}A_{\mathrm{s}}^{*}e^{i(k_{\mathrm{p}}-k_{\mathrm{s}})x} + k_{\mathrm{p+i}}k_{\mathrm{p}}A_{\mathrm{p+i}}A_{\mathrm{p}}^{*}e^{i(k_{\mathrm{p+i}}-k_{\mathrm{p}})x} \\ &+ k_{2\mathrm{p}}k_{\mathrm{p+s}}A_{2\mathrm{p}}A_{\mathrm{p+s}}^{*}e^{i(k_{2\mathrm{p}}-k_{\mathrm{p+s}})x} + k_{2\mathrm{p+i}}k_{2\mathrm{p}}A_{2\mathrm{p+i}}A_{2\mathrm{p}}^{*}e^{i(k_{2\mathrm{p+i}}-k_{2\mathrm{p}})x} \\ &+ k_{3\mathrm{p}}k_{2\mathrm{p+s}}A_{3\mathrm{p}}A_{2\mathrm{p+s}}^{*}e^{i(k_{3\mathrm{p}}-k_{2\mathrm{p+s}})x} + k_{3\mathrm{p+i}}k_{3\mathrm{p}}A_{3\mathrm{p+i}}A_{3\mathrm{p}}^{*}e^{i(k_{3\mathrm{p+i}}-k_{3\mathrm{p}})x} \\ &+ k_{4\mathrm{p}}k_{3\mathrm{p+s}}A_{4\mathrm{p}}A_{3\mathrm{p+s}}^{*}e^{i(k_{4\mathrm{p}}-k_{3\mathrm{p+s}})x} + k_{4\mathrm{p+i}}k_{4\mathrm{p}}A_{4\mathrm{p+i}}A_{4\mathrm{p}}^{*}e^{i(k_{4\mathrm{p+i}}-k_{4\mathrm{p}})x} \\ &+ k_{5\mathrm{p}}k_{4\mathrm{p+s}}A_{5\mathrm{p}}A_{4\mathrm{p+s}}^{*}e^{i(k_{5\mathrm{p}}-k_{4\mathrm{p+s}})x}\Big)e^{-ik_{\mathrm{i}}x}\end{aligned} \tag{C.1}$$

$$\begin{aligned}\frac{dA_{\mathrm{s}}}{dx} = \frac{\beta}{2}\Big(&k_{\mathrm{i}}k_{\mathrm{p}}A_{\mathrm{p}}A_{\mathrm{i}}^{*}e^{i(k_{\mathrm{p}}-k_{\mathrm{i}})x} + k_{\mathrm{p+s}}k_{\mathrm{p}}A_{\mathrm{p+s}}A_{\mathrm{p}}^{*}e^{i(k_{\mathrm{p+s}}-k_{\mathrm{p}})x} \\ &+ k_{2\mathrm{p}}k_{\mathrm{p+i}}A_{2\mathrm{p}}A_{\mathrm{p+i}}^{*}e^{i(k_{2\mathrm{p}}-k_{\mathrm{p+i}})x} + k_{2\mathrm{p+s}}k_{2\mathrm{p}}A_{2\mathrm{p+s}}A_{2\mathrm{p}}^{*}e^{i(k_{2\mathrm{p+s}}-k_{2\mathrm{p}})x} \\ &+ k_{3\mathrm{p}}k_{2\mathrm{p+i}}A_{3\mathrm{p}}A_{2\mathrm{p+i}}^{*}e^{i(k_{3\mathrm{p}}-k_{2\mathrm{p+i}})x} + k_{3\mathrm{p+s}}k_{3\mathrm{p}}A_{3\mathrm{p+s}}A_{3\mathrm{p}}^{*}e^{i(k_{3\mathrm{p+s}}-k_{3\mathrm{p}})x} \\ &+ k_{4\mathrm{p}}k_{3\mathrm{p+i}}A_{4\mathrm{p}}A_{3\mathrm{p+i}}^{*}e^{i(k_{4\mathrm{p}}-k_{3\mathrm{p+i}})x} + k_{4\mathrm{p+s}}k_{4\mathrm{p}}A_{4\mathrm{p+s}}A_{4\mathrm{p}}^{*}e^{i(k_{4\mathrm{p+s}}-k_{4\mathrm{p}})x} \\ &+ k_{5\mathrm{p}}k_{4\mathrm{p+i}}A_{5\mathrm{p}}A_{4\mathrm{p+i}}^{*}e^{i(k_{5\mathrm{p}}-k_{4\mathrm{p+i}})x}\Big)e^{-ik_{\mathrm{s}}x}\end{aligned} \tag{C.2}$$

$$\frac{dA_{\mathrm{p}}}{dx} = \frac{\beta}{2}\Big(- k_{\mathrm{i}}k_{\mathrm{s}}A_{\mathrm{i}}A_{\mathrm{s}}e^{i(k_{\mathrm{i}}+k_{\mathrm{s}})x} + k_{\mathrm{p+i}}k_{\mathrm{i}}A_{\mathrm{p+i}}A_{\mathrm{i}}^{*}e^{i(k_{\mathrm{p+i}}-k_{\mathrm{i}})x} + k_{\mathrm{p+s}}k_{\mathrm{s}}A_{\mathrm{p+s}}A_{\mathrm{s}}^{*}e^{i(k_{\mathrm{p+s}}-k_{\mathrm{s}})x} + k_{2\mathrm{p}}k_{\mathrm{p}}A_{2\mathrm{p}}A_{\mathrm{p}}^{*}e^{i(k_{2\mathrm{p}}-k_{\mathrm{p}})x} + k_{2\mathrm{p+i}}k_{\mathrm{p+i}}A_{2\mathrm{p+i}}A_{\mathrm{p+i}}^{*}e^{i(k_{2\mathrm{p+i}}-k_{\mathrm{p+i}})x} + k_{2\mathrm{p+s}}k_{\mathrm{p+s}}A_{2\mathrm{p+s}}A_{\mathrm{p+s}}^{*}e^{i(k_{2\mathrm{p+s}}-k_{\mathrm{p+s}})x} + k_{3\mathrm{p}}k_{2\mathrm{p}}A_{3\mathrm{p}}A_{2\mathrm{p}}^{*}e^{i(k_{3\mathrm{p}}-k_{2\mathrm{p}})x} + k_{3\mathrm{p+i}}k_{2\mathrm{p+i}}A_{3\mathrm{p+i}}A_{2\mathrm{p+i}}^{*}e^{i(k_{3\mathrm{p+i}}-k_{2\mathrm{p+i}})x} + k_{3\mathrm{p+s}}k_{2\mathrm{p+s}}A_{3\mathrm{p+s}}A_{2\mathrm{p+s}}^{*}e^{i(k_{3\mathrm{p+s}}-k_{2\mathrm{p+s}})x} + k_{4\mathrm{p}}k_{3\mathrm{p}}A_{4\mathrm{p}}A_{3\mathrm{p}}^{*}e^{i(k_{4\mathrm{p}}-k_{3\mathrm{p}})x} + k_{4\mathrm{p+i}}k_{3\mathrm{p+i}}A_{4\mathrm{p+i}}A_{3\mathrm{p+i}}^{*}e^{i(k_{4\mathrm{p+i}}-k_{3\mathrm{p+i}})x} + k_{4\mathrm{p+s}}k_{3\mathrm{p+s}}A_{4\mathrm{p+s}}A_{3\mathrm{p+s}}^{*}e^{i(k_{4\mathrm{p+s}}-k_{3\mathrm{p+s}})x} + k_{5\mathrm{p}}k_{4\mathrm{p}}A_{5\mathrm{p}}A_{4\mathrm{p}}^{*}e^{i(k_{5\mathrm{p}}-k_{4\mathrm{p}})x}\Big)2e^{-ik_{\mathrm{p}}x} \tag{C.3}$$

$$\frac{dA_{\mathrm{p+i}}}{dx} = \frac{\beta}{2}\Big(- k_{\mathrm{i}}k_{\mathrm{p}}A_{\mathrm{i}}A_{\mathrm{p}}e^{i(k_{\mathrm{i}}+k_{\mathrm{p}})x} + k_{2\mathrm{p}}k_{\mathrm{s}}A_{2\mathrm{p}}A_{\mathrm{s}}^{*}e^{i(k_{2\mathrm{p}}-k_{\mathrm{s}})x} + k_{2\mathrm{p+i}}k_{\mathrm{p}}A_{2\mathrm{p+i}}A_{\mathrm{p}}^{*}e^{i(k_{2\mathrm{p+i}}-k_{\mathrm{p}})x} + k_{3\mathrm{p}}k_{\mathrm{p+s}}A_{3\mathrm{p}}A_{\mathrm{p+s}}^{*}e^{i(k_{3\mathrm{p}}-k_{\mathrm{p+s}})x} + k_{3\mathrm{p+i}}k_{2\mathrm{p}}A_{3\mathrm{p+i}}A_{2\mathrm{p}}^{*}e^{i(k_{3\mathrm{p+i}}-k_{2\mathrm{p}})x} + k_{4\mathrm{p}}k_{2\mathrm{p+s}}A_{4\mathrm{p}}A_{2\mathrm{p+s}}^{*}e^{i(k_{4\mathrm{p}}-k_{2\mathrm{p+s}})x} + k_{4\mathrm{p+i}}k_{3\mathrm{p}}A_{4\mathrm{p+i}}A_{3\mathrm{p}}^{*}e^{i(k_{4\mathrm{p+i}}-k_{3\mathrm{p}})x} + k_{5\mathrm{p}}k_{3\mathrm{p+s}}A_{5\mathrm{p}}A_{3\mathrm{p+s}}^{*}e^{i(k_{5\mathrm{p}}-k_{3\mathrm{p+s}})x}\Big)e^{-ik_{\mathrm{p+i}}x} \tag{C.4}$$

$$\frac{dA_{\mathrm{p+s}}}{dx} = \frac{\beta}{2}\Big(- k_{\mathrm{s}}k_{\mathrm{p}}A_{\mathrm{s}}A_{\mathrm{p}}e^{i(k_{\mathrm{s}}+k_{\mathrm{p}})x} + k_{2\mathrm{p}}k_{\mathrm{i}}A_{2\mathrm{p}}A_{\mathrm{i}}^{*}e^{i(k_{2\mathrm{p}}-k_{\mathrm{i}})x} + k_{2\mathrm{p+s}}k_{\mathrm{p}}A_{2\mathrm{p+s}}A_{\mathrm{p}}^{*}e^{i(k_{2\mathrm{p+s}}-k_{\mathrm{p}})x} + k_{3\mathrm{p}}k_{\mathrm{p+i}}A_{3\mathrm{p}}A_{\mathrm{p+i}}^{*}e^{i(k_{3\mathrm{p}}-k_{\mathrm{p+i}})x} + k_{3\mathrm{p+s}}k_{2\mathrm{p}}A_{3\mathrm{p+s}}A_{2\mathrm{p}}^{*}e^{i(k_{3\mathrm{p+s}}-k_{2\mathrm{p}})x} + k_{4\mathrm{p}}k_{2\mathrm{p+i}}A_{4\mathrm{p}}A_{2\mathrm{p+i}}^{*}e^{i(k_{4\mathrm{p}}-k_{2\mathrm{p+i}})x} + k_{4\mathrm{p+s}}k_{3\mathrm{p}}A_{4\mathrm{p+s}}A_{3\mathrm{p}}^{*}e^{i(k_{4\mathrm{p+s}}-k_{3\mathrm{p}})x} + k_{5\mathrm{p}}k_{3\mathrm{p+i}}A_{5\mathrm{p}}A_{3\mathrm{p+i}}^{*}e^{i(k_{5\mathrm{p}}-k_{3\mathrm{p+i}})x}\Big)e^{-ik_{\mathrm{p+s}}x} \tag{C.5}$$

$$\frac{dA_{2\mathrm{p}}}{dx} = \frac{\beta}{2}\Big(- k_{\mathrm{i}}k_{\mathrm{p+s}}A_{\mathrm{i}}A_{\mathrm{p+s}}e^{i(k_{\mathrm{i}}+k_{\mathrm{p+s}})x} - k_{\mathrm{s}}k_{\mathrm{p+i}}A_{\mathrm{s}}A_{\mathrm{p+i}}e^{i(k_{\mathrm{s}}+k_{\mathrm{p+i}})x} - \frac{k_{\mathrm{p}}^{2}A_{\mathrm{p}}^{2}}{2}e^{i(k_{\mathrm{p}}+k_{\mathrm{p}})x} + k_{2\mathrm{p+i}}k_{\mathrm{i}}A_{2\mathrm{p+i}}A_{\mathrm{i}}^{*}e^{i(k_{2\mathrm{p+i}}-k_{\mathrm{i}})x} + k_{2\mathrm{p+s}}k_{\mathrm{s}}A_{2\mathrm{p+s}}A_{\mathrm{s}}^{*}e^{i(k_{2\mathrm{p+s}}-k_{\mathrm{s}})x} + k_{3\mathrm{p}}k_{\mathrm{p}}A_{3\mathrm{p}}A_{\mathrm{p}}^{*}e^{i(k_{3\mathrm{p}}-k_{\mathrm{p}})x} + k_{3\mathrm{p+i}}k_{\mathrm{p+i}}A_{3\mathrm{p+i}}A_{\mathrm{p+i}}^{*}e^{i(k_{3\mathrm{p+i}}-k_{\mathrm{p+i}})x} + k_{3\mathrm{p+s}}k_{\mathrm{p+s}}A_{3\mathrm{p+s}}A_{\mathrm{p+s}}^{*}e^{i(k_{3\mathrm{p+s}}-k_{\mathrm{p+s}})x} + k_{4\mathrm{p}}k_{2\mathrm{p}}A_{4\mathrm{p}}A_{2\mathrm{p}}^{*}e^{i(k_{4\mathrm{p}}-k_{2\mathrm{p}})x} + k_{4\mathrm{p+i}}k_{2\mathrm{p+i}}A_{4\mathrm{p+i}}A_{2\mathrm{p+i}}^{*}e^{i(k_{4\mathrm{p+i}}-k_{2\mathrm{p+i}})x} + k_{4\mathrm{p+s}}k_{2\mathrm{p+s}}A_{4\mathrm{p+s}}A_{2\mathrm{p+s}}^{*}e^{i(k_{4\mathrm{p+s}}-k_{2\mathrm{p+s}})x} + k_{5\mathrm{p}}k_{3\mathrm{p}}A_{5\mathrm{p}}A_{3\mathrm{p}}^{*}e^{i(k_{5\mathrm{p}}-k_{3\mathrm{p}})x}\Big)e^{-ik_{2\mathrm{p}}x} \tag{C.6}$$

$$\frac{dA_{2\mathrm{p+i}}}{dx} = \frac{\beta}{2}\Big(- k_{\mathrm{i}}k_{2\mathrm{p}}A_{\mathrm{i}}A_{2\mathrm{p}}e^{i(k_{\mathrm{i}}+k_{2\mathrm{p}})x} - k_{\mathrm{p}}k_{\mathrm{p+i}}A_{\mathrm{p}}A_{\mathrm{p+i}}e^{i(k_{\mathrm{p}}+k_{\mathrm{p+i}})x} \tag{C.7}$$
$$+ k_{3\mathrm{p}}k_{\mathrm{s}}A_{3\mathrm{p}}A_{\mathrm{s}}^{*}e^{i(k_{3\mathrm{p}}-k_{\mathrm{s}})x} + k_{3\mathrm{p+i}}k_{\mathrm{p}}A_{3\mathrm{p+i}}A_{\mathrm{p}}^{*}e^{i(k_{3\mathrm{p+i}}-k_{\mathrm{p}})x}$$
$$+ k_{4\mathrm{p}}k_{\mathrm{p+s}}A_{4\mathrm{p}}A_{\mathrm{p+s}}^{*}e^{i(k_{4\mathrm{p}}-k_{\mathrm{p+s}})x} + k_{4\mathrm{p+i}}k_{2\mathrm{p}}A_{4\mathrm{p+i}}A_{2\mathrm{p}}^{*}e^{i(k_{4\mathrm{p+i}}-k_{2\mathrm{p}})x}$$
$$+ k_{5\mathrm{p}}k_{2\mathrm{p+s}}A_{5\mathrm{p}}A_{2\mathrm{p+s}}^{*}e^{i(k_{5\mathrm{p}}-k_{2\mathrm{p+s}})x}\Big)e^{-ik_{2\mathrm{p+i}}x}$$
$$\frac{dA_{2\mathrm{p+s}}}{dx} = \frac{\beta}{2}\Big(- k_{\mathrm{s}}k_{2\mathrm{p}}A_{\mathrm{s}}A_{2\mathrm{p}}e^{i(k_{\mathrm{s}}+k_{2\mathrm{p}})x} - k_{\mathrm{p}}k_{\mathrm{p+s}}A_{\mathrm{p}}A_{\mathrm{p+s}}e^{i(k_{\mathrm{p}}+k_{\mathrm{p+s}})x} \tag{C.8}$$
$$+ k_{3\mathrm{p}}k_{\mathrm{i}}A_{3\mathrm{p}}A_{\mathrm{i}}^{*}e^{i(k_{3\mathrm{p}}-k_{\mathrm{i}})x} + k_{3\mathrm{p+s}}k_{\mathrm{p}}A_{3\mathrm{p+s}}A_{\mathrm{p}}^{*}e^{i(k_{3\mathrm{p+s}}-k_{\mathrm{p}})x}$$
$$+ k_{4\mathrm{p}}k_{\mathrm{p+i}}A_{4\mathrm{p}}A_{\mathrm{p+i}}^{*}e^{i(k_{4\mathrm{p}}-k_{\mathrm{p+i}})x} + k_{4\mathrm{p+s}}k_{2\mathrm{p}}A_{4\mathrm{p+s}}A_{2\mathrm{p}}^{*}e^{i(k_{4\mathrm{p+s}}-k_{2\mathrm{p}})x}$$
$$+ k_{5\mathrm{p}}k_{2\mathrm{p+i}}A_{5\mathrm{p}}A_{2\mathrm{p+i}}^{*}e^{i(k_{5\mathrm{p}}-k_{2\mathrm{p+i}})x}\Big)e^{-ik_{2\mathrm{p+s}}x}$$
$$\frac{dA_{3\mathrm{p}}}{dx} = \frac{\beta}{2}\Big(- k_{\mathrm{i}}k_{2\mathrm{p+s}}A_{\mathrm{i}}A_{2\mathrm{p+s}}e^{i(k_{\mathrm{i}}+k_{2\mathrm{p+s}})x} - k_{\mathrm{s}}k_{2\mathrm{p+i}}A_{\mathrm{s}}A_{2\mathrm{p+i}}e^{i(k_{\mathrm{s}}+k_{2\mathrm{p+i}})x}$$
$$- k_{\mathrm{p}}k_{2\mathrm{p}}A_{\mathrm{p}}A_{2\mathrm{p}}e^{i(k_{\mathrm{p}}+k_{2\mathrm{p}})x} - k_{\mathrm{p+i}}k_{\mathrm{p+s}}A_{\mathrm{p+i}}A_{\mathrm{p+s}}e^{i(k_{\mathrm{p+i}}+k_{\mathrm{p+s}})x}$$
$$+ k_{3\mathrm{p+i}}k_{\mathrm{i}}A_{3\mathrm{p+i}}A_{\mathrm{i}}^{*}e^{i(k_{3\mathrm{p+i}}-k_{\mathrm{i}})x} + k_{3\mathrm{p+s}}k_{\mathrm{s}}A_{3\mathrm{p+s}}A_{\mathrm{s}}^{*}e^{i(k_{3\mathrm{p+s}}-k_{\mathrm{s}})x}$$
$$+ k_{4\mathrm{p}}k_{\mathrm{p}}A_{4\mathrm{p}}A_{\mathrm{p}}^{*}e^{i(k_{4\mathrm{p}}-k_{\mathrm{p}})x} + k_{4\mathrm{p+i}}k_{\mathrm{p+i}}A_{4\mathrm{p+i}}A_{\mathrm{p+i}}^{*}e^{i(k_{4\mathrm{p+i}}-k_{\mathrm{p+i}})x}$$
$$+ k_{4\mathrm{p+s}}k_{\mathrm{p+s}}A_{4\mathrm{p+s}}A_{\mathrm{p+s}}^{*}e^{i(k_{4\mathrm{p+s}}-k_{\mathrm{p+s}})x} + k_{5\mathrm{p}}k_{2\mathrm{p}}A_{5\mathrm{p}}A_{2\mathrm{p}}^{*}e^{i(k_{5\mathrm{p}}-k_{2\mathrm{p}})x}\Big)e^{-ik_{3\mathrm{p}}x}$$

(C.9)

$$\frac{dA_{3\mathrm{p+i}}}{dx} = \frac{\beta}{2}\Big(- k_{\mathrm{i}}k_{3\mathrm{p}}A_{\mathrm{i}}A_{3\mathrm{p}}e^{i(k_{\mathrm{i}}+k_{3\mathrm{p}})x} - k_{\mathrm{p}}k_{2\mathrm{p+i}}A_{\mathrm{p}}A_{2\mathrm{p+i}}e^{i(k_{\mathrm{p}}+k_{2\mathrm{p+i}})x} \tag{C.10}$$
$$- k_{\mathrm{p+i}}k_{2\mathrm{p}}A_{\mathrm{p+i}}A_{2\mathrm{p}}e^{i(k_{\mathrm{p+i}}+k_{2\mathrm{p}})x} + k_{4\mathrm{p}}k_{\mathrm{s}}A_{4\mathrm{p}}A_{\mathrm{s}}^{*}e^{i(k_{4\mathrm{p}}-k_{\mathrm{s}})x}$$
$$+ k_{4\mathrm{p+i}}k_{\mathrm{p}}A_{4\mathrm{p+i}}A_{\mathrm{p}}^{*}e^{i(k_{4\mathrm{p+i}}-k_{\mathrm{p}})x} + k_{5\mathrm{p}}k_{\mathrm{p+s}}A_{5\mathrm{p}}A_{\mathrm{p+s}}^{*}e^{i(k_{5\mathrm{p}}-k_{\mathrm{p+s}})x})e^{-ik_{3\mathrm{p+i}}x}$$
$$\frac{dA_{3\mathrm{p+s}}}{dx} = \frac{\beta}{2}\Big(- k_{\mathrm{s}}k_{3\mathrm{p}}A_{\mathrm{s}}A_{3\mathrm{p}}e^{i(k_{\mathrm{s}}+k_{3\mathrm{p}})x} - k_{\mathrm{p}}k_{2\mathrm{p+s}}A_{\mathrm{p}}A_{2\mathrm{p+s}}e^{i(k_{\mathrm{p}}+k_{2\mathrm{p+s}})x}$$
$$- k_{\mathrm{p+s}}k_{2\mathrm{p}}A_{\mathrm{p+s}}A_{2\mathrm{p}}e^{i(k_{\mathrm{p+s}}+k_{2\mathrm{p}})x} + k_{4\mathrm{p}}k_{\mathrm{i}}A_{4\mathrm{p}}A_{\mathrm{i}}^{*}e^{i(k_{4\mathrm{p}}-k_{\mathrm{i}})x}$$
$$+ k_{4\mathrm{p+s}}k_{\mathrm{p}}A_{4\mathrm{p+s}}A_{\mathrm{p}}^{*}e^{i(k_{4\mathrm{p+s}}-k_{\mathrm{p}})x} + k_{5\mathrm{p}}k_{\mathrm{p+i}}A_{5\mathrm{p}}A_{\mathrm{p+i}}^{*}e^{i(k_{5\mathrm{p}}-k_{\mathrm{p+i}})x}\Big)e^{-ik_{3\mathrm{p+s}}x}$$

(C.11)

$$\frac{dA_{4p}}{dx} = \frac{\beta}{2}\Big(- k_i k_{3p+s} A_i A_{3p+s} e^{i(k_i+k_{3p+s})x} - k_s k_{3p+i} A_s A_{3p+i} e^{i(k_s+k_{3p+i})x} \tag{C.12}$$
$$- k_p k_{3p} A_p A_{3p} e^{i(k_p+k_{3p})x} - k_{p+i} k_{2p+s} A_{p+i} A_{2p+s} e^{i(k_{p+i}+k_{2p+s})x}$$
$$- k_{p+s} k_{2p+i} A_{p+s} A_{2p+i} e^{i(k_{p+s}+k_{2p+i})x} - \frac{k_{2p}^2 A_{2p}^2}{2} e^{i(k_{2p}+k_{2p})x}$$
$$+ k_{4p+i} k_i A_{4p+i} A_i^* e^{i(k_{4p+i}-k_i)x} + k_{4p+s} k_s A_{4p+s} A_s^* e^{i(k_{4p+s}-k_s)x}$$
$$+ k_{5p} k_p A_{5p} A_p^* e^{i(k_{5p}-k_p)x}\Big) e^{-ik_{4p}x}$$

$$\frac{dA_{4p+i}}{dx} = \frac{\beta}{2}\Big(- k_i k_{4p} A_i A_{4p} e^{i(k_i+k_{4p})x} - k_p k_{3p+i} A_p A_{3p+i} e^{i(k_p+k_{3p+i})x} \tag{C.13}$$
$$- k_{p+i} k_{3p} A_{p+i} A_{3p} e^{i(k_{p+i}+k_{3p})x} - k_{2p} k_{2p+i} A_{2p} A_{2p+i} e^{i(k_{2p}+k_{2p+i})x}$$
$$+ k_{5p} k_s A_{5p} A_s^* e^{i(k_{5p}-k_s)x}\Big) e^{i(-k_{4p+i})x}$$

$$\frac{dA_{4p+s}}{dx} = \frac{\beta}{2}\Big(- k_s k_{4p} A_s A_{4p} e^{i(k_s+k_{4p})x} - k_p k_{3p+s} A_p A_{3p+s} e^{i(k_p+k_{3p+s})x} \tag{C.14}$$
$$- k_{p+s} k_{3p} A_{p+s} A_{3p} e^{i(k_{p+s}+k_{3p})x} - k_{2p} k_{2p+s} A_{2p} A_{2p+s} e^{i(k_{2p}+k_{2p+s})x}$$
$$+ k_{5p} k_i A_{5p} A_i^* e^{i(k_{5p}-k_i)x}\Big) e^{-ik_{4p+s}x}$$

$$\frac{dA_{5p}}{dx} = \frac{\beta}{2}\Big(- k_i k_{4p+s} A_i A_{4p+s} e^{i(k_i+k_{4p+s})x} - k_s k_{4p+i} A_s A_{4p+i} e^{i(k_s+k_{4p+i})x} \tag{C.15}$$
$$- k_p k_{4p} A_p A_{4p} e^{i(k_p+k_{4p})x} - k_{p+i} k_{3p+s} A_{p+i} A_{3p+s} e^{i(k_{p+i}+k_{3p+s})x}$$
$$- k_{p+s} k_{3p+i} A_{p+s} A_{3p+i} e^{i(k_{p+s}+k_{3p+i})x} - k_{2p} k_{3p} A_{2p} A_{3p} e^{i(k_{2p}+k_{3p})x}$$
$$- k_{2p+i} k_{2p+s} A_{2p+i} A_{2p+s} e^{i(k_{2p+i}+k_{2p+s})x}\Big) e^{-ik_{5p}x}$$

C.2 Quasi Phase Matching Matlab

```
clear

addpath '/home/tom/Desktop/QPM_JTWPA'%make this where the functions
    for eta are stored
a1=0.15;
b1=0.2;

m=474;

```

```
9  x=[0:4000]
10
11 phi0 = 2.067833848*10^-15;
12 Cj=235e-15;
13 Ic=1.8e-6;
14
15 C0=32e-15;
16 Lg=88e-12;
17 w0=1/sqrt(Lg*C0)
18 wj=1/sqrt(Lg*Cj)
19 wp = 2*pi*15*10^9;
20 Z=sqrt(Lg/C0);
21 fc=2/(2*pi*sqrt(Lg*(C0+4*Cj)))
22 Ap0=0.53*w0/wp;
23 Ip0=0.72e-6;
24 Is0=50e-9;
25 BetaL=2*pi*Lg*Ic/phi0
26 maxBeta=BetaL/2;
27 fplot=0:.1e9:fc+1e9
28 w=fplot.*2.*pi
29 kplot=acos(1-((w.^2))./(2.*(w0.^2)*(1-(w.^2)./(wj^2))));
30
31 wsfac = 8./15;
32
33 ws = wsfac.*wp;
34
35 w=[wp,ws]
36
37 Ap0 = Z*2*pi*Ip0/(phi0*wp);
```

```
38 As0 = Z*2*pi*Is0/(phi0*ws);
39
40 maxGamma=0;
41 fs=8e9;
42 wp=2*pi*15e9
43 ws=fs*2*pi
44 if ismembertol(ws,0.5*wp,0.001);
45
46 else
47     w = [wp,ws];
48     wc = 2*wp;
49     sort(w)
50     lenw1=1;
51     lenw2=2;
52     checker=0;
53     while checker<1
54         tic
55         if lenw1==lenw2
56             checker=checker+1
57         end
58         lenw1=length(w);
59         for i=1:length(w)
60             for j=1:length(w)
61
62                 a = w(i) + w(j);
63                 b = w(i) - w(j);
64                 check1 = ismembertol(a,w,0.001);
65                 check2 = ismembertol(b,w,0.001);
66
```

```
67                  %PUMP MEDIATED 3WM COMMENT THIS AND CORRESPONDING
                        END FOR NON
68                  %PUMP MEADIATED 3WM
69                  if mod(w(i),wp)==0 || mod(w(j),wp)==0 && b>1e9
70                      if check1==0 && a<wc+1e6
71                          w = [w,a];
72                      end
73                      if check2==0 && b>0
74                          w = [b,w];
75                      end
76                  end
77
78                  for k=1:length(w)
79                      mm(1)=w(i)+w(j)+w(k);
80                      mm(2)=w(i)+w(j)-w(k);
81                      mm(3)=w(i)-w(j)-w(k);
82
83                      for idx = 1:length(mm)
84                      check = ismembertol(mm(idx),w,0.0001);
85
86                          %PUMP MEDIATED VIA THE MAG SQUARE ~|Ap|^2
                                check
87                          if (mod(w(i),wp)==0 && mod(w(j),wp)==0) ||
                                (mod(w(j),wp)==0 && mod(w(k),wp)==0) ||
                                (mod(w(k),wp)==0 && mod(w(i),wp)==0)
88                          %PUMP MEDIATED VIA SINGLE PUMP ~Ap check
89                          %if (mod(w(i),wp)==0 ) || (mod(w(j),wp)==0)
                                || (mod(w(k),wp)==0)
```

```
90                                  if check==0 && mm(idx)<wc+1e6 && mm(idx
                                        )>0.1
91                                      w = [w,mm(idx)];
92                                  end
93                              end
94                          end
95                      end
96                  end
97
98                  Astring{i}=['A(',num2str(i),')'];
99                  Aconjstring{i}=['conj(A(',num2str(i),'))'];
100                 kstring{i}=['k(',num2str(i),')'];
101
102             end
103             lenw2=length(w);
104             toc
105         end
106         w=sort(w);
107         f=w./(2*pi)
108
109         dAstring=cell(1,length(w));
110
111         for i=1:length(w)
112             for j=1:length(w)
113
114                 if i>j
115                     mixing_matrix3wm(i,j)=w(i)-w(j);
116                 elseif i<=j
117                     mixing_matrix3wm(i,j)=w(i)+w(j);
```

```
118                 end
119                 if   ismembertol(mixing_matrix3wm(i,j),w,0.0001)==0
120                     mixing_matrix3wm(i,j)=0;
121                 end
122             end
123         end
124
125          for i=1:length(w)
126             for j=1:length(w)
127                 if ismembertol(mixing_matrix3wm(i,j),w)==1
128
129
130                 idx=find(abs(mixing_matrix3wm(i,j)-w)<1);
131                     if i>j
132                         dAstring{idx}=[dAstring{idx},' +2*(maxBeta/4).*
                            ',kstring{i},'.*',kstring{j},'.*',Astring{i
                            },'.*',Aconjstring{j},'.*exp(1i.*(',kstring{
                            i},'-',kstring{j},').*x)'];
133
134         %                 mixing_matrix2(i,j)=w(i)-w(j);
135                     elseif i<j
136                         dAstring{idx}=[dAstring{idx},'-2*(maxBeta/4).*'
                            ,kstring{i},'.*',kstring{j},'.*',Astring{i},
                            '.*',Astring{j},'.*exp(1i.*(',kstring{i},'+'
                            ,kstring{j},').*x)'];
137         %                 mixing_matrix2(i,j)=w(i)+w(j);
138                     elseif i==j
139                         dAstring{idx}=[dAstring{idx},'-(maxBeta/4).*(',
                            kstring{i},'.^2).*(',Astring{i},'.^2)','.*
```

```
                    exp(1i.*(',kstring{i},'+',kstring{j},').*x)'
                    ];
140             end
141         end
142     end
143 end
144
145 MMsss=zeros([length(w) length(w) length(w)]);
146 MMssd=zeros([length(w) length(w) length(w)]);
147 MMsdd=zeros([length(w) length(w) length(w)]);
148 MMddd=zeros([length(w) length(w) length(w)]);
149
150 for i=1:length(w)
151     for j=1:length(w)
152         for k=1:length(w)
153             sssfg(i,j,k)=w(i)+w(j)+w(k);
154             ssdfg(i,j,k)=w(i)+w(j)-w(k);
155             sddfg(i,j,k)=w(i)-w(j)-w(k);
156             if ismembertol(sssfg(i,j,k),w,0.0001)==1
157                 if i==j && i==k;
158                     idx=find(abs(sssfg(i,j,k)-w)<1);
159                     MMsss(i,j,k)=sssfg(i,j,k);
160                     if (mod(w(i),wp)==0 && mod(w(j),wp)==0) ||
                            (mod(w(j),wp)==0 && mod(w(k),wp)==0) ||
                            (mod(w(k),wp)==0 && mod(w(i),wp)==0)
161
162                         dAstring{idx}=[dAstring{idx},' -1i.*(
                                maxGamma/8).*',kstring{i},'.*',
                                kstring{j},'.*',kstring{k},'.*',
```

```
                    Astring{i},'.*',Astring{j},'.*',
                    Astring{k},'.*exp(1i.*(',kstring{i},
                    '+',kstring{j},'+',kstring{k},').*x)
                    '];
163                 end
164             else
165
166                 idx=find(abs(sssfg(i,j,k)-w)<1);
167                 MMsss(i,j,k)=sssfg(i,j,k);
168                 if (mod(w(i),wp)==0 && mod(w(j),wp)==0) ||
                        (mod(w(j),wp)==0 && mod(w(k),wp)==0) ||
                        (mod(w(k),wp)==0 && mod(w(i),wp)==0)
169
170                     dAstring{idx}=[dAstring{idx},' -1i
                        .*3.*(maxGamma/8).*',kstring{i},'.*'
                        ,kstring{j},'.*',kstring{k},'.*',
                        Astring{i},'.*',Astring{j},'.*',
                        Astring{k},'.*exp(1i.*(',kstring{i},
                        '+',kstring{j},'+',kstring{k},').*x)
                        '];
171                 end
172             end
173         end
174
175         if ismembertol(ssdfg(i,j,k),w,0.0001)==1
176             idx=find(abs(ssdfg(i,j,k)-w)<1);
177             MMssd(i,j,k)=ssdfg(i,j,k);
178             if (mod(w(i),wp)==0 && mod(w(j),wp)==0) || (mod
                    (w(j),wp)==0 && mod(w(k),wp)==0) || (mod(w(k
```

```
                ),wp)==0 && mod(w(i),wp)==0)
179
180             if i==j && i==k;
181                 dAstring{idx}=[dAstring{idx},' +1i
                        .*3.*(maxGamma/8).*',kstring{i},'.*'
                        ,kstring{j},'.*',kstring{k},'.*',
                        Astring{i},'.*',Astring{j},'.*',
                        Aconjstring{k},'.*exp(1i.*(',kstring
                        {i},'+',kstring{j},'-',kstring{k},')
                        .*x)'];
182             else
183                 dAstring{idx}=[dAstring{idx},' +1i
                        .*6.*(maxGamma/8).*',kstring{i},'.*'
                        ,kstring{j},'.*',kstring{k},'.*',
                        Astring{i},'.*',Astring{j},'.*',
                        Aconjstring{k},'.*exp(1i.*(',kstring
                        {i},'+',kstring{j},'-',kstring{k},')
                        .*x)'];
184             end
185         end
186     end
187
188     if  ismembertol(sddfg(i,j,k),w,0.0001)==1
189         idx=find(abs(sddfg(i,j,k)-w)<1);
190         MMsdd(i,j,k)=sddfg(i,j,k);
191         if (mod(w(i),wp)==0 && mod(w(j),wp)==0) || (mod
                (w(j),wp)==0 && mod(w(k),wp)==0) || (mod(w(k
                ),wp)==0 && mod(w(i),wp)==0)
192             if i==j && i==k;
```

```
193                                 dAstring{idx}=[dAstring{idx},' -1i
                                        .*3.*(maxGamma/8).*',kstring{i},'.*'
                                        ,kstring{j},'.*',kstring{k},'.*',
                                        Astring{i},'.*',Aconjstring{j},'.*',
                                        Aconjstring{k},'.*exp(1i.*(',kstring
                                        {i},'-',kstring{j},'-',kstring{k},')
                                        .*x)'];
194                             else
195                                 dAstring{idx}=[dAstring{idx},' -1i
                                        .*6.*(maxGamma/8).*',kstring{i},'.*'
                                        ,kstring{j},'.*',kstring{k},'.*',
                                        Astring{i},'.*',Aconjstring{j},'.*',
                                        Aconjstring{k},'.*exp(1i.*(',kstring
                                        {i},'-',kstring{j},'-',kstring{k},')
                                        .*x)'];
196                             end
197                         end
198                     end
199                 end
200             end
201         end
202
203         Ip0=.72e-6;
204         %Is0=5e-9;
205         Is0=46e-9;
206         Z=sqrt(Lg/C0);
207         phi0 = 2.067833848*10^-15;
208         w0=2/(sqrt(Lg*(C0+4*Cj)));
209         w0=1/sqrt(Lg*C0);
```

```
wj=1/sqrt(Lg*Cj);
Ap0 = Z*2*pi*Ip0/(phi0*wp);
As0 = Z*2*pi*Is0/(phi0*ws);

k=acos(1-((w.^2))./(2.*(w0.^2)*(1-(w.^2)./(wj^2))));
 for i=1:length(w)
    if i==1
        dA1string{i}=strjoin(['[(',string(dAstring{i}),').*exp
            (-1i.*',kstring{i},'.*x);']);
    elseif i==length(w)
        dA1string{i}=strjoin(['(',string(dAstring{i}),').*exp
            (-1i.*',kstring{i},'.*x)]']);
    else
        dA1string{i}=strjoin(['(',string(dAstring{i}),').*exp
            (-1i.*',kstring{i},'.*x);']);
    end

    if ismembertol(w(i),wp)==1
        A0(i)=Ap0;
    elseif ismembertol(w(i),ws)==1
        A0(i)=As0;
    else
        A0(i)=0;
    end
end

dA=strcat(dA1string{:});
dAtemp=str2func(strcat('@(x,A,k,maxBeta,maxGamma) ', dA));
dAfunc=@(x,A)dAtemp(x,A,k,maxBeta,maxGamma);
```

```
236
237     [x,A] = ode45(dAfunc, x ,A0);
238     I=(phi0./(Z.*2*pi)).*w.*abs(A);
239     PdBm=10*log10((I.^2)*Z*1e3);
240
241     for i=1:length(w)
242         if i==1
243             dASquarestring{i}=strjoin(['[dAetaSquare(x,m).*(',
                    string(dAstring{i}),').*exp(-1i.*',kstring{i},'.*x);
                    ']);
244         elseif i==length(w)
245             dASquarestring{i}=strjoin(['dAetaSquare(x,m).*(',string
                    (dAstring{i}),').*exp(-1i.*',kstring{i},'.*x)]']);
246         else
247             dASquarestring{i}=strjoin(['dAetaSquare(x,m).*(',string
                    (dAstring{i}),').*exp(-1i.*',kstring{i},'.*x);']);
248         end
249
250         if ismembertol(w(i),wp)==1
251             A0(i)=Ap0;
252         elseif ismembertol(w(i),ws)==1
253             A0(i)=As0;
254         else
255             A0(i)=0;
256         end
257     end
258
259     dASquare=strcat(dASquarestring{:});
```

```
260     dASquaretemp=str2func(strcat('@(x,A,k,maxBeta,maxGamma,m) ',
            dASquare));
261     dASquarefunc=@(x,A)dASquaretemp(x,A,k,maxBeta,maxGamma,m);
262
263     [x,A] = ode45(dASquarefunc, x ,A0);
264
265     ISquare=(phi0./(Z.*2*pi)).*w.*abs(A);
266
267     PdBmSquare=10*log10((ISquare.^2)*Z*1e3);
268
269     for i=1:length(w)
270         if i==1
271             dASinestring{i}=strjoin(['[dAetaSine(x,m).*(',string(
                    dAstring{i}),').*exp(-1i.*',kstring{i},'.*x);']);
272         elseif i==length(w)
273             dASinestring{i}=strjoin(['dAetaSine(x,m).*(',string(
                    dAstring{i}),').*exp(-1i.*',kstring{i},'.*x)]']);
274         else
275             dASinestring{i}=strjoin(['dAetaSine(x,m).*(',string(
                    dAstring{i}),').*exp(-1i.*',kstring{i},'.*x);']);
276         end
277
278         if ismembertol(w(i),wp)==1
279             A0(i)=Ap0;
280         elseif ismembertol(w(i),ws)==1
281             A0(i)=As0;
282         else
283             A0(i)=0;
284         end
```

```
285     end
286
287     dASine=strcat(dASinestring{:});
288     dASinetemp=str2func(strcat('@(x,A,k,maxBeta,maxGamma,m) ',
            dASine));
289     dASinefunc=@(x,A)dASinetemp(x,A,k,maxBeta,maxGamma,m);
290
291     [x,A] = ode45(dASinefunc, x ,A0);
292
293     ISine=(phi0./(Z.*2*pi)).*w.*abs(A);
294
295     PdBmSine=10*log10((ISine.^2)*Z*1e3);
296
297     for i=1:length(w)
298         if i==1
299             dATaperstring{i}=strjoin(['[dAetaTaper(x,m,a1,b1).*(',
                    string(dAstring{i}),').*exp(-1i.*',kstring{i},'.*x);
                    ']);
300         elseif i==length(w)
301             dATaperstring{i}=strjoin(['dAetaTaper(x,m,a1,b1).*(',
                    string(dAstring{i}),').*exp(-1i.*',kstring{i},'.*x)]
                    ']);
302         else
303             dATaperstring{i}=strjoin(['dAetaTaper(x,m,a1,b1).*(',
                    string(dAstring{i}),').*exp(-1i.*',kstring{i},'.*x);
                    ']);
304         end
305
306         if ismembertol(w(i),wp)==1
```

```
307             A0(i)=Ap0;
308         elseif ismembertol(w(i),ws)==1
309             A0(i)=As0;
310         else
311             A0(i)=0;
312         end
313     end
314
315     dATaper=strcat(dATaperstring{:});
316     dATapertemp=str2func(strcat('@(x,A,k,maxBeta,maxGamma,m,a1,b1)
        ', dATaper));
317     dATaperfunc=@(x,A)dATapertemp(x,A,k,maxBeta,maxGamma,m,a1,b1);
318
319     [x,A] = ode45(dATaperfunc, x ,A0);
320
321     ITaper=(phi0./(Z.*2*pi)).*w.*abs(A);
322
323     PdBmTaper=10*log10((ITaper.^2)*Z*1e3);
324 end
325
326 plotcols={'r','b','g','m','c','m'}
327
328 figure(1)
329 j=1;
330 for i=[3,2,1]
331     plot(x,PdBmTaper(:,i),'-','color',plotcols{j},'LineWidth',3)
332     hold on
333     plot(x,PdBm(:,i),':','color',plotcols{j},'LineWidth',2)
334     j=j+1;
```

```
335 end
336 ax=gca;
337 ax.FontSize=22;
338 ylim([-120 -70])
339 xlabel('Node [n]','Interpreter','latex')
340 ylabel('Power [dBm]','Interpreter','latex')
341 idx=find(abs(dAetaTaper(x,m,a1,b1) - 0)<0.01)
342 plot(x(idx),PdBmTaper(idx,2),'k*','LineWidth',3,'MarkerSize',15)
343 legend(['Pump - QPM'],['Pump'],['Signal - QPM'],['Signal'],['Idler
    - QPM'],['Idler'],['$\eta(x)=0$'],'Interpreter','latex')
344 hold off
345
346 figure(2)
347 j=1;
348 for i=[3,6]
349     plot(x,PdBmTaper(:,i),'-','color',plotcols{j},'LineWidth',3)
350     hold on
351     plot(x,PdBm(:,i),':','color',plotcols{j},'LineWidth',2)
352     j=j+1;
353 end
354 hold off
355 ax=gca;
356 ax.FontSize=22;
357 ylim([-150 -70])
358 xlabel('Node [n]','Interpreter','latex')
359 ylabel('Power [dBm]','Interpreter','latex')
360 legend(['Pump - QPM'],['Pump'],['SHG - QPM'],['SHG'],'Interpreter',
    'latex')
361
```

```
362 figure(3)
363 j=1;
364 for i=[1,2,4,5]
365     plot(x,PdBmTaper(:,i),'-','color',plotcols{j},'LineWidth',3)
366     hold on
367     plot(x,PdBm(:,i),':','color',plotcols{j},'LineWidth',2)
368     j=j+1;
369 end
370 hold off
371 ax=gca;
372 ax.FontSize=22;
373 ylim([-150 -70])
374 xlabel('Node [n]','Interpreter','latex')
375 ylabel('Power [dBm]','Interpreter','latex')
376 legend(['Idler - QPM'],['Idler'],['Signal - QPM'],['Signal'],['$P_
    {\mathrm{p+i}}$ - QPM'],['$P_{\mathrm{p+i}}$'],['$P_{\mathrm{p+s
    }}$ - QPM'],['$P_{\mathrm{p+s}}$'],'Interpreter','latex')
```

Bibliography

[1] Frank Arute, Kunal Arya, and Martinis John M. Babbush, Ryan *et. al*. Quantum supremacy using a programmable superconducting processor. *Nature*, 574(7779):505–510, Oct 2019.

[2] Y. Nakamura, Yu. A. Pashkin, and J. S. Tsai. Coherent control of macroscopic quantum states in a single-cooper-pair box. *Nature*, 398(6730):786–788, Apr 1999.

[3] Carlton M. Caves. Quantum limits on noise in linear amplifiers. *Phys. Rev. D*, 26:1817–1839, Oct 1982.

[4] G. Floquet. Sur les équations différentielles linéaires à coefficients périodiques. *Annales scientifiques de l'École Normale Supérieure*, 2e série, 12:47–88, 1883.

[5] J. Boussinesq. Essai sur la theorie des eaux courantes. *Memoires presentes par divers savants a l'Academie des Sciences de l'Institut National de France*, 23(1), 1877.

[6] E. Mathieu. Mémoire sur le mouvement vibratoire d'une membrane de forme elliptique. *Journal de Mathématiques Pures et Appliquées*, 13:137–203.

[7] P. A. Franken, A. E. Hill, C. W. Peters, and G. Weinreich. Generation of optical harmonics. *Phys. Rev. Lett.*, 7:118–119, Aug 1961.

[8] Robert W. Boyd. Chapter 1 - the nonlinear optical susceptibility. In Robert W. Boyd, editor, *Nonlinear Optics (Third Edition)*, pages 1 – 97. Academic Press, Burlington, third edition edition, 2008.

[9] Alan Keith Walton. *Network Analysis and Practice*. Cambridge University Press, Cambridge, 1987.

[10] Williams. J. M. Private Communication, 2020.

[11] T. Dixon, J.W. Dunstan, G.B. Long, J.M. Williams, P.J. Meeson, and C.D. Shelly. Capturing complex behavior in josephson traveling-wave parametric amplifiers. *Phys. Rev. Applied*, 14:034058, Sep 2020.

[12] B.D. Josephson. Possible new effects in superconductive tunnelling. *Physics Letters*, 1(7):251 – 253, 1962.

[13] P. W. Anderson and J. M. Rowell. Probable observation of the josephson superconducting tunneling effect. *Phys. Rev. Lett.*, 10:230–232, Mar 1963.

[14] A. B. Zorin. Josephson traveling-wave parametric amplifier with three-wave mixing. *Phys. Rev. Applied*, 6:034006, Sep 2016.

[15] H. Zimmer. Parametric amplification of microwaves in superconducting josephson tunnel junctions. *Applied Physics Letters*, 10(7):193–195, 1967.

[16] L. Kuzmin, K. Likharev, V. Migulin, and A. Zorin. Quantum noise in josephson-junction parametric amplifiers. *IEEE Transactions on Magnetics*, 19(3):618–621, 1983.

[17] A. Smith, R. Sandell, J. Burch, and A. Silver. Low noise microwave parametric amplifier. *IEEE Transactions on Magnetics*, 21(2):1022–1028, 1985.

[18] B. Yurke, L. R. Corruccini, P. G. Kaminsky, L. W. Rupp, A. D. Smith, A. H. Silver, R. W. Simon, and E. A. Whittaker. Observation of parametric amplification and deamplification in a josephson parametric amplifier. *Phys. Rev. A*, 39:2519–2533, Mar 1989.

[19] A. Wallraff, D. I. Schuster, A. Blais, L. Frunzio, R.-. S. Huang, J. Majer, S. Kumar, S. M. Girvin, and R. J. Schoelkopf. Strong coupling of a single photon to a superconducting qubit using circuit quantum electrodynamics. *Nature*, 431(7005):162–167, Sep 2004.

[20] I. Siddiqi, R. Vijay, F. Pierre, C. M. Wilson, M. Metcalfe, C. Rigetti, L. Frunzio, and M. H. Devoret. Rf-driven josephson bifurcation amplifier for quantum measurement. *Phys. Rev. Lett.*, 93:207002, Nov 2004.

[21] François Mallet, Florian R. Ong, Agustin Palacios-Laloy, François Nguyen, Patrice Bertet, Denis Vion, and Daniel Esteve. Single-shot qubit readout in circuit quantum electrodynamics. *Nature Physics*, 5(11):791–795, Nov 2009.

[22] N. Boulant, G. Ithier, P. Meeson, F. Nguyen, D. Vion, D. Esteve, I. Siddiqi, R. Vijay, C. Rigetti, F. Pierre, and M. Devoret. Quantum nondemolition readout using a josephson bifurcation amplifier. *Phys. Rev. B*, 76:014525, Jul 2007.

[23] Connor D. Shelly, Christopher Checkley, and Victor T. Petrashov. Hybrid quantum interferometer in bifurcation mode as a latching quantum readout. *Phys. Rev. Applied*, 15:034070, Mar 2021.

[24] Philip Krantz, Yarema Reshitnyk, Waltraut Wustmann, Jonas Bylander, Simon Gustavsson, William D Oliver, Timothy Duty, Vitaly Shumeiko, and Per Delsing. Investigation of nonlinear effects in josephson parametric oscillators used in circuit quantum electrodynamics. *New Journal of Physics*, 15(10):105002, oct 2013.

[25] Philip Krantz. *The Josephson parametric oscillator–From microscopic studies to single-shot qubit readout*. Chalmers Tekniska Hogskola (Sweden), 2016.

[26] Philip Krantz, Andreas Bengtsson, Michaël Simoen, Simon Gustavsson, Vitaly Shumeiko, W. D. Oliver, C. M. Wilson, Per Delsing, and Jonas Bylander. Single-shot read-out of a superconducting qubit using a josephson parametric oscillator. *Nature Communications*, 7(1):11417, May 2016.

[27] M. A. Castellanos-Beltran and K. W. Lehnert. Widely tunable parametric amplifier based on a superconducting quantum interference device array resonator. *Applied Physics Letters*, 91(8):083509, 2007.

[28] M. Hatridge, R. Vijay, D. H. Slichter, John Clarke, and I. Siddiqi. Dispersive magnetometry with a quantum limited squid parametric amplifier. *Phys. Rev. B*, 83:134501, Apr 2011.

[29] Baleegh Abdo, Flavius Schackert, Michael Hatridge, Chad Rigetti, and Michel Devoret. Josephson amplifier for qubit readout. *Applied Physics Letters*, 99(16):162506, 2011.

[30] Alexis L Cullen. Theory of the travelling-wave parametric amplifier by professor. 1959.

[31] Byeong Ho Eom, Peter K. Day, Henry G. LeDuc, and Jonas Zmuidzinas. A wideband, low-noise superconducting amplifier with high dynamic range. *Nature Physics*, 8(8):623–627, Aug 2012.

[32] Henry G. Leduc, Bruce Bumble, Peter K. Day, Byeong Ho Eom, Jiansong Gao, Sunil Golwala, Benjamin A. Mazin, Sean McHugh, Andrew Merrill, David C. Moore, Omid Noroozian, Anthony D. Turner, and Jonas Zmuidzinas. Titanium nitride films for ultrasensitive microresonator detectors. *Applied Physics Letters*, 97(10):102509, 2010.

[33] O. Yaakobi, L. Friedland, C. Macklin, and I. Siddiqi. Parametric amplification in josephson junction embedded transmission lines. *Phys. Rev. B*, 87:144301, Apr 2013.

[34] Kevin O'Brien, Chris Macklin, Irfan Siddiqi, and Xiang Zhang. Resonant phase matching of josephson junction traveling wave parametric amplifiers. *Phys. Rev. Lett.*, 113:157001, Oct 2014.

[35] T. C. White, J. Y. Mutus, I.-C. Hoi, R. Barends, B. Campbell, Yu Chen, Z. Chen, B. Chiaro, A. Dunsworth, E. Jeffrey, J. Kelly, A. Megrant, C. Neill, P. J. J. O'Malley, P. Roushan, D. Sank, A. Vainsencher, J. Wenner, S. Chaudhuri, J. Gao, and John M. Martinis. Traveling wave parametric amplifier with josephson junctions using minimal resonator phase matching. *Applied Physics Letters*, 106(24):242601, 2015.

[36] C. Macklin, K. O'Brien, D. Hover, M. E. Schwartz, V. Bolkhovsky, X. Zhang, W. D. Oliver, and I. Siddiqi. A near–quantum-limited josephson traveling-wave parametric amplifier. *Science*, 2015.

[37] B. Tan and G. Yassin. Design of a uniplanar resonance phase-matched josephson traveling-wave parametric amplifier. In *2017 10th UK-Europe-China Workshop on Millimetre Waves and Terahertz Technologies (UCMMT)*, pages 1–4, 2017.

[38] M. T. Bell and A. Samolov. Traveling-wave parametric amplifier based on a chain of coupled asymmetric squids. *Phys. Rev. Applied*, 4:024014, Aug 2015.

[39] A. B. Zorin. Quasi-phasematching in a poled traveling-wave josephson parametric amplifier with three-wave mixing, 2021.

[40] Kaidong Peng, Mahdi Naghiloo, Jennifer Wang, Gregory D Cunningham, Yufeng Ye, and Kevin P O'Brien. Near-ideal quantum efficiency with a floquet mode traveling wave parametric amplfier, 2021.

[41] Katie Porsch. *Exploring the period doubling bifurcation*. PhD thesis, 2017.

[42] Alexander B. Zorin and Yuriy Makhlin. Period-doubling bifurcation readout for a josephson qubit. *Phys. Rev. B*, 83:224506, Jun 2011.

[43] Morten Kjaergaard, Mollie E. Schwartz, Jochen Braumüller, Philip Krantz, Joel I.-J. Wang, Simon Gustavsson, and William D. Oliver. Superconducting qubits: Current state of play. *Annual Review of Condensed Matter Physics*, 11(1):369–395, Mar 2020.

[44] Jacob Dunstan. *Instabilities in Arrays of Coupled SQUIDs*. PhD thesis, Royal Holloway, University of London, 2020.

[45] George Long. *Studies of phenomena arising from the non-linearity of the Josephson junction*. PhD thesis, Royal Holloway, University of London, 2019.

[46] Yong S Joe, Arkady M Satanin, and Chang Sub Kim. Classical analogy of fano resonances. *Physica Scripta*, 74(2):259–266, jul 2006.

[47] Mikhail F. Limonov, Mikhail V. Rybin, Alexander N. Poddubny, and Yuri S. Kivshar. Fano resonances in photonics. *Nature Photonics*, 11(9):543–554, Sep 2017.

[48] M. Simoen, C. W. S. Chang, P. Krantz, Jonas Bylander, W. Wustmann, V. Shumeiko, P. Delsing, and C. M. Wilson. Characterization of a multimode coplanar waveguide parametric amplifier. *Journal of Applied Physics*, 118(15):154501, 2015.

[49] Hank Zumbahlen. *The Op Amp*. Elsevier/Newnes Press,, Burlington, MA :, 2008.

[50] S. R. Whiteley. Josephson junctions in spice3. *IEEE*, 23(S):2902, 1991.

[51] David M Pozar. *Microwave engineering; 3rd ed.* Wiley, Hoboken, NJ, 2005.

[52] D. Staelin. .6.013 electromagnetics and applications. spring 2009. License: Creative Commons BY-NC-SA. `https://ocw.mit.edu/`.

[53] Sidney Shapiro. Josephson currents in superconducting tunneling: The effect of microwaves and other observations. *Phys. Rev. Lett.*, 11:80–82, Jul 1963.

[54] P. A. Franken, A. E. Hill, C. W. Peters, and G. Weinreich. Generation of optical harmonics. *Phys. Rev. Lett.*, 7:118–119, Aug 1961.

[55] National Instruments. Instrument fundamentals: Complete guide.

[56] Marc Jankowski, Carsten Langrock, Boris Desiatov, Alireza Marandi, Cheng Wang, Mian Zhang, Christopher R. Phillips, Marko Lončar, and M. M. Fejer. Ultrabroadband nonlinear optics in nanophotonic periodically poled lithium niobate waveguides. *Optica*, 7(1):40–46, Jan 2020.

[57] M Houe and P D Townsend. An introduction to methods of periodic poling for second-harmonic generation. *Journal of Physics D: Applied Physics*, 28(9):1747–1763, sep 1995.

[58] Searbhán Ó Peatáin, Tom Dixon, Phil J. Meeson, Jonathan Williams, Sergey Kafanov, and Yuri A. Pashkin. The effect of parameter variations on the performance of the josephson travelling wave parametric amplifiers, 2021.

[59] C. M. Wilson, G. Johansson, A. Pourkabirian, M. Simoen, J. R. Johansson, T. Duty, F. Nori, and P. Delsing. Observation of the dynamical casimir effect in a superconducting circuit. *Nature*, 479(7373):376–379, Nov 2011.

[60] Marat Khabipov, Victor Gaydamachenko, Christoph Kissling, Ralf Dolata, and Alexander B Zorin. Superconducting microwave resonators with non-centrosymmetric nonlinearity. *Superconductor Science and Technology*, 2022.

[61] Luca Fasolo, Angelo Greco, Emanuele Enrico, Fabrizio Illuminati, Rosario Lo Franco, David Vitali, and Patrizia Livreri. Josephson traveling wave parametric amplifiers as non-classical light source for microwave quantum illumination. *Measurement: Sensors*, 18:100349, 2021.

[62] Arne L. Grimsmo and Alexandre Blais. Squeezing and quantum state engineering with josephson travelling wave amplifiers. *npj Quantum Information*, 3(1):20, Jun 2017.